RECONSTRUCTING THE TOP QUARK IN A SEARCH FOR A PAIR-PRODUCED SUPERSYMMETRIC PARTNER IN THE ALL-HADRONIC PLUS MISSING ENERGY FINAL STATE USING 139 FB^{-1} OF $\sqrt{S} = 13$ TEV PROTON-PROTON COLLISIONS DELIVERED BY THE LARGE HADRON COLLIDER AND COLLECTED BY THE ATLAS DETECTOR

by

JOHAN SEBASTIAN BONILLA CASTRO

A DISSERTATION

Presented to the Department of Physics
and the Graduate School of the University of Oregon
in partial fulfillment of the requirements
for the degree of
Doctor of Philosophy

December 2019

DISSERTATION APPROVAL PAGE

Student: Johan Sebastian Bonilla Castro

Title: Reconstructing the Top Quark in a Search for a Pair-Produced Supersymmetric Partner in the All-Hadronic plus Missing Energy Final State Using 139 fb^{-1} of $\sqrt{s} = 13$ TeV Proton-Proton Collisions Delivered by the Large Hadron Collider and Collected by the ATLAS Detector

This dissertation has been accepted and approved in partial fulfillment of the requirements for the Doctor of Philosophy degree in the Department of Physics by:

Eric Torrence	Chair
Stephanie A. N. Majewski	Advisor
Timothy Cohen	Core Member
Geraldine Richmond	Institutional Representative

and

Kate Mondloch	Interim Vice Provost and Dean of the Graduate School

Original approval signatures are on file with the University of Oregon Graduate School.

Degree awarded December 2019

DISSERTATION ABSTRACT

Johan Sebastian Bonilla Castro

Doctor of Philosophy

Department of Physics

December 2019

Title: Reconstructing the Top Quark in a Search for a Pair-Produced Supersymmetric Partner in the All-Hadronic plus Missing Energy Final State Using 139 fb^{-1} of $\sqrt{s} = 13$ TeV Proton-Proton Collisions Delivered by the Large Hadron Collider and Collected by the ATLAS Detector

The Large Hadron Collider (LHC), the world's most powerful particle accelerator, is operated by the CERN laboratory near Geneva, Switzerland and was built to probe the tera-electron-volt energy scale in search of New Physics. ATLAS is one of several international collaborations at CERN and uses a 7,000-ton general purpose detector to collect collision data from the LHC. The top quark is the most massive particle under the Standard Model and carries the largest Yukawa coupling to the recently discovered Higgs Boson, making it sensitive to effects of heavy new physics.

Supersymmetry offers a diverse class of theoretical models providing potential solutions to the most salient phenomenological inconsistencies of modern particle physics, namely it provides a mechanism for stabilizing the Higgs boson mass while predicting the existence of several new particles at the tera-scale. This dissertation presents a search for the pair production of a supersymmetric partner to the top quark, the stop ($\tilde{t}$), using 139 fb^{-1} of proton-proton collision data collected by the

ATLAS detector during Run 2 of the Large Hadron Collider (LHC) at a center of mass energy of $\sqrt{s} = 13$ TeV.

This dissertation focuses on understanding the hadronic top decay and its reconstruction with the ATLAS trackers and calorimeters, as well as estimating the Standard Model $t\bar{t}$ background to the search in the signal regions design to be sensitive to boosted and semi-resolved top decays. The experimental signature of the search presented is: at least four jets originating from two hadronically-decaying top quarks and large missing transverse energy from the pair of stable, light, and neutral supersymmetric neutralinos (χ_1^0). No excesses over the expected Standard Model predictions were observed and exclusion limits can be placed to stop masses up to 1.25 TeV, assuming a 100% branching fraction of $\tilde{t} \to t\chi_1^0$.

This dissertation includes previously published and unpublished co-authored material.

CURRICULUM VITAE

NAME OF AUTHOR: Johan Sebastian Bonilla Castro

GRADUATE AND UNDERGRADUATE SCHOOLS ATTENDED:

University of Oregon, Eugene, OR (2014-2019)
Stanford University, Stanford, CA (2010-2014)

DEGREES AWARDED:

Doctor of Philosophy, Physics, 2019, University of Oregon
Bachelor of Science, Physics, 2014, Stanford University
Bachelor of Science, Mathematics, 2014, Stanford University

AREAS OF SPECIAL INTEREST:

Physics Beyond the Standard Model
Dark Matter
Top Quark Reconstruction
Science Communication and Outreach
Traditional Cooking
Horticulture

PROFESSIONAL EXPERIENCE:

Graduate Research Assistant, University of Oregon, Eugene, OR (2015-2019)

Graduate Teaching Fellow, University of Oregon, Eugene, OR (2014-2015)

Lead Peer Tutor for Physics and Math, Center for Teaching and Learning, Stanford University, Stanford, CA (2011-2014)

GRANTS, AWARDS AND HONORS:

Graduate Research Fellowship Program – Honorable Mention, National Science Foundation, 2015.

Gates Millennium Scholars Program – Awardee, Bill and Melinda Gates Foundation, Funded 2014-2018 (Awarded 2010).

PUBLICATIONS:

ATLAS Collaboration (2016). Search for the Supersymmetric Partner of the Top Quark in the Jets + E_T^{miss} Final State at $\sqrt{s} = 13$ TeV with the ATLAS Detector. *38th International Conference on High Energy Physics*, CERN Document: ATLAS-CONF-2016-077.

ATLAS Collaboration (2017). Search for a scalar partner of the top quark in the jets plus missing transverse momentum final state at $\sqrt{s} = 13$ TeV with the ATLAS Detector. *Journal of High Energy Physics*, JHEP_135P_0917.

ATLAS Collaboration (2019). Search for new phenomena produced in association with a ttbar pair and large missing transverse energy with no leptons at $\sqrt{s} = 13$ TeV (139 fb^{-1}). *In Progress*

ACKNOWLEDGEMENTS

I wish to dedicate this milestone to my family, as they have been the driving fire behind my success. I thank my parents, Douglas Herberth Bonilla Ramirez and Maria Enid Bonilla Castro, who taught me the value of hard work and planted my curiosity for nature; if it weren't for their sacrifices, I would not have had the opportunity to pursue my education. I also wish to thank my brilliant life partner, Hollis Lindley Gehrett, for her steadfast support, encouragement, and showing me compassion is the best path out of hardship. Thank you to my elder siblings, Karol Tatiana Villanueva Bonilla and Douglas Herbert Bonilla Medina, who have always cared for me and taught me perseverance.

Navigating the academic arena could not have been possible without the guidance of my advisors, past and present, as well as all the teachers who believed in me and encouraged my career as a scientist. I thank my grade school teachers, especially those at Hialeah Senior High School, who pushed me to believe college was attainable. Thank you to my advisor, Prof. Stephanie Alexis Ninos Majewski, for the invaluable advice and mentorship throughout my time in Oregon. I am especially appreciative to Prof. Timothy Cohen for fostering a safe space to learn, and developing my confidence. I would also like to thank Profs. Eric Torrence and Geraldine Richmond for being a familiar source of knowledge and inspiring me to perform the finest research.

To my friends, close and far, I owe an insatiable debt for your patience, attention, and understanding. I would like to extend a special thank you to Anne McGinley for her support and unwavering friendship, Dr. Walter Howard Hopkins for being an exceptional role-model and mentor, and Dr. Edouard Hay

for reminding me that life's pleasures are pivotal to success and happiness. I would also like to acknowledge the help of fellow doctoral candidates Joel Doss, Alice Greenberg, and Kara Zappitelli for being the physicists a friend needs and the friends a physicist needs throughout the years.

I would like to recognize the Gates Millennium Scholars Program for providing the funds for my education, and A Community for Minorities in STEM for the support network to help me feel less far from home. Finally, I thank the University of Oregon's ATLAS group for the space to grow and learn:

- Faculty: Profs. James Brau, Laura Jeanty, Stephanie A. N. Majewski, David Strom, and Eric Torrence.
- Past Students: Drs. Benjamin Allen, Elizabeth Caitlin Brost, John S. Myers, Ian Michael Snyder, and Chaowaroj 'Max' Wanotayaroj.
- Current Students: Jason Barkeloo, Galen Rhoades Gledhill, Marija Glisic, Aaron Kilgallon, Nicholas Luongo, Amanda Steinhebel, and Anni Xiong.
- Postdoctoral Scientists: Drs. Aparajita Dattagupta, Christopher Dudley, Giulia Gonella, Jochen Jens Heinrich, Ismet Siral, and Kate Whalen.

Gracias infinitas a mi familia en Costa Rica, sin ustedes no tuviera estas alas.

¡Pura Vida!

TABLE OF CONTENTS

LIST OF FIGURES

Figure Page

Figure Page

LIST OF TABLES

Table Page

Table Page

When you think of the sky, what do you see?

I picture the night.

My sky has layers of depth;

clouds float close and far,

and the stars twinkle as if affixed

to the velvet curtain of the infinite background.

Are those clouds,

so different in their character,

created in the same nature?

And nebulae?

Are they like my clouds?

Why would they be?

I prefer to wonder,

why would they not be?

Are the threads of the fabric

primordial clouds

at the limit of divinity?

I am arrogant enough to believe

we can understand

what we cannot touch.

I also think there will always be

another storm on the horizon.

I hope we find our way

to think beyond

the clouds we chase.

CHAPTER I

THE STANDARD MODEL OF PARTICLE PHYSICS

Particle physics is the study of the fundamental objects of our universe. Our understanding of these building-blocks has changed considerably since Democritus first argued the existence of indivisible *ἄτομος* (atoms). Our interpretations are born out of and encourage further experiment: J. J. Thomson's "plum-pudding" atomic model was refined through Rutherford-Geiger-Marsden's work with cathode rays into a classical interpretation of electrons orbiting a nucleus, which in turn motivated the integration of relativistic dynamics into fundamental theory.[45][46] Ever since, we have continued to probe nature at smaller and smaller scales in hopes of one day understanding the structure of fundamental particles.

At the turn of the twentieth century, scientists had knowledge of Einstein's relativistic theories and were beginning to interpret nature through the symmetries of Noether's work.[47][48][49][50] The nascent field of particle physics was fertilized with experimental results through the 1900's with results suggesting classical theories of fundamental physics objects needed to be extended to account for new (relativistic) behavior. What physics needed at the time (and still needs today), is guidance in understanding *which* symmetries nature has chosen to respect.

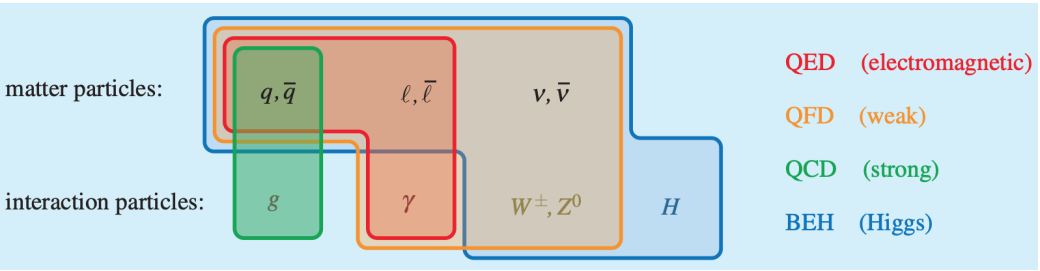

FIGURE 1.1. Connections between particles of the Standard Model.[1]

The Standard Model (SM) of particle physics is the most complete and successful fundamental theory to date. The theory encodes properties of the particles we see in nature (matter) as *fields* existing throughout all space-time. The interactions between the matter particles can be mediated through gauge bosons, some massive (W/Z) and others massless (photon, gluon), or through Yukawa interactions with the newly discovered Higgs boson. The theory is summarized by a *Lagrangian* describing all interactions between the particles (fields). Their connections are summarized in Figure 1.1. One of the most profound characteristics of the SM is its description of the proton as a composite object: it has three valence quarks enveloped by a "sea" of quark-gluon interactions.

1.1. The Symmetries and Lagrangian of the Standard Model

If we think back on nature, particularly on the α^+ and β^- rays Rutherford studied, it is inarguable that natural symmetries exists: the manifest Noether charge of the this symmetry group is the familiar electric charge (Q). Abstractly, this a manifestation of the *rank-1 unitary group* $U(1)$. The difference between *special* unitary groups ($SU(n)$) and their supergroup ($U(n)$) is that the former requires the unit norm of the group to be real valued; complex-valued groups can always be represented by an extension of the corresponding real-valued group $U(N) = SU(N) \otimes U(1)$.

An important motivator behind the choice of symmetries considered by the SM Lagrangian was Lorentz invariance. Since there are six generators of the Lorentz group, three spatial boosts and three rotations, we can associate it with the SO(4) group. Interestingly, one can also create a group with six generators by introducing *handedness* to $SU(2)$ groups, i.e. $SO(4) = SU(2)_L \otimes SU(2)_R$. This

is useful because we notice a similar handedness behavior in naturally occurring electroweak (EW) processes.

The full form of the SM Lagrangian can be compactly written as as a concatenation of a few terms and their hermitian conjugates ($H.C.$): the gauge covariant kinetic terms (Kinetics and Gauge-Interactions), the Higgs potential (Higgs), and the Yukawa couplings (Yukawa):[1]

$$\begin{aligned}\mathcal{L} = &-\frac{1}{4}F_{\mu\nu}F^{\mu\nu} + i\bar{\psi}\not{D}\psi + H.C. \text{ (Kinetics and Gauge-Interactions)} \\ &+ |D_\mu\phi|^2 + V(\phi) \text{ (Higgs)} \\ &+ \psi_i y_{ij}\psi_j\phi + H.C. \text{ (Yukawa)}.\end{aligned} \tag{1.1}$$

The first line encodes the massless vector-gauge fields into $F^{\mu\nu}$ and their interactions with the matter spinor-fields (ψ) through the $\not{D}$ operator, further detailed in Section 1.2. Spontaneous symmetry breaking, described in Section 1.3, results from a complex scalar doublet boson (ϕ) with a non-zero vacuum expectation value (VEV). Section 1.4 details how this scalar doublet, commonly referred to as the Higgs boson, can generate mass terms forbidden by gauge-invariance through Yukawa couplings (y_{ij}).

1.2. Kinetic Interactions of the Standard Model

For each gauge-symmetry of the theory, we write down a field tensor $F^{\mu\nu}$ in the Lagrangian: for the $SU(3)$ group of the strong force there are eight gluon fields G^a_μ, whereas the electroweak groups $SU(2)$ and $U(1)$ produce three W^i_μ fields and one B_μ (respectively). The interaction terms of Equation 1.1 are the only ones allowable by gauge invariance and prohibit mass terms from appearing explicitly

Field	$SU(3)$	$SU(2)$	$U(1)_Y$
$L = \begin{pmatrix} \nu_L \\ e_L \end{pmatrix}$	-	$\square$	$-\frac{1}{2}$
e_R	-	-	-1
ν_R	-	-	0
$Q = \begin{pmatrix} u_L \\ d_L \end{pmatrix}$	$\square$	$\square$	$\frac{1}{6}$
u_R	$\square$	-	$\frac{2}{3}$
d_R	$\square$	-	$-\frac{1}{3}$
ϕ (H)	-	$\square$	$\frac{1}{2}$

TABLE 1.1. The group charges of SM fields. The $\square$ symbol indicates the field transforms in the fundamental representation of the group, and - indicates the field is uncharged.[36]

in the Lagrangian. The slashed gauge covariant derivatives operator, $\not{D}_\mu$, encodes Lorentz invariance for fermions in the Lagrangian. The total $SU(3)_C \otimes SU(2)_L \otimes U(1)_Y$ gauge covariant derivative depends on the massless gauge fields and their couplings (g_C, λ_α, g_L, σ_j, and g_Y) :

$$D_\mu = \partial_\mu - ig_C\lambda_\alpha G^\alpha_\mu - ig_L T_j W^j_\mu - \frac{i}{2} g_Y Y \ B_\mu. \tag{1.2}$$

For each fermion in the model, there is an interaction term; the charges we set on each of the fermions are inspired by the phenomena we measure. For example, leptons are assigned no color charge and thus do not contribute to the terms involving G^α_μ. A summary of the gauge-charges associated to each of the SM matter fields is show in Table 1.1.

The chiral nature (handedness) of the SM is manifests due to the fact that left-handed fermions are doublets under weak interactions, while the right-handed components are singlets. A theory exhibiting this effect is known as a *chiral gauge theory*. We combine the left-handed $SU(2)_L$ group with $U(1)_Y$, where Y is the hyper-charge, and we associate the residual symmetry after EW symmetry breaking

with the EM charge (Q). The physical bosons of the broken symmetry are the massive $W^{\pm}$ and Z, and the massless photon.

1.3. Spontaneous Symmetry Breaking and the Higgs Boson

A spontaneously broken symmetry is so-called because the original global symmetry is broken with a particular choice of the potential and its minimum. The spontaneity refers to the fact that the symmetry in question is respected at high energies, but broken at some lowerer energy scale. The mechanism yields massless *goldstone bosons*[51], one for every generator of the broken symmetry: for the case of electroweak symmetry breaking (EWSB), the symmetries $SU(2)_L \otimes U(1)_Y$ provide the generators $(W_\mu^{1,2,3}, B_\mu)$ forming the covariant derivative of Equation 1.2. The second line of the Lagrangian in Equation 1.1 contains the symmetry breaking mechanism. The complex scalar field $\phi(H)$ creates a potential $V(\phi)$:

$$V(\phi) = -\frac{1}{2}\mu^2\phi^\dagger\phi + \frac{1}{4}\lambda(\phi^\dagger\phi)^2, \tag{1.3}$$

where μ and λ are the mass and self-coupling parameters.

The field settles into its *vacuum expectation value* (VEV) at the minimum of this potential:

$$\text{VEV} \equiv v \equiv \frac{\mu^2}{\lambda} \text{ such that } \langle\phi\rangle = \frac{1}{\sqrt{2}}\begin{pmatrix} 0 \\ v \end{pmatrix}. \tag{1.4}$$

Figure 1.2 shows the shape of the potential for a choice of $|\lambda| > 0$ and $|\mu| < 0$, exemplifying how a non-zero VEV can be achieved.

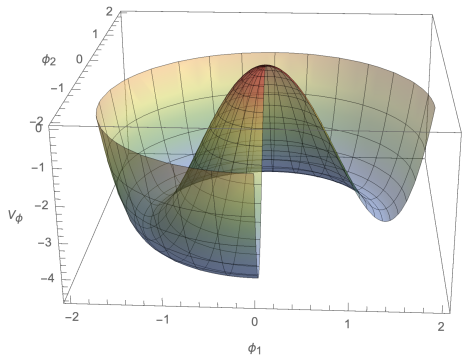

(a)

FIGURE 1.2. Spontaneous symmetry breaking potential well shape.

The complex scalar field can be written in terms of the VEV,

$$\phi = \begin{pmatrix} \phi_1 \\ \phi_2 \end{pmatrix} = \frac{1}{\sqrt{2}} \begin{pmatrix} 0 \\ v + h \end{pmatrix}. \tag{1.5}$$

Geometrically, this choice is one point along the minimum equipotential ring of Figure 1.2.

If we expand the gauge covariant derivative about this scalar field representation, we encounter a dependence on the VEV:

$$\begin{aligned} (D^\mu \phi)^\dagger (D_\mu \phi) &= \frac{v^2}{8} \left| \begin{pmatrix} g_L W_\mu^1 - i g_L W_\mu^2 \\ -g_L W_\mu^3 + g_Y B_\mu \end{pmatrix} \right|^2 \\ &= \frac{v^2}{8} \left(g_L^2 \left(\left(W_\mu^1\right)^2 + \left(W_\mu^2\right)^2 \right) + g_Y \left(W_\mu^3 - g_Y B_\mu \right)^2 \right). \end{aligned} \tag{1.6}$$

For a non-zero VEV, the four massless electroweak goldstone bosons are mixed to produce three massive bosons (the $W_\mu^\pm$ and Z_μ) and a massless A_μ.

$$W_\mu^\pm \equiv \frac{1}{\sqrt{2}}\left(W_\mu^1 \mp iW_\mu^2\right) \text{ such that } m_W = \frac{g_L v}{2}, \tag{1.7}$$

$$Z_\mu \equiv \frac{1}{\sqrt{g_L^2+g_Y^2}}\left(g_Y W_\mu^3 + g_L B_\mu\right) \text{ such that } m_Z = \frac{v}{2}\sqrt{g_L^2+g_Y^2}, \tag{1.8}$$

$$A_\mu \equiv \frac{1}{\sqrt{g_L^2+g_Y^2}}\left(g_Y W_\mu^3 + g_L B_\mu\right) \text{ such that } m_A = 0. \tag{1.9}$$

Since we have measured the masses of the W and Z bosons, we know the VEV value to be

$$v = 246 \text{ GeV}. \tag{1.10}$$

Furthermore, we can interpret the mass of the physical Higgs boson to be

$$m_h^2 = -2\mu^2 = \lambda v^2. \tag{1.11}$$

In 2012, the ATLAS and CMS collaborations discovered a new scalar particle with a mass of 125 GeV.[52][53] The new particle has been shown to have properties characteristic to the *Higgs* boson mediating the EWSB described above.

The SU(3) symmetry of the strong force is unaffected by the spontaneous symmetry breaking of the other groups, yielding massless gluons.

1.4. The Yukawa Interaction and Fermion Mass Generation

The gauge invariance of the SM symmetries prohibit explicit fermion mass terms, such as $m\bar{\psi}\psi$. The Yukawa interaction is a creative work-around to this problem, it assumes the existence of a scalar field ϕ coupling to both chiral fermion

fields ψ_L, ψ_R. After EWSB, the chiral symmetry is broken and the non-zero VEV creates Lagrangian terms of the form

$$\begin{aligned} \mathcal{L} &\propto \bar{\psi}_L y_{ij} \psi_R \phi + H.C. \rightarrow \bar{\psi}_L y_{ij} \psi_R (\phi + v) + H.C. \\ &= (\bar{\psi}_i y_{ij} \psi_j \phi + H.C.) + (\bar{\psi}_i y_{ij} \psi_j v + H.C.). \end{aligned} \tag{1.12}$$

The terms proportional to ϕ are Higgs-fermion interactions, whereas those proportional to v are the mass couplings parameterized through matrix elements (y_{ij}). The masses of the various quarks are obtained by connecting the term in the Lagrangian with the measured mass of the fermion,

$$m_f = y_f \frac{v}{\sqrt{2}}. \tag{1.13}$$

More precisely, there are three sets of Yukawa matrices (Y_U, Y_D, Y_E). Two result from the left-handed quarks (Q_L) interacting with up- versus down-type right-handed quarks (u_R, d_R) through the Higgs (ϕ), and the rest are due to the left-handed leptons (L_L) interacting with right-handed leptons (e_R) through the Higgs:

$$\mathcal{L} \propto \bar{Q}_L Y_U u_R \tilde{\phi} + \bar{Q}_L Y_D u_R \tilde{\phi} + \bar{L}_L Y_E e_R \tilde{\phi} + H.C.. \tag{1.14}$$

For the quarks, the up and down type matrices are diagonalized differently and their bases outer-product forms the unitary 3x3 Cabbibo-Kobayashi-Maskawa (CKM) matrix,

$$V \equiv U_{uL} U_{dL}^{\dagger}. \tag{1.15}$$

The off-diagonal entries quantifies the strength of electroweak interaction (mixing) between quark flavors, also known as *charged-current flavor changing interactions*, and explains the decays of second and third generation quarks.

Revisited in Section 2.1, these Yukawa interactions appear in radiative corrections to the Higgs mass. The top quark has the largest Yukawa coupling of any fermion and therefore could provide the greatest sensitivity to physics beyond the Standard Model.

1.5. Fundamental Particles of the Standard Model

In the previous sections, I have summarized the field theory of the Standard Model. The particles we see in nature are interpreted to be manifestations of the fundamental fields at various energy scales. We assigned the charges of the natural particles to the fundamental fields of the theory, and measure observables of the scale-dependent Lagrangian terms to test its validity. In the SM, left-handed fermions are grouped into doublets and their right-handed partners are singlets. When we measure the mass of a particle, we are probing the Yukawa mass term mixing both fermion chiral states.

Each of the fundamental fermion fields of Table 1.1 are assigned quantum properties to match their interactions with the gauge bosons:

- Spin (J) describes an intrinsic angular momentum. Bosons have integer spin and fermions fractional. A scalar particle has spin-0, a spinor (matter fermion) has spin-$\frac{1}{2}$, and the gauge bosons have spin-1.

- Weak-Charge (I_3) describes the handedness of the field. Left(right)-handed particles are assigned $+(-)\frac{1}{2}$ charge.

– Hypercharge (Y) is the $U(1)$ quantum charge. After EWSB, the residual $U(1)$ symmetry is interpreted as the electric charge (Q). The charges are related through $Q = I_3 + Y$.

– Color is the charge corresponding to the $SU(3)$ QCD gauge symmetry; the gluon carries two color charges and quarks one.

QCD is asymptotically free at short distances, meaning that colored objects can propagate freely within the proton. On the other hand, quarks and gluons *hadronize* and form colorless, multi-parton bound states as they propagate over long distances. The exception to this is the top quark, whose large mass allows for an on-shell W-decay before it hadronizes. In experiment we cannot see the bare quark, rather we observe their bound states or decays. Leptons can exist in their bare state, although neutrinos oscillate between their flavors as they traverse space. Table 1.2 below summarizes some physical properties of the fundamental particles we have discovered so far. For compactness, only the left-handed quarks and leptons are listed in the table.

1.6. Successes of the Standard Model

Despite our intentions to discover physics beyond the Standard Model, the half-a-century-old theory is resoundingly successful. After the W boson was discovered at CERN, the arguments of a four-generator EWSB mechanism guided the field to the discovery of the Z boson at precisely the mass described in Equation 1.8.[54] With three massive bosons in hand, the Standard Model required the existence of the scalar behind the symmetry breaking, which was the primary

Type	Mass	Lifetime	Q	J	Y	P	Color
e	0.511 MeV	stable	-1	$1/2$	$-\frac{1}{2}$	$-1/2$	0
ν_e	small	oscillates	0	$1/2$	$-\frac{1}{2}$	$+1/2$	0
μ	106 MeV	$\mathcal{O}(10^{-6})s$	-1	$1/2$	$-\frac{1}{2}$	$-1/2$	0
ν_μ	small	oscillates	0	$1/2$	$-\frac{1}{2}$	$+1/2$	0
τ	1776 MeV	$\mathcal{O}(10^{-13})s$	-1	$1/2$	$-\frac{1}{2}$	$-1/2$	0
ν_τ	small	oscillates	0	$1/2$	$-\frac{1}{2}$	$+1/2$	0
u	2.2 MeV	stable	$+2/3$	$1/2$	$+1/3$	$+\frac{1}{2}$	r/g/b
d	4.7 MeV	$\mathcal{O}(10^{-8})$s	$-1/3$	$1/2$	$+1/3$	$-\frac{1}{2}$	r/g/b
s	95 MeV	$\mathcal{O}(10^{-8})$s	$-1/3$	$1/2$	$+1/3$	$-\frac{1}{2}$	r/g/b
c	1.275 GeV	$\mathcal{O}(10^{-12})$s	$+2/3$	$1/2$	$+1/3$	$+\frac{1}{2}$	r/g/b
b	4.18 GeV	$\mathcal{O}(10^{-12})$s	$-1/3$	$1/2$	$+1/3$	$-\frac{1}{2}$	r/g/b
t	173 GeV	$\mathcal{O}(10^{-25})$s	$+2/3$	$1/2$	$+1/3$	$+\frac{1}{2}$	r/g/b
γ	0	stable	0	1	0	0	0
$W^\pm$	80.4 GeV	$\mathcal{O}(10^{-25})$s	±1	1	0	±1	0
Z	91.2 GeV	$\mathcal{O}(10^{-25})$s	0	1	0	0	0
g	0	-	0	1	0	0	double ($c\bar{c}$)
H	125 GeV	$\mathcal{O}(10^{-22})$s	0	0	+1	$-\frac{1}{2}$	0

TABLE 1.2. The quantum numbers of SM particles. For all quarks except the top, the lifetime is take to be that of the simplest meson containing the quark at hand ($\pi^\pm, K^\pm, D^\pm, B^\pm$).

motivator for building the Large Hadron Collider.[55] Figure 1.3 shows a summary of recent SM measurements performed by the ATLAS collaboration, none of the analyses to date show significant deviation from SM predictions.

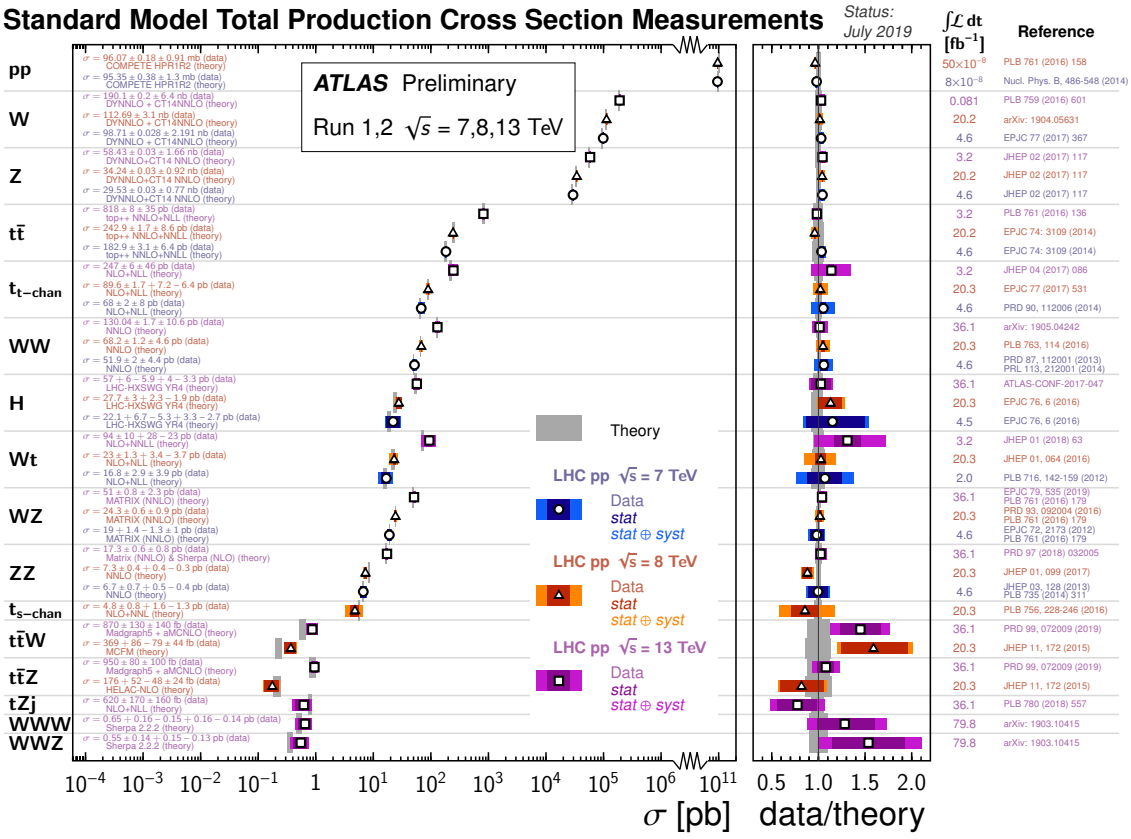

FIGURE 1.3. Summary of Standard Model analyses results measured by the ATLAS Collaboration.[2]

CHAPTER II

PHYSICS BEYOND THE STANDARD MODEL

The Standard Model attempts, very successfully, to explain the physical phenomena produced at experiments throughout the years. It explains the Strong, Weak, and Electromagnetic forces under a single Lagrangian, while providing a mechanism for fermion masses through the Higgs boson. Still, there are a number of issues to point out that suggest the theory is not the complete representation of the universe we perpetually strive to find.

- Fine-Tuning of the Higgs Mass: The measured mass of the Higgs is approximately 125 GeV, but the scale-dependent radiative corrections need to be precisely tuned to arbitrarily high precisions. This is described in more detail in Section 2.1.

- Non-Zero Neutrino Masses: Ever since the discovery of neutrino oscillations, we know that these neutral leptons bear non-zero masses.[56] As fermions, neutrinos can acquire masses through the Higgs Mechanism. The problem with this mechanism is that the Higgs' Yukawa couplings to neutrinos would inexplicably be $\frac{m_\nu}{m_t} \sim 10^{-10}$ times smaller than that of the top quark. There are other extensions to the SM that can explain the minuscule masses of the neutrinos, but none have been experimentally verified to date.

- Gravity: It is possible to include a tensor gauge field (in contrast to the vector fields of the other three forces) into the Lagrangian of the SM. We notice that gravitational interactions are subdominant to any of the other

forces. We have to ask the question that the SM fails to explain, why is gravity so weak?

- Dark Matter: Later described in Section 2.2, Dark Matter is the term used to explain gravitationally-interacting non-luminous material. There is no particle in the SM that exhibits the characteristics, and more importantly the abundance, of the observed phenomena.

- Unification: We are often driven to explain seemingly different phenomena as a single fundamental process. For example, the SM successfully unifies the weak interactions with electromagnetism at the EWSB scale. We are then tempted to hope that at some energy scale exists in which the strong force is unified with the electroweak, a feature absent from the SM.

The search presented in this dissertation is motivated by these outstanding questions, turning to supersymmetry as a potential solution to some of them.
In the following sections I will elaborate on some of these motivating issues.
Supersymmetry predicts a collection of new particles that contribute with opposite signs to the radiative correction than their SM partners, mitigating the problem of Higgs' fine-tuning. By enforcing R-parity, explained in Section 2.3.1, we ensure that one of these new particles is neutral and stable (Dark Matter candidate).

2.1. The Hierarchy and Naturalness Problems

Quantum Field Theories (QFTs) often lead to divergent integrals at short distances (high energies), but there are ways to systematically address some of these issue to make predictions about long-distance (low energy) physics. Renormalization is the processes of formally eliminating all such divergences,

ensuring consistent observable calculations regardless of the scheme used to do so. The Standard Model is a renormalizable theory.

Λ_{UV} is the parameter used to characterize ultra-violet (short-distance) behavior of divergences and sets the upper energy scale of the theory. When we write the renormalized form of the Lagrangian, part of the expression is scheme dependent and the rest depends on Λ_{UV} logarithmically or stronger:

$$\mathcal{L}_{Renormalized} = \mathcal{L}_{invariant} + \mathcal{L}_{log}(\ln \Lambda_{UV}) + \mathcal{L}_1(\Lambda_{UV}) + \mathcal{L}_2(\Lambda_{UV}^2) + \cdots . \tag{2.1}$$

The first term is finite and calculable. The logarithmically divergent term contains dimensionless operators (e.g. gauge and Yukawa). The remaining terms are of dimensionfull quantities of increasing order/rank.

The mass parameter of the SM scalar Higgs doublet (μ) is UV-sensitive. More specifically, the Higgs boson physical mass ($m_{H,phys} \approx$ 125 GeV) is affected by all massive particles through quantum corrections; the crux of the problem is that this effect appears at all scales and requires significant *fine-tuning* dependent on Λ_{UV}.

$$m_{H,phys}^2 = -2\mu^2 \;=\; m_{bare}^2 + \sum_{fermions} k_f m_f^2 + \sum_{bosons} k_b m_b^2 \tag{2.2}$$

$$= \quad + \quad + \quad + \tag{2.3}$$

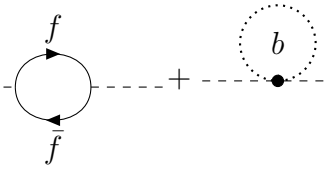

$$= \; m_{H,bare}^2 - \frac{|\lambda_f|^2}{8\pi^2}\Lambda_{UV}^2 + \frac{|\lambda_b|^2}{8\pi^2}\Lambda_{UV}^2 \tag{2.4}$$

The *naturalness problem* with the Higgs mass is that the left hand side of the equation is on the order of 100 GeV^2, but the right side is explicitly dependent on an arbitrarily large Λ_{UV}. The problem of fine-tuning is present as all scales: for any

choice of renormalization scale, the ever-growing scale-dependent terms must be balanced (fine-tuned) to arbitrarily high precision to result in an EW-scale value. In short, the theory requires a mysterious balance of very large numbers to yield a measurable, real, and (relatively) small number.

Spontaneous symmetry breaking of the electroweak force, as described in Section 1.1, explains the masses of the W^+, W^-, and Z bosons. The measured masses of the electroweak bosons set the vacuum expectation value at 246 GeV. This natural scale of the electroweak force is closely related to the physical measured value of the scalar boson mass.

Particle physicists often refer to *the hierarchy problem* as a motivator for physics beyond the Standard Model. Crudely, the hierarchy problem is a lack of explanation behind a clear order in nature. For example, the mass difference between the W and Z electroweak bosons is explained by the scale of the Higgs VEV. Still, no such explanation exists for the physical mass of the scalar boson observed at $\sim$ 125 GeV. In this dissertation, many issues related to the he problems remain and motivate the search presented:

- What mechanism 'protects' the mass of the Higgs to the GeVscale? A symmetry can 'protect' contributions from problematic, high energy terms by forbidding (or adding) certain Lagrangian terms such as Dirac masses. For the case of fermion masses, chiral symmetry offer the protection. Does one such mechanism exist for the Higgs mass?

- Why is the scale of gravity so weak compare to the other forces? In practice one can set couplings to take on the relatively small values we need to make the theory compatible, but there is no fundamental reason in the theory behind the hierarchy of the force strengths.

2.2. Dark Matter

Gravity is compatible with the SM and we can assume its effects are negligible at the scales relevant to collider experiments. However, gravitational interactions of baryonic matter do not explain the astrophysical evidence for Dark Matter. This term is used as a catch-all phrase for gravitationally interacting, non-luminous matter that is measured to be almost five times as abundant as baryonic matter.[57] Two examples of clear evidence for Dark Matter comes from astrophysical observations. The first is the series of observations made by Vera Rubin in the late 1960's and early 1970's.[58] She found that the stars rotating around galaxies did not follow the classical gravitational velocities and could not be reconciled with relativistic approximations or cold hadronic matter (planets, dust, etc.). More specifically, the orbital velocity (v) of a star around a galaxy of radius (r) depends in the amount of mass density (ρ) within the Gaussian sphere,

$$M(r) = 4\pi r^2 \rho \tag{2.5}$$

$$v(r) = \sqrt{\frac{M(r)}{r}} \propto \sqrt{r}. \tag{2.6}$$

If a star's orbit is beyond the mass core of the galaxy, we expect the mass to approach a limit $M(r \to R_{galaxy}) \sim M_{lumi}$. Beyond this radius we expect the object to behave as if it were orbiting a massive point source,

$$v(r) = \frac{M_{lumi}}{r} \propto \frac{1}{r}. \tag{2.7}$$

When measuring the orbital velocities of starts in and outside the core, one would expect the behavior to change at R_{galaxy}, which is the size of the luminous mass

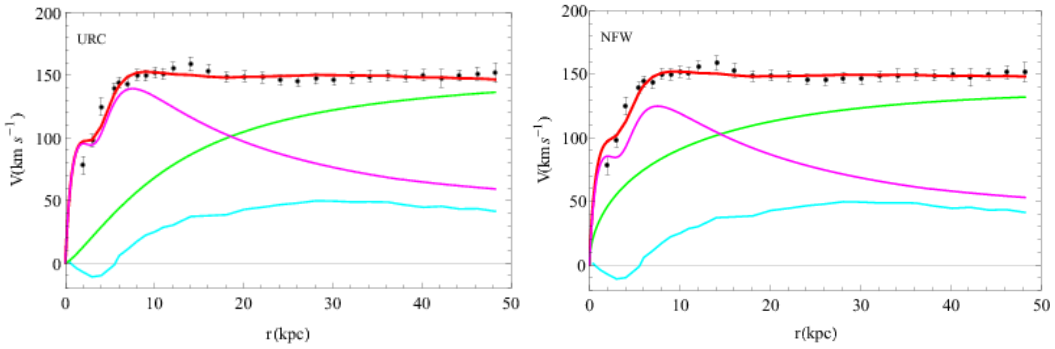

(a) URM Stellar Rotation Modeling (b) NFW Stellar Rotation Modeling

FIGURE 2.1. Measured orbital velocity of stars within the galaxy NGC 3198. The data is fit to the Universal Rotation Curve (URC, left) and Navarro–Frenk–White (NFW, right) mass models (red lines) by considering the halo cored component (green lines), the stellar disk (magenta lines), and the neutral hydrogen disk (cyan line). Stellar orbital velocities are compared to their distance from galaxy center. The behavior behaves as $\sqrt{r}$, suggesting diffuse non-luminous gravitationally interacting matter.[3]

core of the galaxy. What Vera saw in her data was that the velocities were much larger and behaved as $v \propto \sqrt{r}$ beyond $r > R_{galaxy}$. At first, the discrepancy was attributed to dust, planets, and other non-stellar objects, but the contributions of these sources have been since measured to be too small to explain the observations. Today, we believe there exists diffuse, gravitationally interacting, non-luminous (dark) matter that forms a *halo* extending beyond the luminous edges of a galaxy. If one adds this extraneous *Dark Matter*, the orbital velocities of the outer most stars orbit behave as $v \sim \sqrt{r}$, which is consistent the observation. Recent measurements of stellar rotations have continued to suggest the existence of Dark Matter, as shown in Figure 2.1.

The second example is the Bullet Cluster, shown in Figure 2.2, which shows how two types of matter are stratified as galaxy clusters pass through each other. The baryonic matter is decelerated through SM-interactions, but a halo of weakly-interacting matter can still be detected through its gravitational lensing.[59]

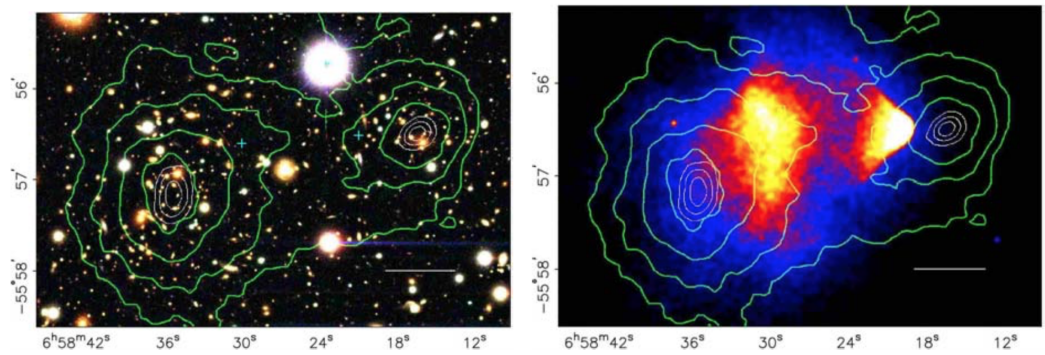

(a) Bullet Cluster in visible frequencies. The contours are gravitational equipotentials.

(b) X-ray frequency image of the Bullet Cluster superimposed with gravitational lensing contours.

FIGURE 2.2. Galaxy cluster 1E0657-558, also known as the Bullet Cluster. Two galaxy clusters collided, forming gas shock-waves and separating the gravitational center (contour centroids) from the luminous, interacting matter (false color).[4]

2.3. Supersymmetry as an Extension to the Standard Model

Up to this point I have detailed issues with the Standard Model that urge us to believe there must be more to nature to what we know, but I have not proposed a concrete solution. How exactly do we fix the hierarchy problem, if it seems that each new fermion just adds to the problem? Although the SM explains the masses of fermions and electroweak bosons, it does not come close to explaining the physical evidence for Dark Matter.

In the following subsections, I will explain the theoretical structure and select features of *supersymmetry* (SUSY). In particular, I will motivate the theory as a solution to the UV-sensitivity of the Higgs boson bare mass (the so-called hierarchy problem).

2.3.1. Superpartners to SM Particles

Supersymmetry (SUSY) assumes a fundamental connection between fermions and bosons: for each SM fermion (boson) field there exists a new SUSY boson (fermion) field with identical properties save the differing spins. In addition, one can consider multiple super-symmetries of the universe but we will consider just the single SUSY in our SM extension.

The simplest choice of field structure, called *chiral/matter* super-multiplets, has $n_B = n_f = 2$ degrees of freedom and is formed by partnering a fermion with two real scalars (equivalent to a single complex scalar). The next simplest structure, the *gauge/vector* multiplet, has the same number of degrees of freedom and swaps the complex scalar for a vector boson, which must be massless (prior to SSB) in order to conserve gauge invariance. One may be curious if it is possible to pair a SM gauge-boson with a spin-$^3/_2$ fermion, but this leads to inconsistencies.

To assign SM particles to their appropriate super-multiplets and identify their super-partners, we recognize that all SM fermions must reside in chiral super-multiplets. This is due to the fact they are the only structures with the transformation properties matching the observed SM particles (i.e. left- and right-handed fermions transforming differently). The super-partners of SM gauge-bosons are called *gauginos* and belong in *gauge* multiplets. One can construct higher order super-multiplets, but these have been shown to be reducible to the above two structures. Reflecting this organization scheme, we call the scalar super-partners to SM fermions sfermions ('s' for scalar) and the spin$-^1/_2$ super-partners to the SM gauge bosons gauginos ('ino' meaning '-like'). A summary of the SUSY particles is listed in Table 2.1.

Super-Multiplet		spin-0	spin-$\frac{1}{2}$	$SU(3)_C$, $SU(2)_L$, $U(1)_Y$
(s)quarks	Q	$\left(\tilde{u}_L, \tilde{d}_L\right)$	(u_L, d_L)	$\left(3, 2, \frac{1}{6}\right)$
	$\bar{u}$	$\tilde{u}_R^*$	$u_R^\dagger$	$\left(\bar{3}, 2, -\frac{2}{3}\right)$
	$\bar{d}$	$\tilde{d}_R^*$	$d_R^\dagger$	$\left(\bar{3}, 2, \frac{1}{3}\right)$
(s)leptons	L	$(\tilde{\nu}, \tilde{e}_L)$	(ν, e_L)	$\left(1, 2, -\frac{1}{2}\right)$
	$\bar{e}$	$\tilde{e}_R^*$	$e_R^\dagger$	$(1, 1, 1)$
Higgs(inos)	H_u	(H_u^+, H_u^0)	$\left(\tilde{H}_u^+, \tilde{H}_u^0\right)$	$\left(1, 2, \frac{1}{2}\right)$
	H_d	$\left(H_d^0, H_d^-\right)$	$\left(\tilde{H}_d^0, \tilde{H}_d^-\right)$	$\left(1, 2, -\frac{1}{2}\right)$

TABLE 2.1. Particle contents of a minimal SUSY theory.

2.3.2. Stabilizing the Higgs Mass

We described the naturalness and hierarchy problems relating to the Higgs mass in Section 2.1 and can be summarized by

$$m_{H,phys}^2 = m_{bare}^2 + \sum_{fermions} k_f m_f^2 + \sum_{bosons} k_b m_b^2 \tag{2.8}$$

$$= \quad + \quad + \quad . \tag{2.9}$$

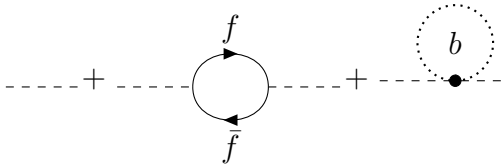

When calculating the bare mass of the Higgs boson, each additional fermion coupling to the scalar through terms of the form $\lambda_f \phi_H \bar{f} f$ adds a non-zero contribution to the sum:

$$\Delta m_{H,bare}^2 = -\frac{|\lambda_f|^2}{8\pi^2}\Lambda_{UV}^2. \tag{2.10}$$

A massive scalar coupling to the Higgs field through a term of the form $\lambda_s |\phi_H|^2 |\phi_s|^2$ likewise adds a non-zero contribution to the sum:

$$\Delta m_{H,bare}^2 = \frac{\lambda_s}{16\pi^2}\left[\Lambda_{UV}^2 - 2m_s^2 \ln {}^{\Lambda_{UV}}/_{m_s} + \dots\right]. \tag{2.11}$$

Notice the differing absolute sign of the two expressions; fermions contribute negative contributions and scalar positive ones. Each of these terms is unique to the fundamental particle at hand, and their sum yields an arbitrarily large number that must be fine-tuned to result in the electroweak scale.

SUSY balances the terms by postulating that for each SM fermion (boson) there exists a SUSY boson (fermion) that contributes with an opposite sign to the Higgs' radiative corrections. However, the masses of the new SUSY particles do not need to be the same. In this broken-SUSY, we trade the sensitivity of the Higgs mass to the renormalization scale with the mass differences between SM particles and their SUSY partners.

2.3.3. R-Parity

The Standard Model has an accidental symmetry (emergent, rather than enforced) leading to Baryon (B) and Lepton (L) number conservation. In contrast to the SM, gauge-invariance does not prohibit B- or L-violating terms to appear in the SUSY Lagrangian. An example B-violating term that can be included in the super-potential $\mathcal{V}^{SUSY}$ for a theory with quark super-multiplets carrying $Q_{i,B} = \frac{1}{3}, \tilde{u}_{i,B} = \tilde{d}_{i,B} = -\frac{1}{3}$ is

$$B - Violating : \mathcal{V}^{SUSY}_{\Delta B=1} \propto \frac{1}{2}\lambda^{ijk}_{B}\tilde{u}_i\tilde{d}_j\tilde{d}_k. \tag{2.12}$$

Similarly, we can introduce L-violation through the following term for lepton super-multiplets carrying $L_{i,L} = 1$

$$L - Violating : \mathcal{V}^{SUSY}_{\Delta L=1} \propto \frac{1}{2}\lambda^{ijk}L_iL_j\tilde{e}_k + \lambda^{ijk}_{L}L_iQ_j\tilde{d}_k + \mu^{i}_{L}L_iH_u. \tag{2.13}$$

The most direct consequence of these L/B-violating terms with unsuppressed $\lambda_L^{ijk}, \lambda_B^{ijk}$, and μ_L^i couplings is that the SM up quark, and therefore the proton, is no longer stable. Without conserving these quantities, SUSY interactions provide a decay pathway for the proton. The proton's lifetime has been measured to be much longer than the current age of the universe, motivating us to enforce a symmetry prohibiting the B/L-violating terms.

One possible symmetry conserving Baryon and Lepton number is *matter-parity*, which assigns to each field a conveniently-defined quantum number encoding B/L-conservation:

$$P_M = (-1)^{3(B-L)}. \tag{2.14}$$

All quark and lepton super-multiplets are set to carry $P_M = -1$, while the Higgs super-multiplets bear $P_M = +1$; the gauge super-multiplets do not carry either B or L-number and consequently carry $P_M = +1$. This B- and L-conserving symmetry could be extended by including spin and defining *R-parity*:

$$P_R = (-1)^{3(B-L)+2s}. \tag{2.15}$$

This definition is equivalent to Equation 2.14, since the product $(-1)^{2s}$ of particles involved in any angular-momentum-conserving vertex is necessarily positive. The subtly occurs within the super-multiplets: with P_R the component particles of a super-multiplet no longer have the same quantum number. Therefore, the R-parity conserving theory has SM-like particles (including the Higgs) with $P_R = +1$, whereas the new sparticles have opposite parity $P_R = -1$. R-parity conserving SUSY, as in the models considered for this dissertation, each vertex (interaction) must conserve the parity charge.

For the purpose of the search presented in this dissertation, the primary phenomenological consequences are as follows:

- Sparticle pair-production: If we begin with only SM particles (protons at the LHC), the R-parity is $P_R = +1$. If there is to be any sparticle production, the process must be R-parity positive. Therefore, a sparticle cannot be produced singly; it must be produced in association to another sparticle, e.g. $pp \rightarrow \tilde{g}\tilde{g},\ \tilde{g}\tilde{q}, or\ \tilde{q}\tilde{q}$.

- Stable LSP: When a sparticle is produced, it carries opposite R-parity to all SM particles. Thus, the final state must include a particle whose R-parity opposes any SM particle. In other words, there necessarily exists a *least-massive stable particle* (LSP) at the end of every SUSY decay chain.

- Dark Matter Candidate: The LSP is defined as the lightest particle carrying $P_R = -1$, and since this quantity must be conserved the LSP is stable. If the LSP is neutral and does not interact at tree level with photons. However, the LSP is free to interact gravitationally. This makes it an attractive candidate explaining the gravitationally-interacting particulate matter we call Dark Matter.

2.3.4. SUSY Breaking

We clearly do not live in a universe with unbroken SUSY, since we have looked and see no evidence of partner particles at the masses of already-discovered particles. As is true for many symmetries of nature, SUSY is restored at high energies and broken at low energies. To provide a realistic SUSY theory, we need to add SUSY-invariant terms to the Lagrangian that spontaneously break

at high energies. In the SM, a single complex scalar field with a non-zero VEV leads to a unique spontaneous symmetry breaking mechanism. In SUSY, there are two types of auxiliary fields (D and F) that can produce a variety of SUSY-breaking mechanisms: D-type SUSY-breaking is due to gauge super-multiplets, whereas F-type mechanisms arise from chiral super-multiples having non-zero VEVs. Some example SUSY models, their symmetry breaking strategies, and their characteristics are:

- Gauge-Mediated: F-type mechanism with a gravitino LSP. The masses of the squarks' and sleptons' depend solely on their gauge properties, creating the mass degeneracy with natural suppression of flavor violations in the SUSY sector.

- Gravity-Mediated: F-type mechanism sometimes referred to as mSUGRA (minimal SUper-GRAvity). It reduces the number of free parameters to a handful and is heavily constrained by experiment.

- Extra-Dimensions: D-type mechanism in a framework with 11 space-time dimensions. The theory claims that SM particles and forces are bound to a four-dimensional membrane, whereas weakly interacting fields can propagate across the entire space.

- MSSM: Both D- and F–type mechanisms are possible for the class of minimal supersymmetric theories. An attractive feature is that the gauge couplings unify at a high energy scale. Further details on the MSSM are available in Appendix A.

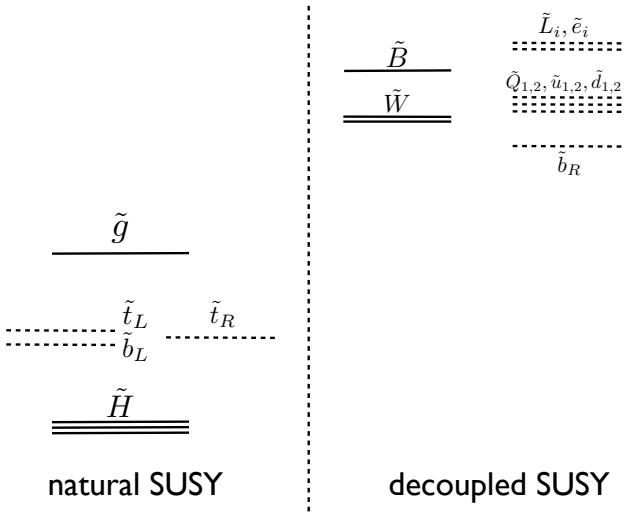

FIGURE 2.3. Mass hierarchy of the simplified SUSY model.[5]

For the models presented in this dissertation, the mechanism is irrelevant because we optimize on a simplified model with decoupled top partners (illustrated by Figure 2.3).

2.3.5. Experiment Feedback

SUSY is a framework that has had several decades to evolve using extensive feedback from experiments. For example, some SUSY-breaking models may include CP-violating and flavor-mixing terms:

$$\mathcal{L} \sim -\tilde{\bar{u}} m^2_{\tilde{u}} \tilde{u}^\dagger - \tilde{\bar{d}} m^2_{\tilde{d}} \tilde{d}^\dagger - \tilde{\bar{e}} m^2_{\tilde{e}} \tilde{e}^\dagger \tag{2.16}$$

connects the up/down/charged-lepton SM particles with their super-partners through the $m^2_{\tilde{u}/\tilde{d}/\tilde{e}}$ matrices, and

$$\mathcal{L} \sim -\tilde{\bar{u}} a_u \tilde{Q} H_u - \tilde{\bar{d}} a_d \tilde{Q} H_d - \tilde{\bar{e}} a_e \tilde{L} H_d + (c.c) \tag{2.17}$$

connects the left and right handed (s)leptons though the Higgs scalars through the $a_{u/d/e}$ coupling matrices. If any of these matrices were to be non-diagonal, then there will be an appreciable mixing; limits on flavor-changing neutral currents in the SM can constrain the form and parameters of SUSY theories.

For the leptons, any natural choice of off-diagonal entires in the mass-squared coupling matrix $m^2_{\tilde{e}}$ predict branching ratios of $\mu \rightarrow e + \gamma$ on the order of 10^{-6}. Experimental observation of the muon decay has put a strong upper bound of the branching ratio at 5.7×10^{-13}. The off-diagonal entries of the a_e matrix are also constrained, especially when we also consider $\mu \rightarrow e/\mu + \gamma$ bounds. Thus, we can assume that a phenomenologically motivated SUSY should not include appreciable flavor-mixing terms as in Equation 2.16.

Off-diagonal entries in the $m^2_{\tilde{u}/\tilde{d}}$ and $a_{u/d}$ matrices above result in interactions between squarks and the SM strange quarks. The presence of such terms result in an enhancement to the mass-splitting of the neutral Kaon. The experimental bound on the mass-spliting is on the order of 10^{-12} MeV, which implies less than a 10^{-3} relative ratio between the diagonals and off-diagonal entries.

2.4. Simplified SUSY Models

Searches can consider particular signal models and optimize a selection based on their kinematics. If we are to design an analysis in search of SUSY, we need to make many deliberate choices (simplifications). We assume a *simplified SUSY model* conserving R-parity with direct stop production through gluon-gluon fusion. The hope is that the model provides enough kinematic variety to cover the phase-space of a variety of theories.

2.4.1. Top Partners

From a naturalness argument, we expect the third generation of squarks to be the most degenerate from their SM partners. In addition, the gluino mass contributes radiative correction in a two-loop diagram and therefore should not be much heavier than the third generation of squarks. Thus, we assume a model with natural scales $m_{\tilde{g}} > m_{\tilde{t}}, m_{\tilde{b}} \sim \mathcal{O}(TeV)$ and decouple the scale of all other sparticles and interactions.

Although a strong motivator behind SUSY is balancing SM particles' radiative corrections to the Higgs mass, broken SUSY does not produce a perfect cancellation. The less degenerate sparticles are from their SM partners, the more fine-tuning needs to be done. This motivates our search for the SUSY partner to the top quark; since it is has the largest one-loop contribution to the Higgs mass, limits on stop models provide the strongest constraints on SUSY theories.

From an experimental point of view, the production of stops only depends on the value of the cross-section of the scalar. At the LHC, the task of producing recommendations is handled centrally by the LHC SUSY Cross-Section working group. The cross-sections of sparticle production in Figure 2.4 is calculated at *next-to-leading order* in linear (NLO) and logarithmic (NLL) terms, and falls with increasing mass.[6]

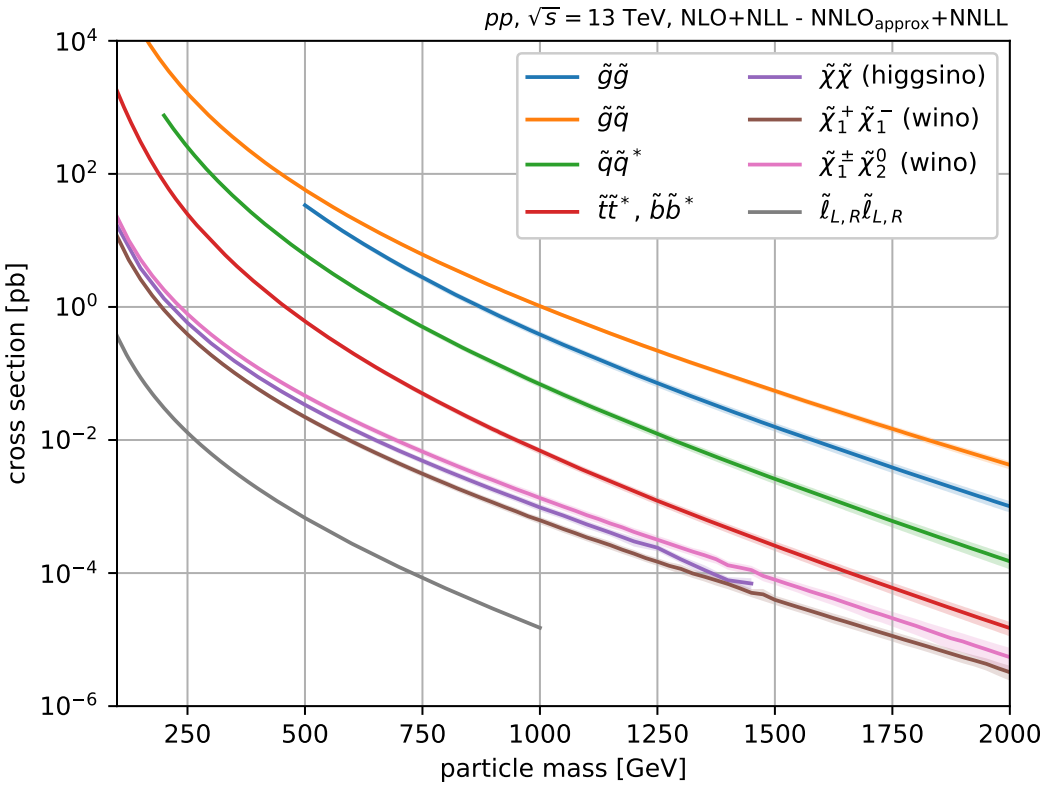

FIGURE 2.4. Cross sections of squark, slepton, and gluino production. The stop is shown in red.[6]

2.4.2. SUSY at the LHC

At the LHC, squarks are produced at higher rates than sleptons and gauginos. Gluinos do have a higher cross section than stops, but the phase-space unexplored is much greater for the top partners. The decay of the stop can exhibit a variety of topologies. For the material in this dissertation I will assume that stops ($\tilde{t}$) always decay to a SM top quark (t) and a neutralino ($\tilde{\chi}_1^0$), as shown in Figure 2.5. The neutralino is the lightest (stable) SUSY particle and is electrically neutral, making it a possible candidate for Dark Matter.

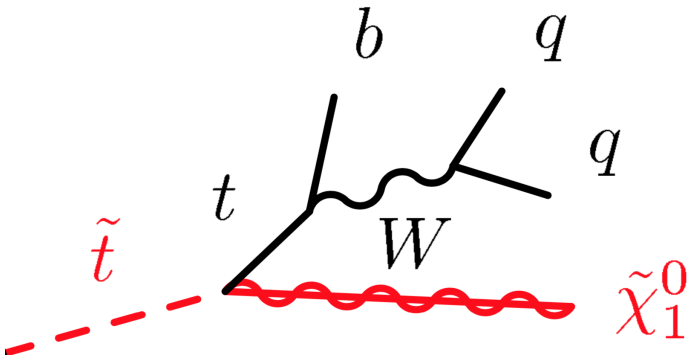

FIGURE 2.5. Diagram of a stop ($\tilde{t}$) decay, assumed to be 100% to top (t) + netralino ($\tilde{\chi}_1^0$).[7]

Past searches for R-parity conserving SUSY in ATLAS have placed significant limits on the masses of gluinos and squarks of the first and second generations. [60] In addition, recent results from ATLAS [61] and CMS [62] exclude top squark masses below about 1.05 TeV for $m_{\tilde{\chi}_1^0} << m_{\tilde{t}}$, assuming $B = 100\%$. Figure 2.6 summarizes recent ATLAS SUSY searches.[8]

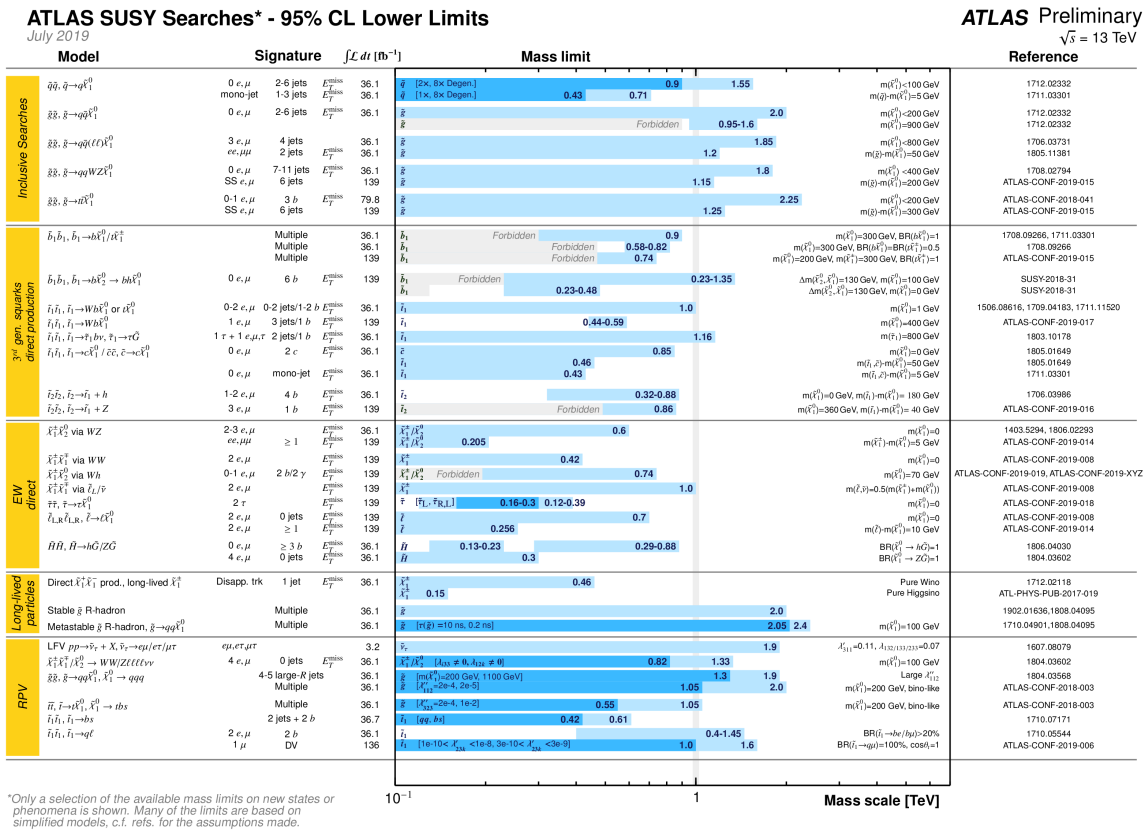

FIGURE 2.6. Summary of ATLAS SUSY results.[8]

CHAPTER III

THE LARGE HADRON COLLIDER

The Large Hadron Collider is a 27-km circumference collider straddling the Franco-Helvetic border and capable of accelerating particles up to 99.999997828% the speed of light. The Large Hadron Collider is the last stage in a series of subsequent accelerations performed by various machines culminating in proton-proton collisions at a center of mass energy of 13 TeV. Following beam injection, the LHC uses alternating bending and shaping magnets throughout the machine to guide the protons in their circular path and a series of Radio-Frequency (RF) Cavities for longitudinal acceleration. The pair of counter-circulating proton beams are then focused to a collision point approximately 16x16 μm^2 at four interaction points around the accelerator.[63]

The following chapter details the evolution of particle accelerators in Section 3.1.1 as precursors to the construction of the LHC Complex at CERN, later discussed in Section 3.1.3. The particle beam dynamics of the LHC are briefly covered in Section 3.2, whereas the magnet technology is described in Section 3.3.

3.1. On Accelerators

3.1.1. The Evolution of Particle Accelerators

Particle accelerators define a class of tools developed to probe the interactions of various particles and materials. The energy of the outgoing particles is increased through electric fields, whereas their trajectories are shaped through magnets and

physical barriers. The principle governing accelerator design is universal: add energy to a system while confining it to a desired shape in momentum-space.

Throughout the 20th century, accelerators have developed from simple drift tubes to CERN's 13 TeV Large Hadron Collider complex. Developments in cryogenics, magnet technology, and superconductivity have all contributed to the development of the field.

Earnest Rutherford, born in 1870 New Zealand, began advocating for construction of particle accelerators following his studies on alpha particles; he emphasized the potential of probing the atomic nucleus with energies greater than the naturally produced alpha particles. Concurrently, George Gamow, a Russian-born theoretical physicist, formulated the 'Gamow tunneling' phenomenon which modeled quantum tunneling of the Coulomb potential. The publication urged Irish physicists Cockcroft and Walton to apply the principle to protons, as opposed to the heavier alpha particles, guiding them to the conclusion that splitting an atom could be possible with a 8-meter series of discharge tubes. In 1932, their efforts were rewarded when they successfully split a lithium atom into two alpha particles with the world's first linear accelerator.[64]

One of the dominant limitations of early 20th century linear accelerators was the impracticality of creating a large potential difference in a single cavity. A solution was proposed by Rolf Wideroe, a Norwegian physicist, who developed on the idea of a Swedish-born physicist, Gustav Ising, to synchronize a series of drift tube of varying lengths and fields to obtain a larger voltage gain than the applied voltage, giving way to the first Radio Frequency (RF) driven linear accelerator.[65]

The concept of RF-driven linear accelerators (linacs) was extended in the United States by Orlando Lawrence and David Sloan as they devised the

Cyclotron, a machine which accelerates charged particles through a high electric field gap between two 'D'-shaped cavities.[66] With the cyclotron, the potential gradient only needed to be high over a short distance (gap) as opposed to over several drift tubes in series. In addition, the same potential gradient perpetually accelerated the spiraling particles on each pass. An interesting characteristic of this design is the constant period of the spiraling particle; despite the energy increase, the time elapsed between passes through the accelerating gap is constant. This powerful characteristic of cyclotrons drastically improved the energies accessible to physicists, becoming the first machine to surpass the MeV barrier.

The next major leap in accelerator technology came in 1945 with the development of the synchrotron, a device that hybridized linac accelerating technology with the multi-pass design of cyclotrons.[67] In addition, there was a significant drop in the voltages required for operation when compared to a standard cyclotron accelerating deuterons. Particles are accelerated at one or more gaps around a well-defined orbit, where cavities with resonant RF electric fields are synchronized to the orbital period of the electrons. For relativistic particles, the orbital frequency is essentially constant: as the energy increases, the magnetic field is increased to maintain a stable orbit.

3.1.2. A Brief History of CERN

As Europe struggled with the post-WWII reconstruction, scientific research in the continent came to a virtual halt. Thus, the Conseil Européen pour la Recherche Nucléaire (European Council for Nuclear Research) was formed in 1952 as a provisional organizational body to build a laboratory in the outskirts of Geneva, Switzerland. Following its construction in 1954, the CERN acronym was kept

for the laboratory and the governing body was reformed into the Organisation Européenne pour la Recherche Nucléaire (European Organization for Nuclear Research).[68]

In 1957, just a few years after breaking ground, CERN's began use of their first particle accelerator, the Synchrocyclotron (SC). The 5-m diameter machine was a type of cyclotron capable of accelerating protons at 600 MeV towards fixed targets within the machine. In 1959, CERN's first true synchrotron, the Proton Synchrotron (PS), began accelerating particles with energies up to 25 GeV. The PS is the oldest particle accelerator still operating in the LHC complex.

In the early 1970's, experiments at CERN began demanding higher beam intensities to probe more rare processes. The Proton Synchrotron Booster (PSB) was installed in 1972 to address this need and increase the particle flux delivered to experiments. The PSB output feeds the PS, which in tun injects into the Super Proton Synchrotron (SPS). The new SPS, completed in 1976, was 7-km in circumference and collided protons with anti-protons at unprecedented energy of 400 GeV. Before either the PSB and SPS were built, the protons in the PS were supplied directly by CERN's LINAC1; the second generation LINAC2 was commissioned in 1978 and was the principle proton linac used in the accelerator complex during Run 2. Data analysis of SPS collisions would eventually lead to the discovery of the W and Z bosons in 1973 and 1983.[69]

The tunnel that the LHC uses was build two decades before the accelerator was proposed. On February 8, 1988 the two ends of the 27-km circular tunnel met and the Large Electron Positron (LEP) collider it was intending to house first circulated beams on July 14th, 1989. Throughout its decade of operation, accelerator research and upgrades steadily increased the energies of the machine

from 45 to 104.5 GeV per beam.[70] At LEP, a 125 GeV Higgs would have been produced either in association to a 91 GeV Z-boson, or, less frequently, through vector-boson fusion (VBF). The Higgs evaded searches at LEP since the machine's maximum center of mass energy was just below the ZH resonance and the luminosity too low for a discovery through VBF production.

In the hunt of the Higgs boson, physicists at CERN proposed retro-fitting LEP's tunnel with state-of the-art magnets and RF-accelerator technology to build a new machine, the Large Hadron Collider. After the United States cancelled the Superconducting Super Collider in 1994, construction of the new machine jump-started and new tunnels and experimental caverns were excavated over the following decade. At on September 10th, 2008 (10:28am CEST) the LHC circulated its first beams, setting a then-world-record collision energy of 7 TeV.

3.1.3. The Modern Large Hadron Collider Complex

A proton begins its journey to collision in a hydrogen bottle within the LINAC2.[1] The hydrogen atoms are ionized and the protons are accelerated to 50 MeV. They are then guided into the PSB, a four-ring synchrotron designed to store, amass, and accelerate protons with energies of 1.4 MeV. The proton packets are subsequently injected into the PS where the are accelerated to 25 GeV. Before ejection, the PS shapes the proton bunches into the 25 ns spacing required shared by both the SPS and the LHC. The 400MHz protons bunches are further accelerated in the SPS to 450 GeV and finally directed into the LHC to performs their final acceleration to 6.5 TeV per proton beam.[71] Figures 3.1a and 3.1b illustrate the LHC accelerating paths.

[1]LINAC 4 has recently replaced LINAC2 in preparation for Run 3

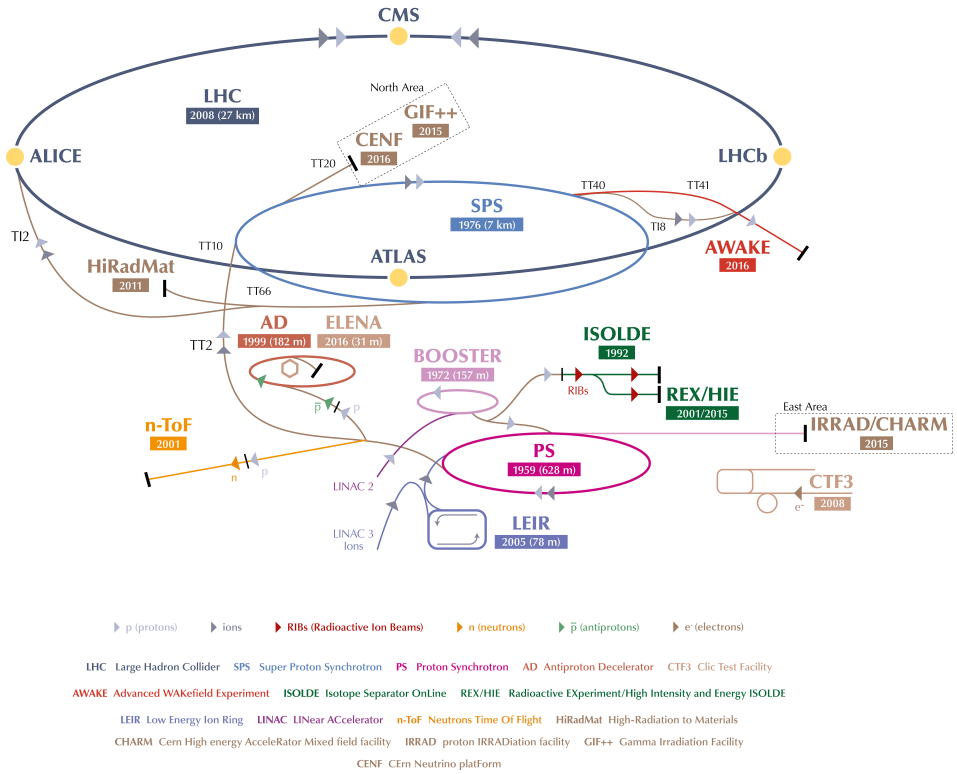

(a) LHC accelerator complex commissioning years.

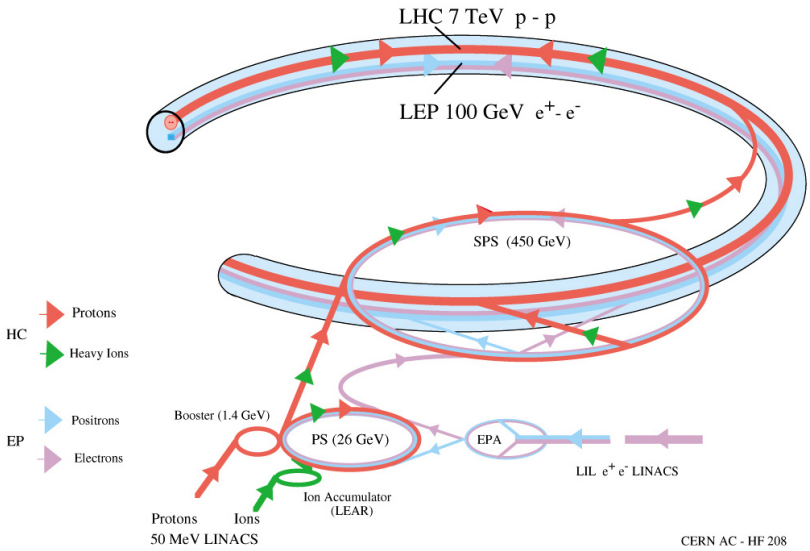

(b) LHC injection path.

FIGURE 3.1. The CERN accelerator complex. The top figure (a) are the years each machine was commissioned and below (b) is the injection sequence of the CERN accelerators in the LEP and LHC era.[9][10]

The accelerating RF-cavities are localized to a short stretch in the eastern-most sector of the LHC. Protons that arrive in-time are pulled and pushed in-phase along a set of RF cavities. Particles arriving early or late will oscillate about the bunch center until either locking into the nominal mode or completely fall out of synchronicity. There are two sets of accelerating cavities, one for each beam; each set is composed of two cryomodules containing four RF cavities with an inter-cell spacing of 1122 mm.[63][72] The RFs inject approximately 485 kW per turn to circulating protons in the ramping stage of LHC. Once the protons have been accelerated to the collision energy, the LHC enters the *flat-top* acceleration stage where the RFs inject approximately 7 keV to compensate for the synchrotron radiation losses as the beam circulates.

The LHC beams travel along separate beam tubes along the ring, except at four interaction points where the beams are crossed and the protons allowed to collide. As opposed to fixed target experiments whose center of mass energies grow as the square root of the accelerator energy, the protons in the LHC are designed to collide head on in the lab-frame. It is at these interaction points that the ATLAS[18], CMS[73], ALICE[74], and LHCb[75] detectors are placed. Four other technical access points exist along the LHC, one of these housing the accelerating RF-cavities.

The primary design of the LHC was for proton-proton physics, but the machine can also accelerate heavy nuclei to study high-Z QCD interactions. The experiments of the LHC have the option of recording the heavy ion data when the special runs occurred at various intervals in Run 2. ATLAS was not designed to study heavy-ion physics, yet there is a strong group within the collaboration dedicated to analyzing heavy-ion data.

3.2. Protons at the LHC

Whereas a LINAC looses no energy to synchrotron radiation, it is severely limited to the single acceleration length inherit to its design. In other words, LINACs are limited by luminosity and size, whereas circular colliders compromise its multi-pass design with losing energy with each deflection. The relativistic form of the energy loss to synchrotron radiation of a charged particle traversing a magnetic field orthogonal to its trajectory is given by the following:[25]

$$P' = \frac{q^2(a')^2}{6\pi\epsilon_0} \Rightarrow P = \frac{q^2(\gamma^2 a_\perp)^2}{6\pi\epsilon_0} = \frac{q^2\gamma^4 a_\perp^2}{6\pi\epsilon_0} = \frac{q^4 B^2\beta^2\gamma^2}{6\pi\epsilon_0 m_0^2} \tag{3.1}$$

$$P = \frac{q^4 B^2\beta^2}{6\pi\epsilon_0 m_0^2}\left(\frac{E}{m_0}\right)^2 \approx \frac{q^4 B^2 E^2}{6\pi\epsilon_0 m_0^4}; \text{ for } v \sim c \tag{3.2}$$

Since the value of B is set by the radius and energy of the LHC, the power radiated by a particle at the LHC is inversely proportional to its mass to the four power. Some colliders built after LEP, such as the Tevatron at FermiLab, reached higher energies by using more massive colliding particles such as protons and anti-protons.[76] The choice of using protons for both colliding beams dilutes to cost and the ability to produce enough anti-protons to meet the luminosity demand of the machine.

One significant disadvantage of colliding hadrons is the irreducible longitudinal momentum uncertainty imbedded in their composite nature. During a hard scattering collision, it is the constituents (partons) that interact and each carries a fraction of the total hadron's momentum. The parton distribution function (PDF) describes the probability density for finding a parton with a certain longitudinal momentum fraction x at resolution scale Q^2. For protons in the LHC,

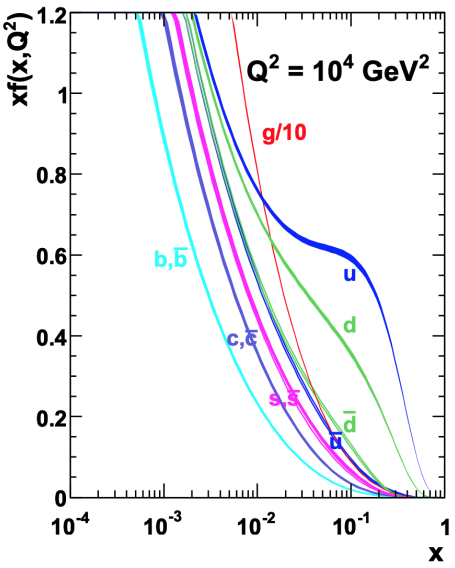

FIGURE 3.2. Example parton distribution function for $Q^2 = 10^4$ GeV^2.[11]

$Q^2 \sim 0.1 - 1$ TeV^2 and an example distribution is shown in Figure 3.2.[11] At each collision, the value of the fractional momentum carried by the colliding partons is unknown and thus an uncertainty in the longitudinal momentum must always be considered.

At the energies of the LHC, the PDF indicates that the primary collision mode is gluon-gluon fusion.

3.2.1. Luminosity

The total integrated luminosity is a the amount of data delivered by the LHC or collected by the experiments and is measured in inverse barns (b^{-1}). The instantaneous luminosity is a dynamic measure of the rate of collisions occurring at the interaction point. The machine luminosity depends primarily on the number protons per bunch (N_p), the number of bunches (n_b), the RMS length of the bunches (σ_z), the Lorentz factor of the protons (γ_p), the machine orbital frequency (f_{rev}), the normalized transverse emittance of the beam (ϵ_n), the beam amplitude

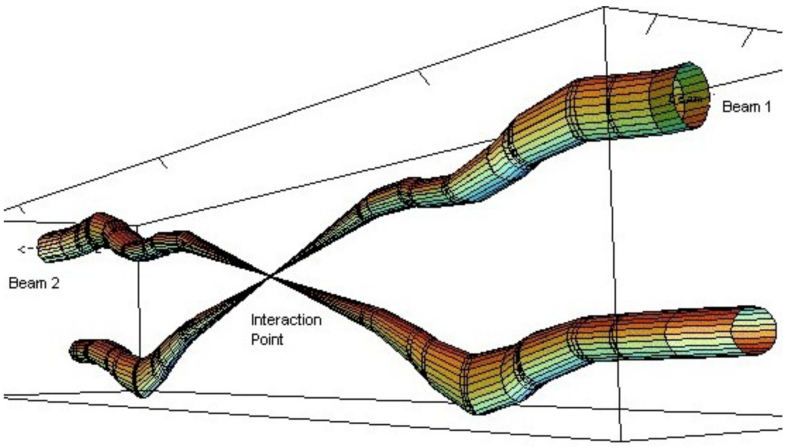

FIGURE 3.3. Visualization of the β^* amplitude function of the proton beam as it approaches and leaves the Interaction Point.[12]

function minimum (β^*), as well as the beam crossing angle (θ_c) and its transverse RMS beam size (σ^*) at the IP:[77]

$$L = \frac{N_p^2 n_b f_{rev} \gamma_p}{4\pi\epsilon_n \beta^* \sqrt{1 + \left(\frac{\theta_c \sigma_z}{2\sigma^*}\right)^2}}. \tag{3.3}$$

Figure 3.3 shows a cartoon of the β^* amplitude functions squeezing before collision at the interaction point.

During Run 1 of the LHC, a total of 5.46 (22.8) fb^{-1} of 7 (8) TeV data was delivered between 2010-2011(2012).[78][15] The machine and detectors were upgraded during the two-year shutdown, and Run 2 began in 2015. The total integrated luminosity delivered by the LHC, compared to what was collected by ATLAS, is shown in Figure 3.4. The results in this dissertation use the whole Run 2 dataset of 139 fb^{-1} at a center of mass energy of $\sqrt{s}$ =13 TeV.[79]. Figure 3.5 compares the integrated luminosity measured at the ATLAS Interaction Point across various years.

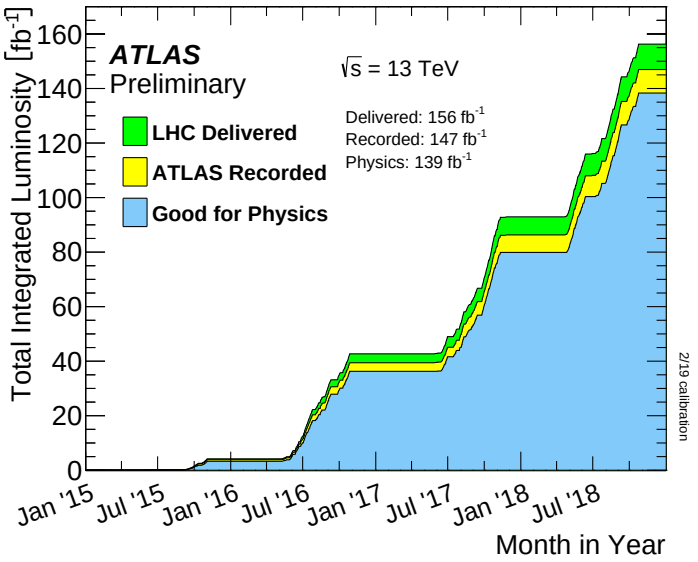

FIGURE 3.4. Total integrated luminosity delivered by the LHC (green), recorded by ATLAS (yellow), and available for physics analysis (blue).[13]

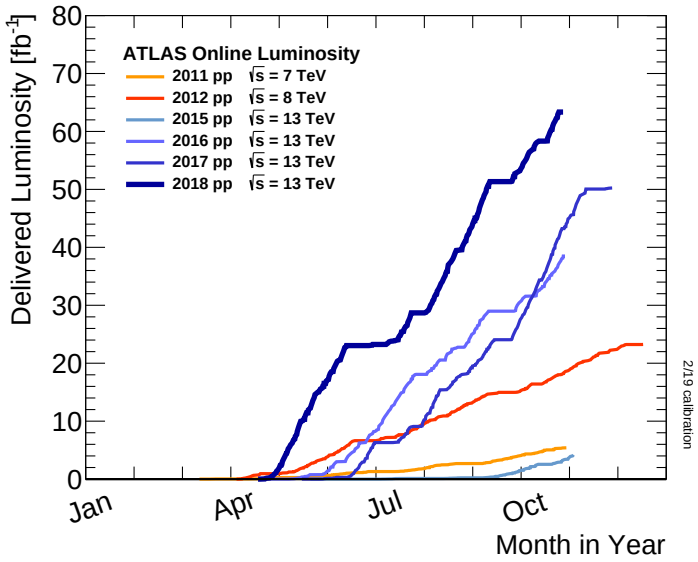

FIGURE 3.5. Total integrated luminosity measured by ATLAS in various years across Run 1 and Run 2.[13]

The LHC operates at the 400 MHz frequency of the RF-cavities, which is a multiple of orbital frequency $f_{rev} = 11.245$ kHz and corresponds to a 2.5 ns spacing between RF slots. Not all RF slots are occupied by protons during a fill, rather the LHC accommodates the experiments' request to fill one of every 10 RF slots with protons. In total, there are 35640 RF buckets per beam and during most of Run 2 only 2556 of those were filled during operation.[71] There are on the order of 10^{11} protons in each bunch yielding an instantaneous luminosity on the order of 10^{34} cm^{-2} s^{-1}.

Since LHC injection only occurs once per fill, the highest number of protons are present at the beginning of every fill and decreases at an exponential rate as the protons collide and scatter. At the request of the experiments, the LHC *levels* the beams to reduce the collision cross-section, and thus the number of collisions, through various means. The first scheme used separated the beams at the stat of the fill and brought them closer as the run progressed. In the last year of Run 2, a technique known as β^*-leveling was used by manipulating the β^*-function (beam focus) to maintain a regulated luminosity as the beam intensity tapers.[80] Figure 3.6 shows the effect of leveling on the instantaneous luminosity through the beam separation technique.[14]

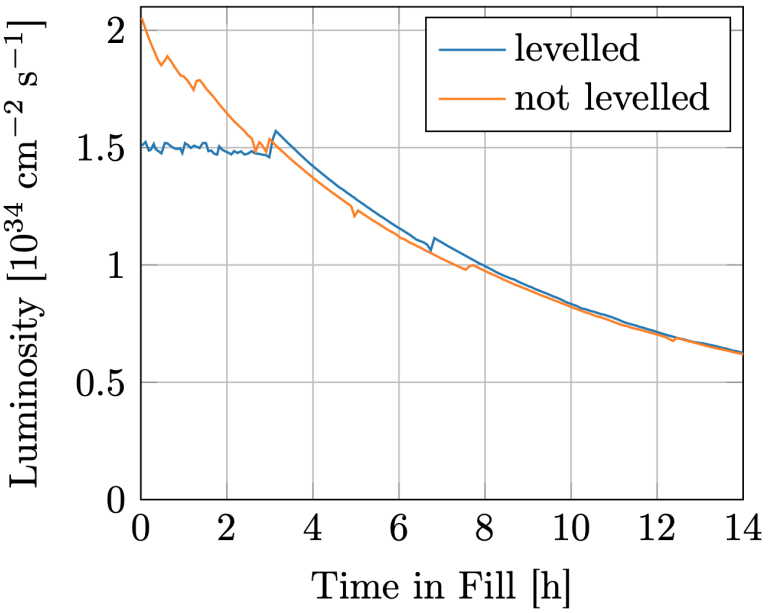

FIGURE 3.6. The instantaneous luminosity during LHC test fills 6358 (not leveled) and 6360 (leveled).[14]

3.2.2. Pileup

Elastic processes are defined by the conservation of an incident particle's kinetic energy. At the LHC, these kinds of processes occur when protons barely brush past one another, subtly deflecting their trajectories and leaving the structure of the hadron intact. The more interesting interactions, inelastic collisions, dissociate the constituent partons from the proton and occur with a total cross-section of 0.1 barns leading to a rate on the order of 10^9 events/sec. This implies that for the given average luminosity and 25 ns bunch-spacing, there are an average of 25 inelastic interactions per bunch crossing (pileup $< \mu >= 25$).

ATLAS was designed to collect 13 TeV data in Run 2 at $< \mu >= 25$, but the LHC delivered much higher instantaneous luminosities than planned. The pileup profile gradually shifted upward with each subsequent year of operation. Figure 3.7

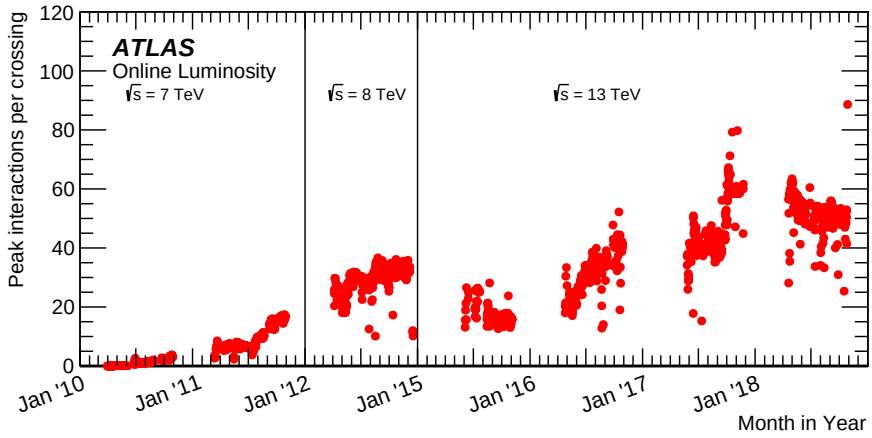

FIGURE 3.7. The average pileup $\langle\mu\rangle$ of LHC fills during 7, 8, and 13 TeV runs.[15]

shows the average pileup conditions in ATLAS during 8 TeV runs in 2012 and Figure 3.8 contrasts the profiles across the various years of Run 2.

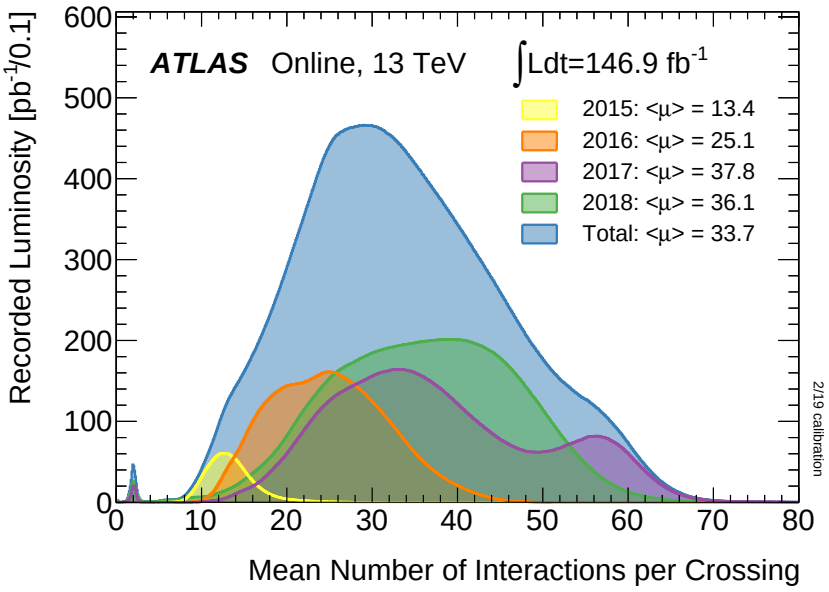

FIGURE 3.8. Superimposed pileup profiles of various years during 13 TeV collisions of Run 2.[13]

3.3. Magnets of the LHC

The LHC is a synchrotron composed of 9135 magnets. To bend particles, dipole magnets fill most of the tunnel. Quadrupoles are used to focus the beam at various points along its trajectory. Sextupoles and other correcting magnetic optics help minimize the momentum spread, whereas physical collimators address the spatial spread.

3.3.1. Bending Dipoles

The choice of a circular collider for the LHC necessitates strong bending magnets that can dynamically adjust to the increasing energy. To bend the 7 TeV protons the LHC is designed to circulate, CERN utilized its predecessor's (LEP) 27-km tunnel, but had to invest in developing magnets to cope with the order of magnitude rise in beam energy. The magnetic force needed to steer $m_P \sim$ 1 GeV protons at 7 TeV at the LHC can be compared to LEP's $m_e \sim 0.5$ MeV electrons/positrons at ~ 100 GeV as:

$$\frac{F_B^{LHC}}{F_B^{LEP}} = \frac{p_{LEP}}{p_{LHC}} \frac{B_{LHC}}{B_{LEP}} \Rightarrow B_{LHC} \sim (10^1 - 10^2) \times B_{LEP}. \tag{3.4}$$

Hence, the LHC upgrade to the tera-scale pivoted on the bending magnet performance. The upper energy bound of the LHC is a consequence of the size limitations of the tunnel and the affordability of bending magnets.

To maximize the force imparted onto a particle, the effective magnetic field should be orthogonal with the particle's trajectory. Dipole magnets serve as the ideal candidate for this task as they produce a uniform magnetic field in the direction of interest. The 15 m-long dipole magnets used at the LHC are

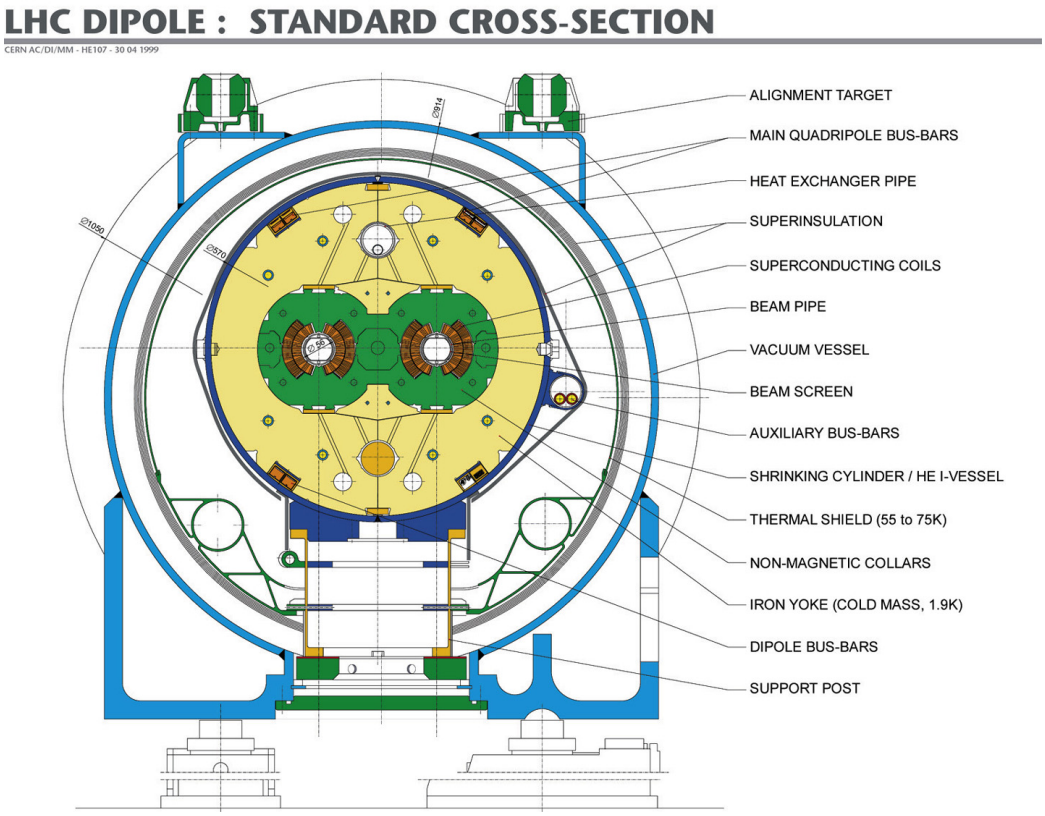

FIGURE 3.9. Cross-section of an LHC dipole bending magnet. The particle moves in/out of the page, the magnetic field points vertically and the resulting deflection is lateral.[16]

superconducting, cooled to 1.9 K with liquid He^3, and generate their fields by running 11.6 kAmps of current through the NbTi Rutherford wires.[81] The 1232 main dipoles create a field of 8-9 T each and are curved to account for the particles' changing trajectory with the cavities with a sagitta of about 9 mm. This implies a 2812.36 m radius of curvature, which is necessarily smaller than the radius of the LHC as only part of the 27 km ring is used for bending. Figure 3.9 shows the cross-section of a dipole magnet.

3.3.2. Focusing Quadrupoles

Quadrupole magnets have a cross-like magnetic polarity, the field squeezes charged particles in one direction while spreading them in the orthogonal direction. Therefore, quadrupole magnets are used as focusing optics spaced between dipoles and shaping optics with alternating orientations to achieve the focusing performance desired. There are a total of 392 quadrupoles throughout the LHC ring. Each 3 m-long quadrupole can produce a magnetic field gradient of 223-241 T/m and are constructed with the same material as the dipoles.[81] Contrasting the bending magnets, the quadrupoles are straight and are aligned to within 100 μm, an order of magnitude more precise than their dipole counterparts. Figure 3.10 shows a picture of the cross-section of a quadrupole magnet.

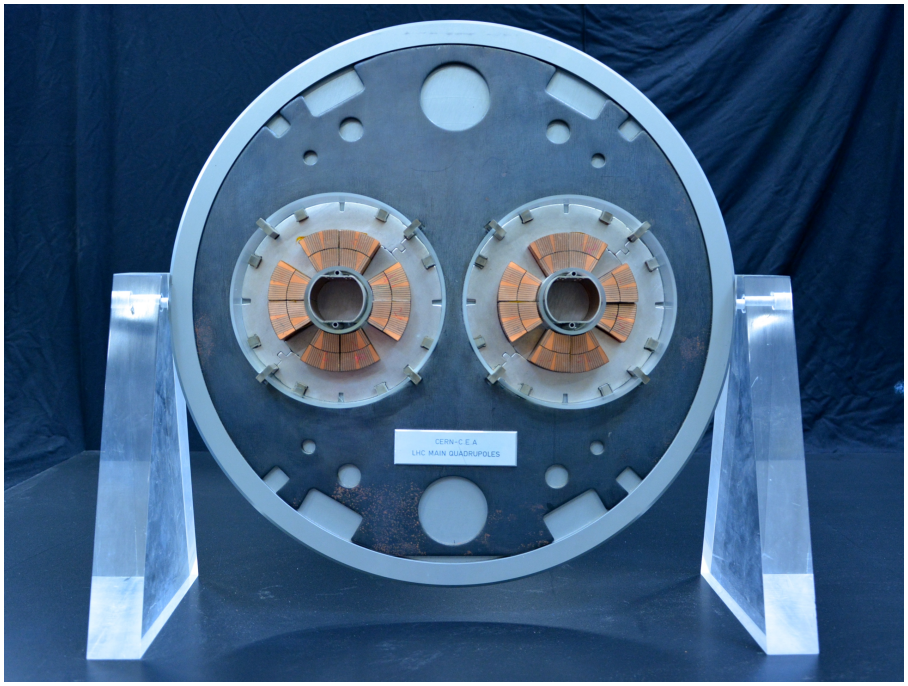

FIGURE 3.10. Picture of cross-section of an LHC quadrupole focusing magnet. The particle moves in/out of the page, the magnetic field lines flow from the corners and form a cross-like pattern, focusing vertically/horizontally and defocusing horizontally/vertically.[17]

CHAPTER IV

THE ATLAS DETECTOR

The ATLAS detector was first proposed in 1992 by a newly formed ATLAS collaboration of 88 institutes in a Letter of Intent to the CERN council.[82] Its purpose was to collect proton-proton data to serve a wide variety of physics analyses. The design of the detector was driven by the collision conditions delivered by the LHC. ATLAS was first commissioned in 2008, but continues to be upgraded with each shutdown of the LHC.[83] The following sections describe the ATLAS sub-detectors and trigger system during Run 2 of the LHC, as well as a dedicated section to upgrades relevant to this dissertation. An overview image of ATLAS is illustrated in Figure 4.1.

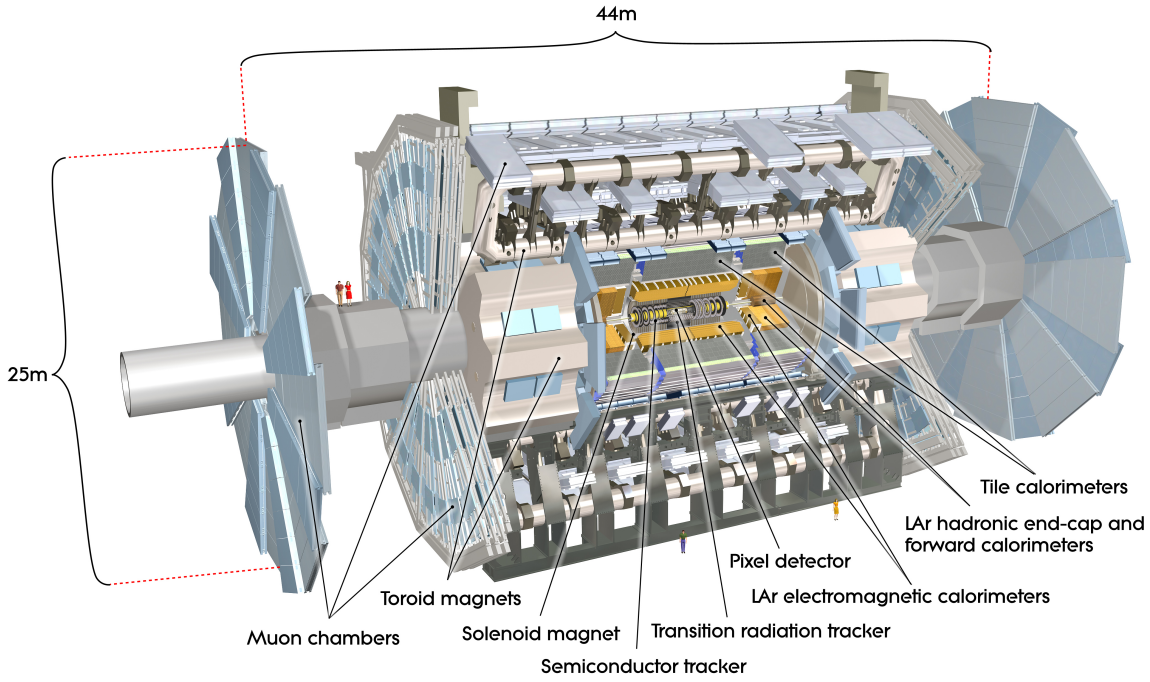

FIGURE 4.1. Simulated image of the ATLAS detector.[18]

4.1. Natural Coordinates

With respect to the LHC, a Cartesian set of coordinates can be used to describe ATLAS with the Nominal Interaction Point 1 of the collider, where ATLAS is centered, serving as the origin. In this right-handed system, the $\hat{z}$ axis runs counter-clockwise along the beam pipe when viewed from above. The $\hat{x}$ and $\hat{y}$ axes describe the transverse plane, with $\hat{x}$ pointing towards the center of the LHC ring and $\hat{y}$ pointing upwards. The coordinate system is complete, but certainly not the most convenient to describe physics objects in ATLAS. It is important to adopt a coordinate system that utilizes the symmetries of the detector while accurately representing the physics of objects across the wide energy spectrum ATLAS is designed to capture.

For particles originating from LHC collisions, the actual proton-proton interactions usually occur close but not exactly at $\hat{z} = 0$. From the nominal interaction point, collisions at the LHC have a mean spread of approximately 16 μm in both the transverse directions.[63] In addition, there is a significant longitudinal uncertainty of the incident parton energies as described in Section 3.2. This imposes restrictions on our coordinate system choices to being Lorentz invariant along the $\hat{z}$ direction. This problem is not present in the transverse plane where the parton energy uncertainty is below the mean spread of collisions, making it ideal for defining conserved physics quantities such as Missing Transverse Energy (E_T^{miss}). As a result, ATLAS uses an azimuthal coordinate, ϕ, to describe the angular space of the plane transverse to the LHC beam pipe, with $\phi = 0$ running right-handedly with the $\hat{z}$ axis.

For physics objects, it is necessary to define an observable describing the longitudinal angle from the beam pipe, θ, that is Lorentz-invariant in boosts

along the $\hat{z}$ direction. The radius coordinate from the center of ATLAS, r, is not invariant under such transformations and only useful to describing fixed hardware. *Rapidity* is an observable that can be defined as:

$$y = \frac{1}{2}\ln\left(\frac{E+p_z}{E-p_z}\right). \tag{4.1}$$

Using the identities of logs, inverses, and $\tanh\theta = \frac{e^{\theta}-e^{-\theta}}{e^{\theta}+e^{-\theta}}$, we can rewrite the definition:

$$\begin{aligned}
y &= \ln\sqrt{\frac{E+p_z}{E-p_z}} = \ln\frac{\sqrt{E+p_z}\sqrt{E+p_z}}{\sqrt{E-p_z}\sqrt{E+p_z}} \\
&= \ln\left(\frac{E+p_z}{\sqrt{E^2-p_z^2}}\right) = \ln\left(\frac{E+p_z}{M_T}\right) \\
&= \tanh^{-1}\left(\tanh\left(\ln\left(\frac{E+p_z}{M_T}\right)\right)\right) = \tanh^{-1}\left(\frac{\frac{E+p_z}{M_T}-\frac{M_T}{E+p_z}}{\frac{E+p_z}{M_T}+\frac{M_T}{E+p_z}}\right) \\
&= \tanh^{-1}\left(\frac{E^2+2Ep_z+p_z^2-M_T^2}{E^2+2Ep_z+p_z^2+M_T^2}\right) = \tanh^{-1}\left(\frac{(E+p_z)p_z}{(E+p_z)E}\right) \\
&= \tanh^{-1}\left(\frac{p_z}{E}\right).
\end{aligned} \tag{4.2}$$

Under a Lorentz boost the coordinate in Eq. 4.1 transforms to

$$y' = \frac{1}{2}\ln\left(\frac{E+p_z}{E-p_z}\right) + \ln\sqrt{\frac{1-\beta}{1+\beta}} = y - \tanh^{-1}\beta. \tag{4.3}$$

This result implies that any difference between rapidities of two objects is Lorentz invariant for boosts, β, along the $\hat{z}$ direction. More explicitly,

$$y_2' - y_1' = (y_2 - \tanh^{-1}\beta) - (y_1 - \tanh^{-1}\beta) = y_2 - y_1. \tag{4.4}$$

However, to precisely measure y one must have good resolution of both the energy and the longitudinal component of the momentum vector of highly energetic particles, which is challenging to do at the LHC. We can reformulate Equation 4.1 in order to use the approximation $p \gg m$ and expand about $\frac{m}{p_{tot}} \sim 0$:

$$\begin{aligned} y &= \frac{1}{2}\ln\left(\frac{E+p_z}{E-p_z}\right) \\ &= \frac{1}{2}\ln\left(\frac{\sqrt{p_{tot}^2+m^2}+p_z}{\sqrt{p_{tot}^2+m^2}-p_z}\right) \\ &= \frac{1}{2}\ln\left(\frac{p_{tot}\sqrt{1+\frac{m^2}{p_{tot}^2}}+p_z}{p_{tot}\sqrt{1+\frac{m^2}{p_{tot}}}-p_z}\right) \\ &\approx \frac{1}{2}\ln\left(\frac{1+\frac{p_z}{p_{tot}+\frac{m^2}{2p_{tot}}+\ldots}}{1-\frac{p_z}{p_{tot}+\frac{m^2}{2p_{tot}}+\ldots}}\right) \\ &\approx \frac{1}{2}\ln\left(\frac{1+\frac{p_z}{p_{tot}}}{1-\frac{p_z}{p_{tot}}}\right). \end{aligned} \tag{4.5}$$

By definitions $\frac{p_z}{p_{tot}} \equiv \cos\theta$, $1-\sin\theta = 2\sin^2\frac{\theta}{2}$, and $1+\cos\theta = 2\cos^2\frac{\theta}{2}$, we can simplify the relation to

$$\begin{aligned} y &\approx \frac{1}{2}\ln\left(\frac{\cos^2\frac{\theta}{2}}{\sin^2\frac{\theta}{2}}\right) \\ &\approx -\ln\tan\frac{\theta}{2}. \end{aligned} \tag{4.6}$$

This leads to the definition of *pseudorapidity*:

$$\eta = -\ln\tan\frac{\theta}{2}, \tag{4.7}$$

which is almost identical to rapidity, except that the $p_{tot} \gg m$ relativistic approximation is taken such that the result is independent of particle momenta,

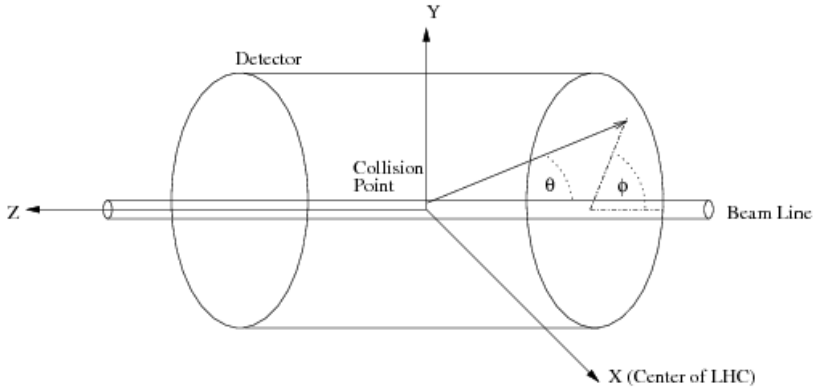

FIGURE 4.2. Coordinate systems of ATLAS. Image obtained from [19].

and is approximately Lorentz invariant under longitudinal boosts along the beam axis. At the center of the barrel ($\theta = \frac{\pi}{2}$) $\eta = 0$ and towards the beam-pipe ($\theta \to 0$) $\eta \to \infty$.

A schematic of this coordinate system is included in Figure 4.2.

4.2. The Inner Detectors

The primary goals of ATLAS hardware nearest the collision point is to precisely locate particle vertices, track their trajectories outward, and measure their mometa. To do this, the hardware needs to balance radiation hardiness with cost and performance to efficiently and reliably collect physics data. The ATLAS Inner Detector provides tracking information within $|\eta| < 2.5$ and is composed of various concentric subsystems surrounded by a superconducting solenoid encased in a cryostat at $r = 1.15$ m. The solenoid produces a constant 2 T axial magnetic field along the beam-axis which bends charged particles inversely proportional to the transverse momenta. The tracking subsystems utilize a variety of technologies to provide information for offline software to reconstruct into complete particle trajectories.

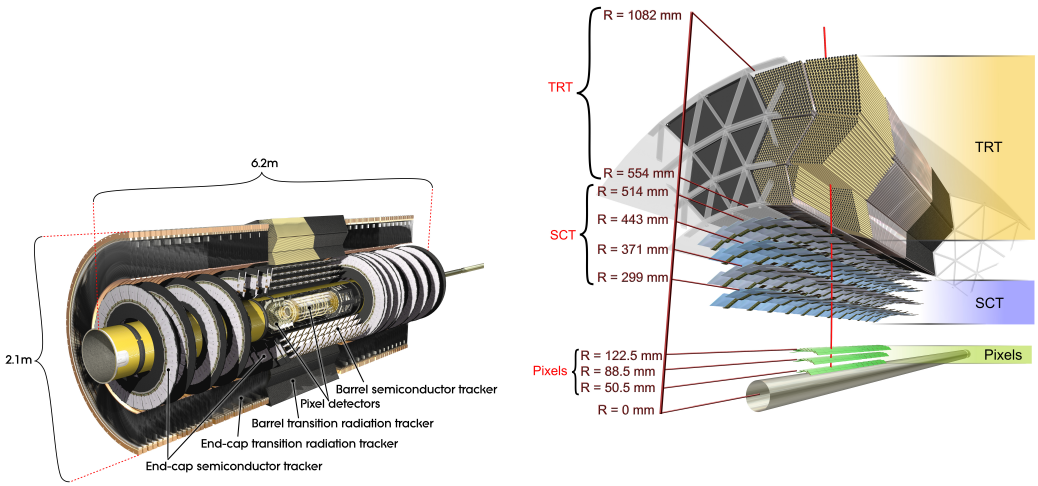

(a) Barrel view of the inner detector (b) Slice view of the inner detector

FIGURE 4.3. The ATLAS Inner Detectors.[18]

The tracking system in ATLAS needs to cope with the 25 ns collision period at which the LHC operates. The beam pipe set the minimum radius that a detector could be placed and the closest tracking system is just 3.3 cm from the beam axis. At this distance, radiation doses and average occupancy are too high for gaseous detectors. For these reasons, ATLAS decided on three tracking subsystems: the closest is composed of silicon pixel detectors, followed by the semi-conductor tracker (SCT), and finally the outmost system is the gas-based transition radiation tracker (TRT). Simulated images of the Inner Detector is shown in Figures 4.3a and 4.3b.

4.2.1. Pixel

The closest subsystem to the interaction point is the Pixel detector whose main purpose is to sample the trajectories of charged particle as they enter the ATLAS detector in order to reconstruct primary and secondary vertex locations. Of all detector systems in ATLAS, Pixel has the highest granularity and resolution at

10 μm in the $\hat{\phi}$ direction and 115 μm in the $\hat{z}$ direction. This is achieved with over 80 million independent n^+ pixel detectors, the majority measuring 50 μm x 400 μm (ϕ, z), divided across 1744 modules.[84] Theses modules are held in place with staves that form a turbine-fan pattern with slight overlap to ensure full azimuthal coverage.

The subsystem is split into a barrel section and two endcaps on either side. The detector is further tiered in three barrel layers at $r = 50.5$, 88.5, and 122.5 mm, covering a longitudinal range of $|z| < 400.5$ mm and yielding good tracking resolution within $|\eta| < 2.5$. It is worth noting that the innermost barrel layer is of particular importance, since it alone determines the impact parameter resolution. The end-caps serve to cover higher η ranges and are each composed of three 60.8 mm-thick rings perpendicular to the barrel layers at $z = 495$, 580, and 650 mm. Each of these rings have an inner radius of 88.8 mm and an outer radius of 149.6 mm.

4.2.2. IBL

During the first long shutdown of the LHC, an additional tracking subsystem, the Insertable B-Layer (IBL), was installed on ATLAS in 2014.[85] This new layer was placed at $r = 3.3$ cm between the new, smaller-radius ($r = 2.5$ cm) beryllium LHC beam pipe and the first Pixel layer. The new layer improves vertexing by not only decreasing the distance to the collisions, but also by adding an additional fourth hit-point for reconstruction software to use.

The IBL is the first large scale application of 3D sensors and CMOS 130 nm technology and consists of 14 carbon fiber staves, each measuring 2 cm in width,

64 cm in length, and a 14 degree tilt for full hermiticity. The new layer was build around the new beam pipe and then inserted into ATLAS. [86]

4.2.3. SCT

The semi-conductor tracker (SCT) is a subsystem that uses less expensive p-in-n micro-strip detectors to provide supplemental tracking information for vertexing at moderate radii from the collision point.[87] The barrel of the SCT is sectioned into four layers, the closest at $r = 299$ mm, the second at 374 mm, the third at 443 mm, and the outmost layer at 514 mm. The η coverage of barrel does not extend far beyond $|\eta| < 1.0$, but the end-caps provide tracking information up to $|\eta| < 2.5$.

The SCT is composed of 4088 independent sensor modules, of those 2112 form the barrel layers and the remaining 1976 are split between the end-cap discs. Each module consists of two strip sensors, tilted at 40 mrad with respect to one another and adhered to either side of a thermally conductive pyrolytic graphite baseboard. Each sensor had 768 readout strips, totaling 1536 readout channels per sensor. In total, there are over 6 million sensors within the SCT.

4.2.4. TRT

The Transition Radiation Tracker (TRT) uses an array of gas-filled drift tubes to detect relativistic charged particles, distinguishing it from the rest of the silicon-based inner detectors.[88] The TRT is the outermost tracking system at $r \in [554, 1082]$ mm with an eta covered within $|\eta| < 2.0$ and sits between the SCT and the calorimeter pre-sampler. The small distance from the interaction point (lever arm for $\vec{r} \times \vec{B}$) prevents the closer subsystems from accurately measuring

high momentum particles. The larger cavity occupied by the TRT provides the space for high momentum particles to bend enough for the tracker to reconstruct a radius.

As a charged particle traverses the TRT, it encounters electromagnetic refractive index boundaries through polymer fibers (foils) that fill the space between the 70 μm-thick Kapton drift tubes in the barrel (end-caps). A photon can be emitted by charged particles as they transition from one index to the other to account for the discontinuity in the materials' electric fields and the efficiency of producing the photons rises with momentum and number of transitions. The high-Z noble gas is ionized by the 5-30 keV photons within the 4 mm-inner-diameter tubes, and the signal is detected through gold-coated tungsten anodes at the tubes' axes.[89] The energy loss due to the transition radiation is negligible for GeV-scale particles used in ATLAS analyses, rather the photons are used as minimally perturbing probes of the position of the charged particle as it arcs within the TRT cavity. A total of 372,032 tubes compose the TRT and are layered coaxially to the $\hat{z}$-axis in the barrel and perpendicularly for the end-caps. Each 160 cm drift tube in the TRT is fabricated identically and cut to the lengths required by the geometry of the various modules, 144 cm in the barrel and 37 cm in the end-caps.

The initial design of the tubes was to contain a mixture of 70% Xenon as the active medium, 27% CO_2 to increase charge drift velocity, and 3% O_2 for noise suppression and stability. The medium between the drift tubes is flushed with CO_2 for cooling and to avoid TR photons depositing energy outside the tubes. In 2012, a series of leaks developed in the Xe recirculating system that averaged 150 liters of gas lost per day, which implies $1,500$ CHF in losses per day. The leaks affected

$\frac{1}{4}$ of the barrel and 2 of 28 end caps modules, pushing ATLAS to replace the gas mixture in these tubes to use much cheaper Argon gas instead of Xenon.

4.3. The Calorimeters

As particles move through the inner detector, only a small fraction of energy is deposited into ATLAS. The purpose of the calorimetry is to absorb the energy of the particles and help distinguish its type. ATLAS chose to install two classes of calorimeters: a liquid argon electromagnetic calorimeter (LAr) and a scintillating tile hadronic calorimeter (TileCal). The former is designed to measure the energies of electromagnetically interacting particles and contains the showers of electrons and photons; the latter is designed to absorb hadronic showers regardless of EM charge. Muons behave as minimum ionizing particles and are not absorbed within the ATLAS calorimeters, rather they travel beyond the muon spectrometer and only leave trace deposits of energy.

It is important that the calorimeters provide complete and uniform angular coverage in order to calculate observables such as Missing Transverse Energy (E_T^{miss}), as well as maintain excellent energy and directional resolution in a harsh radiation environment. The calorimeters provide good hermeticity and have complete azimuthal coverage through a pseudo-rapidity range $|\eta| < 4.9$ (~ 5 degrees from beam-axis). The barrels of both calorimeters are each supplemented with two end-cap sections (EMEC and HEC), as well as additional LAr Forward (FCal) detectors. The LAr and Tile barrel/end-cap interface is roughly at $|\eta| = 1.4$, with the FCal covering $3.2 < |\eta| < 4.9$.

The liquid Argon in LAr was chosen for radiation hardiness, in contrast to CMS's sensitive lead-tungstate crystals. ATLAS also chose to place the

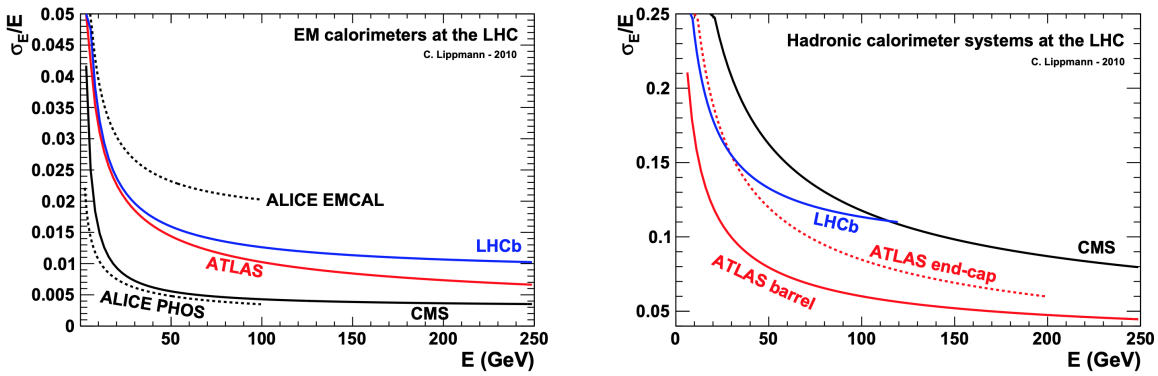

FIGURE 4.4. Comparing energy resolutions of the various calorimeters at the LHC. [20]

superconducting solenoid before most of the calorimetry, whereas CMS encases all of it within the magnet. Not constrained by the size of a cryostat, ATLAS was able to afford a hadronic calorimeter with better energy resolution than its sister experiment. A summary of the four major experiements' calorimetery performance is shown in Figure 4.4.

A computer generated image of the ATLAS calorimetry is shown in Figure 4.5, and Figure 4.6 shows a cartoon illustrating the calorimeter sections particles interact with at varying $|\eta|$.

4.3.1. LAr

LAr is positioned just outside the inner detector and is the closest of the calorimeters to the interaction point. It is divided into a barrel (EMB), two end-caps (EMEC), and a forward calorimeter (FCal). A central cryostat encloses the EMB and the superconducting solenoid, whereas two other cryostats house the EMEC, HEC, and FCal. The barrel covers the region $|\eta| < 1.475$, with some overlap with its end-caps at $1.375 < |\eta| < 3.2$. The FCal extends the coverage to $|\eta| < 4.9$. These barrel and end-caps are further organized into four calorimetry

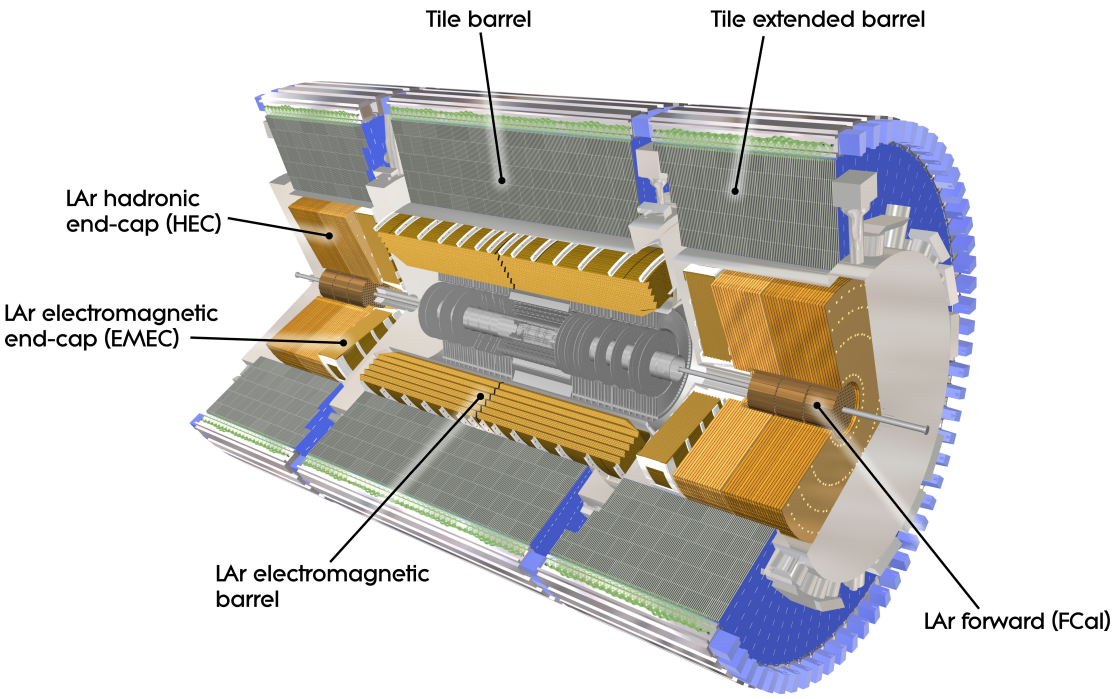

FIGURE 4.5. Simulated image of the ATLAS calorimeters: LAr and TileCal.[18]

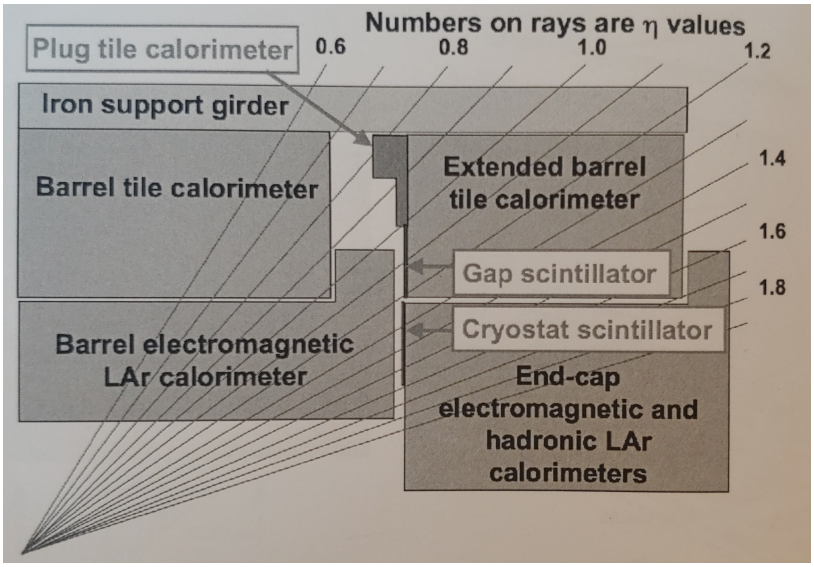

FIGURE 4.6. Interactions with the calorimeter sections for various $|\eta|$.[21]

layers, and sometimes three in certain η ranges.[22] ATLAS's choice of hardier liquid argon technology over the scintillating EM calorimeters used in other LHC experiments, such as CMS and ALICE, has already been implemented in previous collider experiments such as Hera and CDF/D0.

In the EMB and EMEC, ATLAS features accordion-like arrangements of corrugated sheets of lead whose gaps are filled liquid argon, as shown in Figure 4.7. The active material of the calorimeter is the intrinsically radiation resistant monoatomic argon and the lead is used as passive material. The high-Z lead plates absorb some of the passing charged particle's energy through Brehmstralung processes, creating showers of electrons and photons flooding the liquid argon gaps. These particles then ionize the argon, which provide the physical signal used to measure the total deposited energy. Alternating 2 mm-thick lead sheets with a 4 mm liquid argon gap result an effective radiation length of X_0=1.55 cm, effectively making LAr a 25 X_0-thick calorimeter.

The FCal uses a different architecture to cope with the increased radiation close to the beam pipe and at high η. The calorimeter is a matrix of 30,000 metal rods encased in LAr-filled tubes, as shown in Figure 4.8. The rods at the center of the tubes are approximately 5 cm-thick and made of copper in the layer closest to the beam pipe, and of tungsten in the subsequent layers. The LAr gap between the rod and the tube wall ranges from 0.25-0.5 mm , providing an active material for detection. Groups of 4-9 rods are grouped to make cells measuring 2.0-5.6 cm^2.

LAr places the readout services at the front and back end of the modules, avoiding additional deal material before the calorimeters already affecting the energy resolution. Despite this creative solution, the inner detectors' total material affect the sensitivity and calibration limitations of LAr to such an effect as to

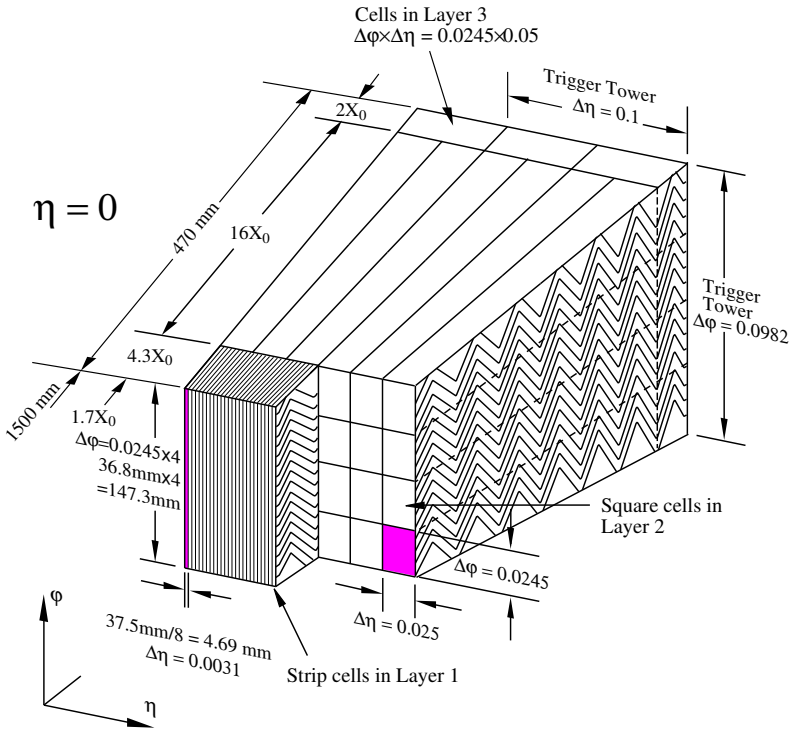

FIGURE 4.7. Schematic of the Liquid Argon Calorimeter accordion geometry and layering.[22]

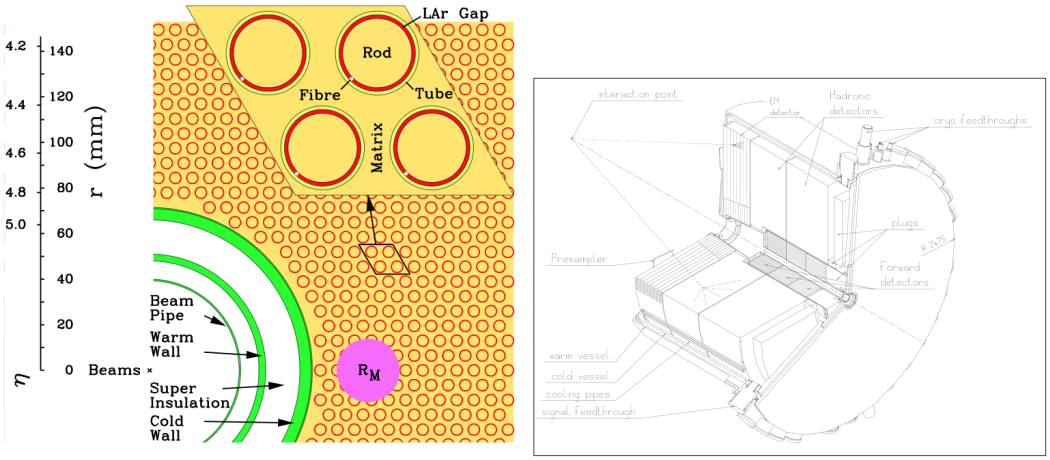

(a) Picture of FCal rods and their geometry. (b) Schematic of an end-cap cryostat.

FIGURE 4.8. LAr Forward detector rod matrix and cryostat schematic.[23]

necessitate an additional EM calorimeter layer, the pre-sampler. This independent detector uses 11 mm of liquid argon to capture the showering resulting from

interactions with the tracking material before the main LAr calorimeter. Figure 4.9 shows the amounts of material present before and within LAr.

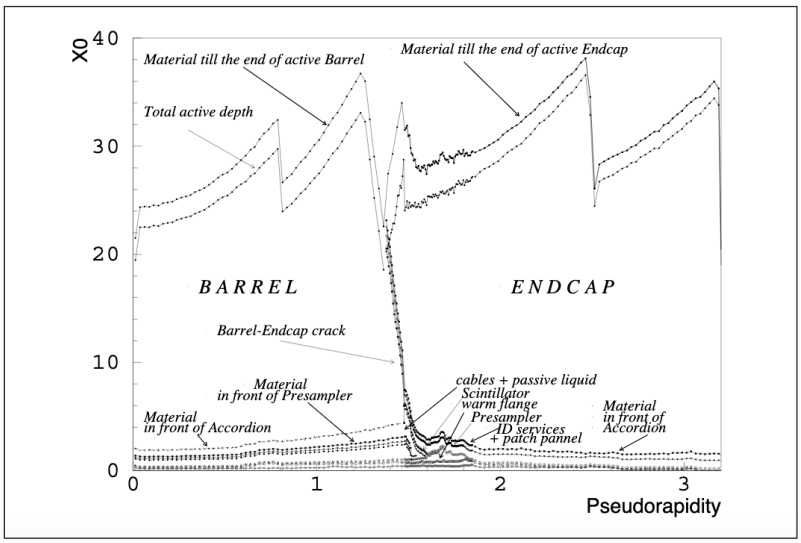

FIGURE 4.9. Material within LAr in radiation lengths.[23]

LAr uses a hardware-based signal pulse shaper, in additional to filtering software, to cope with the high pileup conditions at the LHC. As described in Section 3.2.2, low energy particles from nearby collisions, in space or time, can contribute to the instantaneous signal shape of each calorimeter cell readout. A clever solution to filter the component of the pulse of interest over the pileup is to convolve the calorimeter pulses with the pulse shaping response function on Figure 4.10. The result is an output signal whose amplitude is proportional to the current at time $t = 0$, synchronized with LHC collisions. Out of time pileup contributions to the signal are averaged away due to the null-integral of the pulse shaping function. Pile up does affect the timing and height of the output signal, but on average only the resolution of the amplitude is affected. In addition, the accordion geometry minimizes adverse effects of the detectors electronics on rise-time of the input current signal.

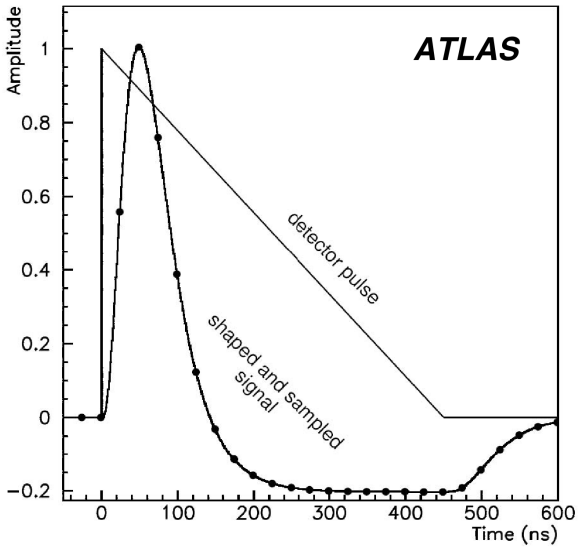

FIGURE 4.10. Shapes of Liquid Argon calorimeter current pulse in the detector and of the signal output after shaping. The dots indicate an ideal position of samples separated by 25 ns.[22]

4.3.2. Tile

The hadronic tile calorimeter (TileCal) is designed to completely contain hadronic showers of EM-neutral particles and any remaining electromagnetic showers surviving the 9.7 radiation lengths of the preceding detectors. TileCal is divided longitudinally into three sections, a barrel and two end-caps. A set of 64 modules covers the full azimuthal range, each covering $\Delta\phi = 0.1$. The end-caps each have one set, but the barrel has two sets of 64 modules. Each module, drawn in Figure 4.11, contains alternating layers of steel and scintillating tiles. Hadrons that reach TileCal will interact with the steel, showering the scintillators with electrons and photons. The resulting signal is transmitted to photo-multiplier tubes (PMTs) and read through wavelength-shifting optical fibers. This signal is then amplified and digitized for export to the trigger system.[24]

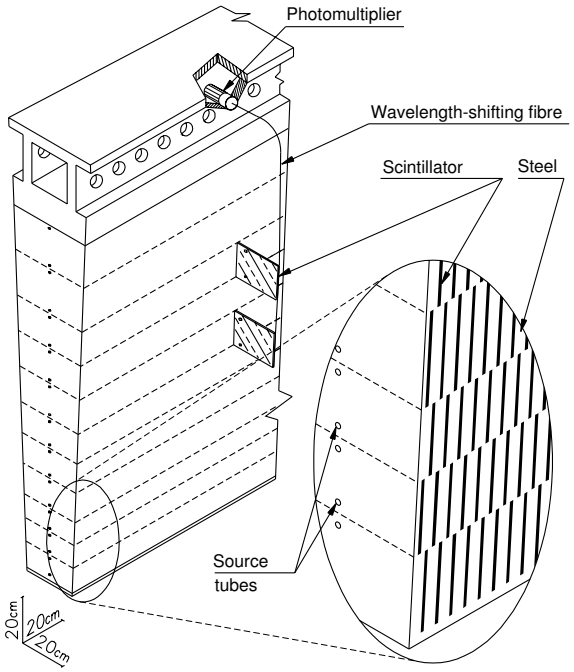

FIGURE 4.11. Example schematic of a Tile Calorimeter module. The steel and scintillators alternate for any particle's incidence angle.[24]

TileCal is at a distance of $r = 2.29$ m and has a radial length of 1.64 m; its central barrel covers the range $|\eta| < 1.0$ and is enhanced by the two extensions that cover $1.0 < |\eta| < 1.7$. Any particle showers developing at larger η are fully contained by the LAr hadronic end caps. The effective absorption length of TileCal is approximately $\lambda \sim 7.0$ in the barrel and rises slowly as the material transversed by particles increase with η; in the forward end-caps, the effective absorption length can be as high as 14, as shown in Figure 4.12. Since the central TileCal section only extends to $|\eta| < 1.0$, there is a physical gap between this and the barrel extension sections. In this void, a special plug tile calorimeter and gap scintillator is placed to compensate by the drop in effective λ.

The various active components of TileCal are intermittently calibrated to optimize its energy responses. The scintillating tiles are calibrated by moving a

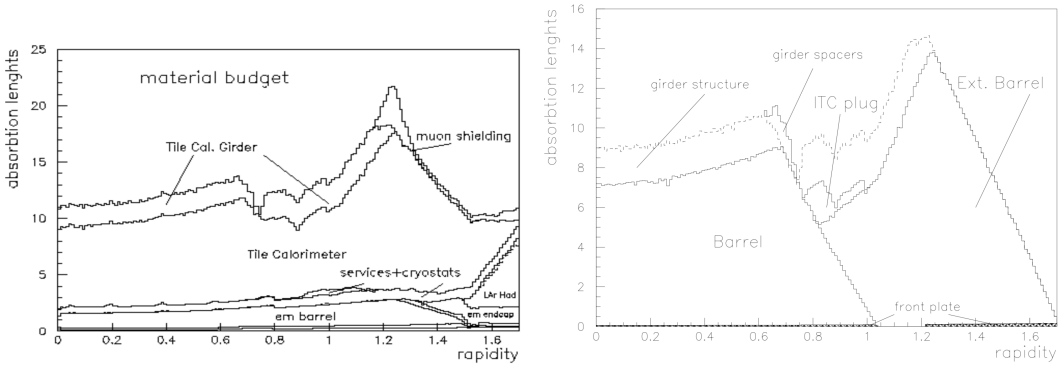

(a) Material budget for all ATLAS systems. Effective absorption lengths as a function of pseudo-rapidity.[24]

(b) Material budget for the ATLAS Tile calorimeter. Effective absorption lengths as a function of pseudo-rapidity.[24]

FIGURE 4.12. Material present within ATLAS. In the EM calorimeter the term used is radiation lengths, where as in the hadronic calorimeter it is absorption lengths. The hadronic calorimeter is designed to fully contain all particle showers.[24]

radioactive source, Cs^{137}, through a tubing system traversing the middle of each tile and adjusting the PMT voltages as needed. The PMTs have a dedicated fiber optic that is coupled to a reference laser whose wavefront imitates that of scintillator signals. Finally, to cope with the average current present during data-taking as a result of minimum bias event, an integrator system regulates the PMT voltages every 10 ms.

4.4. The Muon System

The outermost subsystem in ATLAS is designed to detect high momentum muons and contain any residual hadronic radiation surviving the calorimeters. Highly relativistic muons interact weakly with matter and thus can only physically samples, rather than fully absorbed. Hence the muon system implements two tracking approaches, one excelling at momentum and spacial resolution while the other can export precise timing information for triggering. To improve momentum

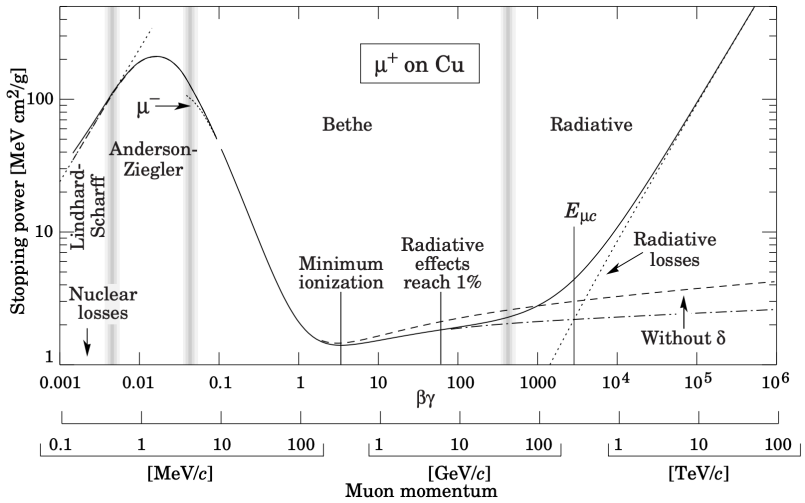

FIGURE 4.13. Energy absorption per unit mass of copper interacting with muons at varying momenta.[25]

resolution, a toroidal magnetic field surrounds the perimeter of the detector and bends the electrically-charged muons.

4.4.1. Minimally Ionizing Particles

Electrons lose their energy in matter primarily through brehmstralung radiation emitted from nuclear interactions with matter. More massive, relativistic, charged particles interact mostly with the electrons in the material and ionize or excited them. In particular, the instantaneous energy loss as a function of the relativistic coefficients γ and β is described by the Bethe-Bloch equation

$$-\frac{dE}{dx} = k_1 \frac{Z}{\beta^2}\left[\frac{1}{2}\ln\frac{k_2\beta^2\gamma^2 T_{max}}{I^2} - \beta^2 - k_3\right], \tag{4.8}$$

where Z is the nuclear charge of the material and k_i are constants characterizing the material and traversing particle properties. Figure 4.13 shows such a function for a muon interacting with copper.

Within ATLAS, a muon interacts with a variety of materials as it traverses the inner detectors and calorimeters. The resulting behavior of muons with momenta at or above a GeV are as particles imparting minimal ionization in the material and increasing radiative effects at higher momentum. On average, a muon loses a few GeV of its momentum before reaching the spectrometer. The muon system acts as a spectrometer rather than a calorimeter since the muon energy is not absorbed, but rather their trajectories are sampled.

4.4.2. The ATLAS Superconducting Toroid Magnets

As charged particles emerge from the calorimeters, they encounter a toroidal magnetic field created by superconducting magnets. Since the ATLAS calorimeters are designed to fully contain electromagnetic and hadronic showers, only muons are expected to contribute significantly to spectrometer activity. Sometime, very high energy hadronic showers could survive interacting with the calorimeters and deposit their remaining energy into the muon spectrometer. Resolving these objects is discussed in Section 7.4.

The ATLAS toroid Magnet system consists of eight Barrel coils, and two sets of eight coils in the End-Caps. All structures in the system are radially symmetric with respect to the beam axis. The End-Cap coils systems are rotated by 22.5 degrees with respect to the Barrel coils in order to provide radial overlap and optimize the bending power at the interface of both coil systems.[90] The coils are made of a 20.5 kA aluminum-stabilized NbTi superconductor. Each barrel coil has an axial length of 25.3 m and run along the radial axis from $r = 9.4 - 20.1$ m; end-cap coils are 5 m long and run through $r = 1.65 - 10.7$ m. The peak field provided

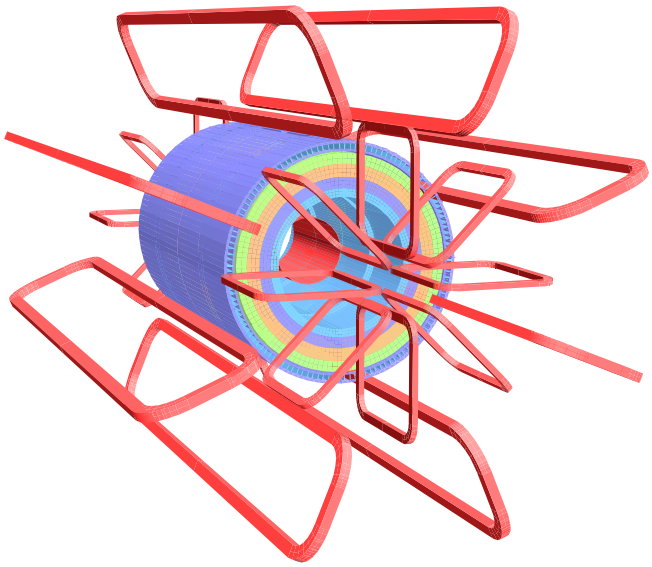

FIGURE 4.14. Simulated model of the toroid magnets in ATLAS.[18]

by the coils is approximately 4 T. A simulated model of the magnets is shown in Figure 4.14.

4.4.3. The Muon Spectrometer

The radius of curvature for a particle of charge q traveling perpendicular to an external magnetic field of strength B with momentum p is $R = \frac{p}{qB}$. The arc (L) can be reconstructed from tracking hits along the trajectory. The sagitta (and it's uncertainty) can be defined from at least three points:

$$s = y_3 - \frac{y_1 + y_2}{2} = \frac{L^2}{8R}; \delta s = \sqrt{\frac{3}{2}\delta y}. \tag{4.9}$$

A series of dedicated tracking and triggering modules are used to provides these points to reconstruct the particles reaching the spectrometer.

ATLAS uses high-Z gas mixtures to interact with muons in three classes of detectors throughout the spectrometer: monitored drift tubes (MDTs) and cathode

strip chambers (CSCs) for tracking, complimented by resistive plate chambers (RPCs) and thin-gap chambers (TGCs) for triggering. The eta coverage of the muon trigger system extents to $|\eta| < 2.4$, and the tracking is available up to $|\eta| < 2.7$.[26]

The barrel section consists of three layers of MDT tracking and RPC triggering, the closest is against the inner wall of the superconducting toroid at $r = 5$ m, the middle layer sits within the toroid rings at $r = 7.5$ m, and the furthest barrel layers are stationed against the outer perimeter of the toroid system at $r = 10$ m. Unlike the open-air barrel toroid, the end-cap toroid is enclosed in a cryostat, forcing the spectrometry in the end-caps to lie mostly outside magnetic fields. The end-caps are organized into four radially symmetric discs on each end of the barrel and positioned upstream, around, and downstream of the end-cap toroid at $|z| = 7.4, 10.5, 14$, and 21.5 m. Figure 4.15 shows the lateral and longitudinal cross-sections of the spectrometer.

The ATLAS MDTs are 30 mm-diameter aluminum tubes containing a mixture of 93% Argon to 7% CO_2 and a 50 μm-thick gold-plated tungsten-rhenium wire operating at a 3.08 kV. The characteristic drift time of the MDTs is determined by the longest electron path (the 15 mm tube radius) and is approximately 700 ns, which is unacceptably long for the nominal 25 ns LHC collision interval. The main advantage of the MDT system is their high momentum resolution enhanced by precision spatial calibration provided by the Resnik alignment system. At very high $|\eta|$, the average occupancy is too high for MDTs, thus ATLAS uses the hardier CSCs to cope with the larger background rate.

The timing resolution needed for effective triggering is supplied by the RPCs and TGCs. By minimizing the maximal drift distance in a high-Z gas cavity, both

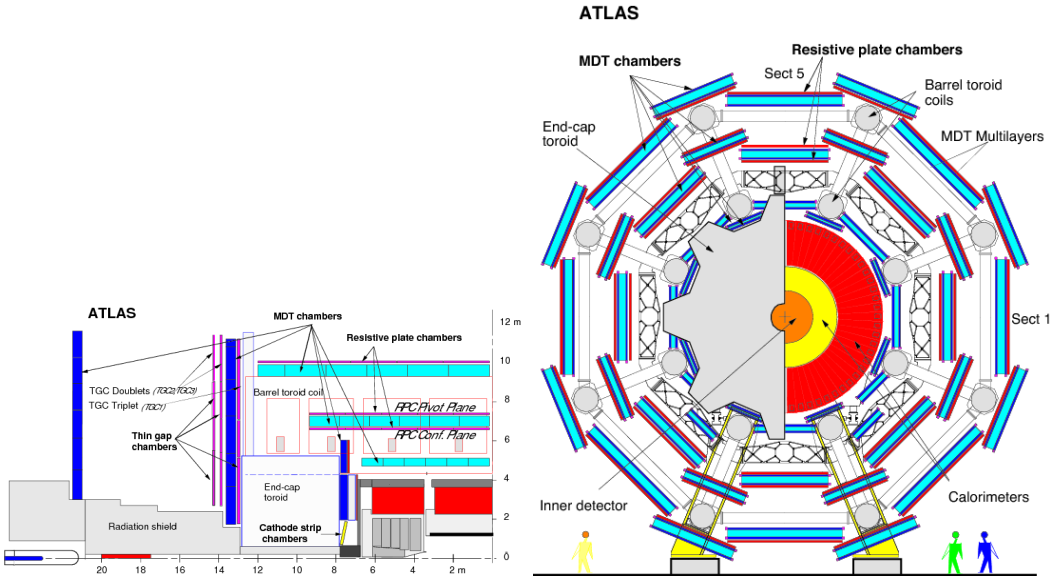

(a) Lateral view of the muon spectrometer (b) Cross-sectional view of the muon spectrometer

FIGURE 4.15. The ATLAS Muon Spectrometer.[26]

classes of detectors have temporal resolution of a few ns. The active gas in RPC is a mixture of 94.7 : 5 : 0.3% respectively of $C_2H_2F_4$/Iso-C_4H_10/SF_6, where as TGC cavities are flushed with 55 : 45% of $C0_2$/n-pentane. Normally a particle showers within the gas cavities propagates in 'avalanches', orderly cascades in the direction of the external electric field, but internal fields due to the free ion separation in the cavity can generate internal magnetic fields distorting the preferential direction of the shower. When the internal electric fields become comparable to the external fields, the cascading direction becomes isotropic a streamer, a finger-like current path, can form leading to arcs and localized plasma regions. To avoid streamer development, the hydrocarbons and CO_2 moecules provide rotation and vibrational modes which quench stream-producing photons.

CHAPTER V

ATLAS EVENT RECONSTRUCTION

5.1. Trigger System

A major point in the design of ATLAS was retrieving and recording the overwhelming data flow from the detector in an efficient and scalable form. The task is performed by the trigger and data acquisition system (TDAQ) and is strongly constrained by the machine conditions of the LHC and computing resources available to the collaboration. More specifically, the ATLAS trigger systems must cope with the 40 MHz bunch crossing rate of LHC, as well as the $\langle\mu\rangle \sim 50$ average interactions per bunch crossing, to reduce the rate to the $\sim$ 1 kHz recording bandwidth budgeted by the experiment. In Run 2, the ATLAS trigger system was divided into a hardware-based Level-1 Trigger (L1) and a newly merged software-based High Level Trigger (HLT).[91] The overall logic flow of the ATLAS trigger system is illustrated in Figure 5.1.

The proton bunch spacing of 25 ns implies that the particles emerging from a collision can travel a maximum of $\Delta X < c \times 25$ ns ~ 7.5 m, roughly the distance from the IP to the beginning of the Muon Spectrometer; at any given time, the various ATLAS sub-detectors are relaying signals originating from up to three different bunch crossings.[21]. The challenge of timing and combing the subsystems' readouts by bunch crossing is made possible by the modularity of ATLAS, since the subsystems have the capacity to independently export the information necessary in parallel and on-demand to the trigger system components.

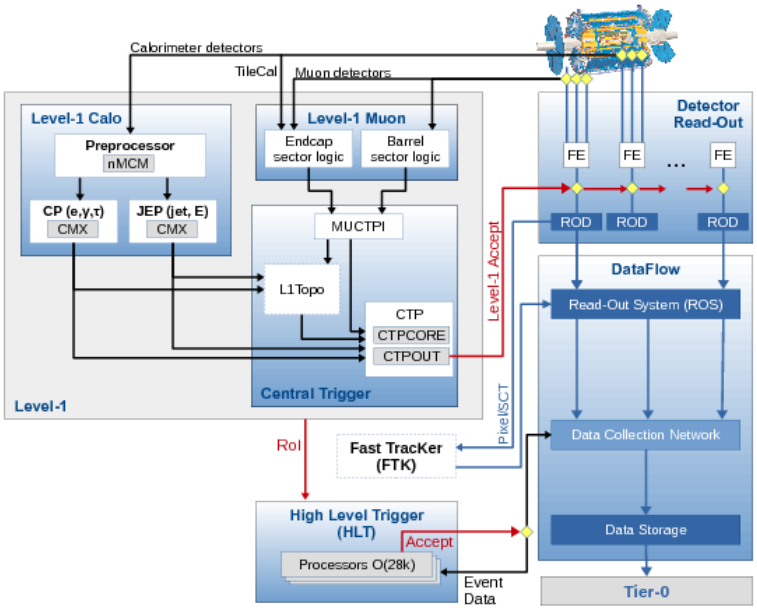

FIGURE 5.1. Data flow in the ATLAS trigger system. Hardware Level 1 triggers seed the software high level triggers, whose output is exported to the tier0 computing farm.[27]

5.1.1. Level-1 Triggers

The L1 trigger decision is formed by the Central Trigger Processor (CTP), which receives inputs from the L1 calorimeter (L1Calo) and L1 muon (L1Muon) triggers, as well as the Minimum Bias Trigger Scintillators (MBTS), LUCID Cherenkov counter, and Zero-Degree Calorimeter (ZDC) subsystems. The time it takes to export the triggered information is several times larger than the proton bunch spacing, therefore the CTP applies a preventive *dead-time* to limiting data collection. To avoid the effects of the adjacent bunch crossing to the collision of interest, a *simple dead-time* sets the minimum time between two consecutive L1 accepts. On the other hand, *complex dead-time* is enforced between L1 accepts to avoid the front-end buffers from overflowing. The size of these buffers vary by sub-

detector and typically holds up to $\sim$ 100 events in memory. In 2015 running, the simple dead-time was set to 4 bunch-crossings (100 ns).[92]

The L1 trigger logic is divided into the central, calorimeter, and muon trigger systems. Since the dominant backgrounds at the LHC are QCD processes, the L1Calo and L1Muon trigger systems are designed to identify electroweak objects and high momentum jets. The output of L1Calo and L1Muon are fed to the central trigger which exports the η/ϕ coordinates of relevant Regions of Interest (ROIs) to the HLT if a positive decision is reached. The ROIs in L1 are identified using a sliding-window algorithm, which sums the total energy deposited in a square η/ϕ windows and triggering if the sum surpasses certain energy thresholds (e.g. L1_J15, L1_EM20, L1_XE110). The decision time for the L1 triggers is on the order of 2 μs and reduces the data rate from 40 MHz to 100 kHz.[91]

5.1.2. High Level Triggers

After passing L1 triggers, events are buffered in the Read-Out System (ROS) and processed by the HLT. The HLT receives Region-of-Interest (RoI) information from L1, which are used for coarse reconstruction in the trigger algorithms. If an event is accepted by the HLT, it is transferred to local storage at the experimental site and exported to the Tier-0 facility at CERN's Data Centre for offline reconstruction.

The HLT uses tracking information from the inner detectors to group the origins of the tracks into primary vertices (PVs), of which a reconstructed effective mass equal to the four-vector sum of all objects associated to the PV is calculated for each. If the HLT reaches a positive decision, only the objects matched to the PV with highest effective mass are saved and passed on for permanent storage.

The HLT is allotted much longer computation time allowance (a few seconds) and receives full granularity information from the detector subsystems to reconstruct physics objects and event observables, such as M_{eff} and E_T^{miss}, at a higher sophistication than is possible at L1.

On export from the HLT, the average event file size is $\sim$ 1.5 Mb yielding a data flux of tens of Gb/s if recording at an event rate of 1kHz. This data exits the ATLAS site and travels $\sim$ 1 km to the CERN Data Centre, where it is further processed for permanent storage on the Worldwide LHC Computing Grid along with the data of the other LHC experiments. The grid is composed of over 170 computing farms spread across 42 countries and is used for long-term data storage and large-scale data analysis. With Run 2 conditions, the grid stores $\sim 50 - 70$ Pb of experiment data per year and is expected to increase at least an order of magnitude with the High-Luminosity LHC.[93]

5.2. Particle Showering and Hadronization

At the LHC, the predominant (hardest) interactions are gluon-gluon and quark-gluon. The protons fragment during collision and their partons interact, as shown in Figure 5.2. The produced particles radiate and interact with the detector material as they outward. Before interacting with ATLAS, the quarks and gluons radiate to produce colorless objects in a process called hadronization. The resulting mesons and hadrons, as well as leptons and photons, interact with in the calorimeters and produce a cascading shower of lower momentum particles. Muons interact the least and survive to the spectrometer. Combining the information from the tracker, calorimeters, and the muon spectrometer allows us to identify particles from the collision.

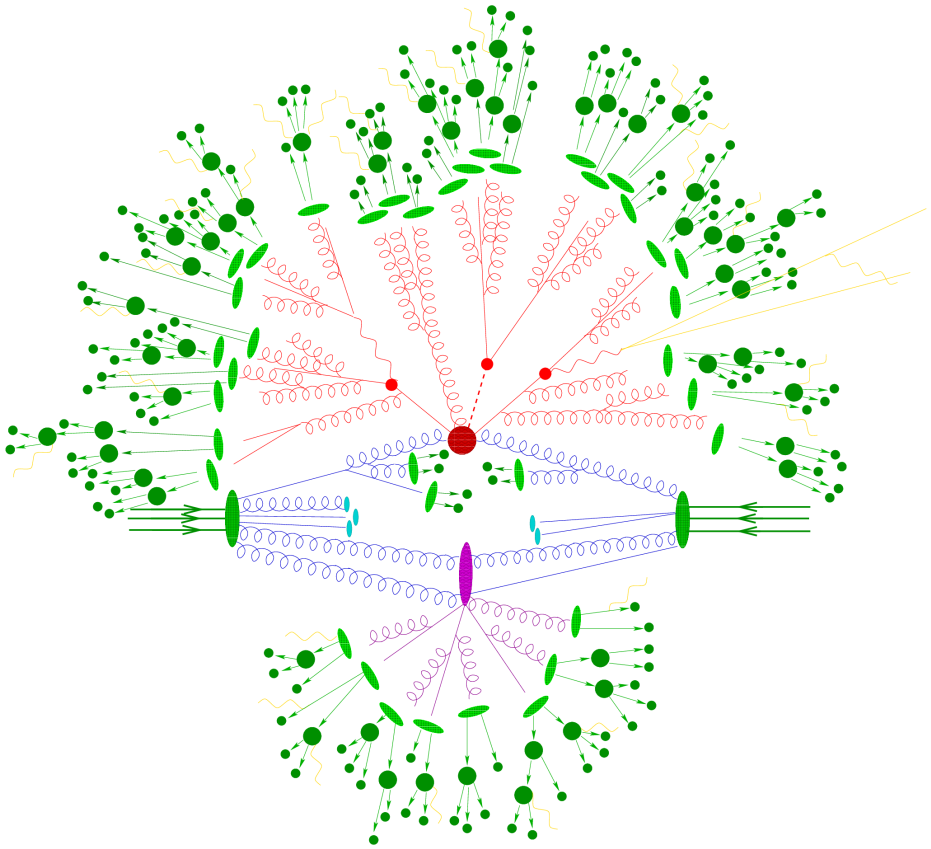

FIGURE 5.2. Cartoon of a proton-proton collision and resulting parton interactions. The red dot is the primary hard collision, the solid (dotted) red lines represent promptly-decaying on(off)-shell partons followed by its radiative showering, the light green ovals are the transition of partons to hadrons, and the dark green ovals correspond to hadron decays. The purple ovals are the secondary hard scattering from other proton constituents and the small blue ovals represent spectator partons.[28]

Immediately following the collision, produced particles can radiate gluons and photons. The shower shape within the electromagnetic calorimeter differs between photons, electrons, and charged pions. Photons and electrons interact strongly with LAr and should be completely contained within the closer calorimeter, hence any significant hadronic calorimeter activity is likely to be due to charged and/or neutral hadrons originating from quarks or gluons. Similarly, the hadronic calorimeter is designed to fully contain the showers of colored objects produced

from collisions. In analysis, we can identify the calorimeter activity of a muon candidate with hits on the muon spectrometer to differentiate them from jets. A summary of these interactions is shown in Figure 5.3.

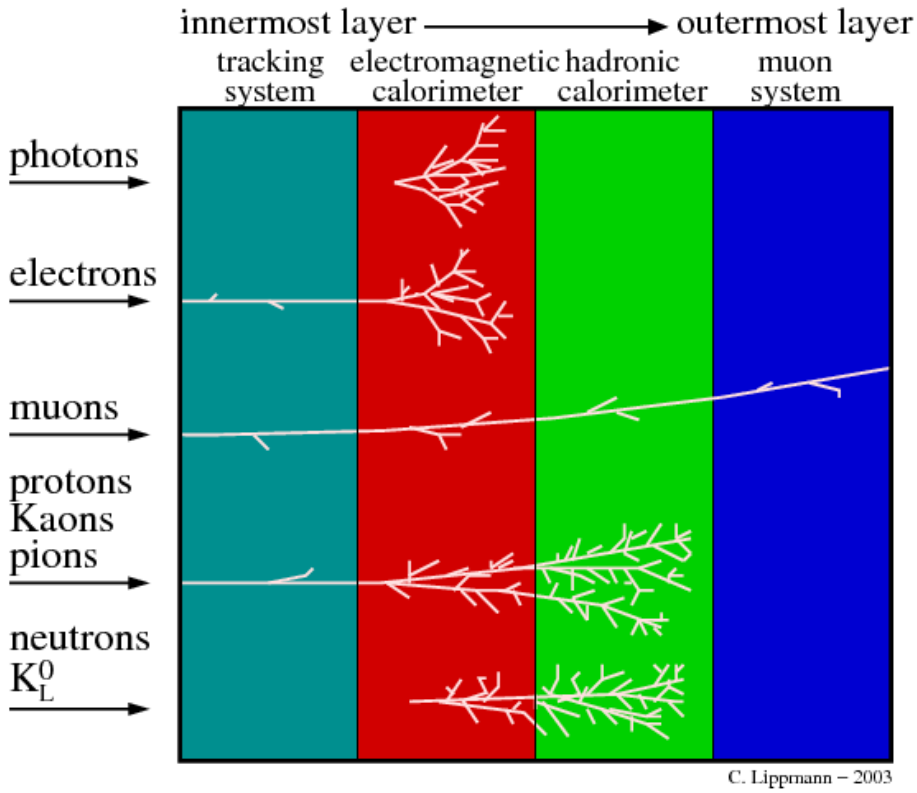

FIGURE 5.3. Summary of particles' interactions with general purpose detectors, such as ATLAS. Photons do not leave tracks and shower completely within the EM calorimeter. Electrons leave tracks and shower completely within the EM calorimeter. The shower shapes of electrons and photons differ and are used to identify the objects. Hadrons (pions, protons, neutrons, etc.) leave tracks if charged and their showers completely contained in the hadronic calorimeter. Muons leave tracks throughout the ATLAS subsystems.[20]

General-purpose detectors like ATLAS are designed to take advantage of the position and material of its sub-detectors to differentiate between produced particles: the tracker is closest, followed by the calorimeters, and the muon spectrometer sits at the perimeter. This strategic positioning of the sub-detectors

serves as the first level of object identification. The cartoon on Figure 5.4 summarizes the various particles and their interactions with ATLAS.

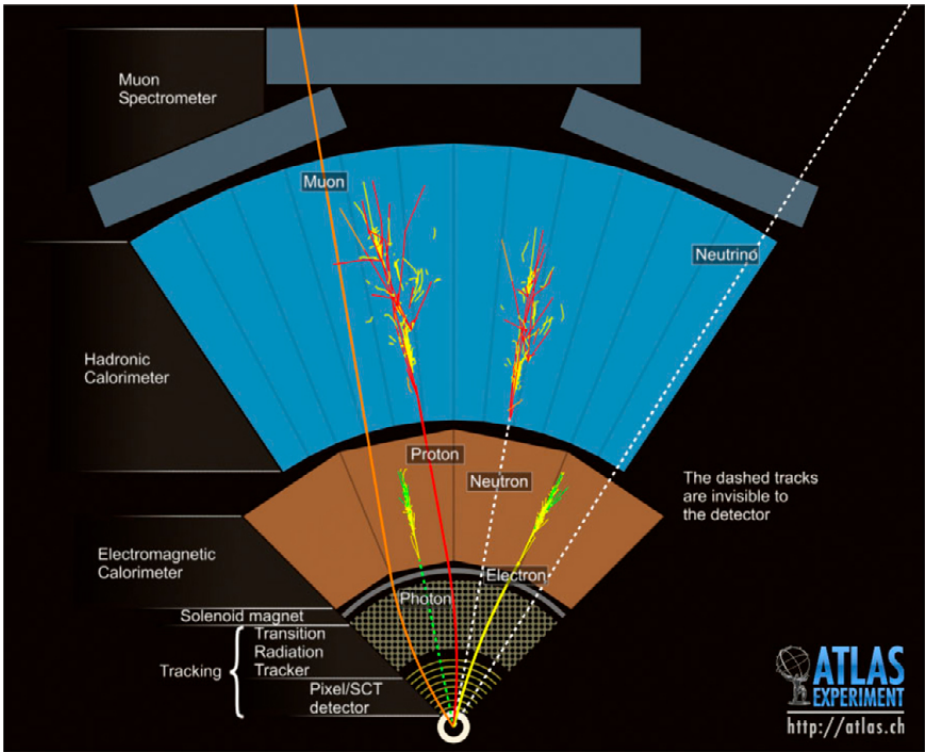

FIGURE 5.4. Quarter section of the ATLAS detector in the azimuthal plane. The collision point is at the vertex, interactions with sub-detectors are represented by the solid lines, and the dotted lines indicate the particle passes through undetected.[29]

Reconstructing the tracks and associating them to the calorimeter and spectrometer activity is essential to differentiating between the produced particles. Since only charged particles interact with the tracking medium, we can associate isolated calorimeter activity without tracks as photons. Muons at the GeV scale act as minimally ionizing particles, depositing only a small fraction of their momenta in the trackers, calorimeters, and the muon spectrometer.

5.3. Jet Definition

Jets are the catch-all objects for significant calorimeter activity and are defined by the clustering algorithm grouping the input calorimeter objects. Hard non-jet objects such as electrons, muons, and photons, all deposit energy in the calorimeter and could be classified as jets; it is necessary to define the hard non-jet objects and remove calorimeter objects associated to those objects in order to correctly define the jets. Furthermore, since the ATLAS calorimeters are non-compensating sampling detectors, jets are calibrated in offline analysis.

5.3.1. Topological Clustering

Calorimeter cells are grouped into continuous objects (topo-clusters) through a seed-and-collect protocol.[94] The key observable in the clustering is the cell signal significance

$$\mathcal{S}^{EM}_{cell} = \frac{E^{EM}_{cell}}{\sigma^{EM}_{cell,noise}}, \text{ where } \sigma^{EM}_{cell,noise} \equiv \sqrt{\sigma^2_{electronic} + \sigma^2_{pileup}}. \tag{5.1}$$

The cell energy and noise resolution are measured at the *EM-scale*. Seeds are defined by cells with significances greater 4. The protocol then clusters any neighboring cells with positive significance (energy). If any of the perimeter cells have a significance greater than 2, then the clustering proceeds with the secondary seed.

The raw proto-clusters formed in the above algorithm are often too large to provide accurate measurement of the energy flow.[94] The layered information of the Tile and LAr calorimeters are used to split the objects into the final topoclusters.

5.3.2. Standard ATLAS Jets

The jets used by the vast majority of ATLAS analyses, including the one presented in this dissertation, are built from EM-scale topoclusters grouped into jets using the anti-k_{T} algorithm with radius parameter $R = 0.4$. The anti-k_{T} algorithm clusters the softest objects onto harder objects. The resulting shapes of the objects using this algorithm are characteristically circular for high momentum jets and crescent-shaped for close-by subleading jets, as shown in Figure 5.5.[30]

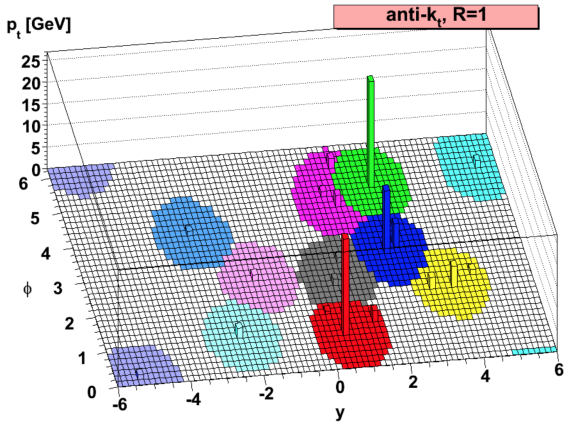

FIGURE 5.5. The anti-k_{T} algorithm produces circular jets; if two jets are nearby, the sub-leading jet will take on a crescent shape.[30]

Initial pseudo-jets are defined by the coordinates and momenta of the topoclusters; they are assigned zero mass. All psuedo-jets are assigned a pair-wise distance measure (d_{ij}) with respect to all other pseudo-jets:

$$d_{ij} = min(k_{t,i}^{-2}, k_{t,j}^{-2}) \frac{\Delta\eta_{ij}^2 + \Delta\phi_{ij}^2}{R^2}. \tag{5.2}$$

The anti-k_{T} algorithm weighs the physical distances between the pseudo-jets by minimum of the squared inverses of the momenta. The algorithm is recursive and

iterates until all pseudo-jets are separated by at least the R-parameter in $\eta - \phi$-space. The resulting objects are R=0.4 anti-k_{T} jets.

5.3.3. ATLAS Calibration Chain

Jets are composed of a shower of particles, approximately 2/3 of the hadrons are charged and 1/3 are neutral. Only the charged particles interact with LAr and contribute to the EM-scale momenta. To account for the portion of the showers absorbed by the hadronic calorimeter, jets are calibrates through simulation and data-driven techniques. The calibrations are provided on a collaboration-wide basis and are binned in η, ϕ, and p_T. [31].

The origin point assumed during jet clustering (finding) is not necessarily the collision point. In order to correct this, all jets are oriented with their origins at the hard-scatter vertex. Since EM-scale measurements are particularly sensitive to pileup effects, the next corrections applied are energy subtractions based on the area and momentum of the jet, as well as the number of primary vertices and measured μ (hard-interactions):

$$p_T^{corr} = p_T^{reco} - \rho \times A - \alpha \times (N_{PV} - 1) - \beta \times \mu. \tag{5.3}$$

The behavior of jets is studied in simulation to correct the energy and direction of the jets. This is done by measuring the energy response between the reconstructed jet (E_{reco}) and it's simulation-level object (E_{truth}):

$$\mathcal{R} = \frac{E_{reco} - E_{truth}}{E_{truth}}. \tag{5.4}$$

Ideally, the mean of the distribution would be centered at 0. In practice, the uncalibrated jets have a shifted mean in the energy response distribution and its mean is taken as the Jet Energy Scale (JES) correction factor. The η of jets is also corrected through simulation studies.

If the jet detector response is measured to be dependent on any observable, a correction can be applied that leaves the JES unchanged. The correction factor is extracted by parameterizing the jet response with the observable at hand:

$$C(x) = \frac{\mathcal{R}^{-1}(x)}{\langle \mathcal{R}^{-}1(x) \rangle}. \tag{5.5}$$

The dependance of each observable considered is removed sequentially and the momentum corrected by

$$p_T^i = C^i(x_i) \times p_T^{i-1} = C^i(x_i) \times C^i(x_{i-1}) \times p_T^{i-2} = \cdots . \tag{5.6}$$

The process known as Global Sequential Calibration (GSC) improves the jet resolution. The full ATLAS calibration chain is summarized in Figure 5.6.

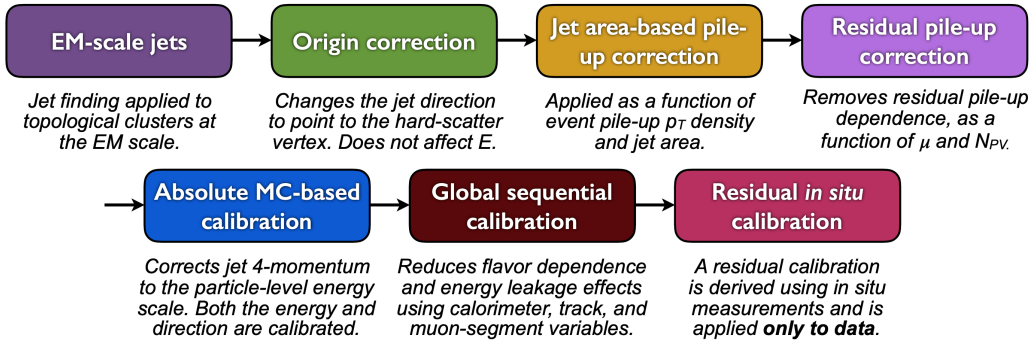

FIGURE 5.6. The ATLAS calibration chain used for standard EMTopo jets.[31]

5.3.4. JES in $t\bar{t}$ + $E_{\mathrm{T}}^{\mathrm{miss}}$ Analysis

The analysis presented in this dissertation uses fully calibrated R=0.4 anti-k_{T} EMTopo jets for most selections. The top candidates are constructed by clustering these input jets into larger-R jets, described later in Section 6.3. A major benefit to this approach is that the uncertainties due to the JES are propagated from the smaller, better resolved R=0.4 jets into the larger-R top candidates.[95] In addition, the pileup corrections applied to the small-R jets makes the large-R jets robust against the effect.

The JES is a single value used to scale the energy of the jet depending on its momentum and location in the detector. Fluctuations of the scale can greatly influence the calculation of higher-level variables like top candidate mass. The ATLAS Jet/EtMiss working group provides the collaboration with JES calibrations and recommendations, but the evaluation on the uncertainty of this effect in the phase space specific to our analysis is documented in Section 10.1. A plot illustrating the behavior of the JES as a function of jet momentum and pseudo-rapidity is shown in Figure 5.7.

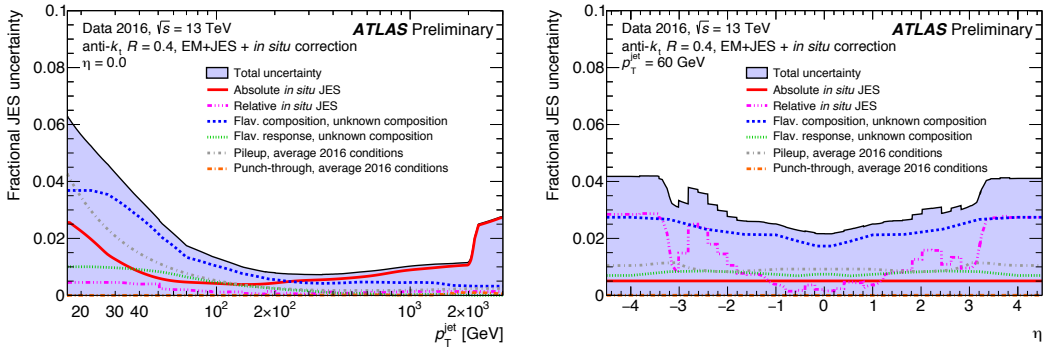

(a) JES for R=0.4 anti-k_{T} EMTopo jets as a function of transverse momentum.

(b) JES for R=0.4 anti-k_{T} EMTopo jets as a function of pseudo-rapidity.

FIGURE 5.7. ATLAS JES recommendations for EMTopo jets.[32]

5.3.5. In-Situ Jet Energy Resolution

After all calibrations have been performed, the resolution on the jet energy (JER) can can be measured. The JER is taken to be the width of the energy response between the calibrated jet and a well-resolved reference object. The standard ATLAS jets used in the analysis have their JER measured using a combination of such methods, but I will focus the discussion on the dijet direct-balance method.

The *Dijet Balance Method* extracts the relative JER of reconstructed jets by examining the transverse momentum (p_T) asymmetry between the two highest momentum jets in dijet-rich events,

$$A = \rho \frac{p_{T,1} - p_{T,2}}{p_{T,1} + p_{T,2}}, \tag{5.7}$$

where ρ is a ± 1 random sign.

We assume that the asymmetry is normally distributed and use a Gaussian fit to quantify the scale of the fluctuations in the asymmetry distribution. Since jet collections are ordered in p_T, we randomize the overall sign of the computed asymmetries and fit a Gaussian function. For balanced jets, the width of the asymmetry distribution is given by:

$$\sigma(A) \simeq \frac{\sqrt{\sigma^2(p_{T,1}) + \sigma^2(p_{T,2})}}{\langle p_T^1 + p_T^2 \rangle} \simeq \frac{1}{\sqrt{2}} \frac{\sigma(\bar{p}_T)}{\bar{p}_T}, \tag{5.8}$$

where $\sigma(A)$ is the width of the asymmetry distribution and $\left(\frac{\sigma(\bar{p}_T)}{\bar{p}_T}\right)$ is the relative jet p_T resolution. To relate the asymmetry width to the relative jet energy resolution (JER), we need an additional assumption that the two jets have similar

rapidities. For this study, it is safe to assume that the measured rapidity and pseudorapidity of the jets are identical. This is guaranteed by requiring that both jets are in the same η region and have similar p_T. With this additional assumption, the relative jet p_T resolution also becomes the relative JER.

In summary, by satisfying

$$p_{T,1} \simeq p_{T,2} \simeq \bar{p}_T \text{ and } |\eta_1| \simeq |\eta_2| \in [0, 0.8] \text{ or } [0.8, 2.5] \ , \tag{5.9}$$

we can then relate the width σ_A to the relative JER by

$$\text{Relative JER } = \frac{\sigma(\bar{p}_T)}{\bar{p}_T} = \sqrt{2}\sigma_A(\bar{p}_T). \tag{5.10}$$

The results are provide for various $\bar{p}_T$ and pseudo-rapidity (η) bins. Further information on the JER studies performed for my ATLAS qualification task can be found in Appendix B.

CHAPTER VI

SEARCH STRATEGY

Supersymmetry (SUSY) [96] at the TeV-scale is strongly motivated by the potential for SUSY to be a solution to the hierarchy problem, as described in Section 2.1. The largest contributions to the radiative corrections of the Higgs mass are from partners to the third generation quarks, the stop and sbottom. The analysis presented in this dissertation focuses on the direct production of a new SUSY scalar particles (stop) which couple to the top quark via a Yukawa-like coupling due to the high top quark mass. If these hypothetical new particles decay, at least a fraction of the time, into stable neutral particles, the $t\bar{t} + E_{\mathrm{T}}^{\mathrm{miss}}$ channel then becomes particularly relevant for a dedicated search. The parameters of interest of the simplified model considered in $t\bar{t} + E_{\mathrm{T}}^{\mathrm{miss}}$ analysis are: the top squark mass ($m_{\tilde{t}}$), the lightest supersymmetric particle (LSP) mass ($m_{\tilde{\chi}_1^0}$) and the branching ratio of the top squark to top quark (B).

With the Run 2 of the LHC now concluded, we may further explore SUSY phase space with four times the data than previous publications. We start below by introducing briefly the new physics model considered in this work and highlight a few peculiarities of the all-hadronic $t\bar{t} + E_{\mathrm{T}}^{\mathrm{miss}}$ final state. Similar searches focusing on semi-leptonic and dilepton decay modes of the top quark (or of the $W^{(*)}$) are currently in progress. This analysis is designed to be orthogonal to those searches in order to allow for a global combination of all relevant channels in a future publication.

6.1. Experimental Signature of All-Hadronic Stop Decays

The search for direct production of third-generation squarks (assuming the masses of all other sparticles to be out of reach) is therefore of upmost interest. The $t\bar{t}$ $+E_{\mathrm{T}}^{\mathrm{miss}}$ analysis is sensitive to the production channel $pp \rightarrow \tilde{t}\,\tilde{t} + X$, where two stop decay modes considered were:

- 2-body decay (on-shell top): $\tilde{t} \rightarrow t + \tilde{\chi}_1^0$, or
- 3-body [4-body] decay (off-shell top) [off-shell top, off-shell W]: $\tilde{t} \rightarrow b + W^{[*]} + \tilde{\chi}_1^0$.

In all cases, all-hadronic decays of the top quarks (or of the $W^{[*]}$ in the $b + W^{[*]} + \tilde{\chi}_1^0$ modes) are considered. The Feynman diagram for the process is shown in Figure 6.1.

The all-hadronic top channel is challenging due to the large number of jets and the absence of leptons, which lead respectively to a busy environment and a high background from SM top and QCD processes. However, this channel presents the advantage of a relatively high all-hadronic branching ratio of top decays and the absence of invisible SM particles (neutrinos) in the final state. In our signal, the $E_{\mathrm{T}}^{\mathrm{miss}}$ originates only from the searched invisible particles.

Explicitly, the experimental signature is multiple jets and high $E_{\mathrm{T}}^{\mathrm{miss}}$. The dominant background sources are:

- $Z \rightarrow \nu\bar{\nu}$ plus additional b-jets,
- lepton+jets $t\bar{t}$ events, which contain $W \rightarrow e/\mu/\tau + \nu$ decays where the lepton is either lost or mis-identified as a jet (and have high $E_{\mathrm{T}}^{\mathrm{miss}}$ due to the escaping neutrino),

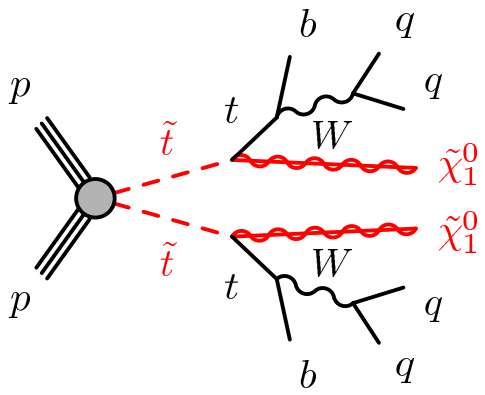

FIGURE 6.1. Feynman diagram for the stop models optimized.[33]

– $W \to \ell\bar{\nu}$ plus additional b-jets,

– $t\bar{t} + Z$, where both tops decay hadronically and $Z \to \nu\bar{\nu}$, and

– Wt-channel single top decays, where one W decays hadronically and one leptonically.

6.2. Executive Summary of Contributions

The full breadth of the $t\bar{t}$ $+E_{\mathrm{T}}^{\mathrm{miss}}$ analysis is beyond the scope of this dissertation and I will focus on large missing transverse energy signatures ($E_{\mathrm{T}}^{\mathrm{miss}} >$ 250 GeV) assuming a 100% branching fraction of $\tilde{t} \to t\chi_1^0$. More specifically, the bulk of my work in the full Run 2 analysis was dedicated to understanding the $t\bar{t}$ background to the two-bodied non-compressed scenarios. Below is a list of the institutes participating in the analysis and their physics responsibilities within the team:

– Analysis Contacts:

  * Dr. Matthias Saimpert (DESY, Germany)

  * Dr. Walter Howard Hopkins (Argonne National Laboratory)

- Oregon
    - $t\bar{t}$ Estimation: Non-Compressed, Two-Body (Author's Contribution)
    - Z + jets Estimation: Non-Compressed, Two-Body
- Sheffield
    - $t\bar{t}$ Estimation: Compressed, Two-Body
    - ttZ Estimation
    - Multijet Estimation
    - Fit Results
- Freiburg
    - SR Optimization
    - Fit Results
- Tokyo
    - W + jets Estimation
    - Single Top Estimation
- Melbourne
    - Four Body Signal Region and Background Estimation

In the following sections, I will describe the $t\bar{t} + E_{\mathrm{T}}^{\mathrm{miss}}$ analysis focusing on my contributions to the search. At times I will be using the results of studies produced by other team members. The ATLAS analysis is in mature stages of publication and the appropriate guidelines for unpublished data are satisfied.

6.3. Top Reconstruction

For signal regions targeting the pair production of non-compressed $\tilde{t} \to t + \chi_1^0$, the reconstruction of two decaying top quarks in the event helps to reduce the background from QCD, W + jets, Z + jets, and lepton+jets $t\bar{t}$ background. Top candidates are identified within the $t\bar{t}$ $+E_{\mathrm{T}}^{\mathrm{miss}}$ analysis through the jet-mass of *reclustered* large-R jets. Conversely, compressed signal regions exploit the correlations between ISR jet and the $\vec{E}_{\mathrm{T}}^{miss}$.

When a top quark decays, it results in a b-quark and an on-shell W-boson. The opening angle between the top daughters decreases with increasing top-parent momentum, roughly $\Delta R = \frac{2M}{p_T}$. Jet reclustering is performed using the anti-k_{T} algorithm with a large distance parameter (e.g., $R = 1.2$) over the calibrated anti-k_{T} $R = 0.4$ jet collection. Figure 6.2 illustrates the reclustering and provides a two-dimensional distribution of the top-p_{T} and the opening angle of its daughters showing that most top decay are contained within a distance parameter of $R = 1.2$.

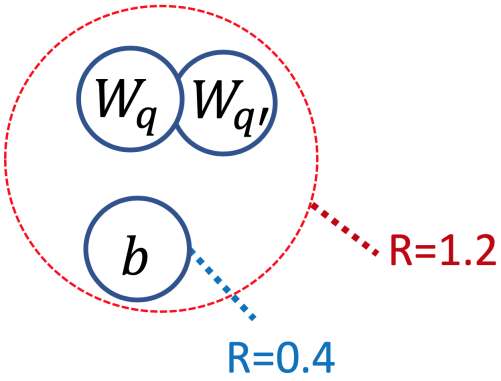

(a) Cartoon showing reclustering of input R=0.4 jets into top-candidate R=1.2 jets.

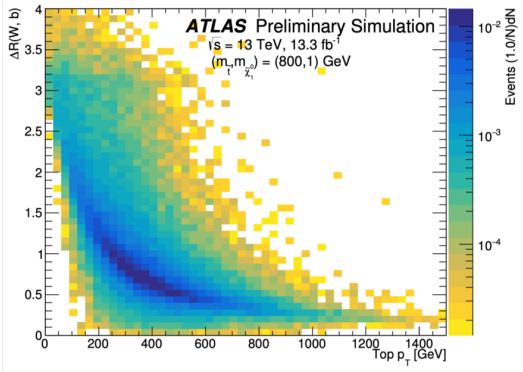

(b) Opening angle (y-axis) of the top-daughters with respect to the $p_{\mathrm{T}}$of the top-parent (x-axis).[33]

FIGURE 6.2. Top candidates are defined as the leading and subleading (in p_{T}) large-R reclustered jets.

The highest (second highest) p_{T} reclustered jet is designated as the first (second) top candidate and their masses are indicated by $m^0_{jet,R=1.2}, m^1_{jet,R=1.2}$. Furthermore, a reclustered jet is considered as 'b-tagged' if it includes at least one b-tagged calorimeter jet among its constituents. A major benefit of using *calibrated* inputs jets, as opposed to raw calorimeter topoclusters, is that the resulting large-R jet is less sensitive to resolution effects. Various optimization studies in previous iterations of the ATLAS all-hadronic stop search have found that this method using $R = 1.2$ (top candidate) and $R = 0.8$ (W candidate) results yields the best signal sensitivity.

6.4. Trigger Strategy of $t\bar{t} + E_T^{miss}$ Analysis

The analysis is performed with the full ATLAS-Run 2 pp collision data sample recorded at $\sqrt{s} = 13$ TeV, i.e. combining data collected during the years 2015, 2016, 2017 and 2018. Given our experimental signature of many jets and large $E_{\mathrm{T}}^{\mathrm{miss}}$ we have the option of triggering on the visible or invisible features. Due to the large hadronic background of the LHC, the $E_{\mathrm{T}}^{\mathrm{miss}}$ is the best initial discriminant and our choice of trigger.

Events are required to fulfill standard data quality requirements corresponding to the 'All_Good' good run list (GRL), meaning that all relevant ATLAS detector components are required to be functioning normally. Events are required to pass either the lowest unprescaled missing transverse energy trigger (0- and 1-lepton regions) or single lepton trigger (2- and 3-lepton regions). The integrated luminosities of the total data sample is 139 ± 2 fb^{-1}.

6.4.1. Missing Energy Trigger

The triggers used in the 0/1-lepton regions are based on the missing transverse energy calculated at trigger-level. The Level-1 trigger uses coarse objects to calculate the event's $E_{\mathrm{T}}^{\mathrm{miss}}$(L1XE). The High-Level Trigger (xe) is seeded by the L1 decision, makes more detailed computations with better resolved objects, and typically selects tighter than the preceding trigger. As the run-time trigger rates increased over time, the lowest unprescaled increased its thresholds. Table 6.1 lists the triggers used in the analysis.

Trigger chain names	2015	2016	2017	2018
HLT_xe70_mht	✓			
HLT_xe90_mht_L1XE50 (A-D3)		✓		
HLT_xe100_mht_L1XE50 (D4-F1)		✓		
HLT_xe110_mht_L1XE50 (F2-end)		✓		
HLT_xe110_pufit_L1XE55 (B1-D5)			✓	
HLT_xe110_pufit_L1XE50 (D6-end)			✓	
HLT_xe110_pufit_xe70_L1XE50 (B-C5)				✓
HLT_xe110_pufit_xe65_L1XE50 (C6-end)				✓

TABLE 6.1. Lowest unprescaled missing transverse energy trigger chains used in 2015, 2016, 2017 and 2018 for 0- and 1-lepton selections. A logical OR is performed between the various chains for a given year. Different chains are sometimes used depending on the data-taking Period.

6.4.2. Single Lepton Triggers

For 2/3-lepton regions, the primary motivation for using single-lepton triggers is to increase statistics at low lepton momentum. For electrons, the trigger decision is based on the momentum, impact parameter d_0, and the electron likelihood value. For muons, the trigger also uses the particles' momenta and likelihood value, although the triggers became solely p_{T}-based in later years. The triggers used in the analysis are summarized in Table 6.2.

Trigger chain names	2015	2016	2017	2018
HLT_e24_lhmedium_L1EM20VH	✓			
HLT_e26_lhtight_nod0_ivarloose		✓	✓	✓
HLT_e60_lhmedium	✓			
HLT_e60_lhmedium_nod0		✓	✓	✓
HLT_e120_lhloose	✓			
HLT_e140_lhloose_nod0		✓	✓	✓
HLT_mu20_iloose_L1MU15	✓			
HLT_mu26_ivarmedium		✓	✓	✓
HLT_mu40	✓			
HLT_mu50		✓	✓	✓

TABLE 6.2. Lowest unprescaled single lepton trigger chains used in 2015, 2016, 2017 and 2018 for 2- and 3-lepton selections. A logical OR is performed between the various chains for a given year.

6.5. Signal and Background Simulation

Monte Carlo (MC) simulated events are used to model the SUSY signal and to aid in the description of the background processes. Recommended ATLAS MC samples from the MC16a, MC16d and MC16e campaigns are used to model 2015+2016, 2017 and 2018 data, respectively. The MC16a (MC16d, MC16e) events are weighted to reproduce the observed distribution of the average (actual) number of interactions per bunch crossing of 2015+2016 (2017, 2018) data, as show in Figure 3.8.

6.5.1. Generators and Detector Simulation

The baseline MC samples modeling background were processed through the full ATLAS detector simulation [97] based on GEANT4 [98], but most samples used for systematic uncertainty evaluation were processed through the AtlFast2 fast simulation instead, as well as the nominal signal MC samples. All MC events have additional overlaid minimum bias interactions generated with Pythia 8 [99, 100] to simulate pileup background, and were reconstructed using the same algorithms as the data.

Signal models were all generated with MG5_aMC@NLO 2.2.3 [37] interfaced to PYTHIA 8 [100] for the parton showering (PS) and hadronization and with EvtGen 1.2.0 [101] for the b- and c-hadron decays. The matrix element (ME) calculation was performed at tree level and includes the emission of up to two additional partons for all signal samples. The parton distribution function (PDF) set used for the generation of the signal samples is NNPDF2.3LO [102] with the A14 [103] set of tuned underlying-event and shower parameters (UE tune). The ME–PS matching was performed with the CKKW-L prescription [104] , with a

matching scale set to one quarter of the mass of the $\tilde{t}$, or $\tilde{g}$ for the gluino pair production model. All signal cross sections are calculated to approximate next-to-next-to-leading order in the strong coupling constant, adding the resummation of soft gluon emission at next-to-next-to-leading-logarithmic accuracy (approximate NNLO+NNLL) [105, 106, 107, 108]. The nominal cross section and the uncertainty are derived using the PDF4LHC15_mc PDF set, following the recommendations of Ref. [109].

6.5.2. Sample Details

SM background samples were generated with different MC event generators depending on the process. Details of the generators and parton showering used for different processes are shown in Table 6.3.

Process	ME event generator	ME PDF	PS and hadronisation	UE tune	Cross-section calculation
V+jets ($V = W/Z$)	Sherpa 2.2.1 [110]	NNPDF3.0NNLO	Sherpa	Default	NNLO [38]
$t\bar{t} + V$	MG5_aMC@NLO 2.3.3	NNPDF3.0	PYTHIA 8	A14	NLO
tZ	MadGraph5 2.3.3	NNPDF2.3LO	PYTHIA 8	A14	LO
tWZ	MG5_aMC@NLO 2.3.3	NNPDF2.3LO	PYTHIA 8	A14	NLO
$t\bar{t}$	Powheg-Box v2 [111]	NNPDF2.3LO	PYTHIA 8	A14	NNLO+NNLL
Single top	Powheg-Box v2	NNPDF2.3LO	PYTHIA 8	A14	NNLO+NNLL
Diboson	Sherpa 2.2.1-2.2.2	NNPDF3.0NNLO	Sherpa	Default	NLO
Stop, DM, DE signal	MadGraph5 2.6.2	NNPDF2.3LO	PYTHIA 8	A14	NLO
LQ3 signal	MG5_aMC@NLO 2.3.3	NNPDF2.3LO	PYTHIA 8	A14	NLO

TABLE 6.3. Overview of the nominal simulated background samples. NLO [37], NNLO [38], NNLO+NNLL [39, 40, 41, 42, 43, 44].

Alternative $t\bar{t}$ simulation samples were generated using Powheg interfaced to Herwig 7 [112] and aMC@NLO [37] interfaced to Pythia 8 with the A14 tune. The effects of initial and final state radiation (ISR, FSR) were explored by reweighting the baseline $t\bar{t}$ events in a way that reduces (reduces and increases for FSR) parton shower radiation [113] and by using an alternative Powheg + Pythia sample with h_{damp} set to $3m_{\text{top}}$ and tune parameter Var3 increased,

leading to increased ISR. These alternative $t\bar{t}$ samples were simulated using fast-simulation.

Alternative samples of non $t\bar{t}$ processes include the Wt-channel single top production using POWHEG interfaced to HERWIG 7 and aMC@NLO interfaced to PYTHIA 8 with the A14 tune, which is similar to the alternative $t\bar{t}$ sample setup.

Alternative diboson, Z+jets and W+jets configurations are explored by using the parametrization method described in Reference [114]. Finally, alternative $t\bar{t}+V$ configurations include $t\bar{t}+\ell\ell$ ($t\bar{t}+\ell\ell$ and $ttZ(\to \nu\nu qq)$) production generated with MADGRAPH5 2.3.3 interfaced to HERWIG 7 (SHERPA v2.2.1) at truth-level.

The event selection was performed on filtered derivation samples requiring $\sum p_{\mathrm{T}}^{\mathrm{jet}} > 150$ GeV for jets satisfying $p_{\mathrm{T}} > 40$ GeV, $|\eta| < 2.8$. This selection is looser than the one applied in the analysis itself in all selections.

CHAPTER VII

OBJECT DEFINITION AND EVENT PRESELECTION

An important stage in developing an analysis is interpreting the data and defining the particles used to discriminate background from signal. Of most interest to the analysis are electron an muon identification for vetoing, and jet definitions for top reconstruction. Once these objects are chose, we can define the $E_{\mathrm{T}}^{\mathrm{miss}}$ vector and further differentiate between overlapping objects.

7.1. Electrons

The analysis vetoes on either electrons or muons. To be most sensitive, we use a loose selection criteria when identifying baseline electrons. These electron are are required to pass the LooseAndBLayerLH criteria defined by the e/gamma working group, which uses the insertable B-layer and calorimeters to define an electron likelihood observable. They must fall into the fiducial area of the EM calorimeter ($|\eta| < 2.47$) and have $p_{\mathrm{T}} > 4.5$ GeV. In addition, a $z_0 \sin\theta$ track-to-vertex association cut quantifying the minimum distance from the primary vertex along the z-axis is applied.

Signal electrons are defined with the TightLH (FCLoose) identification (isolation) criteria for 1/2/3-lepton control and validation regions. They are required to pass an additional d_0 (minimum distance to primary vertex on xy-plane) track-to-vertex association cut, and the momentum threshold typically raised to $p_{\mathrm{T}} > 20$ GeV. The p_{T} requirements is lowered to $p_{\mathrm{T}} > 4.5$ GeV in the W and $t\bar{t}$-AB 1-lepton control regions where hadronic tau decays are emulated through low p_{T} leptons (see Section 9.3).

Scaling factors (SFs) of order of unity derived from $Z \to ee$ decays are applied on event-level account for differences in reconstruction, trigger, identification and isolation efficiencies between data and simulated events. Electron calorimeter energies are calibrated to the true electron energy in simulation, and residual discrepancies between the energy scale and resolution in the simulation with respect to the data are corrected using the $Z \to ee$ mass peak. Uncertainties associated to lepton efficiencies, energy/momentum scales and resolutions are considered as systematic variations.

7.2. Muons

Baseline muons, also used for lepton veto, are defined within the fiducial area of the muon spectrometer ($|\eta| < 2.8$) and required to pass the MEDIUM criteria defined by the muon performance group. The selection includes passing the recommended $z_0 \sin\theta$ track-to-vertex association cut $p_{\mathrm{T}} > 4$ GeV. Any event including a baseline muons flagged as a 'BADMUON' is discarded; the flag points identifies muons which tend to have a significantly worst momentum resolution than those which pass the veto, and in most cases show a pathological behavior leading to fake $E_{\mathrm{T}}^{\mathrm{miss}}$.

Signal muons are used in 1/2/3-lepton control and validation regions. In addition to the baseline requirements, signal muons are required to pass the MEDIUMLH (FCLoose) identification (isolation) criteria, the d_0 track-to-vertex association cut, and typically the momentum threshold is raised to $p_{\mathrm{T}} > 20$ GeV. The p_{T} requirements is lowered to $p_{\mathrm{T}} > 4$ GeV in the W and $t\bar{t}$-AB 1-lepton control regions where we aim to select specifically low p_{T} leptons (see Section 9.3).

Scaling factors (SFs) of order of unity derived from $Z \rightarrow \mu\mu$ and $J_\psi \rightarrow \mu\mu$ decays are applied to account for differences in trigger, identification, isolation and track to vertex association efficiencies between data and simulated events. Corrections based on the $Z \rightarrow \mu\mu$ and $J_\psi \rightarrow \mu\mu$ mass peaks are applied to the muon momentum. Uncertainties associated to the lepton efficiencies, energy/momentum scales and resolutions are considered as systematic variations.

7.3. Calorimeter Jets

Following the calorimeter object clustering and jet calibrations described in Section 5.3, all calorimeter jets are defined with momenta $p_{\mathrm{T}} > 20$ GeV and lie within the calorimeter fiducial coverage of $|\eta| < 4.5$. Any event containing a jet is flagged as 'LooseBad' (A and B regions) or 'TightBad' (C and D regions) is discarded. [115] Furthermore, signal jets are defined within the tracking fiducial region $|\eta| < 2.8$.

In order to reduce the number of calorimeter jets with large energy fractions from pileup collision vertices, the JetVertexTagger (JVT) algorithm is used [116]. The JVT procedure builds a multivariate discriminant for each jet within $|\eta| < 2.5$ based on the inner detector tracks ghost-associated to the jet; in particular, jets with relatively many high-momentum tracks from pileup vertices are correspondingly less likely to pass the JVT requirement. The rate of calorimeter jets with $p_{\mathrm{T}} > 120$ GeV and high pileup energy fractions is sufficiently small that the JVT requirement is dropped above this threshold. Simulated jets coming from the hard scattering are corrected for JVT efficiency differences with respect to the collision data. Uncertainties associated to the jet calibration as well as the efficiency of the JVT requirement are considered as systematic variations.

7.3.1. Flavor Tagging

Jets are assigned b-tagging discriminant values by the MV2 b-tagging algorithm, evaluating how likelihood of the jet containing a b-hadron. Calorimeter jets with a b-tagging discriminant higher than the cut value corresponding to the 77% fixed-cut working point (WP) are considered as b-jets. This corresponds to a rejection of 110 and 5 for light-flavour jets and c-jets, respectively, in the nominal $t\bar{t}$ simulated sample integrated over p_{T}.

The efficiency and inefficiency of the b-tagging algorithm in the simulation are calibrated separately for b, c and light-flavour jets according to their momenta such that the overall efficiency in the simulation matches that of the data while preserving the total yields per jet flavor. B-tagging calibrations for calorimeter jets are available for $p_{\mathrm{T}} > 20$ GeV and the uncertainties associated to these corrections are considered as systematic variations.

7.3.2. Hadronic Taus

Taus are not explicitly defined in the analysis since they are not selected nor vetoed. The taus present in the events considered for this analysis are therefore treated as calorimeter jets. This has been demonstrated to have a very small impact on the object definition and on the $E_{\mathrm{T}}^{\mathrm{miss}}$ reconstruction. However, due to their large mass taus are the only charged lepton that can decay to hadrons, but also radiating a neutrino in the process. The hadronization process of promptly produced gluons and quarks tend to form many more charged particles than tau decays. To select against these SM high-$E_{\mathrm{T}}^{\mathrm{miss}}$ process, the angles between the jets and the $E_{\mathrm{T}}^{\mathrm{miss}}$ as well as the number of associated tracks, are used to veto events containing tau-like jets.

Hadronic tau candidates are only reconstructed in some of the 0-lepton region (SRA, SRB) in order to veto events; their definition is therefore not used to compute any quantity. Candidate τ jets are defined as any non b-tagged calorimeter jet within the tracker acceptance ($\eta < 2.5$) associated to four tracks or less. Candidates are identified, and the event vetoed, if the closest jet to the $E_{\mathrm{T}}^{\mathrm{miss}}$ is within $\Delta\phi(E_{\mathrm{T}}^{\mathrm{miss}}\,\mathrm{jet}) < \pi/5$. This custom τ identification has been used since the Run 1 iteration of the ATLAS all-hadronic stop search. By including additional topological information but less substructure information with respect to the ATLAS CP τ identification, it allows to reach a higher identification efficiency (at the price of a higher fake rate).

7.3.3. Photons

Photons are not considered in the analysis since they are not selected nor vetoed. In practice, this means that the reconstructed prompt photons present in the events selected in the analysis are treated as calorimeter jets. This has been demonstrated to have a very small impact on the object definition and on the $E_{\mathrm{T}}^{\mathrm{miss}}$ reconstruction.

7.4. Resolving Overlapping Objects

In the case of candidate objects overlapping with each other, all but one object must be removed from the event and tracks assigned to the surviving object. The distance metric used to define overlapping objects is $\Delta R = \sqrt{\Delta\phi^2 + \Delta y^2}$.

To prevent double-counting of electron energy deposits as calorimeter jets, jets within $\Delta R < 0.2$ of a reconstructed electron are removed, unless the electron has $p_{\mathrm{T}} < 100$ GeV and the jet is b-tagged considering the 85% WP

of the MV2 tagger, in which case the electron is removed. This procedure is part of the agreement on a common object definition decided within the third generation subgroup in ATLAS. If the nearest jet surviving the cut is within $\Delta R < 0.04 + 10/p_{\mathrm{T}}$ of the electron, the electron is discarded, to ensure it is cleanly separated from nearby jet activity.

To reduce the background from muons from heavy flavor decays inside calorimeter jets, muons are required to be separated by $\Delta R > 0.04 + 10/p_{\mathrm{T}}$ from the nearest jet, removing the muon if the jet has at least three associated tracks, and removing the jet otherwise. This avoids an inefficiency for high-energy muons undergoing significant energy loss in the calorimeter.

Since the hadronic taus are only used to veto events, no peculiar overlap removal procedure is implemented in case they overlap with another object.

7.5. Missing Transverse Energy

The event $E_{\mathrm{T}}^{\mathrm{miss}}$ can be calculated in a number of ways depending on the information provided. A track-based $E_{\mathrm{T}}^{\mathrm{miss}}$ can be constructed using only inner-detector information, but it is blind to neutral hadrons captured by the Tile calorimeter. The standard ATLAS $E_{\mathrm{T}}^{\mathrm{miss}}$ algorithm adds calorimeter and muon information to the track collection. Furthermore, one can calculate the significance of the $E_{\mathrm{T}}^{\mathrm{miss}}$ based on the resolution and vectors of the hard objects.

7.5.1. Track MET

The track-based $E_{\mathrm{T}}^{\mathrm{miss}}$ is calculated from the sum of the transverse momenta of inner detector tracks with $p_{\mathrm{T}} > 500$ MeV and matched to the primary vertex in each event ($E_{\mathrm{T}}^{\mathrm{miss,track}} = |-\sum_i^{\mathrm{tracks}} p_{\mathrm{T}}^i|$). The azimuthal angle between the track-

based $E_{\mathrm{T}}^{\mathrm{miss}}$ and the calorimeter-based $E_{\mathrm{T}}^{\mathrm{miss}}$ is found to be a good discriminant against events with fake $E_{\mathrm{T}}^{\mathrm{miss}}$and is used in several signal regions. Since the average ratio between charged and uncharged hadrons in jets is consistent in quark and gluon jets, large angles between tracker-only and calorimeter-based $E_{\mathrm{T}}^{\mathrm{miss}}$ definitions is characteristic of pathological events with mis-measured jets. In addition, the tracker does not see photons and high energy muons are difficult to resolve.

7.5.2. Standard MET

The $E_{\mathrm{T}}^{\mathrm{miss}}$ is computed by performing a vectorial sum of the p_{T} of the jets, electrons and muons defined. In analyses defining photons and/or taus, these would be treated as their type instead of calorimeter jets. A custom overlap removal recommended by the Jet/EtMiss working group is performed: the tracks and calorimeter objects associated with each subsequent object are included in the respective $E_{\mathrm{T}}^{\mathrm{miss}}$ term and removed from their parent collections. Once all hard objects have been accounted for, the remaining tracks and calo-clusters are combined into a soft-$E_{\mathrm{T}}^{\mathrm{miss}}$ term. This soft term is calculated from inner detector tracks with $p_{\mathrm{T}} > 500$ MeV matched to the primary vertex to make it more resilient to pileup contamination. A schematic of the data flow is shown in Figure 7.1 and the sequence of building the $E_{\mathrm{T}}^{\mathrm{miss}}$ vector is as follows:

- Electrons
- Photons
- τ-leptons
- Jets

– Muons

– SoftTerm from unused tracks and TopoClusters.

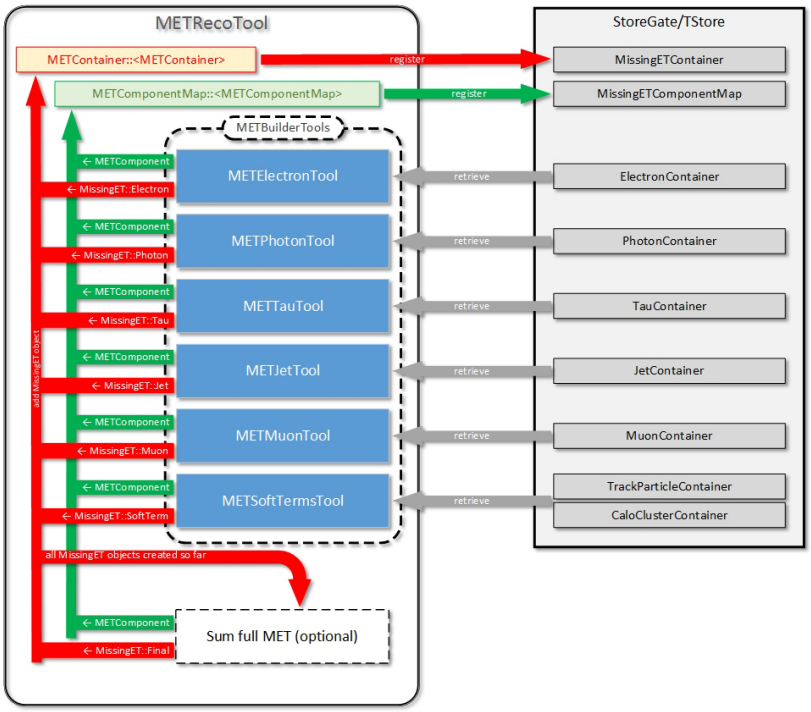

FIGURE 7.1. Flow of information in a standard ATLAS event file for $E_{\mathrm{T}}^{\mathrm{miss}}$ reconstruction. The tool extracts information from the various object containers, identifies the calo-clusters and tracks used by each object, and stores the result in a new container.

In the analysis presented, the default TIGHT $E_{\mathrm{T}}^{\mathrm{miss}}$ working point is used without using the 'forward' JVT algorithm.

7.5.3. Object-Based MET Significance

The effective difference between treating an object as a defined object (electron, muon, tau, photon) as opposed to a jet is primarily due to resolution. Electrons, photons, and muons have much smaller momentum resolution than standard jets–the standard $E_{\mathrm{T}}^{\mathrm{miss}}$ vector does not use this information. The object-

based $E_{\mathrm{T}}^{\mathrm{miss}}$ significance is a variable that returns how significant the $E_{\mathrm{T}}^{\mathrm{miss}}$ is based on the object types, as well as their p_{T} and resolutions. The variable is defined in Eq. 7.1 and is the scalar magnitude of the $E_{\mathrm{T}}^{\mathrm{miss}}$ vector divided by a resolution term.

$$\text{Object based } E_{\mathrm{T}}^{\mathrm{miss}} \text{ sig.} = \frac{|\vec{E}_{\mathrm{T}}^{miss}|}{\sum_{objects} \sqrt{\sigma_{\mathrm{L}}^2(1-\rho_{\mathrm{LT}}^2)}} \tag{7.1}$$

In this equation, $\vec{E}_{\mathrm{T}}^{miss}$ is the vector of missing energy in the transverse plane. σ_{L} it the total expected longitudinal resolution of all objects at a given p_{T}. Likewise ρ_{LT} is the correlation factor between all object longitudinal and transverse object resolutions.

$$\rho_{\mathrm{LT}} = \frac{\sigma_{\mathrm{LT}}^2}{\sqrt{\sigma_{\mathrm{L}}^2 + \sigma_{\mathrm{T}}^2}} \tag{7.2}$$

The resolutions are obtained from a parametrization of the p_{T} and ϕ resolution of each object and transformed to the longitudinal and transverse basis with respect to the direction of the $\vec{E}_{\mathrm{T}}^{miss}$.

If a jet is parallel or anti-parallel to the $\vec{E}_{\mathrm{T}}^{miss}$, as with mismeasured QCD jets, the contribution to the denominator is large and the overall observable small. One the other hand, an object orthogonal to the $\vec{E}_{\mathrm{T}}^{miss}$ contributes lightly to the denominator leading to a large $E_{\mathrm{T}}^{\mathrm{miss}}$ significance.

Of particular importance is the observable's performance with hadronic tau decays. If we consider a $t\bar{t}$ event decaying through a hadronic tau, the lepton's high mass confines the decaying neutrino to be close to the pions formed from the W-boson decay. Since the $\vec{E}_{\mathrm{T}}^{miss}$ is nearly parallel with the tau-jet, the resolution term in the denominator is large and the overall significance low. A cartoon of the object resolutions and their transformation onto the $\vec{E}_{\mathrm{T}}^{miss}$ is shown in Figure 7.2.

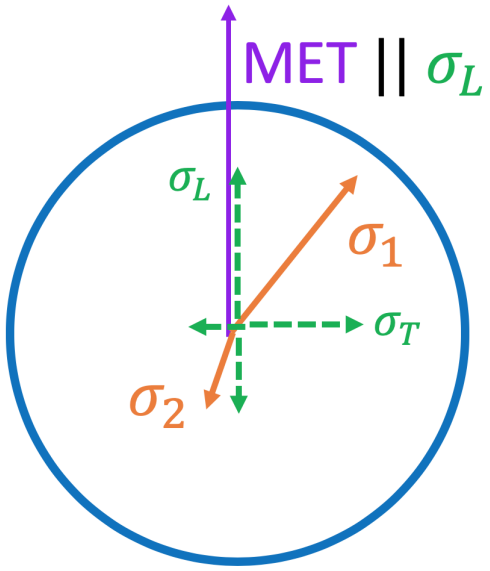

FIGURE 7.2. Each object resolution ($\sigma_{1,2}$) is assigned the direction of its momentum vector. The projection of the resolution vectors onto the $\vec{E}_{\mathrm{T}}^{miss}$ define the denominator of Eq. 7.1.

7.6. Event Preselection

Experiments at the LHC have a wealth of data to search through; analyses must balance signal acceptance efficiency with background rejection when discriminating the data collected. Signal Regions (SR) are designed to be sensitive to the searched particle topologies. The $t\bar{t} + E_{\mathrm{T}}^{\mathrm{miss}}$ analysis defines its various signal regions based on properties of the reconstructed top quarks, as well the constituent jets and their angular separation from the $\vec{E}_{\mathrm{T}}^{miss}$. Furthermore, there are separate optimizations for low mass-splitings between the stop and neutralino (compressed) and higher mass-splittings (non-compressed). In compressed scenarios, the analysis relies on initial-state radiation (ISR) to enhance the $E_{\mathrm{T}}^{\mathrm{miss}}$ of the interaction. This dissertation focuses on the non-compress scenarios.

Once the data trigger has been selected, and the objects used by the analyses defined, a set of event-cleaning selections are applied. For data events only,

the good run list is used to flag problematic runs. In addition, events suffering from noise bursts or possible incomplete events are removed by requiring no errorState in the LAr, Tile and SCT. The jet/muon cleaning requirements mentioned in Section 6.5 and VII reject events with pathological calorimeter objects. In both data and MC, the events must include at least one reconstructed vertex. They must not contain any bad jets nor bad muons (see Section VII), have exactly zero baseline electron and muon, pass the lowest unprescaled $E_{\mathrm{T}}^{\mathrm{miss}}$ trigger described in Section 6.5 and include an offline $E_{\mathrm{T}}^{\mathrm{miss}} > 250$ GeV.

Cut	Data MC
GoodRunLists	✓
Event Cleaning	✓
Bad jet veto	✓
Bad muon veto	✓
N_{PV}	≥ 1
baseline ℓ	0
$E_{\mathrm{T}}^{\mathrm{miss}}$ trigger	✓
$E_{\mathrm{T}}^{\mathrm{miss}}$	> 250 GeV

TABLE 7.1. Summary of the selection applied to all events considered in the analysis.

7.6.1. Common Selections to Two-Body 0-Lepton Regions

The 0-lepton selections described below are used in all two-body signal regions, and their corresponding $t\bar{t}$ and Z + jets validation regions. All data and MC events considered in the two-body 0-lepton regions must contain, in addition to the common preselection, at least 4 calorimeter jets with p_{T} greater than 80, 80, 40, 40 GeV, and at least 1 b-tagged calorimeter jet.

Additional requirements to reject multijet events are included:
Object based $E_{\mathrm{T}}^{\mathrm{miss}}$ sig. must be greater than 5, and the minimum $\Delta\phi$ between the

leading four (two) jets and $E_{\mathrm{T}}^{\mathrm{miss}}$, $\min\left|\Delta\phi\left(\mathrm{jet}^{1-4}, E_{\mathrm{T}}^{\mathrm{miss}}\right)\right|\left(\min\left|\Delta\phi\left(\mathrm{jet}^{1-2}, E_{\mathrm{T}}^{\mathrm{miss}}\right)\right|\right)$, must be greater than 0.4 in the regions presented in this dissertation. Figures 7.3 and 7.4 show various key variables after preselection for the non-compressed two-body scenarios. Only statistical uncertainties are shown and the grey boxes indicate blinded regions. The selection is shown in Table 7.2.

Selection	Criteria
$\mathrm{N}_{\mathrm{jets}}$	≥ 4
$p_{\mathrm{T}}^{j_2}$	> 80 GeV
$p_{\mathrm{T}}^{j_4}$	> 40 GeV
$\min\left\|\Delta\phi\left(\mathrm{jet}^{1-4}, E_{\mathrm{T}}^{\mathrm{miss}}\right)\right\|$	> 0.4
$\mathrm{N}_{\mathrm{b-jet}}$	≥ 2
Object based $E_{\mathrm{T}}^{\mathrm{miss}}$ sig.	> 5
$m_{\mathrm{T}}^{b,\mathrm{min}}$	≥ 50 GeV
$m_{\mathrm{jet},R=1.2}^{1}$	≥ 120 GeV

TABLE 7.2. Summary of the preselection applied in the two body 0-lepton regions for the non-compressed and compressed scenario, on top of the common preselection described in Table 7.1.

Figure 7.4 shows simple jet based distributions. The number of jets and b-tagged jets can be seen in Figure 7.4a and Figure 7.4a respectively. The leading and sub-leading b-jet p_{T} is also shown (7.4c and 7.4d). Finally, 7.4c and 7.4d show the leading and sub-leading jet p_{T} distributions.

7.6.2. Common Selections to Two-Body 1-Lepton Regions

The requirements shown in Table 7.3 are applied in all the one-lepton control regions used in the AB and C analysis (two-body regions). In order to avoid unblinding the one-lepton stop search, the transverse mass of the lepton-$E_{\mathrm{T}}^{\mathrm{miss}}$ system, $m(\ell, E_{\mathrm{T}}^{\mathrm{miss}})$, is required to be smaller than 120 GeV in all one-lepton regions.

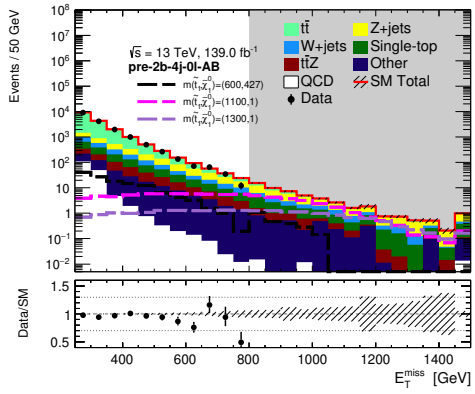

(a) $E_{\mathrm{T}}^{\mathrm{miss}}$

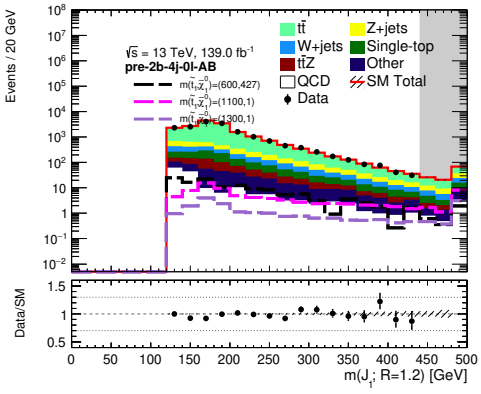

(b) $\mathrm{m}(J_1; \mathrm{R} = 1.2)$

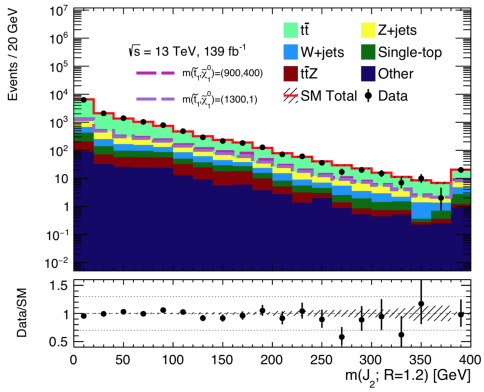

(c) $\mathrm{m}(J_2; \mathrm{R} = 1.2)$

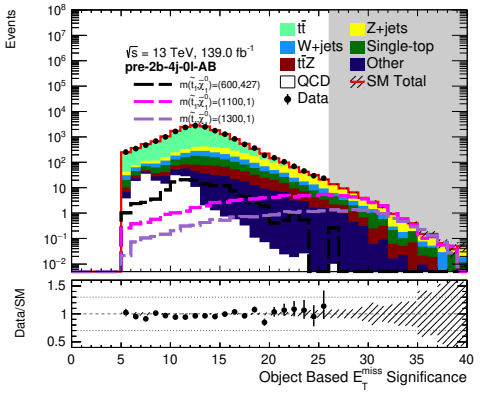

(d) Object based $E_{\mathrm{T}}^{\mathrm{miss}}$ sig. $\left[\sqrt{\mathrm{GeV}}\right]$

FIGURE 7.3. Preselection plots in the 0-lepton channel for non-compressed scenarios. MC16a, MC16d, and MC16e samples are included for all SM backgrounds. The uncertainties only show the statistical error. As soon as one bin has a signal-over-background expectation that exceed 15%, all bins to the right (left) are blinded.

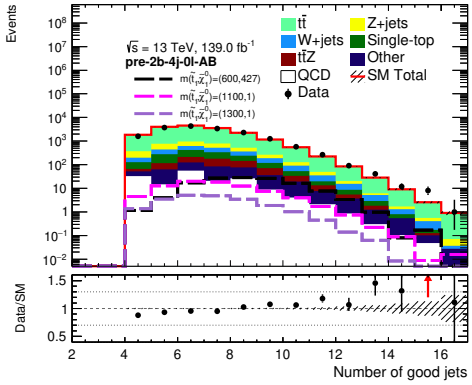

(a) N_{jets}

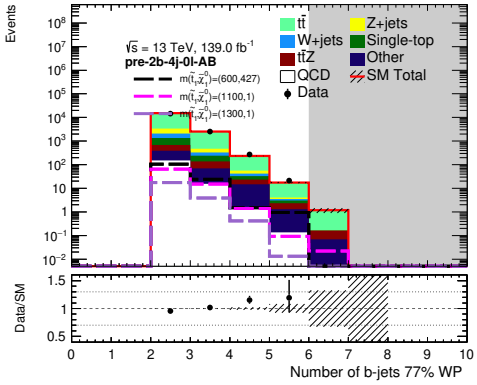

(b) N_{b-jet}

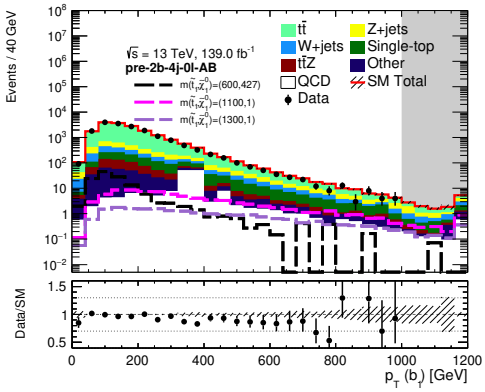

(c) $p_{\mathrm{T}}^{b_1}$

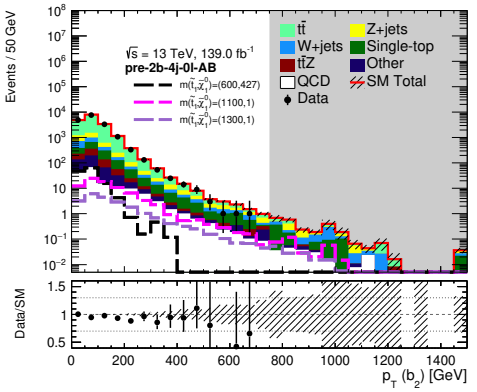

(d) $p_{\mathrm{T}}^{b_2}$

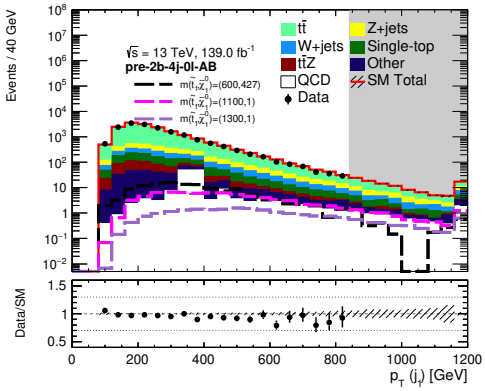

(e) $p_{\mathrm{T}}^{j_1}$

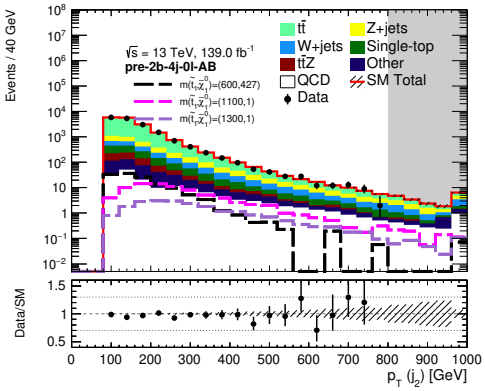

(f) $p_{\mathrm{T}}^{j_2}$

FIGURE 7.4. Preselection plots in the 0-lepton channel for non-compressed scenarios. MC16a, MC16d, and MC16e samples are included for all SM backgrounds. The uncertainties only show the statistical error. As soon as one bin has a signal-over-background expectation that exceed 15%, all bins to the right (left) are blinded.

Variable	Value
signal ℓ	exactly 1
additional baseline ℓ	0
$E_{\mathrm{T}}^{\mathrm{miss}}$ trigger	✓
$E_{\mathrm{T}}^{\mathrm{miss}}$	> 250 GeV
$\mathrm{N}_{\mathrm{jets}}$	≥ 4
$p_{\mathrm{T}}^{j_2}$	> 80 GeV
$p_{\mathrm{T}}^{j_4}$	> 40 GeV
$\mathrm{N}_{\mathrm{b-jet}}$	≥ 1
$m_{\mathrm{T}}\left(\ell, E_{\mathrm{T}}^{\mathrm{miss}}\right)$	< 120 GeV
$\min[\Delta\phi(j_{1-4}, E_{\mathrm{T}}^{\mathrm{miss}})]$	> 0.4

TABLE 7.3. Summary of the selection applied to all events falling in a 1-lepton region in the ABC analysis. The lepton is treated as a non b-tagged jet (impacts $\mathrm{N}_{\mathrm{jets}}$, $p_{\mathrm{T}}^{j_2}$, $p_{\mathrm{T}}^{j_4}$ and $\min[\Delta\phi(j_{1-4}, E_{\mathrm{T}}^{\mathrm{miss}})]$) only in the single top control region.

CHAPTER VIII

SIGNAL REGION DESIGN

8.1. Signal Region Categorization

To boost the sensitivity of the analysis, SRA and SRB are divided into three orthogonal categories defined by the the sub-leading reclustered jet ($R = 1.2$) mass as illustrated in Figure 8.1 (TT, TW, T0). Although not a focus of this dissertation, SRC (compressed) and SRD (four-body) selections are summarized below for completeness.

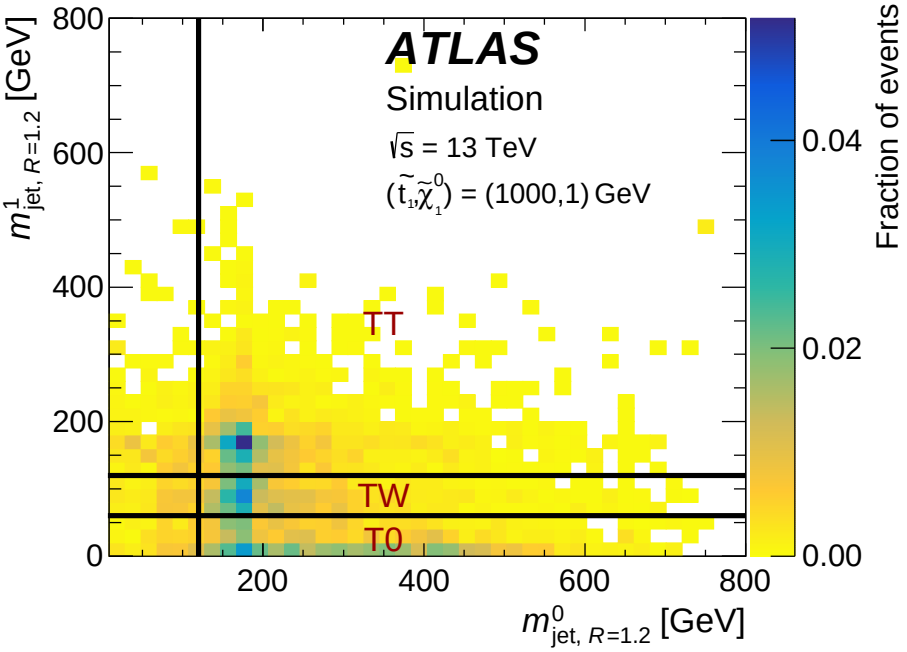

FIGURE 8.1. Illustration of signal-region categories (TT, TW, and T0) based on the $R = 1.2$ reclustered top-candidate masses for simulated direct top-squark pair production with $(m_{\tilde{t}}, m_{\tilde{\chi}_1^0}) = (1000, 1)$ GeV, taken from Ref. [34]. The black lines represent the requirements on the reclustered jet masses.

8.2. Signal Region A: High $\Delta m(\tilde{t}, \chi_1^0)$

Signal Region A (SRA) aims to select signals with high $\tilde{t}$ and $\tilde{\chi}^0$ mass splittings, i.e. high stop masses and low $\tilde{\chi}^0$ masses. These signals tend to produce top quarks with a p_{T} range which can result in collimated top decay products.

The signal region definition is presented in Table 8.1 and is applied after the selection described in Table 7.2. In addition to the requirements on the reclustered jet masses, at least one of their constituents, which is a $R = 0.4$ calorimeter jet, is sometimes required to be b-tagged. The lower cut on m_{T2,χ^2} makes SRA orthogonal to SRB (see Section 8.3 and Table 8.2).

The dominant backgrounds to SRA are Z + jets and $t\bar{t}$ $+Z$. Single top and W + jets have small contributions, and $t\bar{t}$ and diboson processes are expected to have even smaller contributions. The $t\bar{t}$ background is suppressed by the Object based $E_{\mathrm{T}}^{\mathrm{miss}}$ sig. > 25 and $m_{\mathrm{T}}^{b,\mathrm{min}}$ requirements. The N - 1 Object based $E_{\mathrm{T}}^{\mathrm{miss}}$ sig. distributions in TT, TW, and T0 categories are shown in Figure 8.2. The N - 1 distributions of other important variables used in SRA are shown in Figures 8.3 and 8.4. The expected and observed yields are discussed in Section 11.2.

Variable	SRATT	SRATW	SRAT0
$\mathrm{N_{b-jet}}$	≥ 2		
$\mathrm{m}(J_1; \mathrm{R} = 1.2)$	> 120 GeV		
$\mathrm{m}(J_2; \mathrm{R} = 1.2)$	> 120 GeV	$[60, 120]$ GeV	< 60 GeV
$\mathrm{b-tagged}(J_1; \mathrm{R} = 1.2)$	✓		
$\mathrm{b-tagged}(J_2; \mathrm{R} = 1.2)$	✓	-	
$\mathrm{m}(J_1; \mathrm{R} = 0.8)$	> 60 GeV		
$m_{\mathrm{T}}^{b,\mathrm{min}}$	> 200 GeV		
m_{T2,χ^2}	> 450 GeV		
Object based $E_{\mathrm{T}}^{\mathrm{miss}}$ sig.	> 25		
$\Delta R\,(b_1, b_2)$	> 1.0	-	
τ veto	✓		

TABLE 8.1. SRA requirements after the selection in Table 7.2 have been applied.

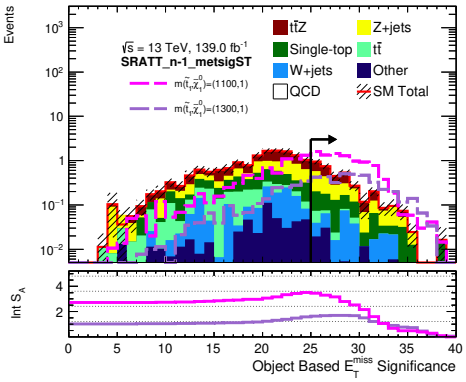

(a) SRA-TT: n-1 Object based $E_{\mathrm{T}}^{\mathrm{miss}}$ sig. $\left[\sqrt{\mathrm{GeV}}\right]$

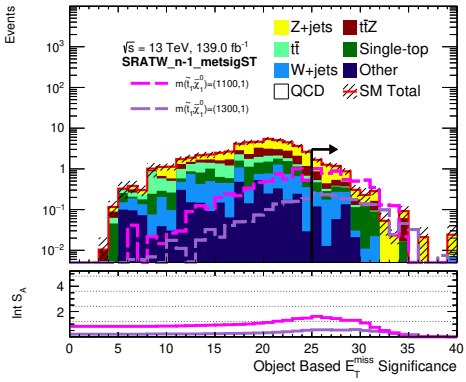

(b) SRA-TW: n-1 Object based $E_{\mathrm{T}}^{\mathrm{miss}}$ sig. $\left[\sqrt{\mathrm{GeV}}\right]$

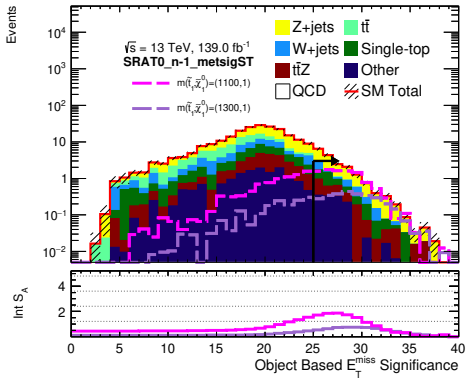

(c) SRA-T0: n-1 Object based $E_{\mathrm{T}}^{\mathrm{miss}}$ sig. $\left[\sqrt{\mathrm{GeV}}\right]$

FIGURE 8.2. Distribution of Object based $E_{\mathrm{T}}^{\mathrm{miss}}$ sig. in all SRA categories (TT, TW, T0) with all selections applied except for the Object based $E_{\mathrm{T}}^{\mathrm{miss}}$ sig. requirement. The arrows indicate the cut applied in SRA. Only statistical uncertainties are shown.

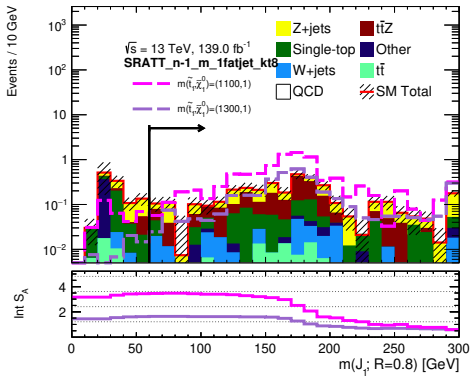

(a) SRA-TT: N-1 $\mathrm{m}(J_1; \mathrm{R} = 0.8)$

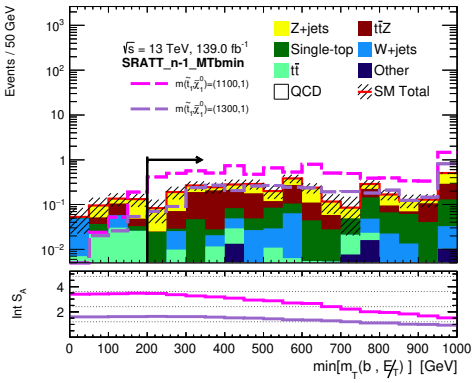

(b) SRA-TT: N-1 $m_{\mathrm{T}}^{b,\mathrm{min}}$

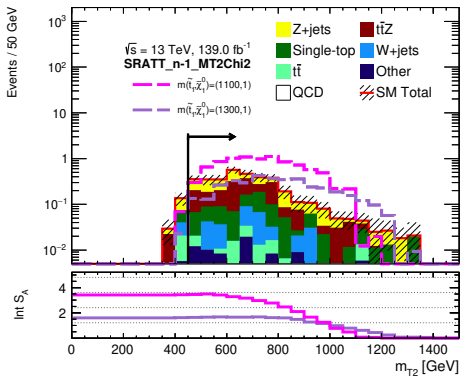

(c) SRA-TT: N-1 m_{T2,χ^2}

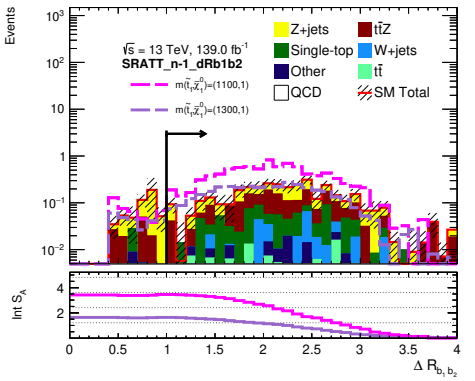

(d) SRA-TT: N-1 $\Delta R\,(b_1, b_2)$

FIGURE 8.3. Distributions of important discriminating variables in the SRA-TT category with all selections applied except for the requirement on the observable shown. The arrows indicate the cut applied in SRA. Only statistical uncertainties are shown.

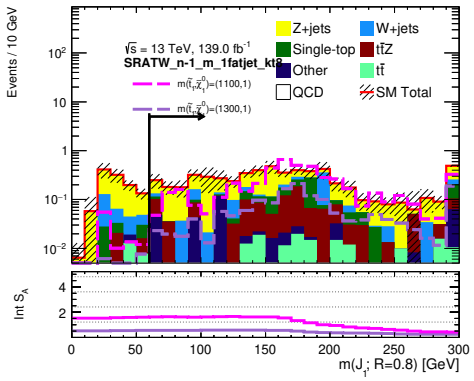

(a) SRA-TW: N-1 $\mathrm{m}(J_1; \mathrm{R} = 0.8)$

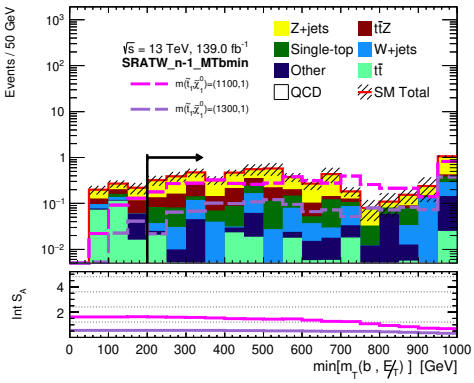

(b) SRA-TW: N-1 $m_{\mathrm{T}}^{b,\mathrm{min}}$

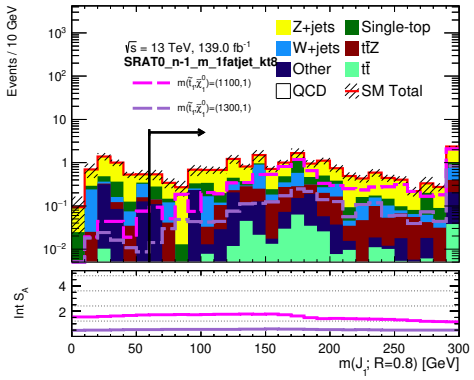

(c) SRA-T0: N-1 $\mathrm{m}(J_1; \mathrm{R} = 0.8)$

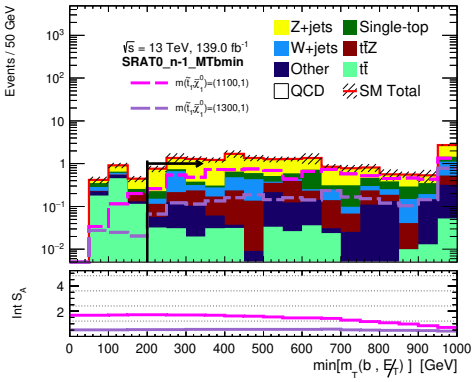

(d) SRA-T0: N-1 $m_{\mathrm{T}}^{b,\mathrm{min}}$

FIGURE 8.4. Distributions of selected discriminating variables in the SRA-TW and T0 categories with all selections applied except for the requirement on the observable shown. The arrows indicate the cut applied in SRA. Only statistical uncertainties are shown.

8.3. Signal Region B: Moderate $\Delta m(\tilde{t}, \chi_1^0)$

Signal Region B (SRB) aims to select signals with $\tilde{t}$ with mass between 300-900 GeV and $\tilde{\chi}^0$ masses within a larger range than the signals targeted by SRA, i.e. lower mass splitting. As for SRA, three categories (TT, TW, T0) are defined based on the sub-leading reclustered jet ($R = 1.2$) mass.

The signal region definition is shown in Table 8.2. The upper cut on m_{T2,χ^2} makes SRB orthogonal to SRA. The dominant backgrounds are Z + jets, $t\bar{t}$ $+Z$, W + jets, and $t\bar{t}$. The N - 1 Object based $E_{\mathrm{T}}^{\mathrm{miss}}$ sig. distributions in TT, TW, and T0 are shown in Figure 8.5. the cut on Object based $E_{\mathrm{T}}^{\mathrm{miss}}$ sig. is harmonized across the TT, TW, and T0 categories. The N - 1 distributions of other variables used in the SRB selection are shown in Figures 8.6, 8.7, and 8.8. The expected and observed yields are discussed in Section 11.2.

Variable	SRB-TT	SRB-TW	SRB-T0
$\mathrm{N}_{\mathrm{b-jet}}$	≥ 2		
$\mathrm{m}(J_1; \mathrm{R} = 1.2)$	> 120 GeV		
$\mathrm{m}(J_2; \mathrm{R} = 1.2)$	> 120 GeV	$\in [60, 120]$ GeV	< 60 GeV
$m_{\mathrm{T}}^{b,\mathrm{min}}$	> 200 GeV		
$m_{\mathrm{T}}^{b,\mathrm{max}}$	> 200 GeV		
m_{T2,χ^2}	< 450 GeV		
Object based $E_{\mathrm{T}}^{\mathrm{miss}}$ sig.	> 14		
$\Delta R\,(b_1, b_2)$	> 1.4		
τ veto	✓		

TABLE 8.2. Summary of selection for SRB.

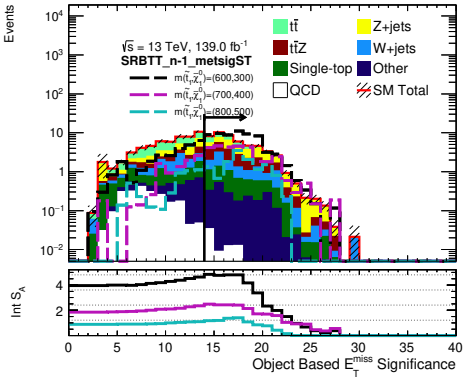

(a) SRB-TT: N-1 Object based $E_{\mathrm{T}}^{\mathrm{miss}}$ sig. $\left[\sqrt{\mathrm{GeV}}\right]$

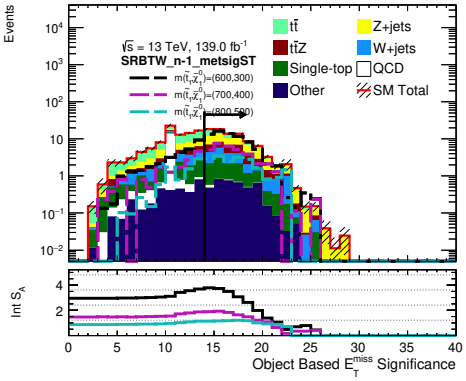

(b) SRB-TW: N-1 Object based $E_{\mathrm{T}}^{\mathrm{miss}}$ sig. $\left[\sqrt{\mathrm{GeV}}\right]$

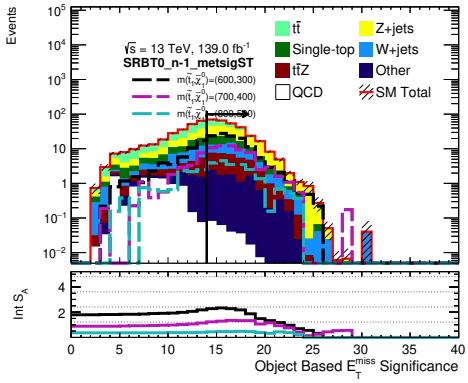

(c) SRB-T0: N-1 Object based $E_{\mathrm{T}}^{\mathrm{miss}}$ sig. $\left[\sqrt{\mathrm{GeV}}\right]$

FIGURE 8.5. Distribution of Object based $E_{\mathrm{T}}^{\mathrm{miss}}$ sig. in all SRB categories (TT, TW, T0) with all selections applied except for the Object based $E_{\mathrm{T}}^{\mathrm{miss}}$ sig. requirement. The arrows indicate the cut applied in SRB. Only statistical uncertainties are shown.

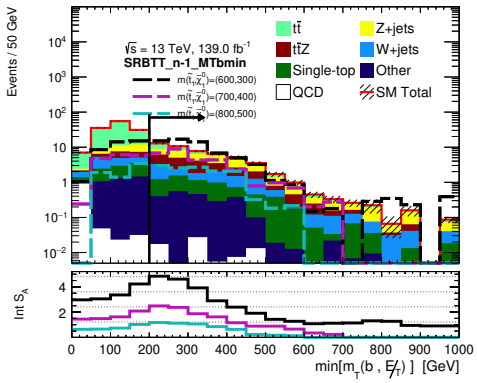

(a) SRB-TT: N-1 $m_{\mathrm{T}}^{b,\mathrm{min}}$

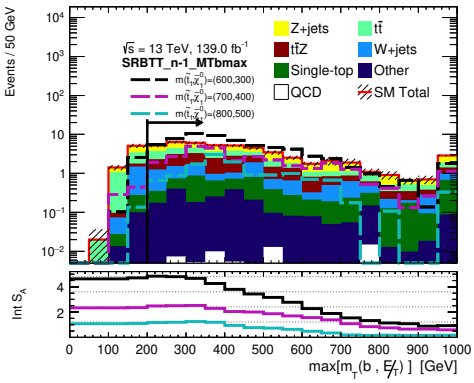

(b) SRB-TT: N-1 $m_{\mathrm{T}}^{b,\mathrm{max}}$

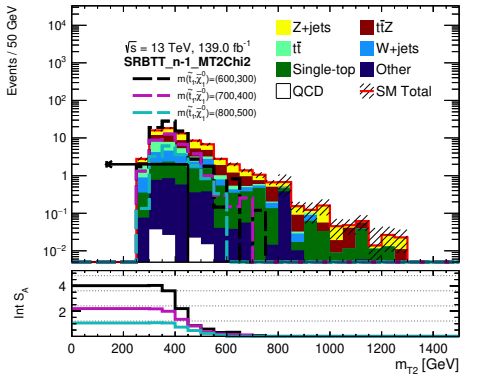

(c) SRB-TT: N-1 m_{T2,χ^2}

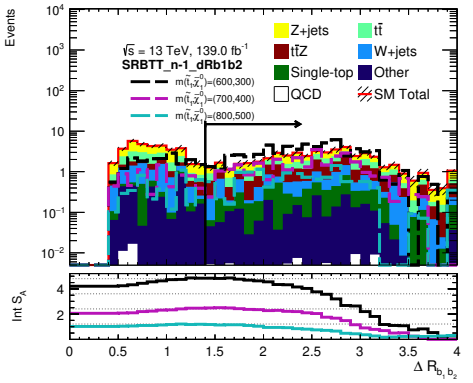

(d) SRB-TT: N-1 $\Delta R\,(b_1, b_2)$

FIGURE 8.6. Distributions of important discriminating variables in the SRB-TT category with all selections applied except for the requirement shown. The arrows indicate the cut applied in SRB. Only statistical uncertainties are shown.

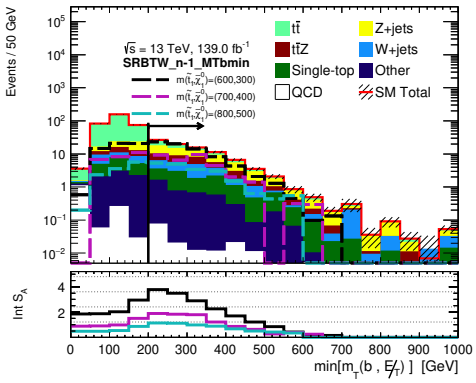

(a) SRB-TW: N-1 $m_{\mathrm{T}}^{b,\mathrm{min}}$

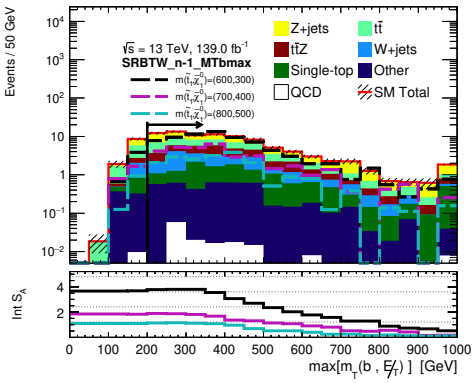

(b) SRB-TW: N-1 $m_{\mathrm{T}}^{b,\mathrm{max}}$

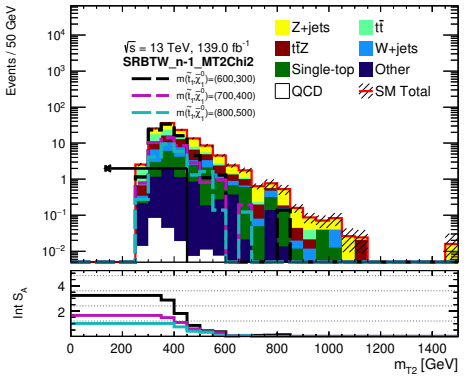

(c) SRB-TW: N-1 m_{T2,χ^2}

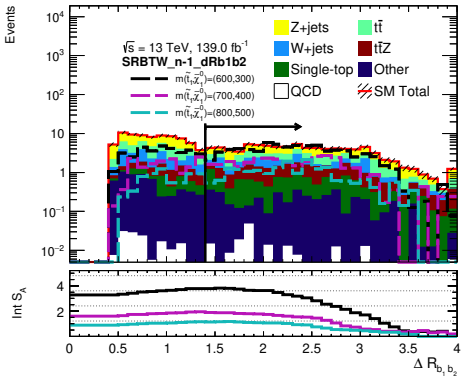

(d) SRB-TW: N-1 $\Delta R\,(b_1, b_2)$

FIGURE 8.7. Distributions of important discriminating variables in the SRB-TW category with all selections applied except for the requirement shown. The arrows indicate cut applied in SRB. Only statistical uncertainties are shown.

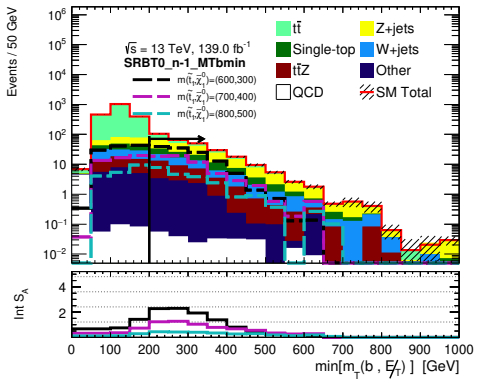

(a) SRB-T0: N-1 $m_{\mathrm{T}}^{b,\mathrm{min}}$

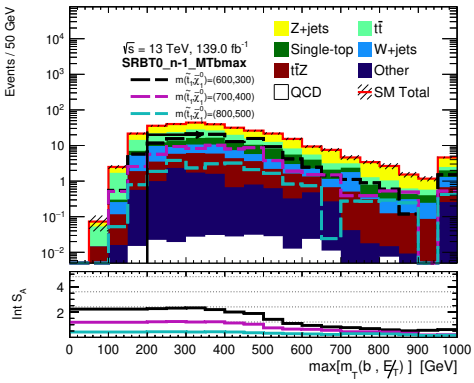

(b) SRB-T0: N-1 $m_{\mathrm{T}}^{b,\mathrm{max}}$

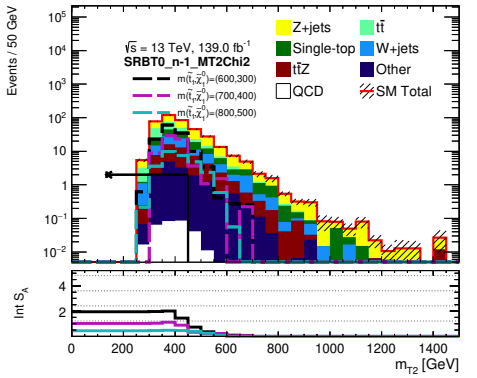

(c) SRB-T0: N-1 m_{T2,χ^2}

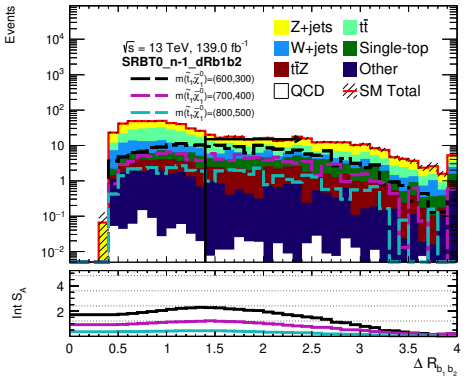

(d) SRB-T0: N-1 $\Delta R\,(b_1, b_2)$

FIGURE 8.8. Distributions of important discriminating variables in the SRB-T0 category with all selections applied except for the requirement shown. The arrows indicate the cut applied in SRB. Only statistical uncertainties are shown.

8.4. Signal Region C: Compressed Two/Three-Body Signatures

Non-boosted two-body signals with $m_{\tilde{t}} - m_{\tilde{\chi}_1^0} \sim m_t$ have a similar signature to the $t\bar{t}$ background. To better discriminate from the background, events including a hard ISR are selected and reconstructed using a recursive jigsaw technique. The method boosts the event in lab frame to the center of mass frame of the collision through the ISR-tagged jet, as illustrated in Figure 8.9. In this boosted frame, the neutralinos recoil against the tops and two hemispheres are identified: one of visible SM particles (tops) and the other of the invisible sparticle system.

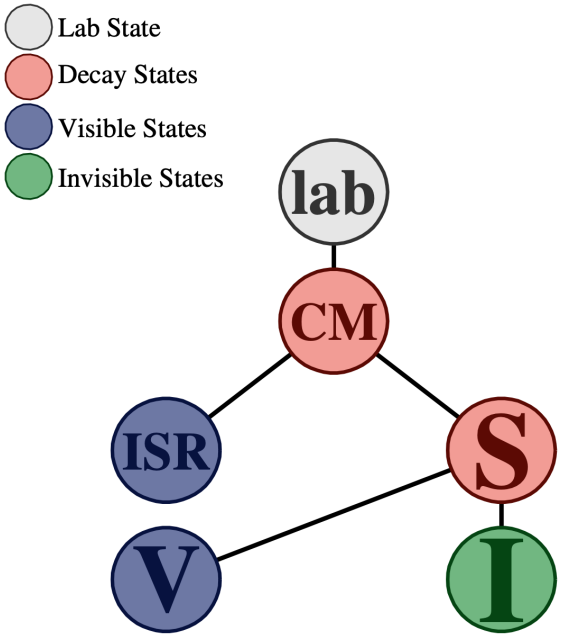

FIGURE 8.9. Cartoon demonstrating the ISR boost and hemispheres identified by the Recursive Jigsaw method.

The SRC definition considered in the analysis is presented in Table 8.3. The R_{ISR} variable scales with the ratio between the neutralino and stop masses, which implies that each compressed two-body signal peaks in significance at a different

values of R_{ISR}. This feature is exploited by binning the signal region into five different bins in R_{ISR} that are fitted simultaneously.

N-1 distributions of important discriminating variables in SRC are presented in Figures 8.10.

Variable	SRC1	SRC2	SRC3	SRC4	SRC5
$N^{\mathrm{S}}_{\mathrm{b-jet}}$	≥ 2				
$N^{\mathrm{S}}_{\mathrm{jet}}$	≥ 4				
$p^{1,\mathrm{S}}_{\mathrm{T},b}$	> 40 GeV				
m_{S}	> 400 GeV				
$\Delta\phi_{\mathrm{ISR},E^{\mathrm{miss}}_{\mathrm{T}}}$	> 3.0				
$p^{\mathrm{ISR}}_{\mathrm{T}}$	> 400 GeV				
$p^{4,\mathrm{S}}_{\mathrm{T}}$	> 50 GeV				
R_{ISR}	0.30–0.40	0.40–0.50	0.50–0.60	0.60–0.70	≥ 0.70

TABLE 8.3. Selection criteria for SRC, in addition to the common preselection requirements described in the Table 7.2. The signal regions are separated into windows based on ranges of R_{ISR}.

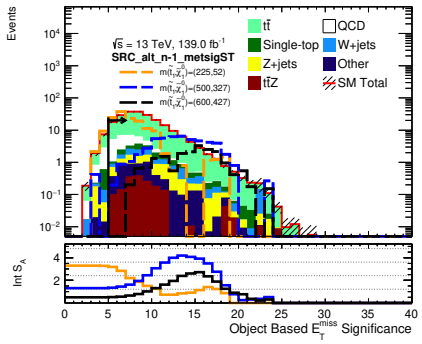

(a) Object-based $E_{\mathrm{T}}^{\mathrm{miss}}$ Sig.> 5.0

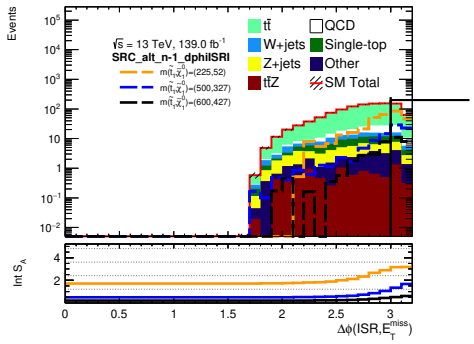

(b) $\Delta\phi_{\mathrm{ISR},E_{\mathrm{T}}^{\mathrm{miss}}} > 3.0$

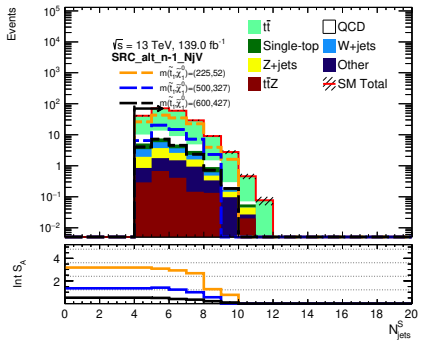

(c) $N_{\mathrm{jet}}^{\mathrm{S}} \geq 4$

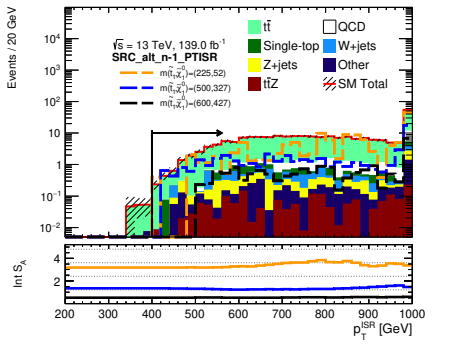

(d) $p_{\mathrm{T}}^{\mathrm{ISR}} > 400$ GeV

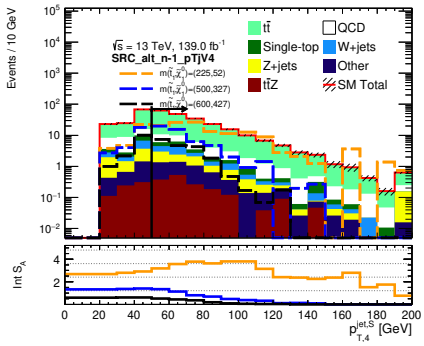

(e) $p_{\mathrm{T}}^{4,\mathrm{S}} > 50$ GeV

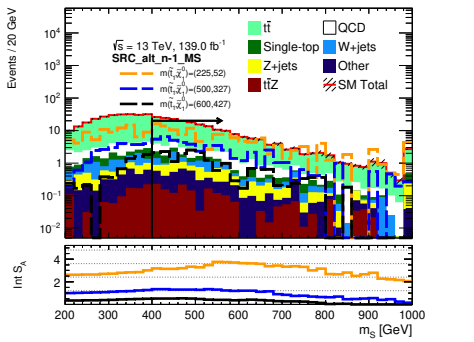

(f) m_{S}

FIGURE 8.10. N-1 distributions for variables used in SRC. The requirements made on the variable in SRC is shown below the plot. The R_{ISR} distribution is not strictly speaking an N-1 plot because there are five R_{ISR} bins that are statistically combined, but nonetheless included. 40% flat systematic is assumed for significance calculations.

8.5. Signal Region D: Four-Body Decays

Signal Region D (SRD) is optimized to be sensitive to four-body decays for which the kinematic properties depend mainly on the mass difference between stop and neutralino. Four-body decays result in low momentum particles which are difficult to reconstruct, especially identify as b-tagged jets. After the common preselection shown in Table 7.1, three sub-regions are defined based on the number of R=0.4 b-tagged calorimeter jets. Variable-radius track jets are used to supplement the inefficiencies of low p_{T} b-tagged jets. Figure 8.11 exemplifies the topology of SRD-like events.

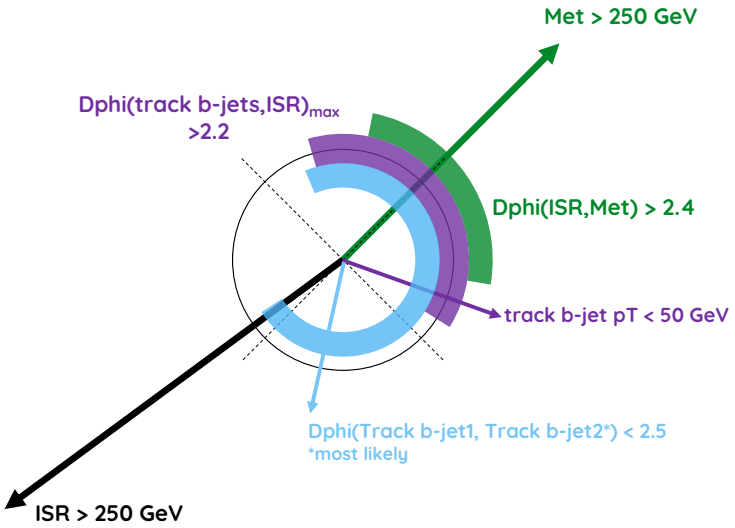

FIGURE 8.11. Cartoon explaining the relative angles defined in SRD selections.

Three benchmark mass differences are considered to optimize the corresponding signal regions:

$m_{\tilde{t}} - m_{\tilde{\chi}_1^0} = 20, 50$ and 80 GeV.

– 20 GeV Mass Splitting: Events with zero calorimeter b-tagged jets and at least one VR b-tagged jet are considered.

– 50 GeV Mass Splitting: Events with exactly one b-tagged jet and at least one VR b-tagged jet are considered.

– 80 GeV Mass Splitting: Events with at least two calorimeter b-tagged jets and no requirement on the number of VR b-tagged jets are considered (in fact, this region does not make use of VR track jets).

The corresponding regions are named SRD0, SRD1 and SRD2 (where the numbers indicates the number of calorimeter b-tagged jets). The regions are designed to be orthogonal to allow for a statistical combination of the three regions. Given the absence of on-shell top quarks and W bosons, the discrimination of the signal from the background relies mainly on angular variables. The final selections were obtained by maximizing the expected significance using a 20% flat systematic uncertainty. The selections are summarized in Table 8.4. N-1 plots for each of the discriminating variables in SRD are shown in Figures 8.12 and 8.13.

	SRD0	SRD1	SRD2
$\mathrm{N}_{\mathrm{b-jet}}$	exactly 0	exactly 1	≥ 2
$\lvert\eta^{b_1}\rvert$	-	< 1.6	-
$\lvert\eta^{b_2}\rvert$	-		< 1.2
$p_{\mathrm{T}}^{b_1}$	-		< 175 GeV
$\lvert\Delta\phi\left(\mathrm{non-b}, b_1\right)\rvert$	-	> 2.2	
$\lvert\Delta\phi\left(\mathrm{non-b}, b_2\right)\rvert$	-		> 1.6
$\mathrm{N}_{\mathrm{b-jet}}^{\mathrm{VR}}$	≥ 1		-
$p_{\mathrm{T}}^{b_1,\mathrm{VR}}$	< 50 GeV	> 10 GeV	-
$p_{\mathrm{T}}^{1,\mathrm{VR}}$	-	< 40 GeV	-
$\lvert\eta^{b_1,\mathrm{VR}}\rvert$	< 1.2	-	
$\max\left\lvert\Delta\phi\left(\mathrm{non-b}, \mathrm{b}^{\mathrm{VR}}\right)\right\rvert$	> 2.2	-	
$\left\lvert\Delta\phi\left(b_1^{\mathrm{VR}}, b_2^{\mathrm{VR}}\right)\right\rvert$	< 2.5	-	
$\min\left\lvert\Delta\phi\left(\mathrm{jet}^{\mathrm{VR}\,1-4}, \mathrm{non-b}\right)\right\rvert$	-	> 1.2	-
$E_{\mathrm{T}}^{\mathrm{miss}}/\sqrt{H_{\mathrm{T}}}$	$> 26\sqrt{\text{ GeV}}$	$> 22\sqrt{\text{ GeV}}$	
$\min\left\lvert\Delta\phi\left(\mathrm{jet}^{1-4}, E_{\mathrm{T}}^{\mathrm{miss}}\right)\right\rvert$	> 0.4	-	

TABLE 8.4. Signal region selections applied on top of the preselection criteria of Table 7.1.

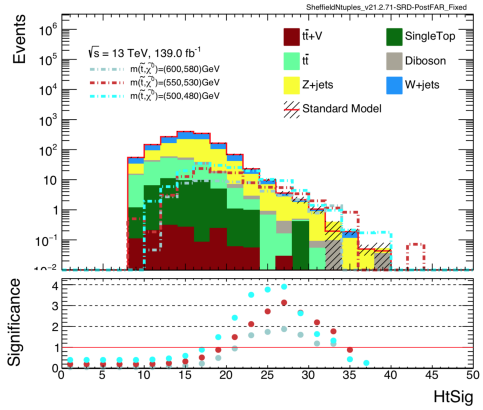

(a) $E_{\mathrm{T}}^{\mathrm{miss}}/\sqrt{H_{\mathrm{T}}} > 26\sqrt{\mathrm{GeV}}$

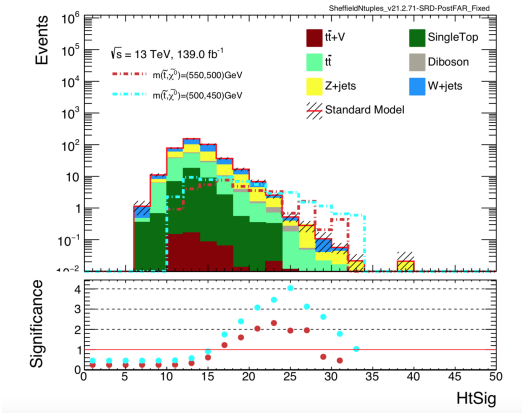

(b) $E_{\mathrm{T}}^{\mathrm{miss}}/\sqrt{H_{\mathrm{T}}} > 22\sqrt{\mathrm{GeV}}$

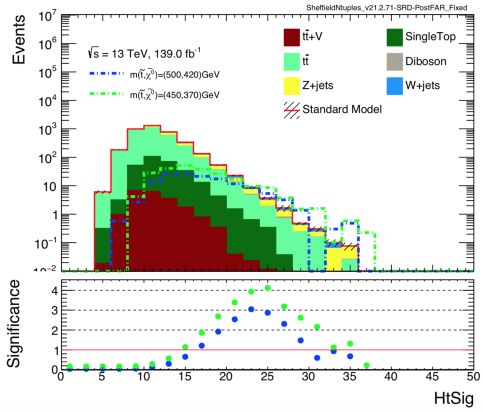

(c) $E_{\mathrm{T}}^{\mathrm{miss}}/\sqrt{H_{\mathrm{T}}} > 24$

FIGURE 8.12. N-1 distributions of HtSig across the three SRDs normalized to 139 fb^{-1} .

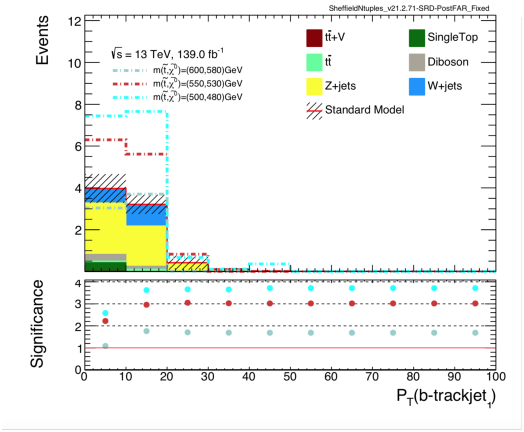

(a) $p_{\mathrm{T}}^{b_1,\mathrm{VR}} < 50$ GeV

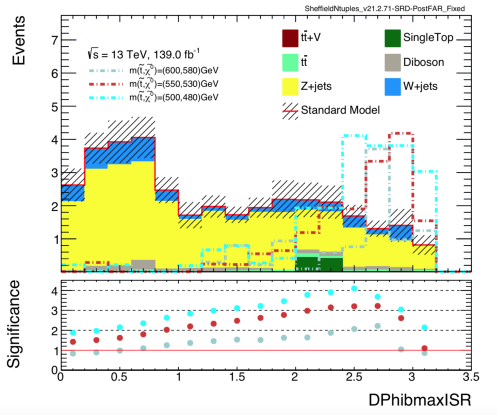

(b) $\max\left|\Delta\phi\left(\mathrm{non-b, b^{VR}}\right)\right| > 2.2$

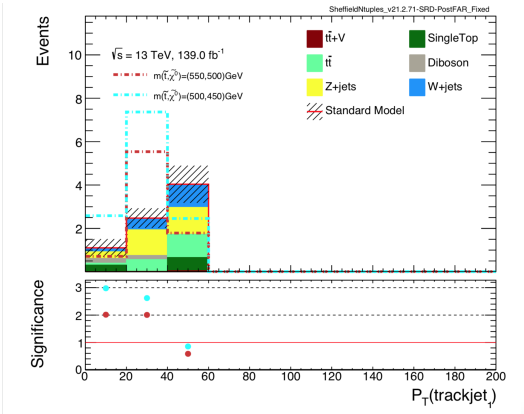

(c) $p_{\mathrm{T}}^{1,\mathrm{VR}} < 40$ GeV

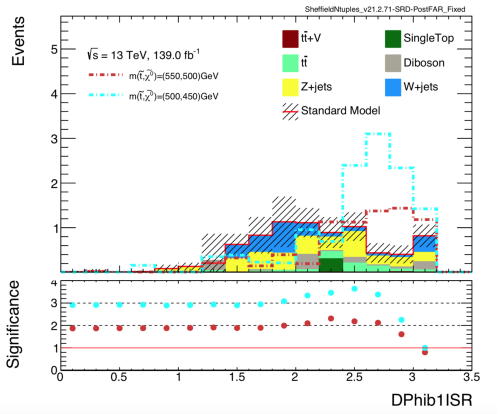

(d) $|\Delta\phi\left(\mathrm{non-b}, b_1\right)| > 2.2$

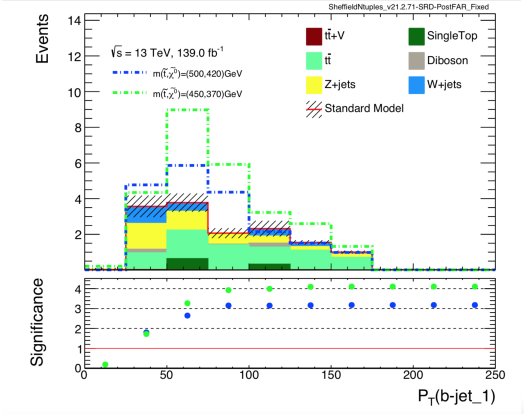

(e) $p_{\mathrm{T}}^{b_1} < 175$ GeV (now included in skim)

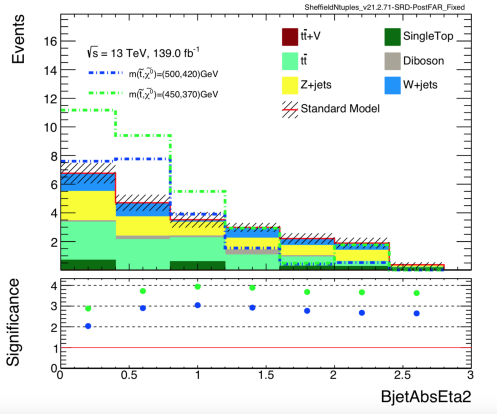

(f) $|\eta^{b_2}| < 1.2$

FIGURE 8.13. Select SRD N-1 distributions normalized to 139 fb^{-1} .

CHAPTER IX

BACKGROUND ESTIMATION

The analysis consists of multiple Signal Regions (SR), each with dedicated Control Regions (CR) to model the specific background behavior. The simulated Monte Carlo background samples are calibrated in a phase space far from our signal regions. Although the overall kinematic distributions have proper shapes, it is not unusual to have a normalization correction specific to the analysis phase space. Control Regions are used to study the various background processes and provide normalization factors to be used in SRs. Since any given background CR contains some amount of contamination from other backgrounds, it is important to execute a simultaneous fit of all CRs. Validation Regions (VR) are designed to be closer in phase-space to the SRs, but low in expected signal contamination. The CR normalization factors are applied in the VRs to measure the performance of the normalization.

My contribution to the analysis was in designing the $t\bar{t}$ CR for non-compressed stop models, as well as its corresponding VR. The immediate distinction from previous analyses is in modeling of the hadronic tau decays present in the SRs through the use of low-p_{T} leptons in the CR and object-based $E_{\mathrm{T}}^{\mathrm{miss}}$ significance discussed in Section 7.5.3. The sections below summarize the backgrounds to the analysis and the regions developed to estimate the expected yields, focusing on the $t\bar{t}$ processes entering SRA and SRB.

9.1. Background Composition

The common experimental signature of the signals searched consists of multiple jets and b-jets with mid to high p_{T} and high $E_{\mathrm{T}}^{\mathrm{miss}}$. The dominant background sources are:

- Semi-leptonic $t\bar{t}$ containing $W \rightarrow \ell\nu$ decays where the lepton is either lost or mis-identified as a jet (see Figure 9.1). A lepton can be mistaken as a jet if an electron or muon falls out of acceptance, or if a hadronically decaying τ lepton is produced. Such events have high $E_{\mathrm{T}}^{\mathrm{miss}}$ due to the escaping neutrino. A mis-identified jets adds uncertainty to the significance of the $E_{\mathrm{T}}^{\mathrm{miss}}$ and raise the value Object based $E_{\mathrm{T}}^{\mathrm{miss}}$ sig.

- Wt-channel single top decays, where one of the W decays hadronically and the other one decays leptonically. Similar to $t\bar{t}$, leptons can be mistaken as a jet if an electron or muon falls out of acceptance or if a hadronically decaying τ lepton is produced. Such events have high $E_{\mathrm{T}}^{\mathrm{miss}}$ due to the escaping neutrino. A mis-identified jet adds uncertainty to the significance of the $E_{\mathrm{T}}^{\mathrm{miss}}$ and raise the value Object based $E_{\mathrm{T}}^{\mathrm{miss}}$ sig.

- $Z \rightarrow \nu\bar{\nu}$ plus additional b-jets from QCD gluon splitting or 'scattering diagrams' (see Fig. 9.2). b-jets from QCD gluon splitting are usually close to each other (low ΔR_{bb}), whereas the b-jets resulting from two independent top decays tend to be well-separated (high ΔR_{bb}). The mass of the top candidates of this background is a result of stochastic combination of high p_T jets.

- $t\bar{t} + Z$, where both tops decay hadronically and the Z decays to $\nu\bar{\nu}$. This is the irreducible background of the analysis.

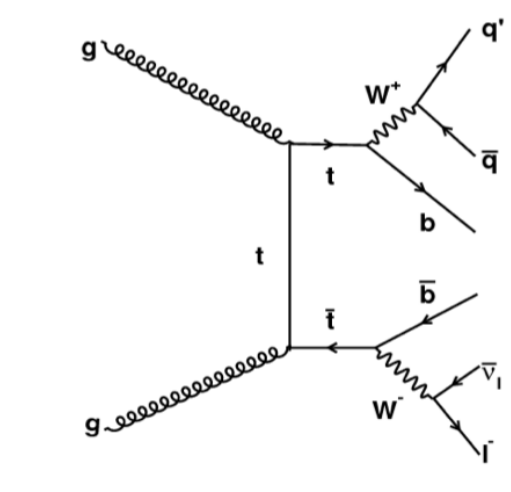

FIGURE 9.1. Schematic representation of the dominant production of semi-leptonic $t\bar{t}$ entering the analysis selection.

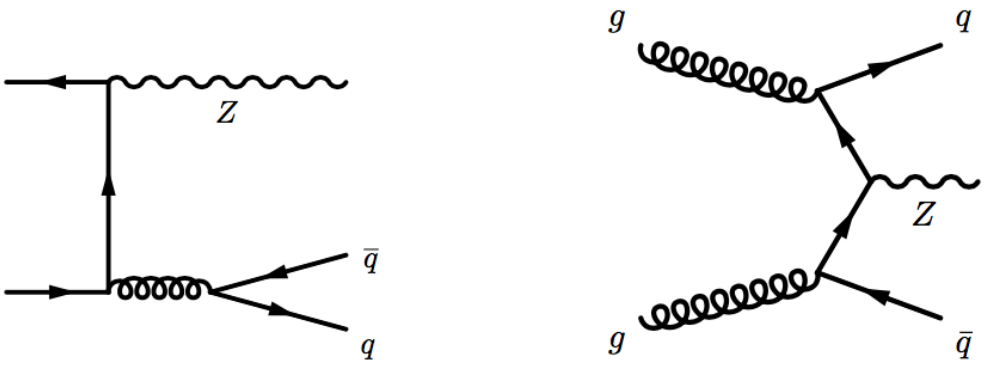

FIGURE 9.2. Schematic representation of the dominant production of Z+jets entering the analysis selection.

In addition, sub-dominant background components include:

- $W \rightarrow \ell\bar{\nu}$, where the lepton is either lost or mis-identified as a jet, plus additional b-jets from QCD gluon splitting or scattering diagrams,
- Di-boson production, where the bosons decay to neutrinos and 0 or 1 lost/mis-identified lepton,
- QCD multijet events with fake MET originating from jet mis-measurement or with hard-scattered jets mistakenly vetoed by the pileup rejection algorithm.

9.2. Discriminating Variables

We expect the following observables to provide good discrimination between signal with moderate to high mass splitting and all backgrounds:

- $E_{\mathrm{T}}^{\mathrm{miss}}$, Object based $E_{\mathrm{T}}^{\mathrm{miss}}$ sig.
- Jet multiplicity and p_{T}
- b-tagged jet multiplicity and p_{T}
- Reclustered jet multiplicity, p_{T} , and mass

9.2.1. Background with Tops

The $t\bar{t}$ and Wt-single top background usually have high $E_{\mathrm{T}}^{\mathrm{miss}}$ due to the escaping neutrino (and possibly the mis-reconstructed or out-of-acceptanc lepton). If the W-boson which decays leptonically originates from a top decay and the related lepton is lost or mis-identified (and therefore at least partly accounted in the $E_{\mathrm{T}}^{\mathrm{miss}}$), a pseudo top reconstruction can be performed by associating the $E_{\mathrm{T}}^{\mathrm{miss}}$

to the correct b-jet. In practice, the transverse mass between the $E_{\mathrm{T}}^{\mathrm{miss}}$ and the closest b-jet in $\Delta\phi$ is used:

$$m_{\mathrm{T}}^{b,\mathrm{min}} = \sqrt{2p_{\mathrm{T}}^{\mathrm{jet}} E_{\mathrm{T}}^{\mathrm{miss}} \left(1 - \cos\Delta\phi(\mathrm{jet}, E_{\mathrm{T}}^{\mathrm{miss}})\right)} \tag{9.1}$$

$m_{\mathrm{T}}^{b,\mathrm{min}}$ has a cut-off value at about the top mass in case the b-jet and the $E_{\mathrm{T}}^{\mathrm{miss}}$ originate from the same top quark decay, and therefore provides very good discrimination between signal and the $t\bar{t}/Wt$-single top background. $m_{\mathrm{T}}^{b,\mathrm{max}}$, using the furthest b-jet in $\Delta\phi$, is also used in for medium mass splittings as a complementary cut. A custom τ-veto is also applied to reject $t\bar{t}$ and Wt-single top background in regions targeting high and medium mass splittings.

Due to the heavier mass states produced in signal events w.r.t the top-quark and the W-boson, the $E_{\mathrm{T}}^{\mathrm{miss}}$ spectrum of background events with $t \rightarrow bW \rightarrow b\ell\nu$ tends to fall quicker than signal at high values. Hence, $E_{\mathrm{T}}^{\mathrm{miss}}$ stays a good discriminant variable to reject further $t\bar{t}$ events, even if a tight preselection cut has already been performed.

As both $t\bar{t}$ and Wt-single top background events involve one misreconstructed leptonic decay, the control regions defined to constrain these backgrounds rely on the selection of (exactly) one correctly reconstructed leptonic decay per event. The lepton is then either treated as a jet (if $p_{\mathrm{T}} > 20$ GeV) or as invisible (if $p_{\mathrm{T}} < 20$ GeV) to stay as close as possible to the signal region kinematics. For low p_{T} leptons, no peculiar treatment is needed as its kinematic has anyway very little impact on $E_{\mathrm{T}}^{\mathrm{miss}}$ and Object based $E_{\mathrm{T}}^{\mathrm{miss}}$ sig. (soft term). The main extrapolation from the control to the signal region is expected to happen on the lepton nature and kinematics.

The $t\bar{t}$ $+Z$ background is an irreducible background and in general resistant to the event selection. However, its small cross section keeps it quite subdominant, except at very high $E_{\mathrm{T}}^{\mathrm{miss}}$. The control region for this background models the $t\bar{t}$ $+Z$ background in a 3-lepton region, selecting $t\bar{t}$ semi-leptonic decays produced in associated with a charged leptonic Z decay.

9.2.2. Background without Tops

The background components without top quarks include usually b-jets originating from QCD gluon splitting to $b\bar{b}$, scattering diagrams or fakes from light-flavor and c-jets. Therefore, asking for at least two tight b-tagged jets in the event is quite efficient at rejecting them. In addition, the angular separation between the two jets with the highest b-tagging weight provides good discrimination against $g \to b\bar{b}$ background, present typically in some W/Z + jets and diboson background events:

$$\Delta R\,(b_1, b_2) = \sqrt{\Delta\eta(b_1, b_2)^2 + \Delta\phi(b_1, b_2)^2} \tag{9.2}$$

A second handle to reject the background without tops is to reconstruct the hadronic top decays directly, also known as top tagging. Top tagging performance depends strongly on the choice of algorithm and the main challenge arises from the fact that the most top tagging techniques depend strongly on the top quark p_{T}, which determines the boost of its decay particles. In this analysis, only signals with very large mass splitting include very highly boosted tops ($p_{\mathrm{T}} > 400$ GeV), the bulk of signals including top quarks with a wide p_{T} spectrum peaking at a lower value. The choice of top tagging algorithm and associated working point is therefore not straightfoward and requires specific studies.

Dedicated studies of top tagging algorithms available within ATLAS have been performed in the analysis and showed encouraging results. However, the calibration of the performance of these taggers is not available for signal samples generated, Therefore, the analysis uses the previous strategy based on the multiplicity, p_{T} and mass of reclustered jets with $R = 0.8, 1.2$ as described in Section 6.3. New to the analysis is using the the presence of a $R = 0.4$ calorimeter b-tagged jets within the constituents of the $R = 1.2$ reclustered jets to improve the discrimination.

Requirements on the stransverse mass (m_{T2,χ^2}) are also made to enhance the signal over background discrimination. This variable is especially powerful in the categories with no exploitable subleading reclustered jets (T0). It relies on a χ^2 estimator to reconstruct top quark decays with lower momenta, where reclustering is sub-optimal. The m_{T2} variable is built from the direction and magnitude of the $E_{\mathrm{T}}^{\mathrm{miss}}$ in the transverse plane as well as the direction of two top quark candidates reconstructed using a χ^2 method. The χ^2 is defined as $\chi^2 = \frac{(m_{\mathrm{cand}} - m_{\mathrm{true}})^2}{m_{\mathrm{true}}}$, where m_{cand} is the candidate mass and m_{true} is set to 80.4 GeV for W candidates and 173.2 GeV for top candidates. Initially, pairs of $R = 0.4$ jets form W candidates which are then used to construct top candidates using additional $R = 0.4$ jets in the event. The top candidates selected by the χ^2 method are only used for the momenta in m_{T2}, while the hypothesis masses for the top quark candidates and the invisible particles are set to 173.2 GeV and 0 GeV, respectively.

The background from multijet events originates from QCD interactions and all-hadronic $t\bar{t}$ and W/Z + jets events. It is estimated with the `JetSmearing` method [117]. This method is data-driven and therefore benefits from reduced detector systematic uncertainties; yet the main advantage to this method is the

substainly greater statistics that can be obtained compared with MC samples. The main assumption of the `JetSmearing` method is that the QCD multijet background is dominated by the mis-measurement of multiple jets. There are other sources of $E_{\mathrm{T}}^{\mathrm{miss}}$ that are not fully taken into account by this data-driven method. These sources include: $E_{\mathrm{T}}^{\mathrm{miss}}$ originating for pileup jets, $E_{\mathrm{T}}^{\mathrm{miss}}$ originating from jet-lepton overlap removal and potentially soft-term $E_{\mathrm{T}}^{\mathrm{miss}}$ sources. However, for this topology, all these sources are assumed to be negligible in the high $E_{\mathrm{T}}^{\mathrm{miss}}$ phase-space of this analysis. This was proven in the last iteration of this analysis.[118]

9.3. Background Predictions

To model each of the backgrounds significantly contaminating the SRs, we develop a set of CRs with varying number of leptons to estimate the expected background yield. An extrapolation is performed from the CRs to the SRs for the differing selections and a normalization factor is calculated in the CR that transferred onto the SR. The number of leptons, as well as their p_{T} selection and treatment, is motivated by the minimization of the extrapolation to the signal region and increasing the statistics and purity of the targeted background.

The normalization of the $t\bar{t}$ (AB, C, D analyses), single top (AB analysis), and W + jets (AB analysis) backgrounds is constrained in dedicated single bin, one-lepton regions, which all require exactly one signal lepton and no additional baseline leptons. The requirements shown in Table 7.3 are applied in all the one-lepton control regions used in the AB and C analyses (two-body regions). In order to avoid unblinding the one-lepton stop search, the transverse mass of the lepton-$E_{\mathrm{T}}^{\mathrm{miss}}$ system, $m(\ell, E_{\mathrm{T}}^{\mathrm{miss}})$, is required to be smaller than 120 GeV in all one-lepton regions.

Similarly, normalizations are calculated for Z + jetsand $t\bar{t}$ +Z in two-lepton and three-lepton control regions (respectively), where the additional leptons are used to reconstruct the Z-boson. Since these regions are very specific to the backgrounds, no common preselection was defined for two-lepton regions as it was for single-lepton regions. One of my contributions to the analysis was to introduce low p_{T}leptons for hadronic tau background modeling of top decays. This was used in three single-lepton CRs, most notably the $t\bar{t}$ CR I developed. I will focus on my contribution below and connect it within the other background predictions of the analysis.

9.3.1. Low p_T Leptons in $t\bar{t}$, W + jets, and single-top CRs

The choice of using low p_T leptons in 1-lepton control region design relies primarily on the truth composition of the particular backgrounds and signal regions at hand. One way of identifying the source parton flavor of anti-k$_{\mathrm{T}}$ R=0.4 EMTopo jets is by using the jet attribute "HadronConeExclTruthLabelID". The value of the decorator corresponds to the PDGID of the particle source; if at least one truth tau-hadron is matched to a jet within $\Delta R < 0.3$ the event is considered "Tau Matched".

Table 9.1 shows the tau-matched yields of the backgrounds across the relevant signal regions. Figure 9.3 shows the relative truth composition of W+jets, single top, and $t\bar{t}$ backgrounds (respectively) passing SRA/SRB selections, whereas Figure 9.4 shows it for the $t\bar{t}$ background in SRC. These results suggest that for the W+jets, and $t\bar{t}$ backgrounds of SRA/SRB, most events contain a soft tau that does not have enough momentum to form a jet passing the baseline p_T threshold. Therefore, the control regions were designed with $p_T^{lep} < 20$ GeV to model the

soft taus in the signal regions. The same argument applies for the single top background to SRA/SRB, but it was challenging to design a high purity control region with low p_T^{lep} and one with $p_T^{lep} > 20$ GeV was chosen. In SRC, the situation is the converse with most $t\bar{t}$ events passing the signal region selections sourced from tau decays that did form hard jets. Thus the $t\bar{t}$ control region for SRC was designed with $p_T^{lep} > 20$ GeV.

Truth Tau-Matched Jets			
Background	Region	Total Yield	Tau-Matched Yield
$t\bar{t}$	SRA	0.62	0.06
	SRB	97.38	14.35
	SRC	175.25	98.04
singletop	SRA	2.38	0.22
	SRB	47.28	7.03
wjets	SRA	1.77	0.0
wjets	SRB	37.07	4.5

TABLE 9.1. The truth composition of $t\bar{t}$ background to SRA and SRB

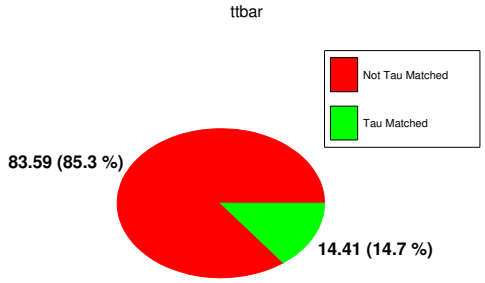

(a)

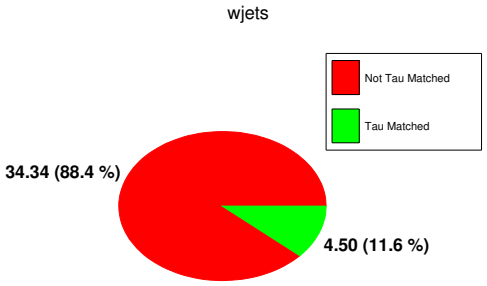

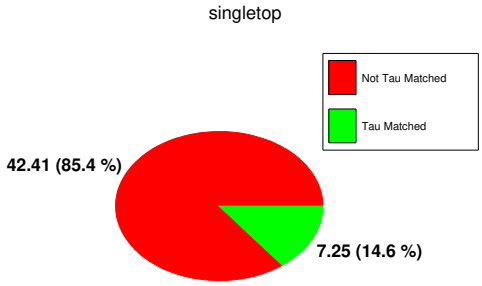

(b) (c)

FIGURE 9.3. Pie charts for SRA/SRB events ratios of $t\bar{t}$, W+jets, and single top simulated backgrounds.

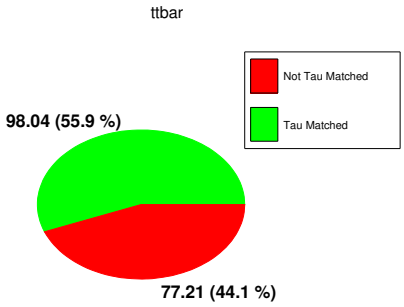

FIGURE 9.4. Pie chart for SRC events ratios of $t\bar{t}$.

9.3.2. Top Control Region for SRA and SRB

The control region presented in this section is designed to study $t\bar{t}$ events passing either SRA or SRB requirements. Albeit, the $t\bar{t}$ background is significant only in SRB and thus the control region is designed to be aligned most with this signal region.

The vast majority of $t\bar{t}$ events in SRB include exactly one leptonic top decay. It has been shown that approximately 15% of $t\bar{t}$ events passing the SRB selection have a truth tau lepton that is associated with a signal jet ($\Delta R < 0.3$), whereas most of the other 85% of events have a soft, hadronically decaying, tau lepton that deposits some energy in the calorimeter, but not enough to be reconstructed as a signal jet. The truth composition of SRB $t\bar{t}$ events motivated the design of CRTAB with soft leptons as a proxy for the low p_{T}, hadronically decaying taus.

To model the soft taus, the control region selection includes exactly one signal electron (muon) with 4.5 (4.0) $< p_{\mathrm{T}}^{\ell} <$ 20 GeV and no additional baseline leptons. Since the soft taus present in the SR do not lead to reconstructed jets, electrons and muons in CRTAB events are not added to the jet collection and instead are treated as their respective lepton objects when computing $E_{\mathrm{T}}^{\mathrm{miss}}$ and Object based $E_{\mathrm{T}}^{\mathrm{miss}}$ sig. .

The control region is designed to be primarily as close as possible to SRB, while maintaining a high purity of $t\bar{t}$ events, relative to the other backgrounds. Thus, the $m_{\mathrm{T}}^{b,\mathrm{min}}$ cut is relaxed to 150 GeV to increase statistics and $\Delta R\,(b,b) > 1.4$ is required to enhance the $t\bar{t}$ purity. The control region selection is shown in Table 9.2. A purity of 68.27% is expected, yielding to a scale factor of about 0.98 ± 0.09, as shown in Table 9.3. Data/MC plots of important variables in CRATAB are shown in Figures 9.5 and 9.6.

CRTAB	
p_T^{ℓ}	< 20 GeV
$\mathrm{N_{b-jet}}$	≥ 2
$\Delta R\,(b, b)$	> 1.4
Object based $E_{\mathrm{T}}^{\mathrm{miss}}$ sig.	> 14
$\mathrm{m}(J_1; \mathrm{R} = 1.2)$	> 120 GeV
$m_{\mathrm{T}}^{b,\mathrm{min}}$	> 150 GeV

TABLE 9.2. Definition of the $t\bar{t}$ control region for SRA and SRB. This selection is applied on top of the selection shown in Table 7.3.

$t\bar{t}$	171.13 ± 1.68	(68.27%)
Z+jets	1.14 ± 0.22	(0.45%)
W+jets	33.95 ± 2.44	(13.52%)
Single Top	32.49 ± 1.34	(12.94%)
$t\bar{t}$ $+Z$	4.54 ± 0.35	(1.82%)
other	7.50 ± 0.75	(2.99%)
SM	250.75 ± 3.37	(100.00%)
$\mathrm{m}(\tilde{t}_1, \tilde{\chi}_1^0)$=(1300,1)	0.19 ± 0.03	(0.08%)
$\mathrm{m}(\tilde{t}_1, \tilde{\chi}_1^0)$=(700,300)	$2.95 \pm 1.12 \pm 1.17$	(1.13%)
Data	247.00 ± 15.72	$(SF : 0.98 \pm 0.09)$

TABLE 9.3. The yields with the selection shown in Table 9.2 applied. The Scale Factor (SF) is defined by the ratio = (Data-$\mathrm{MC_{non-}}_{t\bar{t}}$)/$\mathrm{MC}_{t\bar{t}}$.

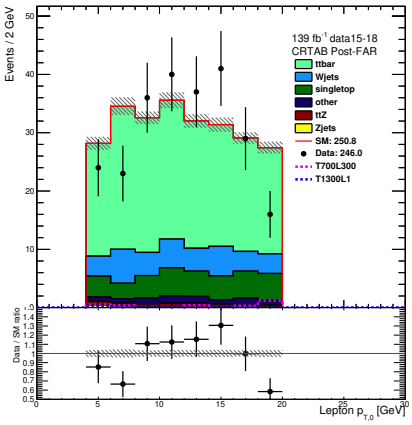

(a) $p_T^{\ell} < 20$ GeV

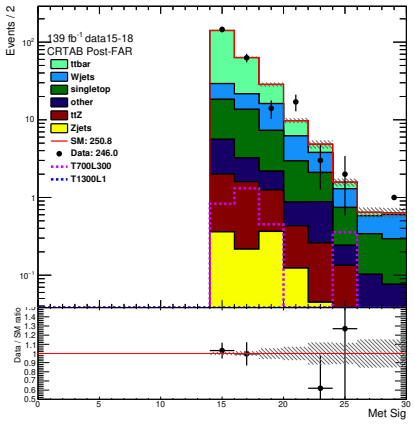

(b) Object based $E_{\mathrm{T}}^{\mathrm{miss}}$ sig. > 14

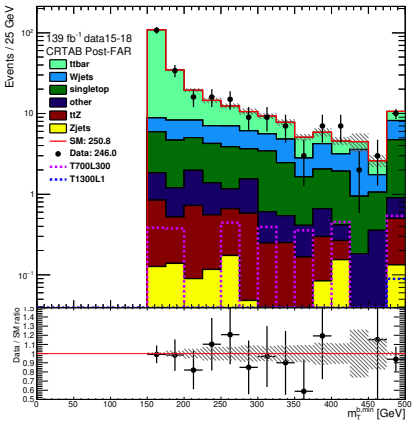

(c) $m_{\mathrm{T}}^{b,\mathrm{min}} > 150$ GeV

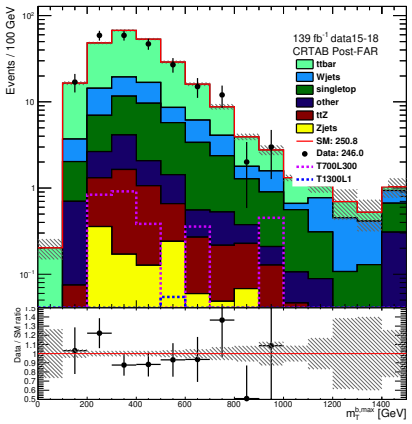

(d) $m_{\mathrm{T}}^{b,\mathrm{max}} > 200$ GeV

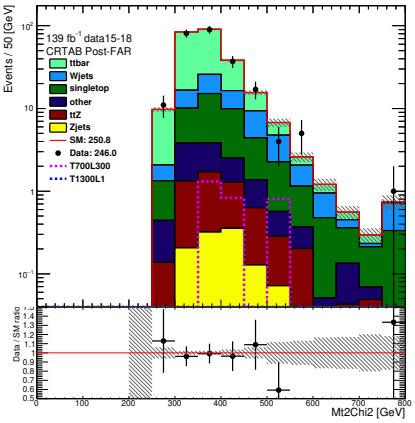

(e) $m_{\mathrm{T}}2\mathrm{chi}2$

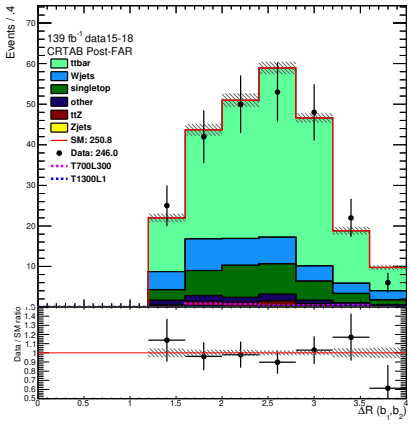

(f) $\Delta R\,(b, b) > 1.4$

FIGURE 9.5. Distributions of variables used in CRTAB.

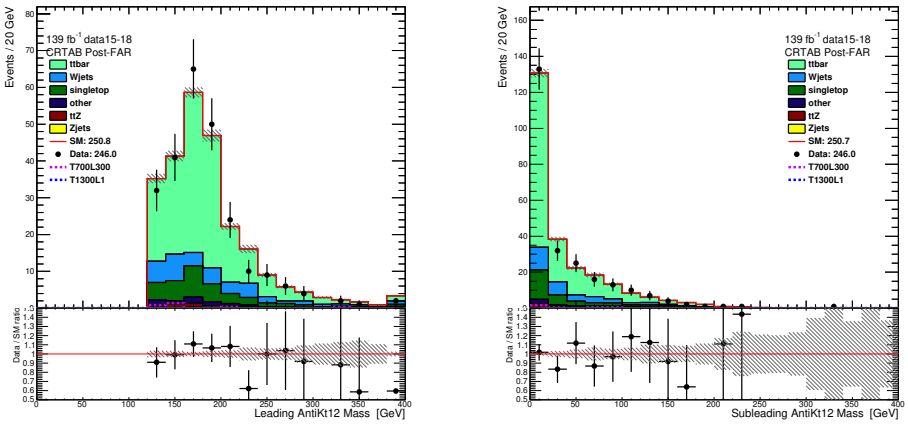

(a) $\mathrm{m}(J_1; \mathrm{R} = 1.2) > 120$ GeV

(b) $\mathrm{m}(J_2; \mathrm{R} = 1.2)$, SRA and SRB extrapolation

FIGURE 9.6. Distributions of variables used in SRA and SRB not used in CRTAB.

9.3.3. Other Single-Lepton Control Regions

The W + jets background is a significant background only in SRB. In order to make the W + jets control region orthogonal to the top control region CRTAB, exactly 1 b-tagged jet is required. The control region selections for the W + jets background in SRB also include exactly one low p_{T} signal lepton modeling the low p_{T} tau leptons. The mass of the leading $R = 1.2$ reclustering jet allows to increase the W + jets purity by rejecting $t\bar{t}$ events, while the exactly 1 b-tag requirement makes it orthogonal to CRTAB.

CRW-AB	
Trigger	$E_{\mathrm{T}}^{\mathrm{miss}}$
$E_{\mathrm{T}}^{\mathrm{miss}}$	≥ 250 GeV
$N_{\ell}^{\mathrm{baseline}}$	1
$p_{\mathrm{T}}^{\mathrm{lep}}$	< 20 GeV
$p_{\mathrm{T}}^{\mathrm{j1}}$,$p_{\mathrm{T}}^{\mathrm{j2}}$,$p_{\mathrm{T}}^{\mathrm{j3}}$,$p_{\mathrm{T}}^{\mathrm{j4}}$	$\geq 80, 80, 40, 40$ GeV
N_{b}	1
$\Delta\phi(\mathrm{j}^{1-4}, E_{\mathrm{T}}^{\mathrm{miss}})$	≥ 0.4
Object based $E_{\mathrm{T}}^{\mathrm{miss}}$ sig.	> 5
$\mathrm{m}(J_1; \mathrm{R} = 1.2)$	< 60 GeV
$m_{\mathrm{T}}^{b,\mathrm{min}}$	> 200 GeV
$\Delta R(b, \ell)$	> 2.0
$m_{\mathrm{T}}\left(\ell, E_{\mathrm{T}}^{\mathrm{miss}}\right)$	< 100 GeV
Object based $E_{\mathrm{T}}^{\mathrm{miss}}$ sig.	> 14

TABLE 9.4. The definitions of CRW-AB with low $p_{\mathrm{T}}^{\mathrm{lep}}$.

$t\bar{t}$	53.20 ± 1.02	(31.06%)
Z+jets	2.09 ± 0.48	(1.22%)
W+jets	99.99 ± 5.04	(58.37%)
Single Top	9.53 ± 0.98	(5.56%)
$t\bar{t}$ $+Z$	0.47 ± 0.12	(0.27%)
Diboson	6.02 ± 1.02	(3.52%)
SM	171.30 ± 5.36	(100.00%)
Data	147.00 ± 12.12	(SF : 0.76)
m($\tilde{t}$,$\tilde{\chi}^0$)=(1100,1)	0.02 ± 0.02	(0.01%)
m($\tilde{t}$,$\tilde{\chi}^0$)=(1300,1)	0.00 ± 0.00	(0.00%)
m($\tilde{t}$,$\tilde{\chi}^0$)=(700,400)	0.54 ± 0.31	(0.33%)

TABLE 9.5. The yield table of CRW-AB with low $p_{\mathrm{T}}^{\mathrm{lep}}$.

Single top backgrounds are only significant in SRA and SRB and therefore only control regions for these regions are defined. The single top control regions are orthogonal to the top and W + jets control regions by using high p_{T} signal leptons ($p_{\mathrm{T}} > 20$ GeV) instead of low p_{T}, also required to reach an acceptable single top purity. To estimate the single top normalization in SRA and SRB, CRSTAB was designed with exactly one lepton and two or more b-jets. To further avoid $t\bar{t}$ contamination, a $m_{l,b,\mathrm{min}} > 100$ GeV requirement is enforced. $m_{l,b,\mathrm{min}}$ is the mass of lepton and closest b-tagged jet. The selection is described in Table 9.6, while the resulting yields are shown in Table 9.7.

CRSTAB	
p_T^{ℓ}	> 20 GeV
$\mathrm{N_{b-jet}}$	≥ 2
$\mathrm{m}(J_1; \mathrm{R} = 1.2)$	> 120 GeV
$m_{\mathrm{T}}^{b,\mathrm{min}}$	> 200 GeV
Object based $E_{\mathrm{T}}^{\mathrm{miss}}$ sig.	> 14
$\Delta R\,(b_1, b_2)$	> 1.4
$m_{\mathrm{T}}\left(\ell, E_{\mathrm{T}}^{\mathrm{miss}}\right)$	< 100 GeV
$m_{l,b,\mathrm{min}}$	$> 100 GeV$
τ veto	✓

TABLE 9.6. The definition CRSTAB after the selection described in Table 7.3 is applied.

$t\bar{t}$	43.58 ± 0.83	(26.71%)
Z+jets	0.25 ± 0.07	(0.15%)
W+jets	39.46 ± 2.46	(24.18%)
Single Top	76.25 ± 1.82	(46.73%)
$t\bar{t}$ $+Z$	1.55 ± 0.23	(0.95%)
Diboson	2.08 ± 0.47	(1.28%)
SM	163.17 ± 3.21	(100.00%)
Data	141.00 ± 11.87	$(SF : 0.71)$
m($\tilde{t}$,$\tilde{\chi}^0$)=(1100,1)	0.09 ± 0.04	(0.05%)
m($\tilde{t}$,$\tilde{\chi}^0$)=(1300,1)	0.02 ± 0.01	(0.01%)
m($\tilde{t}$,$\tilde{\chi}^0$)=(700,400)	1.73 ± 0.64	(1.06%)

TABLE 9.7. The yields of CRSTAB. The Scale Factor (SF) is defined by the ratio = (Data-$\mathrm{MC_{non-SingleTop}}$)/$\mathrm{MC_{SingleTop}}$.

The background in SRC is dominated by $t\bar{t}$ events with exactly one leptonic decay, which represents at least 70 % of the total SM background estimation. To minimize the systematic uncertainty in the extrapolation from control region to signal region selection, CRTC is designed to be as close as possible to SRC as possible. All R_{ISR} bins are included in CRTC, which is a one bin control region used for all R_{ISR} bins in SRC. Table 9.8 summarizes the final selections of CRTC after the common one-lepton selection from Table 7.3. $\Delta\phi_{\mathrm{ISR},E_{\mathrm{T}}^{\mathrm{miss}}}$ is loosened from 3.0 to 2.75 in CRTC to allow for sufficient statistics. The benchmark sample

corresponding to m($\tilde{t}$,$\tilde{\chi}^0$)=(225,52), though probably already excluded by the spin correlation measurement [119], shows naturally a significant contamination in CRTC. In order to limit this contamination, the requirement on $m_{\mathrm{T}}\left(\ell, E_{\mathrm{T}}^{\mathrm{miss}}\right)$ is tightened from 120 GeV to 80 GeV and $m_{\mathrm{V}}/m_{\mathrm{S}} < 0.75$ is added in the selection.

CRTC	
Object based $E_{\mathrm{T}}^{\mathrm{miss}}$ sig.	> 5
$\Delta R(b, \ell)$	< 2.0
$m_{\mathrm{T}}\left(\ell, E_{\mathrm{T}}^{\mathrm{miss}}\right)$	< 100 GeV
$p_{\mathrm{T}}^{\mathrm{ISR}}$	> 400 GeV
m_{S}	≥ 400 GeV
$N_{\mathrm{jet}}^{\mathrm{S}}$	≥ 4
$N_{\mathrm{b-jet}}^{\mathrm{S}}$	≥ 2
$p_{\mathrm{T},b}^{1,\mathrm{S}}$	≥ 40 GeV
$p_{\mathrm{T}}^{4,\mathrm{S}}$	≥ 50 GeV
$m_{\mathrm{V}}/m_{\mathrm{S}}$	< 0.75
$\Delta\phi(\mathrm{ISR}, E_{\mathrm{T}}^{\mathrm{miss}})$	> 3.00

TABLE 9.8. The selections used in CRTC.

The $t\bar{t}$ background is a significant background only in SRD1 and SRD2. This is expected because SRD0 has a b-jet veto which heavily suppresses the $t\bar{t}$ background while SRD1 and SRD2 require exactly one and two b-jets, respectively. After the 1-lepton pre-selection specific to the four-body region described in Table 9.9, the selection further branches in separate control regions, CRDttbar1 and CRDttbar2 designed for the $t\bar{t}$ background normalization. The selections are shown in Table 9.10. It can be noted that CRDttbar1 requires the presence of exactly two b-jets, while the corresponding SRD1 requires one. This is done to enhance the population of the $t\bar{t}$ background. This extrapolation will be validated through the use of a dedicated validation region later in the note. The $E_{\mathrm{T}}^{\mathrm{miss}}/\sqrt{H'_{\mathrm{T}}}$ cut has been relaxed with respect to the corresponding signal regions to enhance

statistics. Selections on $\Delta R(b,\ell)$ and $m(\ell, E_{\mathrm{T}}^{\mathrm{miss}})$ are applied to enhance the $t\bar{t}$ population. Otherwise, all other signal region requirements are kept the same.

Selection	Value
signal ℓ	exactly 1
additional baseline ℓ	0
$E_{\mathrm{T}}^{\mathrm{miss}}$trigger	✓
$E_{\mathrm{T}}^{\mathrm{miss}}$	$>$ 250 GeV
$p_{\mathrm{T(non\,b-jet_1)}}$	$>$ 250 GeV
$\left\lvert\Delta\phi\left(\mathrm{non-b}, E_{\mathrm{T}}^{\mathrm{miss}}\right)\right\rvert$	$>$ 2.4 rad
$E_{\mathrm{T}}^{\mathrm{miss,track}}$	$>$ 30 GeV
$\left\lvert\Delta\phi\left(E_{\mathrm{T}}^{\mathrm{miss}}, E_{\mathrm{T}}^{\mathrm{miss,track}}\right)\right\rvert$	$<\pi/3$ rad
$m(\ell, E_{\mathrm{T}}^{\mathrm{miss}})$	¡ 120

TABLE 9.9. Summary of the preselection applied to the four-body 1-lepton regions in the analysis.

	CRDttbar1	CRDttbar2
$\mathrm{N_{b-jet}}$	exactly 1	≥ 2
p_T^{ℓ}	$>$ 20 GeV	$>$ 20 GeV
$\lvert\eta^{b_1}\rvert$	$<$ 1.6	-
$\lvert\eta^{b_2}\rvert$	-	$<$ 1.2
$p_{\mathrm{T}}^{b_1}$	-	$<$ 175 GeV
$\lvert\Delta\phi\left(\mathrm{non-b}, b_1\right)\rvert$	$>$ 2.2	
$\lvert\Delta\phi\left(\mathrm{non-b}, b_2\right)\rvert$	-	$>$ 1.6
$\mathrm{N_{b-jet}^{VR}}$	≥ 1	-
$p_{\mathrm{T}}^{\mathrm{1,VR}}$	$<$ 40 GeV	-
$\min\left\lvert\Delta\phi\left(\mathrm{jet}^{\mathrm{VR\,1-4}}, \mathrm{non-b}\right)\right\rvert$	$>$ 1.2	-
$E_{\mathrm{T}}^{\mathrm{miss}}/\sqrt{H_{\mathrm{T}}'}$	$>8\sqrt{\text{ GeV}}$	$>14\sqrt{\text{ GeV}}$
$\Delta R(b,\ell)$	$<$ 1.8	
$p_{\mathrm{T}}^{b_1,\mathrm{VR}}$	$>$ 10 GeV	-
$\mathrm{N_{jets}}$	$>$ 2	

TABLE 9.10. Top control region selections applied to estimate the semi-leptonic $t\bar{t}$ background normalization in SRD

9.3.4. Two-Lepton Control Regions

The normalization of the Z + jets background (AB, D analysis) is constrained in a two-bin (AB), or one-bin (D), two-lepton control region. All events in two-lepton control regions (Z + jets AB, Z + jets D) contain exactly two opposite charged, same flavor, signal leptons (electron or muon) with an invariant mass close to the Z mass peak, and no additional baseline leptons. The leptons are treated as invisible particles and the missing transverse energy computed with the leptons treated as invisible is labeled $E_{\mathrm{T}}^{\mathrm{miss}'}$. The data for these regions were collected with the lowest un-prescaled single-lepton trigger. Since one aims to select regions at high Z p_{T} (to mimic high $E_{\mathrm{T}}^{\mathrm{miss}}$ in $Z \rightarrow \nu\nu$ decays in the SR), one has to select anyway at least one high p_{T} lepton ($p_{\mathrm{T}} > 27$ GeV), which makes the use of multi-lepton triggers unnecessary. Table 9.11 summarizes the selection common to all two-lepton CRs.

Variable	Value
signal ℓ	exactly 2, same flavor / opposite sign
additional baseline ℓ	0
single lepton trigger	✓
$E_{\mathrm{T}}^{\mathrm{miss}}$	< 50 GeV
$m(\ell, \ell)$	[81,101] GeV
$E_{\mathrm{T}}^{\mathrm{miss}'}$	> 150 GeV

TABLE 9.11. Summary of the two-lepton selection applied to all regions used for Z + jets background estimations.

In addition to the preselection requirements in Table 9.11, the selection shown in Table 9.12 is used to make Z + jets control regions which have requirements that more closely mirror the selection of SRA and SRB. Two separate control regions are defined (T0, TT-TW) to account for the fact that the Z+jets background is constituted by two main components ($g \rightarrow bb$ and scattering diagrams, see

Section 9.1), which a priori enter the T0 and TT-TW SR in different proportions due to the different $\Delta R\,(b_1, b_2)$ requirement.

Variable	CRZABTT-TW	CRZABT0
Leading p_{T}^{ℓ}	> 27 GeV	
Subleading p_{T}^{ℓ}	> 20 GeV	
$E_{\mathrm{T}}^{\mathrm{miss}'}$	> 200 GeV	
$\mathrm{N_{jets}}$	≥ 4	
$p_{\mathrm{T}}^{j_2}$	> 80 GeV	
$p_{\mathrm{T}}^{j_4}$	> 40 GeV	
$\mathrm{N_{b-jet}}$	≥ 2	
$\mathrm{m}(J_1; \mathrm{R} = 1.2)$	> 80 GeV	
Object based $E_{\mathrm{T}}^{\mathrm{miss}'}$ sig.	> 10	
$m_{\mathrm{T}}^{b,\mathrm{min}'}$	> 150 GeV	
$\mathrm{m}(J_2; \mathrm{R} = 1.2)$	> 60 GeV	< 60 GeV

TABLE 9.12. CRZAB selection.

Process	CRZAB-TT-TW	CRZAB-T0
Diboson	5.35 ± 0.40 (6.93%)	11.64 ± 0.69 (5.95%)
$t\bar{t}$ +Z	17.25 ± 0.33 (22.33%)	23.09 ± 0.36 (11.80%)
W + jets	0.00 ± 0.00 (0.00%)	0.00 ± 0.00 (0.00%)
$t\bar{t}$	0.00 ± 0.00 (0.00%)	20.38 ± 2.32 (4.82%)
Z + jets	54.38 ± 1.23 (70.41%)	159.39 ± 2.36 (81.46%)
Single Top	0.25 ± 0.25 (0.33%)	0.25 ± 0.25 (0.13%)
SM	77.24 ± 1.36 (100.00%)	195.67 ± 15.26 (100.00%)
signal-T1100L1	0.00 ± 0.00 (0.00%)	0.00 ± 0.00 (0.00%)
Data	83 ± 9.43 ($SF : 1.22 \pm 0.18$)	233 ± 15.26 ($SF : 1.23 \pm 0.10$)

TABLE 9.13. Pre-fit yields of CRZAB-TT-TW and CRZAB-T0. The SF is defined by the ratio = (Data-$\mathrm{MC}_{Z\,+\,\mathrm{jets}}$)/$\mathrm{MC}_{Z\,+\,\mathrm{jets}}$.

In addition to the preselection requirements shown in Table 9.11, the selections shown in Table 9.14 are used to make CRDZ0, CRDZ1, and CRDZ2 which have requirements that closely mirror SRD0, SRD1 and SRD2. To enhance the number of events the $E_{\mathrm{T}}^{\mathrm{miss}'}$ and $p_{\mathrm{T(non\,b-jet_1)}}$ cuts are relaxed in CRDZ1 and CRDZ2, and the $E_{\mathrm{T}}^{\mathrm{miss}'}/\sqrt{H_{\mathrm{T}}}$ cut is relaxed in all CRZD. The $E_{\mathrm{T}}^{\mathrm{miss,track}}$cut is removed as it is not necessary in a two-leptons selection. Otherwise, all other SRD

	CRZD0	CRZD1	CRDZ2
N_{b-jet}	exactly 0	exactly 1	≥ 2
E_T^{miss}	< 70 GeV		
Leading p_T^{ℓ}	> 30 GeV		
Subleading p_T^{ℓ}	> 20 GeV		
$E_T^{miss'}$	> 250 GeV	> 150 GeV	> 200 GeV
$p_{T(\text{non b}-\text{jet}_1)}$	> 250 GeV	> 200 GeV	> 250 GeV
$\lvert\Delta\phi\left(\text{non}-\text{b}, E_T^{miss'}\right)\rvert$	> 2.4 rad		
$\lvert\eta^{b_1}\rvert$	-	< 1.6	-
$\lvert\eta^{b_2}\rvert$	-		< 1.2
$p_T^{b_1}$	-		< 175 GeV
$\lvert\Delta\phi\left(\text{non}-\text{b}, b_1\right)\rvert$	-	> 1.8	> 2.2
$\lvert\Delta\phi\left(\text{non}-\text{b}, b_2\right)\rvert$	-		> 1.6
N_{b-jet}^{VR}	≥ 1		-
$p_T^{b_1,VR}$	< 50 GeV	> 10 GeV	-
$p_T^{1,VR}$	-	< 40 GeV	-
$\lvert\eta^{b_1,VR}\rvert$	< 1.2	-	
$\max\lvert\Delta\phi\left(\text{non}-\text{b}, \text{b}^{VR}\right)\rvert$	> 2.2	-	
$\lvert\Delta\phi\left(b_1^{VR}, b_2^{VR}\right)\rvert$	< 2.5	-	
$\min\lvert\Delta\phi\left(\text{jet}^{VR\,1-4}, \text{non}-\text{b}\right)\rvert$	-	> 1.2	-
$E_T^{miss'}/\sqrt{H_T}$	> 12	> 8	> 8
$\min\lvert\Delta\phi\left(\text{jet}^{1-4}, E_T^{miss}\right)\rvert$	> 0.4	-	

TABLE 9.14. Control region selections for the estimation of the Z + jets background in SRD. These requirements are applied in addition to the preselection criteria of Table 9.11.

requirements are kept. Signal contamination is zero primarily due to the cut on the invariant mass of the Z boson.

9.3.5. Three-Lepton Control Regions

The normalization of the $t\bar{t} + Z$ background (AB analysis) is constrained in a single bin, three-lepton control region. Data are recorded using single-lepton triggers. The leptons in these regions are treated as invisible and the newly-formed E_T^{miss} is labeled $E_T^{miss'}$. The $t\bar{t} + Z$ background, where the Z decays into neutrinos, is an irreducible background in this analysis. In the previous Run 2 analysis, the estimation of this background was provided by a one-lepton CR for $t\bar{t} + \gamma$, rather

than a multi-lepton $t\bar{t} + Z$ region, due to low statistics in the $p_{\mathrm{T}}(Z)$ tail [34]. The similar Feynman diagrams corresponding to these two processes motivated this boson replacement strategy. Namely, the photon in the $t\bar{t} + \gamma$ can be chosen to model the kinematics of the Z, with corrections for the coupling and the differing cross sections as a function of p_{T}. A 1-lepton control region strategy was chosen to improve the purity of the $t\bar{t} + \gamma$ process over γ+jets.

However, with the full Run 2 dataset, the $t\bar{t} + Z$ multileptonic process is now reachable with sufficient statistics to design a corresponding CR, as the cross section will be the same up to branching ratios. $t\bar{t}+Z(\rightarrow ll)$, with the di-lepton pair from the Z having similar kinematics as the neutrinos in the signal region. Two final states have been considered: the two-lepton opposite-sign signature (2LOS), where the $t\bar{t}$ system decays hadronically and the Z leptonically; and the 3-lepton scenario where the $t\bar{t}$ system decays semi-leptonically. The studies undertaken in both final states demonstrated that a 3-lepton control region was more adequate due to a higher $t\bar{t} + Z$ purity.

All data and MC events considered in 3-lepton regions must contain in addition to the common preselection two opposite charge signal leptons with same flavor (electron or muon) and one extra signal lepton (either electron or muon). The trilepton control region for $t\bar{t} + Z$ requires exactly three signal leptons (electrons or muons, as defined in Section VII and at least four jets, at least two of which are required to be b-tagged. To collect these events, the lepton triggers described in Table 6.2 are used. To reduce the contamination of fake leptons originating from charge-flips, the sum of the charges of the three leptons is required to equal ± 1. An opposite-sign same-flavour (OSSF) pair of signal leptons is required, whose invariant mass must satisfy $|m_{ll} - m_Z| < 10$ GeV, where

m_Z is taken as the world-averaged mass of the Z from the Particle Data Group (91.19 GeV) [25]. The control region requires in addition that the leading lepton $p_{\mathrm{T}}$is greater than 27 GeV (in order to ensure the single lepton trigger plateau is reached and required by the high Z p_{T} that we are targeting) and that the two subleading leptons have p_{T} greater than 20 GeV (which is part of the signal lepton definition).

The signal lepton identified in the construction of the m_{ll} variable as not associated to the Z and the $E_{\mathrm{T}}^{\mathrm{miss}}$ are assumed to have originated from a W decay as part of the semi-leptonic $t\bar{t}$ decay branch of $t\bar{t}$ $+Z$. To mimic the all-hadronic $t\bar{t}$ branch of $t\bar{t}$ $+Z(\nu\nu)$ in the signal region, both are treated as jets.

Selection	CRttZ-AB
Event selection	Event cleaning (incl. 1L triggers)
Lepton multiplicity	==3 (signal)
Leptons p_{T}	$>$ 27,20,20 GeV
Sum of charges	$\pm$ 1
Jet multiplicity	$\geq$ 4
Jets p_{T}	$>$ 80,80,40,40 GeV (including $E_{\mathrm{T}}^{\mathrm{miss}}$ and p_T(non-Z lep))
b-jet multiplicity	$\geq$ 2
Z-like OSSF pair	Yes
$p_T(ll)_Z$	$>$ 200 GeV

TABLE 9.15. Selections for the 3-lepton $t\bar{t}$ + Z CR. The triggers described in Table 6.2 and the lepton defined in Chapter VII are used.

CRttZ-pT200	
$t\bar{t}+Z$	53.14 ± 0.58
ZW	4.71 ± 0.16
Fakes(MC)	0.55 ± 0.17
others	8.39 ± 0.32
SM	66.79 ± 0.70
Data	59.00 ± 7.68

TABLE 9.16. Pre-fit yields for the 3-lepton region CRttZ-AB.

9.4. Background Validation

9.4.1. Top Validation Region for SRA and SRB

The following $t\bar{t}$ validation region is chosen to be sensitive to both SRA and SRB, in order to reflect the choice made for CRTAB.

Restricting $m_{\mathrm{T}}^{b,\mathrm{min}}$ to the window [150,200] simultaneously orthogonalizes the validation region to SRA and SRB, while probing the physics in the extrapolated $m_{\mathrm{T}}^{b,\mathrm{min}}$ variable. Table 9.17 shows the region definition. The observed and expected yields before applying the full-fit scale factors in VRTAB are shown in Table 9.18. Figure 9.8 shows the distributions of key variables.

The grid of signal points on Figure 9.7 show that most unexcluded signal points have a contamination level below 7% and the strongest contaminating signal point is T500L250 with 14%.

VRTAB	
$E_{\mathrm{T}}^{\mathrm{miss}}$ Trigger	✓
$E_{\mathrm{T}}^{\mathrm{miss}}$	≥ 250
Lepton Veto	no baseline lepton
$\mathrm{N}_{\mathrm{jets}}$	≥ 4
$p_{\mathrm{T}}^{j_2}$	> 80 GeV
$p_{\mathrm{T}}^{j_4}$	> 40 GeV
$\min\left\lvert\Delta\phi\left(\mathrm{jet}^{1-4}, E_{\mathrm{T}}^{\mathrm{miss}}\right)\right\rvert$	≥ 0.4
$\mathrm{N}_{\mathrm{b-jet}}$	≥ 2
$\Delta R\left(b_1, b_2\right)$	> 1.4
Object based $E_{\mathrm{T}}^{\mathrm{miss}}$ sig.	> 14
$\mathrm{m}(J_1; \mathrm{R} = 1.2)$	> 120 GeV
$m_{\mathrm{T}}^{b,\mathrm{min}}$	[150,200] GeV
Tau Veto	Yes

TABLE 9.17. The definition of ttbar control region for SRA and SRB

ttbar	419.55 ± 3.29	(74.81%)
Z+jets	67.74 ± 2.50	(12.13%)
W+jets	21.47 ± 2.00	(3.83%)
Single Top	20.58 ± 1.20	(3.66%)
ttZ	20.16 ± 0.74	(3.60%)
other	10.97 ± 1.17	(1.97%)
SM	560.48 ± 4.95	(100.00%)
$\mathrm{m}(\tilde{t}_1, \tilde{\chi}_1^0)$=(700,300)	36.75 ± 4.15	(6.54%)
$\mathrm{m}(\tilde{t}_1, \tilde{\chi}_1^0)$=(1300,1)	0.60 ± 0.05	(0.11%)
Data	590.00 ± 24.29	-

TABLE 9.18. The yields with the selections on Table 9.17.

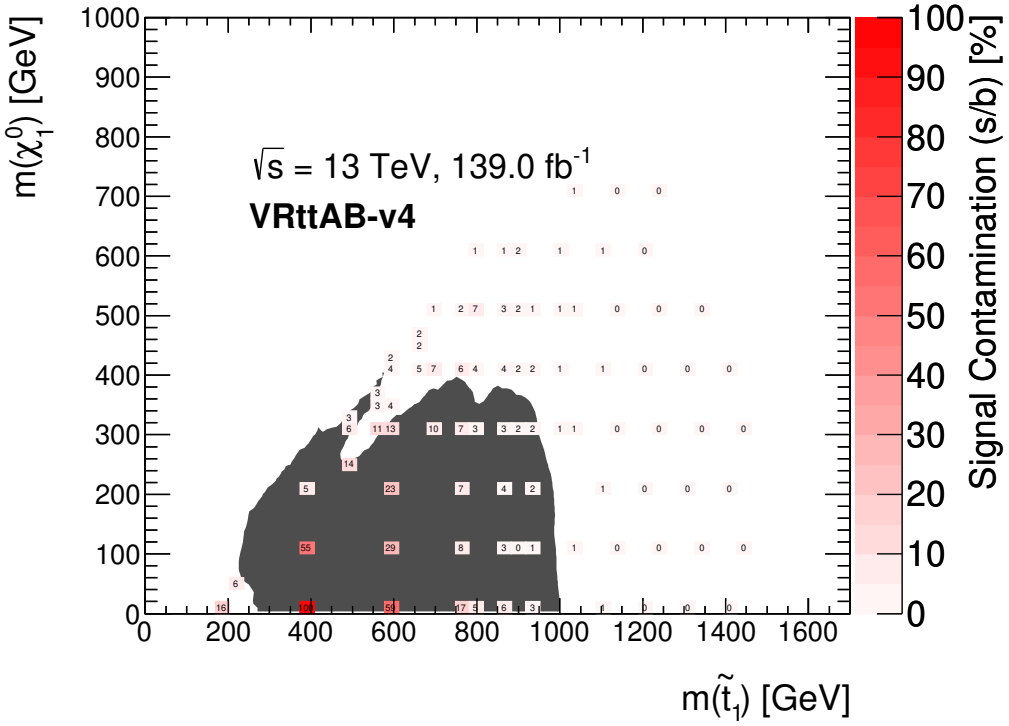

(a) $E_{\mathrm{T}}^{\mathrm{miss}}$

FIGURE 9.7. Signal contamination for VRTAB.

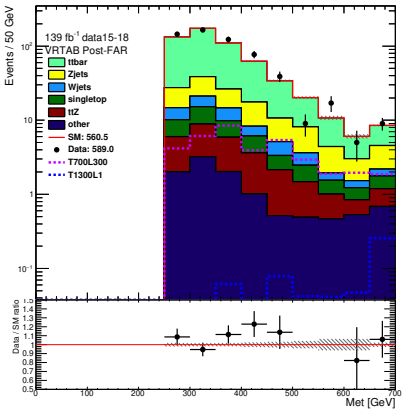

(a) $E_{\mathrm{T}}^{\mathrm{miss}}$

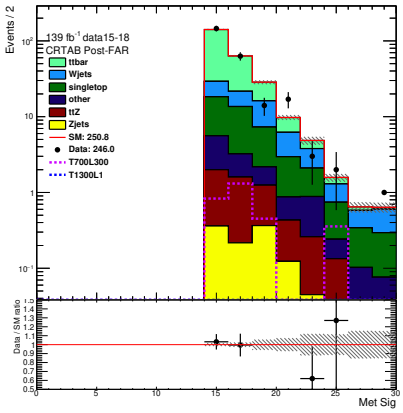

(b) $E_{\mathrm{T}}^{\mathrm{miss}}/\sqrt{\Sigma E_T}$

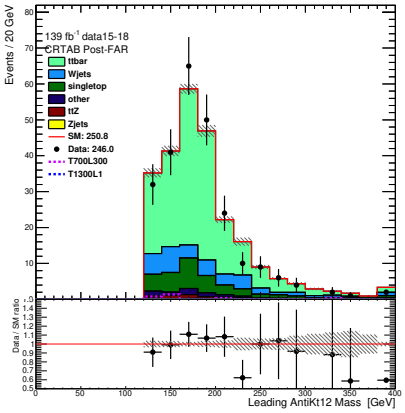

(c) $\mathrm{m}(J_1;\mathrm{R}=1.2)$

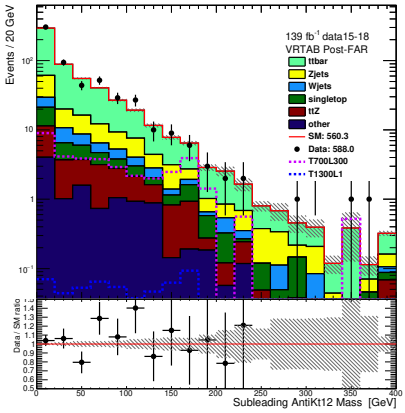

(d) $\mathrm{m}(J_2;\mathrm{R}=1.2)$

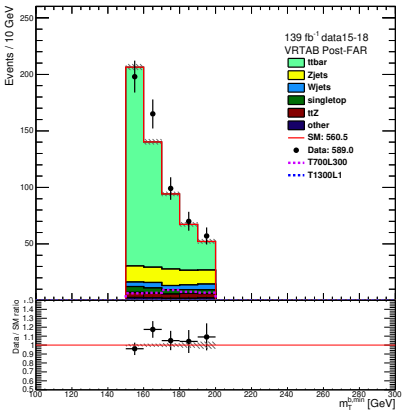

(e) $m_{\mathrm{T}}^{b,\mathrm{min}}$

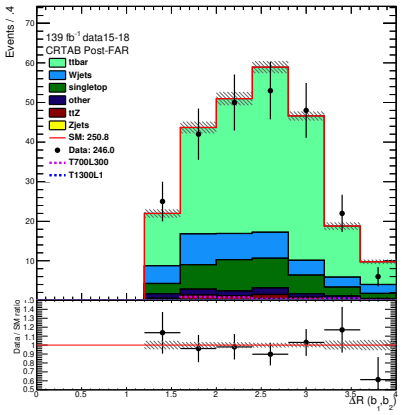

(f) $\Delta R\,(b_1, b_2)$

FIGURE 9.8. Prefit distributions of key variables in VRTAB.

9.4.2. Other Zero-Lepton Validation Regions

9.4.2.1. Top validation region for SRC

The $t\bar{t}$ validation region is defined for the signal region C by a sideband on the $\Delta\phi_{\mathrm{ISR},E_{\mathrm{T}}^{\mathrm{miss}}}$ variable and by applying an additional cut on the $m_{\mathrm{V}}/m_{\mathrm{S}}$ variable, to ensure low signal contamination for all benchmark models considered. The choice of these variables is based on the modelling of the preselection plots, which show a fair agreement between data and MC. Only a sideband in $\Delta\phi_{\mathrm{ISR},E_{\mathrm{T}}^{\mathrm{miss}}}$ is selected instead of inverting the cut to veto configurations where the $E_{\mathrm{T}}^{\mathrm{miss}}$ and ISR are not well separated. It is chosen to match the CR lower cut requirement ($\Delta\phi_{\mathrm{ISR},E_{\mathrm{T}}^{\mathrm{miss}}} > 2.75$). No binning in R_{ISR} is performed because of the limited statistics.

Table 9.19 shows the VRTC definition.

Variable	VRTC
Object based $E_{\mathrm{T}}^{\mathrm{miss}}$ sig.	> 5
$N_{\mathrm{b-jet}}^{\mathrm{S}}$	≥ 2
$N_{\mathrm{jet}}^{\mathrm{S}}$	≥ 4
$p_{\mathrm{T},b}^{1,\mathrm{S}}$	> 40 GeV
m_{S}	> 400 GeV
$\Delta\phi_{\mathrm{ISR},E_{\mathrm{T}}^{\mathrm{miss}}}$	$[2.50 - 3.0]$
$p_{\mathrm{T}}^{\mathrm{ISR}}$	> 400 GeV
$p_{\mathrm{T}}^{4,\mathrm{S}}$	> 50 GeV
$m_{\mathrm{V}}/m_{\mathrm{S}}$	< 0.6 GeV

TABLE 9.19. Selection criteria for VRTC. Requirements that have been changed from the SRC definition are the $\Delta\phi_{\mathrm{ISR},E_{\mathrm{T}}^{\mathrm{miss}}}$ sideband requirement, adding a $m_{\mathrm{V}}/m_{\mathrm{S}}< 0.6$ requirement, and omitting the R_{ISR} binning.

9.4.2.2. Top validation region for SRD (VRTD)

The following validation regions are designed to validate the CRTD1 and CRTD2 predictions. CRTD1 and CRTD2 require the presence of exactly one lepton (electron or muon), while SRD1 and SRD2 select events with zero leptons. Two validation regions, VRTD1 and VRTD2 are designed to validate the extrapolation from zero to one lepton.

The preselection criteria of VRTD1 and VRTD2 are the same as the preselection criteria applied to all SRs and reported in Table 7.1. The selections are then further refined to those reported in Table 9.20. These validation regions are made orthogonal to the corresponding signal regions by reverting the cut on $|\Delta\phi\left(\text{non}-\text{b}, b_1\right)|$. The cut on $E_{\text{T}}^{\text{miss}}/\sqrt{H_{\text{T}}}$ is relaxed with respect to the corresponding signal regions in both validation regions. For VRTD1 the cut on $\min\left|\Delta\phi\left(\text{jet}^{\text{VR }1-4}, \text{non}-\text{b}\right)\right|$ is removed to enhance the number of events. An additional cut on $\Delta R\left(b_1, b_2\right)$ is applied to enhance the $t\bar{t}$ population over the single top one. To meet the skim requirments an upper cut on the transverse momentum of the leading b-jet is introduced for VRTD1, this only removes a small number of events as the region naturally prefers this region. Every other signal region cut remains unchanged.

	VRTD1	VRTD2
$\mathrm{N}_{\mathrm{b-jet}}$	exactly 2	≥ 2
$p_{\mathrm{T(non\,b-jet_1)}}$	> 250 GeV	
$\lvert\eta^{b_1}\rvert$	< 1.6	-
$\lvert\eta^{b_2}\rvert$	-	< 1.2
$p_{\mathrm{T}}^{b_1}$	< 200 GeV	< 175 GeV
$\lvert\Delta\phi\,(\mathrm{non-b}, b_1)\rvert$	< 0.8	< 2.0
$\lvert\Delta\phi\,(\mathrm{non-b}, b_2)\rvert$	-	> 2.0
$\mathrm{N}_{\mathrm{b-jet}}^{\mathrm{VR}}$	≥ 1	-
$p_{\mathrm{T}}^{1,\mathrm{VR}}$	< 60 GeV	-
$E_{\mathrm{T}}^{\mathrm{miss}}/\sqrt{H_{\mathrm{T}}}$	$> 18\sqrt{\ \mathrm{GeV}}$	$> 21\sqrt{\ \mathrm{GeV}}$
$\Delta R\,(b_1, b_2)$	> 2.0 rad	-

TABLE 9.20. VRTD1 and VRTD2 selections applied on top of the preselection criteria of Table 7.1.

9.4.2.3. Z + jets validation region for SRA

The Z + jets validation region is defined for the signal region A by inverting the leading $\mathrm{b-tagged}(J_1; \mathrm{R} = 1.2)$ requirement. Table 9.21 shows the VRZA definition, Table 9.22 the observed and expected yields prefit.

Variable	VRZA
$\mathrm{N}_{\mathrm{b-jet}}$	≥ 2
$\mathrm{m}(J_1; \mathrm{R} = 1.2)$	> 120 GeV
$\mathrm{b-tagged}(J_1; \mathrm{R} = 1.2)$	$= 0$
$m_{\mathrm{T}}^{b,\mathrm{min}}$	> 200 GeV
m_{T2,χ^2}	> 450 GeV
Object based $E_{\mathrm{T}}^{\mathrm{miss}}$ sig.	[14, 26]
τ veto	✓

TABLE 9.21. Selection criteria for VRZA in addition to the selection in Table 7.2. VRZA is made orthogonal to SRA by inverting the $\mathrm{b-tagged}(J_1; \mathrm{R} = 1.2)$ requirement.

Diboson	1.89 ± 0.41	(8.84%)
$t\bar{t}$ +W/Z	2.45 ± 0.24	(11.44%)
W + jets	3.54 ± 0.72	(16.50%)
$t\bar{t}$	2.44 ± 0.14	(11.38%)
Z + jets	10.86 ± 0.83	(50.64%)
Single Top	0.26 ± 0.26	(1.21%)
SM	21.44 ± 1.23	(100.00%)
signal-T1100L1	1.97 ± 0.19	(9.21%)
Data	29.00 ± 5.39	$(SF : 1.70 \pm 0.51)$

TABLE 9.22. Yields for VRZA. Only statistical uncertainties are represented in the uncertainties.

9.4.2.4. Z + jets validation regions for SRB

The Z + jets validation region is defined for the signal region B by inverting the $\Delta R\,(b_1, b_2)$ cut. Two bins are defined, one for T0 and one for TTTW, as one expects a different mixture of $g \rightarrow bb$ and scattering diagrams entering T0 and TTTW SRB and so validating them separately is preferable. Table 9.23 shows the VRZB definitions, Tables 9.24 and 9.25 show the observed and expected yields prefit.

Variable	VRZB-T0	VRZB-TTTW
$\mathrm{N_{b-jet}}$	≥ 2	
$\mathrm{m}(J_1; \mathrm{R} = 1.2)$	> 120 GeV	
$m_{\mathrm{T}}^{b,\mathrm{min}}$	> 200 GeV	
m_{T2,χ^2}	< 450 GeV	
Object based $E_{\mathrm{T}}^{\mathrm{miss}}$ sig.	$[15, 17]$	
$\Delta R\,(b_1, b_2)$	< 1.4	
τ veto	✓	
$\mathrm{m}(J_2; \mathrm{R} = 1.2)$	< 60	> 60 GeV

TABLE 9.23. Selection criteria for VRZB in addition to the selection in Table 7.2. VRZB is made orthogonal to SRB by inverting the $\Delta R\,(b_1, b_2)$ requirement.

Diboson	6.20 ± 0.73	(3.73%)
$t\bar{t}$ +W/Z	12.27 ± 0.45	(7.38%)
W + jets	26.12 ± 2.31	(15.71%)
$t\bar{t}$	63.77 ± 1.03	(38.35%)
Z + jets	46.25 ± 3.15	(27.82%)
Single Top	11.67 ± 1.82	(7.02%)
SM	166.28 ± 4.52	(100.00%)
signal-T1100L1	0.30 ± 0.07	(0.18%)
Data	199.00 ± 14.11	$(SF : 1.71 \pm 0.32)$

TABLE 9.24. Yields for VRZB-TTTW. Only statistical uncertainties are represented in the uncertainties.

Diboson	2.43 ± 0.42	(5.87%)
$t\bar{t}$ +W/Z	4.85 ± 0.31	(11.74%)
W + jets	9.37 ± 1.22	(22.66%)
$t\bar{t}$	12.53 ± 0.46	(30.30%)
Z + jets	10.47 ± 0.88	(25.33%)
Single Top	1.70 ± 0.65	(4.11%)
SM	41.35 ± 1.78	(100.00%)
signal-T1100L1	0.64 ± 0.10	(1.56%)
Data	45.00 ± 6.71	$(SF : 1.35 \pm 0.63)$

TABLE 9.25. Yields for VRZB-TTTW. Only statistical uncertainties are represented in the uncertainties.

9.4.2.5. Z + jets validation region for SRD (VRZD)

This section describes the Z validation regions designed to validate the CRDZ0, CRDZ1, and CRDZ2 predictions reported in Section 9.3.4. The CRDZ require the presence of exactly two leptons (electrons or muons), while the SRD select events with zero leptons. The VRDZ are therefore designed to validate the extrapolation from zero to two leptons. The preselection criteria of the VRZD are the same as the preselection criteria applied to all SRs and reported in Table 7.1. The selections are then further specialised to those reported in Table 9.26. VRDZ0 is made orthogonal to SRD0 by reverting and further restricting the cut on $\max\left|\Delta\phi\left(\text{non}-\text{b}, \text{b}^{\text{VR}}\right)\right|$. VRDZ1 and VRDZ2 are made orthogonal to SRD1 by reverting the cut on $|\Delta\phi\left(\text{non}-\text{b}, b_1\right)|$. The cut on $E_{\text{T}}^{\text{miss}}/\sqrt{H_{\text{T}}}$ is relaxed for VRDZ0 and VRDZ2 to enhance the number of events. For VRDZ1 the cut on $\min\left|\Delta\phi\left(\text{jet}^{\text{VR 1-4}}, \text{non}-\text{b}\right)\right|$ is removed to enhance the number of events. For VRDZ2 the cut on $|\Delta\phi\left(\text{non}-\text{b}, b_2\right)|$ is altered to increase the Z + jets population. Other SRD cuts are left unchanged.

	VRDZ0	VRDZ1	VRDZ2
N_{b-jet}	exactly 0	exactly 1	≥ 2
$p_{T(non\,b-jet_1)}$	> 250 GeV		
$\lvert\eta^{b_1}\rvert$	-	< 1.6	-
$\lvert\eta^{b_2}\rvert$	-		< 1.2
$p_T^{b_1}$	-		< 175 GeV
$\lvert\Delta\phi\,(non-b, b_1)\rvert$	-	< 2.2	
$\lvert\Delta\phi\,(non-b, b_2)\rvert$	-		< 2.0
N_{b-jet}^{VR}	≥ 1		-
$p_T^{b_1,VR}$	< 50 GeV	> 10 GeV	-
$p_T^{1,VR}$	-	< 40 GeV	-
$\lvert\eta^{b_1,VR}\rvert$	< 1.2	-	
$\max\lvert\Delta\phi\left(non-b, b^{VR}\right)\rvert$	< 2.0	-	
$\lvert\Delta\phi\left(b_1^{VR}, b_2^{VR}\right)\rvert$	< 2.5	-	
$E_T^{miss}/\sqrt{H_T}$	$> 25\sqrt{\text{ GeV}}$	$> 22\sqrt{\text{ GeV}}$	$> 22\sqrt{\text{ GeV}}$
$\min\lvert\Delta\phi\left(jet^{1-4}, E_T^{miss}\right)\rvert$	> 0.4	-	

TABLE 9.26. Control region selections for the estimation of the Z + jets background in SRD. These requirements are applied in addition to the preselection criteria of Table 7.1.

9.4.3. Other Validation Regions

9.4.3.1. W validation region for SRD (VRWD)

W + jets is a sub-dominant background in all SRD therefore it is taken straight from Monte Carlo. However, it can make up to 13% of the total background therefore the predictions of the Monte Carlo have been checked by building dedicated one-lepton control regions. The preselection criteria of these one-lepton are the same as the preselection criteria reported in Table 9.9. Further than that additional cuts on $\Delta R(b^{VR}, \ell)$ for VRDW0 or $\Delta R(b, \ell)$ for VRDW1 /VRDW2 , and $m(\ell, E_T^{miss})$ are added to enhance the W population. A cut on $\Delta R\,(b_1, b_2)$ is also added for VRDW2 . The cuts on $E_T^{miss}/\sqrt{H_T}$ is relaxed for all regions. The cut on $E_T^{miss,track}$is relaxed for VRDW0 . The cuts

on $|\Delta\phi\,(\text{non}-\text{b}, b_1)|$ and $|\Delta\phi\,(\text{non}-\text{b}, b_2)|$ for VRDW2 are removed. Other SR selections are unchanged. The complete set of selections is in Table 9.27.

	VRDW0	VRDW1	VRDW2
$\text{N}_{\text{b-jet}}$	exactly 0	exactly 1	≥ 2
$\lvert\eta^{b_1}\rvert$	-	< 1.6	-
$\lvert\eta^{b_2}\rvert$	-		< 1.2
$p_{\text{T}}^{b_1}$	-		< 175 GeV
$\text{N}_{\text{b-jet}}^{\text{VR}}$	≥ 1		-
$p_{\text{T}}^{b_1,\text{VR}}$	< 50 GeV	> 10 GeV	-
$p_{\text{T}}^{1,\text{VR}}$	-	< 40 GeV	-
$\lvert\eta^{b_1,\text{VR}}\rvert$	< 1.2	-	
$\max\left\lvert\Delta\phi\left(\text{non}-\text{b}, \text{b}^{\text{VR}}\right)\right\rvert$	> 2.2	-	
$\left\lvert\Delta\phi\left(b_1^{\text{VR}}, b_2^{\text{VR}}\right)\right\rvert$	< 2.5	-	
$\min\left\lvert\Delta\phi\left(\text{jet}^{\text{VR}\,1-4}, \text{non}-\text{b}\right)\right\rvert$	-	> 1.2	-
$E_{\text{T}}^{\text{miss}}/\sqrt{H_{\text{T}}}$	$> 14\sqrt{\text{ GeV}}$	$> 8\sqrt{\text{ GeV}}$	$> 12\sqrt{\text{ GeV}}$
$\min\left\lvert\Delta\phi\left(\text{jet}^{1-4}, E_{\text{T}}^{\text{miss}}\right)\right\rvert$	> 0.4	-	
$E_{\text{T}}^{\text{miss,track}}$	> 30 GeV	-	
$\Delta R(b,\ell)$ $(\Delta R(b^{VR},\ell))$	(< 1.6)	> 1.8	> 2.2
$m(\ell, E_{\text{T}}^{\text{miss}})$	< 120 GeV		< 100 GeV
$\Delta R\,(b_1, b_2)$	-		¡ 1

TABLE 9.27. VRW selections applied on top of the preselection criteria of Table 9.9.

9.4.3.2. $t\bar{t}+Z$ validation region for SRA and SRB

A 2-lepton validation region overlapping with the Z + jets AB TT-TW CR is defined for $t\bar{t}+Z$. The selection effectively selects the tail of the Z + jets AB TT-TW CR at higher mass of the reclustered-jets, i.e. enforces tighter top reconstruction requirements, to enrich the region in $t\bar{t}+Z$. The overlap has been found to be unavoidable to get an acceptable $t\bar{t}+Z$ purity ($\sim$ 30% is achieved), which decreases significantly the validation power of the region. It is nonetheless

used as an internal cross-check of the fit results. Table 9.28 shows the selection, Table 9.29 the observed and expected yields prefit.

Variable	VRABttZ
Leading p_{T}^{ℓ}	> 27 GeV
Subleading p_{T}^{ℓ}	> 20 GeV
$\mathrm{b-tagged}(J_1; \mathrm{R} = 1.2)$	> 0
$E_{\mathrm{T}}^{\mathrm{miss}'}$	> 150 GeV
$\mathrm{N_{jets}}$	≥ 4
$p_{\mathrm{T}}^{j_2}$	> 80 GeV
$p_{\mathrm{T}}^{j_4}$	> 40 GeV
$\mathrm{N_{b-jet}}$	≥ 2
$\mathrm{m}(J_1; \mathrm{R} = 1.2)$	> 80 GeV
Object based $E_{\mathrm{T}}^{\mathrm{miss}'}$ sig.	> 8
$m_{\mathrm{T}}^{b,\mathrm{min}'}$	> 100 GeV
$\mathrm{m}(J_2; \mathrm{R} = 1.2)$	> 60 GeV
$\mathrm{m}(J_1; \mathrm{R} = 1.2)$	> 140 GeV

TABLE 9.28. VRttZ selection.

Diboson	2.95 ± 0.39	(4.96%)
$t\bar{t}$ $+W/Z$	17.94 ± 0.34	(30.16%)
W + jets	0.00 ± 0.00	(0.00%)
$t\bar{t}$	0.81 ± 0.47	(1.36%)
Z + jets	37.53 ± 1.21	(63.10%)
Single Top	0.25 ± 0.25	(0.43%)
SM	59.48 ± 1.42	(100.00%)
signal-T1100L1	0.00 ± 0.00	(0.00%)
Data	54.00 ± 7.35	$(SF : 0.69 \pm 0.40)$

TABLE 9.29. Pre-fit yields of VRttZAB. The SF is defined by the ratio = (Data-$\mathrm{MC}_{t\bar{t}+Z}$)/$\mathrm{MC}_{t\bar{t}+Z}$.

CHAPTER X

SYSTEMATIC UNCERTAINTIES

Systematic uncertainties are associated with the predictions of all background components and the expected signal yields, and are evaluated in accordance with the ATLAS SUSY Working Group recommendations. The systematic uncertainties can be categorized into two sources: experimental uncertainties due to detector-related effects and theoretical uncertainties due to modeling of physics processes. These systematic uncertainties can impact the expected event yields in the control and signal regions as well as the transfer factors used when extrapolating the background expectation from the control regions to the signal regions.

In addition to the list of systematic uncertainties below, the MC statistical uncertainty will be treated as an additional systematic uncertainty in each bin. To minimize this uncertainty, the analysis uses 'sliced' samples enriched in desired physics.

10.1. Experimental Uncertainties

The following list describes the sources of detector-related uncertainties considered.

Jet Energy Scale (JES) The two main source of uncertainties for jets are uncertainties affecting the calibration of the energy scale (JES) and resolution (JER). The final jet energy scale calibration, generally referred as JES, is a correction relating the calorimeter's response to the true jet energy. The JES uncertainty is derived in bins of p_{T} and η from different in-situ techniques [31] by the Jet/EtMiss group; documentation of the Run 2 JES is in preparation,

preliminary documentation is available in [31]. These variations, up and down, are estimated via the JETUncertainties tool. Uncertainties related to flavor composition and pile-up are included. Following the recommendations from the Jet/EtMiss group, split-JES components are employed in order to reduce the total JES by the proper correlations of the components. It is possible to use the full list of nuisance parameters (77 components) or a strongly reduced configuration of 4 nuisance parameters; the four strongly reduced configurations are used after some investigations and checks, following the Jet/EtMiss and SUSY recommendations.

Jet Energy Resolution (JER) The JER uncertainty is derived as one-side variation by comparing data to MC simulation via the transverse momentum balance between a jet and a reference object such as a photon, Z boson, or multi-jet system in data [31]. The variation in this analysis is estimated by smearing all jets momenta in simulation events with the JetResolution tool, so-called 'SimpleJER' configuration.

Jet Vertex Tagger The uncertainties due to the mistag rate of the pileup suppression algorithm (mistakenly tagging hard scattering jets) is evaluated using the JetJvtEfficiency tool. These uncertainties also take the impact of the MC generator choice into account.

b-tagging The b-tagging uncertainty has some contribution to both signal and backgrounds because of the two b-tagged jets requirement. Scale factor uncertainties in b-tagging are derived by the flavor-tagging working group [120], depending on the kinematics of the jet and the jet flavor. A

reduced nuisance parameter set scheme ('Envelope') is considered, following the preliminary recommendations from the 3G combination group.

$E_{\mathrm{T}}^{\mathrm{miss}}$ *Soft-term Resolution and Scale* The scale and resolution uncertainties of individual objects is propagated to all $E_{\mathrm{T}}^{\mathrm{miss}}$-based variables via the METUtilities tool. Specific systematic uncertainties on the scale and resolution of the $E_{\mathrm{T}}^{\mathrm{miss}}$ soft term have been derived by two different in-situ methods using $Z \to \mu\mu$ events [121] and are considered.

Lepton efficiencies Lepton reconstruction and identification efficiencies have contributions to the backgrounds. For electrons, the uncertainties originate from the e/γ resolution and scale and from the electron reconstruction efficiency. Similarly for muons the uncertainties originate from the muon resolution and reconstruction efficiency, the isolation and the momentum scale. The lepton trigger scale factors are also taken into consideration.

Pileup The uncertainty due to pileup re-weighting of the MC samples is considered as two-sided variation in the event weights. The uncertainties on the $\langle\mu\rangle$ scaling are evaluated changing the nominal re-scaling (1/1.03) to 1.00 and 1/1.18 (SUSYTools default). The interval covers the full difference between applying and not-applying the correction as well as uncertainty on the luminosity measurement, which is expected to dominate.

10.2. SM Background Theoretical Uncertainties

Theory uncertainties affecting the background normalization and kinematic distribution shapes largely impact the background prediction in the signal regions, as they directly affect the background normalization and acceptance

times efficiency. If a background normalization is determined by making use of dedicated control regions, then only systematics affecting the analysis acceptance are relevant. Statistical uncertainties in the evaluation of systematics are neglected in general; where necessary, selection cuts are loosened to make the systematic comparison statistically meaningful. The remainder of this section is dedicated to the discussion on how the theory systematic uncertainties have been derived for each of the background processes considered.

The theoretical uncertainty in each signal region is evaluated by considering variations with respect the default settings and choices for the event generation. For each of the variations considered, the systematic uncertainty is estimated as an uncertainty on the so-called transfer factor, that is, the ratio of the predicted yields between the signal region and the control region(s), in case the normalization of the background is a free parameter in the fit. In case it is not, then the systematic uncertainty is estimated as a normalization uncertainty of the background yield in the signal region.

Uncertainties in each background from scale variations are fully correlated across regions and bins, and uncorrelated between processes. In some cases this may result in the cancellation of uncertainties, while the higher order corrections may not cancel. An alternative fit configuration considering scale variations uncorrelated in all bins will be run to cross check the impact of this assumption.

W/Z + jets *modeling uncertainties* Uncertainties due to the following modeling factors are investigated, as described in Refererence [114]. The matrix element matching scale (ckkw) between jets from the matrix element and the parton shower is varied between 15 GeV and 30 GeV (the nominal value is 20 GeV). The renormalization scale (renorm), the factorisation scale (fac) used for the

parton density functions (PDFs), and the resummation scale for soft gluon emission (qsf) is varied by a factor of 2 and 1/2 each with respect to the nominal value. PDF uncertainties are expected to be small and therefore not considered.The modelling of V plus heavy flavour jets is very difficult. There are significant discrepancies of cross sections between Sherpa 2.2 and MG5_aMC@NLO+Py8 CKKW-L B [122]. The effect on requirements of different heavy flavour jets in W+jets control region and SRBT0 has been confirmed. Therefore, an additional uncertainty in the transfer factor is considered for W + jets, which is normalized in a one-b-tag region and extrapolated to the two-b-tag SRs. The nominal fit configuration treats the different variations as independent nuisance parameters, as recommended by the SUSY group. As a cross-check, the fit is rerun considering a single NP corresponding to the envelope of the variations described above.

$t\bar{t}$ modeling uncertainties Uncertainties due to the modeling of the hard scatter, parton shower, initial state radiation (ISR), final state radiation (FSR), and PDF are considered. Alternative $t\bar{t}$ simulation samples were generated using Powheg interfaced to Herwig 7 [112] and aMC@NLO [37] interfaced to Pythia 8 with the A14 tune. The effects of initial and final state radiation (ISR, FSR) were explored by reweighting the baseline $t\bar{t}$ events in a way that reduces (reduces and increases for FSR) parton shower radiation [113] and by using an alternative Powheg + Pythia sample with h_{damp} set to $3m_{\mathrm{top}}$ and tune parameter Var3 increased, leading to increased ISR. These alternative $t\bar{t}$ samples were simulated using fast-simulation.

single top modeling uncertainties In addition to the uncertainties listed for $t\bar{t}$ modeling, the uncertainty on the interference of Wt with $t\bar{t}$ is evaluated by comparing the 'DS' with 'DR' sample.

$t\bar{t}+\mathrm{X}$ *modeling uncertainties* ISR and FSR uncertainties on the $t\bar{t}+Z$ process are obtained from dedicated samples, varying the Var3c parameter (α_{s}) of the A14 tune used in the nominal aMC@NLO $t\bar{t}+Z$ sample.No other alternative sample being available, the generator and parton-shower systematics are estimated from a standard 6-point (factor 2 up and down) variation of the renormalization and factorization scales.

other physics processes The systematic uncertainties due to di-boson are expected to be sub-dominant and therefore not considered.

10.3. Multi-jet Uncertainties

Uncertainties on the multi-jet background estimated via `JetSmearing` are provided by varying the seed selection and propagating this through the $\Delta\Phi$ corrections.

- `QCDSeedSelValue`: variations on the cut value on $E_{\mathrm{T}}^{\mathrm{miss}}$sig. when selecting seed events. Central value is < 0.1, up variation is < 0.05 and the down variation is < 0.2.
- `QCDSeedMValue`: variation on the definition of $E_{\mathrm{T}}^{\mathrm{miss}}\mathrm{sig.} = \frac{E_{\mathrm{T}}^{\mathrm{miss}}-M}{\sqrt{E_T}}$. The central definition is with the parameter $M = 8$. The variation is with $M = 0$.
- `QCDNormalisation`: flat 30% uncertainty dervied from the normalisation of the multi-jet background in the CRs plus some added conservatism.

10.4. Signal Theory Systematics

Three classes of signal systametics are studied in the context of stop models: factorization and renormalization scale (sc), merging scale of the MadGraph+Pythia8 xqcut (qc), and initial state radiation α_s^{ISR} (var3c). The analysis is emulated in the Simple Analysis framework and uses Truth information to calculate yields (acceptance). Due to limitations in the truth-based framework, some variables are not defined and are 'folded' into an additional uncertanty, namely the tau veto in SRAB, as well as the track-based variables in SRC. The uncertainty is taken as the relative percentage difference in signal yields when applying the full selection versus the folded selection,

$$\sigma_{Fold} = \frac{N_{Fold} - N_{Full}}{N_{Full}}. \tag{10.1}$$

For SRD, VR track jets are not emulated in the framework and the folded uncertainty is estimated to a flat 20%.

The benchmarks selected for the study were T1100L1 (SRA), T800L400 (SRB), T225L52 (SRC1-2), T500L327 (SRC3-5), and T400L380 (SRD). The total uncertainty is the sum in quadrature of the three variations considered, using the largest uncertainty between up/down variations, and the folding uncertainty.

Sample	**Region**	**SC**	**QC**	**VAR3C**	**Folding**	**Uncertainty**
T1100L1	SRA	1.4%	0.9%	1.1%	4.8%	5.2%
T800L400	SRA	4.6%	4.3%	3.6%	9.3%	11.8%
T500L327	SRC	1.3%	7.0%	7.2%	8.5%	13.2%
T400L380	SRD	13.3%	4.2%	1.8%	20.0%	24.5%

TABLE 10.1. Signal systematics relative uncertainties. For each variation, the uncertainty associated with the worst of the up/down variations is used. The sc, qc, var3c, and folding uncertainties are added in quadrature.

10.4.0.1. SRA: T1100L1

Sample	Region	Variation	Raw Yield	Acc*Eff	Error	Uncertainty
T1100L1	SRA	Nominal	1636	0.0548	0.0014	-
T1100L1	SRA	qcDown	51254	0.0543	0.0002	-0.76%
T1100L1	SRA	qcUp	54292	0.0543	0.0002	-0.9%
T1100L1	SRA	scDown	48525	0.054	0.0002	-1.39%
T1100L1	SRA	scUp	48552	0.0541	0.0002	-1.27%
T1100L1	SRA	var3cDown	51351	0.0541	0.0002	-1.13%
T1100L1	SRA	var3cUp	54333	0.0544	0.0002	-0.6%
T1100L1	SRATT	Nominal	551	0.0184	0.0008	-
T1100L1	SRATT	qcDown	18845	0.0198	0.0001	7.83%
T1100L1	SRATT	qcUp	19855	0.0198	0.0001	7.86%
T1100L1	SRATT	scDown	17664	0.0196	0.0001	6.77%
T1100L1	SRATT	scUp	17947	0.0199	0.0001	8.18%
T1100L1	SRATT	var3cDown	18998	0.02	0.0001	8.76%
T1100L1	SRATT	var3cUp	19894	0.0198	0.0001	7.83%
T1100L1	SRATW	Nominal	338	0.0113	0.0006	-
T1100L1	SRATW	qcDown	9688	0.0103	0.0001	-8.91%
T1100L1	SRATW	qcUp	10560	0.0106	0.0001	-6.85%
T1100L1	SRATW	scDown	9306	0.0103	0.0001	-8.65%
T1100L1	SRATW	scUp	9193	0.0102	0.0001	-9.62%
T1100L1	SRATW	var3cDown	9964	0.0105	0.0001	-7.25%
T1100L1	SRATW	var3cUp	10479	0.0105	0.0001	-7.31%
T1100L1	SRAT0	Nominal	649	0.0216	0.0008	-
T1100L1	SRAT0	qcDown	19618	0.0207	0.0001	-4.17%
T1100L1	SRAT0	qcUp	20362	0.0203	0.0001	-5.87%
T1100L1	SRAT0	scDown	18513	0.0206	0.0002	-4.64%
T1100L1	SRAT0	scUp	18447	0.0205	0.0002	-5.17%
T1100L1	SRAT0	var3cDown	19342	0.0204	0.0001	-5.67%
T1100L1	SRAT0	var3cUp	20490	0.0205	0.0001	-5.26%
Sample	**Region**	**Region**	**Full Yield**	**Folded Yield**	**Error**	**Uncertainty**
T1100L1	SRA	Folding	24.41	25.58	-	4.77%
T1100L1	SRATT	Folding	8.62	9.03	-	4.66%
T1100L1	SRATW	Folding	5.1	5.39	-	5.63%
T1100L1	SRAT0	Folding	9.24	9.64	-	4.35%

TABLE 10.2. Signal systematics yields, acceptance, and relative uncertainties using the Simple Analysis framework. The signal grid benchmark used is T1100L1. Note that for folding the weighted yields of full/folded selections are shown.

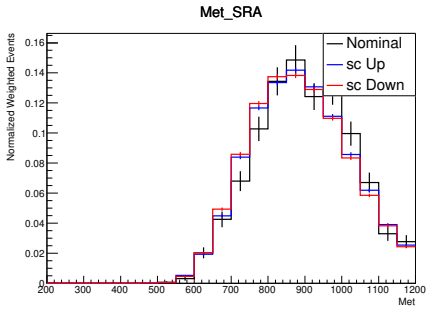

(a) $E_{\mathrm{T}}^{\mathrm{miss}}$

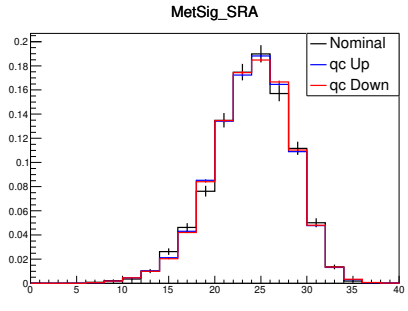

(b) Object based $E_{\mathrm{T}}^{\mathrm{miss}}$ sig. $>$ 14, SRA extrapolation

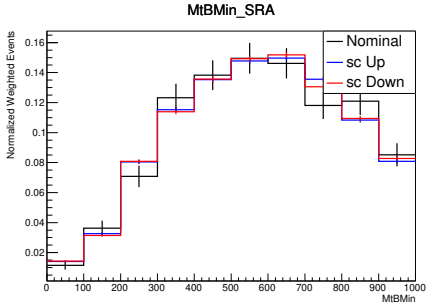

(c) $m_{\mathrm{T}}^{b,\mathrm{min}}$ $>$ 150 GeV, SRA and SRB extrapolation

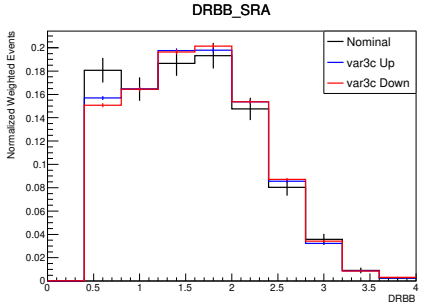

(d) $\Delta R\,(b,b)$is used to increase $t\bar{t}$ purity, SRA extrapolation

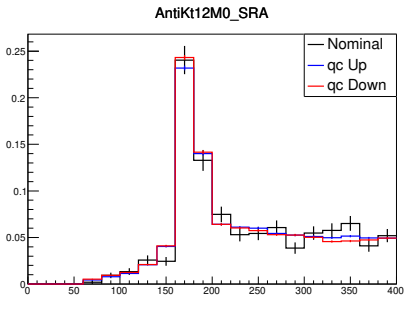

(e) m(J_1; R = 1.2)

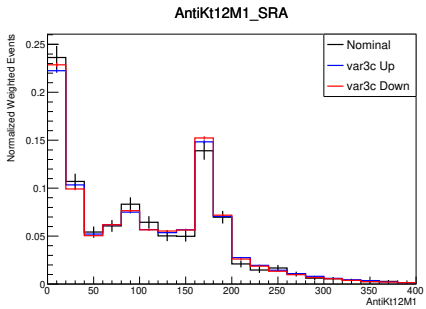

(f) m(J_2; R = 1.2)

FIGURE 10.1. N-1 distributions of variables used in SRA for various systematic variations to signal samples. A T1100L1 sample was used to as a benchmark for all three SRA categories.

10.4.0.2. SRB: T800L400

Sample	Region	Variation	Raw Yield	Acc*Eff	Error	Uncertainty
T800L400	SRB	Nominal	784	0.0261	0.0009	-
T800L400	SRB	qcDown	25272	0.0266	0.0002	1.7%
T800L400	SRB	qcUp	27271	0.0273	0.0002	4.29%
T800L400	SRB	scDown	26858	0.0269	0.0002	2.83%
T800L400	SRB	scUp	27449	0.0274	0.0002	4.64%
T800L400	SRB	var3cDown	25238	0.0266	0.0002	1.73%
T800L400	SRB	var3cUp	25776	0.0271	0.0002	3.56%
T800L400	SRBTT	Nominal	233	0.0078	0.0005	-
T800L400	SRBTT	qcDown	8285	0.0088	0.0001	12.15%
T800L400	SRBTT	qcUp	9115	0.0091	0.0001	16.31%
T800L400	SRBTT	scDown	8886	0.0089	0.0001	13.16%
T800L400	SRBTT	scUp	8960	0.009	0.0001	15.08%
T800L400	SRBTT	var3cDown	8173	0.0086	0.0001	9.82%
T800L400	SRBTT	var3cUp	8500	0.009	0.0001	15.01%
T800L400	SRBTW	Nominal	253	0.0084	0.0005	-
T800L400	SRBTW	qcDown	7489	0.0079	0.0001	-5.89%
T800L400	SRBTW	qcUp	8145	0.0081	0.0001	-2.67%
T800L400	SRBTW	scDown	7958	0.008	0.0001	-4.74%
T800L400	SRBTW	scUp	8263	0.0082	0.0001	-1.82%
T800L400	SRBTW	var3cDown	7610	0.008	0.0001	-4.16%
T800L400	SRBTW	var3cUp	7771	0.0081	0.0001	-2.89%
T800L400	SRBT0	Nominal	298	0.0099	0.0006	-
T800L400	SRBT0	qcDown	9497	0.0099	0.0001	-0.18%
T800L400	SRBT0	qcUp	10010	0.01	0.0001	0.64%
T800L400	SRBT0	scDown	10013	0.01	0.0001	1.04%
T800L400	SRBT0	scUp	10226	0.0101	0.0001	1.83%
T800L400	SRBT0	var3cDown	9454	0.01	0.0001	0.29%
T800L400	SRBT0	var3cUp	9505	0.0099	0.0001	-0.06%
Sample	**Region**	**Region**	**Full Yield**	**Folded Yield**	**Error**	**Uncertainty**
T800L400	SRB	Folding	97.15	106.23	-	9.34%
T800L400	SRBTT	Folding	29.12	31.13	-	6.88%
T800L400	SRBTW	Folding	31.03	34.09	-	9.88%
T800L400	SRBT0	Folding	37.0	41.0	-	10.82%

TABLE 10.3. Signal systematics yields, acceptance, and relative uncertainties using the Simple Analysis framework. The signal grid benchmark used is T800L400. Note that for folding the weighted yields of full/folded selections are shown.

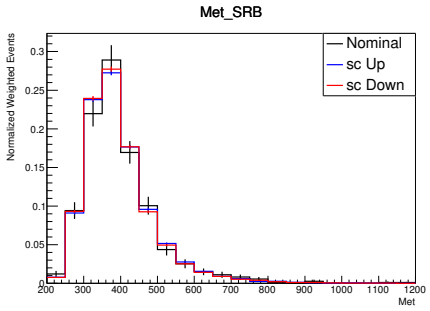

(a) $E_{\mathrm{T}}^{\mathrm{miss}}$

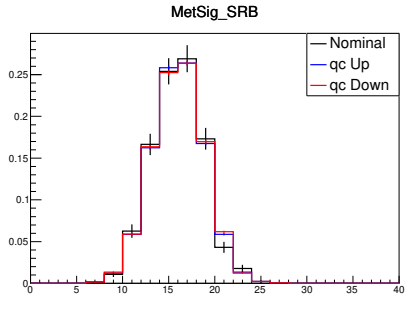

(b) Object based $E_{\mathrm{T}}^{\mathrm{miss}}$ sig. $>$ 14, SRB extrapolation

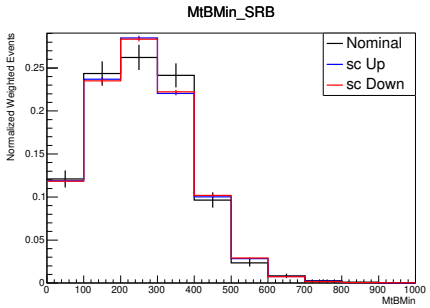

(c) $m_{\mathrm{T}}^{b,\mathrm{min}}$ $>$ 150 GeV, SRB and SRB extrapolation

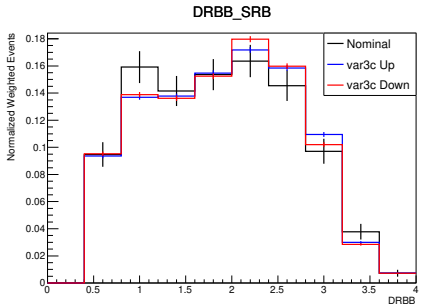

(d) $\Delta R\,(b,b)$is used to increase $t\bar{t}$ purity, SRB extrapolation

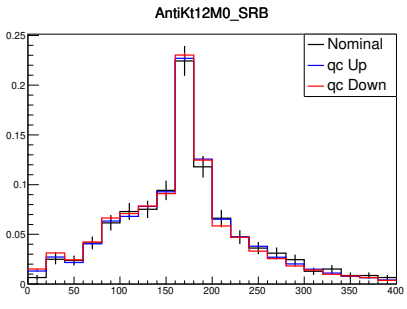

(e) m(J_1; R = 1.2)

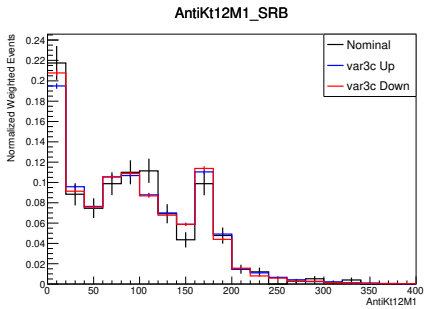

(f) m(J_2; R = 1.2)

FIGURE 10.2. N-1 distributions of variables used in SRB for various systematic variations to signal samples. A T800L400 sample was used to as a benchmark for all three SRB categories.

10.4.0.3. SRC: T500L327 and T225L52

Sample	Region	Variation	Raw Yield	Acc*Eff	Error	Uncertainty
T225L52	SRC1	Nominal	268	0.0001	0.0	-
T225L52	SRC1	qcDown	295	0.0001	0.0	-0.78%
T225L52	SRC1	qcUp	254	0.0001	0.0	-3.79%
T225L52	SRC1	scDown	276	0.0001	0.0	-6.27%
T225L52	SRC1	scUp	291	0.0001	0.0	16.74%
T225L52	SRC1	var3cDown	249	0.0001	0.0	-5.74%
T225L52	SRC1	var3cUp	267	0.0001	0.0	9.3%
T225L52	SRC2	Nominal	146	0.0	0.0	-
T225L52	SRC2	qcDown	124	0.0	0.0	-22.25%
T225L52	SRC2	qcUp	130	0.0	0.0	-8.43%
T225L52	SRC2	scDown	142	0.0	0.0	-9.72%
T225L52	SRC2	scUp	107	0.0	0.0	-16.77%
T225L52	SRC2	var3cDown	109	0.0	0.0	-21.32%
T225L52	SRC2	var3cUp	130	0.0	0.0	0.93%
T500L327	SRC3	Nominal	752	0.0006	0.0	-
T500L327	SRC3	qcDown	767	0.0006	0.0	-4.91%
T500L327	SRC3	qcUp	733	0.0006	0.0	-9.53%
T500L327	SRC3	scDown	833	0.0006	0.0	-4.73%
T500L327	SRC3	scUp	630	0.0006	0.0	-3.58%
T500L327	SRC3	var3cDown	718	0.0006	0.0	-8.0%
T500L327	SRC3	var3cUp	624	0.0006	0.0	-1.28%
T500L327	SRC4	Nominal	1430	0.0012	0.0	-
T500L327	SRC4	qcDown	1523	0.0011	0.0	-0.83%
T500L327	SRC4	qcUp	1427	0.0011	0.0	-5.83%
T500L327	SRC4	scDown	1628	0.0011	0.0	-1.82%
T500L327	SRC4	scUp	1240	0.0012	0.0	0.5%
T500L327	SRC4	var3cDown	1381	0.0011	0.0	-5.71%
T500L327	SRC4	var3cUp	1263	0.0012	0.0	4.22%
T500L327	SRC5	Nominal	132	0.0001	0.0	-
T500L327	SRC5	qcDown	141	0.0001	0.0	-0.72%
T500L327	SRC5	qcUp	135	0.0001	0.0	-2.03%
T500L327	SRC5	scDown	161	0.0001	0.0	5.85%
T500L327	SRC5	scUp	110	0.0001	0.0	-3.85%
T500L327	SRC5	var3cDown	123	0.0001	0.0	-5.97%
T500L327	SRC5	var3cUp	113	0.0001	0.0	1.06%
Sample	**Region**	**Uncertainty**	**Full Yield**	**Folded Yield**	**Error**	**Uncertainty**
T500L327	SRC	Folding	51.19	55.54	-	8.5%
T225L52	SRC1	Folding	123.72	180.15	-	45.60%
T225L52	SRC2	Folding	27.77	37.67	-	35.64%
T500L327	SRC3	Folding	14.96	15.69	-	4.92%
T500L327	SRC4	Folding	28.62	30.92	-	8.05%
T500L327	SRC5	Folding	4.97	5.21	-	4.77%

TABLE 10.4. Signal systematics yields, acceptance, and relative uncertainties using the Simple Analysis framework. The signal grid benchmark used is T500L327 for SRC3-5 and T225L52 for SRC1-2. Note that for folding the weighted yields of full/folded selections are shown.

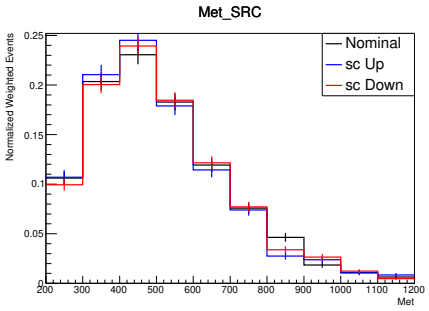

(a) $E_{\mathrm{T}}^{\mathrm{miss}}$

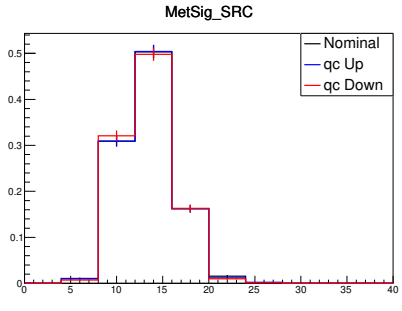

(b) Object based $E_{\mathrm{T}}^{\mathrm{miss}}$ sig. $>$ 14, SRC extrapolation

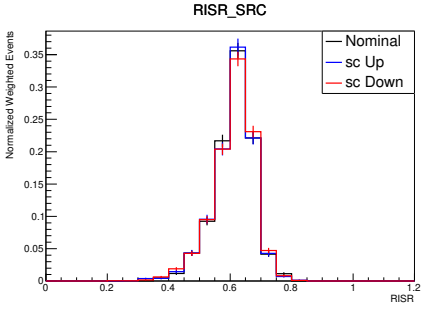

(c) $m_{\mathrm{T}}^{b,\mathrm{min}}$ $>$ 150 GeV, SRC and SRB extrapolation

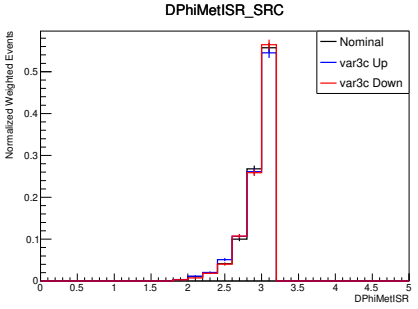

(d) $\Delta R\,(b,b)$is used to increase $t\bar{t}$ purity, SRC extrapolation

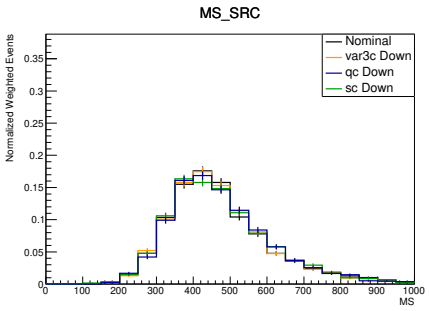

(e) m(J_1; R = 1.2)

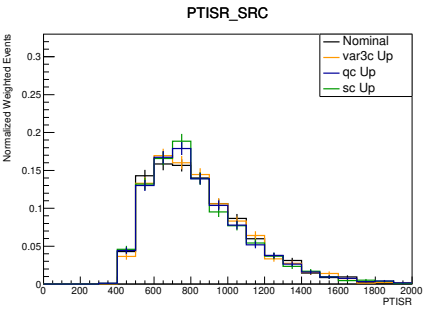

(f) m(J_2; R = 1.2)

FIGURE 10.3. N-1 distributions of variables used in SRC for various systematic variations to signal samples. A T500L400 sample was used to as a benchmark for SRC4-5 categories.

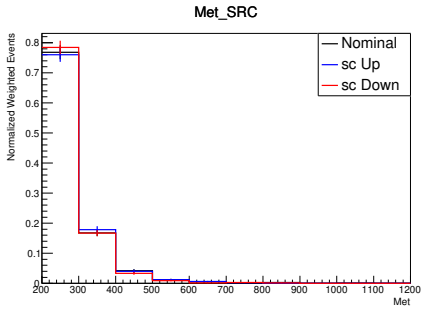

(a) $E_{\mathrm{T}}^{\mathrm{miss}}$

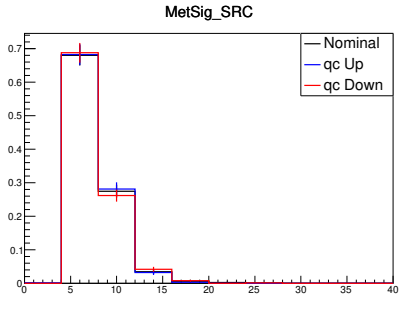

(b) Object based $E_{\mathrm{T}}^{\mathrm{miss}}$ sig. $>$ 14, SRC extrapolation

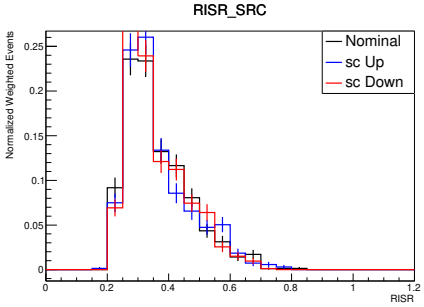

(c) $m_{\mathrm{T}}^{b,\mathrm{min}}$ $>$ 150 GeV, SRC and SRB extrapolation

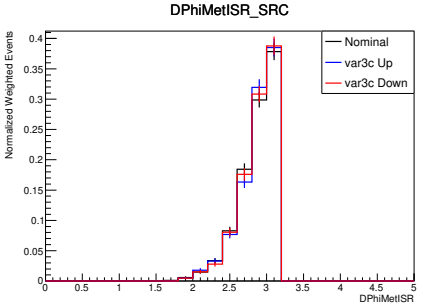

(d) $\Delta R\,(b,b)$is used to increase $t\bar{t}$ purity, SRC extrapolation

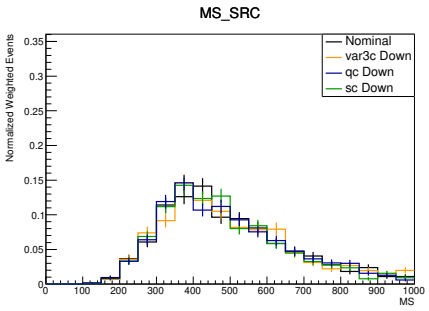

(e) m$(J_1;\mathrm{R}=1.2)$

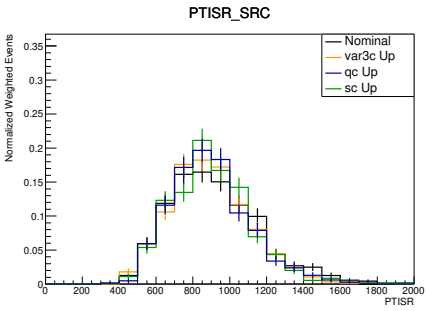

(f) m$(J_2;\mathrm{R}=1.2)$

FIGURE 10.4. N-1 distributions of variables used in SRC for various systematic variations to signal samples. A T225L52 sample was used to as a benchmark for SRC1-3 categories.

10.4.0.4. SRD: T400L380

Sample	Region	Variation	Raw Yield	Acc*Eff	Error	Uncertainty
T400L380	SRD	Nominal	4713	0.0097	0.0001	-
T400L380	SRD	qcDown	975	0.0093	0.0003	-4.24%
T400L380	SRD	qcUp	924	0.0097	0.0003	0.28%
T400L380	SRD	scDown	1022	0.0097	0.0003	0.07%
T400L380	SRD	scUp	1013	0.011	0.0004	13.25%
T400L380	SRD	var3cDown	966	0.0099	0.0003	1.39%
T400L380	SRD	var3cUp	935	0.0099	0.0003	1.79%
T400L380	SRD0	Nominal	1573	0.0033	0.0001	-
T400L380	SRD0	qcDown	329	0.0031	0.0002	-4.8%
T400L380	SRD0	qcUp	298	0.0031	0.0002	-4.09%
T400L380	SRD0	scDown	368	0.0035	0.0002	6.39%
T400L380	SRD0	scUp	345	0.0039	0.0002	17.92%
T400L380	SRD0	var3cDown	306	0.0031	0.0002	-5.09%
T400L380	SRD0	var3cUp	331	0.0036	0.0002	10.77%
T400L380	SRD1	Nominal	2725	0.0056	0.0001	-
T400L380	SRD1	qcDown	568	0.0054	0.0002	-2.67%
T400L380	SRD1	qcUp	555	0.0059	0.0002	4.89%
T400L380	SRD1	scDown	581	0.0055	0.0002	-0.51%
T400L380	SRD1	scUp	580	0.0062	0.0003	10.53%
T400L380	SRD1	var3cDown	580	0.0059	0.0002	6.13%
T400L380	SRD1	var3cUp	519	0.0054	0.0002	-4.01%
T400L380	SRD2	Nominal	415	0.0009	0.0	-
T400L380	SRD2	qcDown	78	0.0008	0.0001	-12.2%
T400L380	SRD2	qcUp	71	0.0008	0.0001	-12.89%
T400L380	SRD2	scDown	73	0.0007	0.0001	-20.28%
T400L380	SRD2	scUp	88	0.001	0.0001	13.1%
T400L380	SRD2	var3cDown	80	0.0008	0.0001	-4.62%
T400L380	SRD2	var3cUp	85	0.0009	0.0001	5.19%
Sample	**Region**	**Region**	**Full Yield**	**Folded Yield**	**Error**	**Uncertainty**
T400L380	SRD0	Folding	36.39	320.11	-	N/A
T400L380	SRD1	Folding	12.87	157.12	-	N/A
T400L380	SRD2	Folding	10.55	43.45	-	N/A

,

TABLE 10.5. Signal systematics yields, acceptance, and relative uncertainties using the Simple Analysis framework. The signal grid benchmark used is T400L380. Note that for folding the weighted yields of full/folded selections are shown.

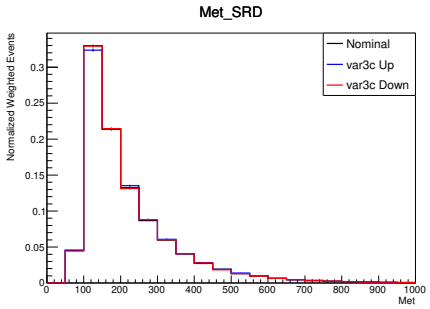

(a) $E_{\mathrm{T}}^{\mathrm{miss}}$

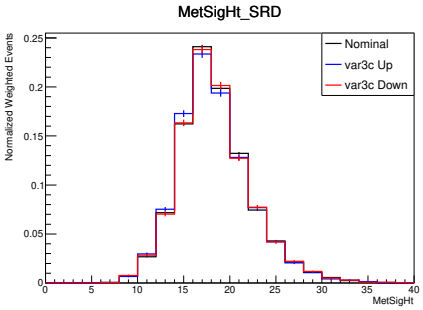

(b) Ht-based $E_{\mathrm{T}}^{\mathrm{miss}}$significance

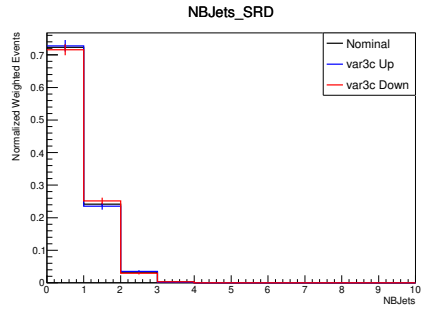

(c) Number of b-tagged R=0.4 anti-kt jets

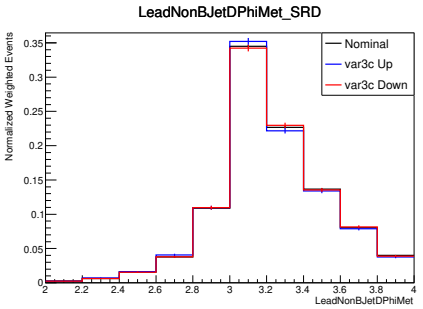

(d) Angular separation between leading non-b-tagged jet and $E_{\mathrm{T}}^{\mathrm{miss}}$

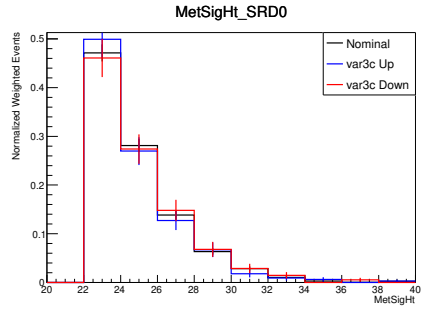

(e) Ht-based $E_{\mathrm{T}}^{\mathrm{miss}}$significance is loosed $26 \rightarrow 22$ for SRD0

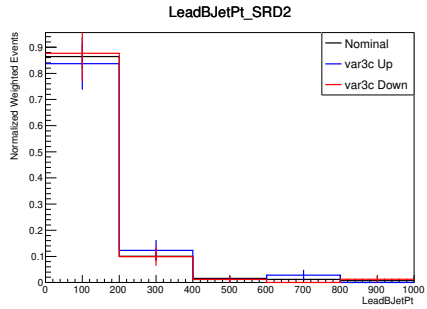

(f) Leading b-tagged Jet p_{T}

FIGURE 10.5. N-1 distributions of variables used in SRD for various systematic variations to signal samples. A T400L380 sample was used as a benchmark for SRD0-2 categories.

CHAPTER XI

RESULTS

The previous chapters detail the strategy of optimizing the signal region and estimating their associated backgrounds. Typically, the normalizations of MC simulation to data need to be adjusted. These normalizations (transfer factors) are derived from data-MC studies in the CRs and transferred to the SRs; since the CRs are far away (in phase-space) from the SRs, an uncertainty on the transfer factor is measured and added in quadrature to the statistical uncertainty. In cases where the background process has a stable transfer factor with respect to any observable present in the CR (and SR), the normalization can be derived from a single-bin region (e.g. $t\bar{t}$ CR for all SRA and SRB categories). If the transfer factor is dependent on such an observable (e.g. subleading reclustered jet mass suggests multiple bins for CRZAB), then the CR is split into multiple sub-regions with stable transfer factors.

The transfer factors can be defined to first order in a single Control Region as the difference in data from non-target MC background yields, divided by the target background MC yield.

$$T = \frac{N_{Data} - N_{Non-TargetBG}}{N_{TargetBG}} \tag{11.1}$$

In an ideal case, there is no non-target BG contamination and the ratio is exactly a normalization between data/MC. In practice, each Control Region bears some amount of contamination from background processes other than the target. Therefore, the transfer factors can be calculated in each CR as-is (pre-fit), or one can perform a simultaneous fit to all floating unknowns (transfer factors) across

all BGs. This fit is colloquially referred to as a 'background-only fit', since it assumes that no signal is present in the (control) regions where the normalizations are calculated. The final normalizations and yields (results) are derived using the HistFitter framework, v.0.62.0. [123]

In this dissertation, I focused on estimating the $t\bar{t}$ background to SRA and SRB categories. The fit is performed combining Signal Regions A and B, described in Sections 8.1. Two more separate fits are performed for regions C and D, focusing on their respective scenarios, but are not included in this dissertation. Since the results presented are currently being analyzed within the ATLAS Collaboration, much of the data information has been omitted.

The correlation matrix between systematics is shown in Figure 11.1. The transfer factor dependence on the systematics is presented in Figure 11.2.

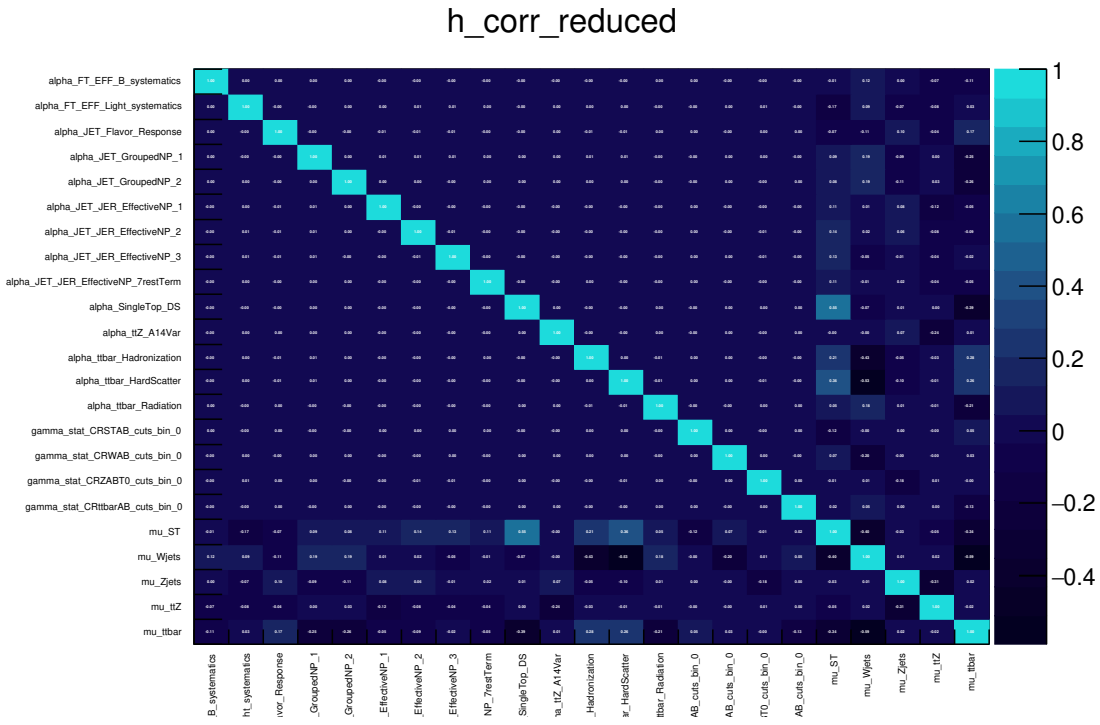

FIGURE 11.1. Correlation matrix for the background only fit performed on region A and region B

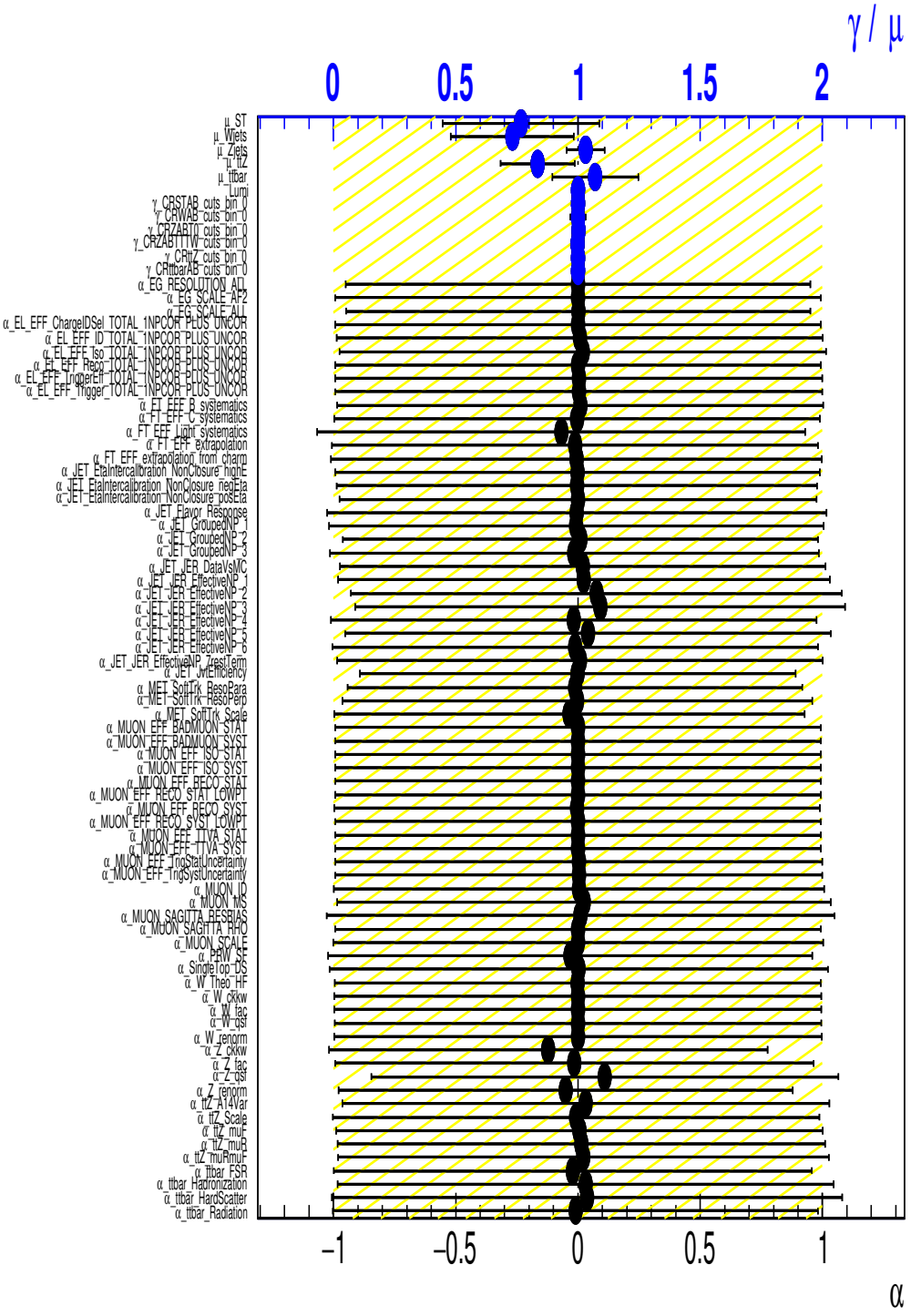

FIGURE 11.2. Fit parameters for the combined fit performed on regions A and B.

11.1. Data Blinding

The process of providing a measurement by analyzing the *data* with well-studied MC-based regions is called *unblinding*. Before this step, all optimizations and studies are done entirely through simulation. Once the analysis regions are fully defined, then the analysis team can request approval from the relevant working groups to observe the data.

The ATLAS Collaboration publishes results as a cohesive unit. The analysis presented in this dissertation is performed by a team of many physicists from a number of institutions, and the final publication must be approved by the collaboration through a series of internal checkpoints. At the time of writing this dissertation, the analysis is not yet fully approved and thus this document cannot provide the plots in full. This document abides by ATLAS guidelines for unpublished ATLAS data to be used in dissertations.

11.2. RegionAB Fit

SRA and SRB are both fit simultaneously with the same combined configuration. The control region strategy used to normalize the various backgrounds is summarized in Table 11.1. The normalization factors were checked in dedicated validation regions and is summarized by Table 11.2.

Sample	Parameters	Regions normalized
$t\bar{t}$	$\mu_{t\bar{t}}$	CRttbarAB
W+jets	μ_{Wjets}	CRWAB
Z+jets	μ_{Zjets}	CRZABT0,CRZAB-TT-TW (single scaling parameter)
Single top	μ_{ST}	CRSTAB
$t\bar{t}$ $+Z$	$\mu_{t\bar{t}+Z}$	CRttZAB

TABLE 11.1. Control region strategy for Signal Regions A and B. All of the parameters are simultaneously fit.

Sample	Region(s)
$t\bar{t}$	VRttbarAB
Z+jets	VRZA, VRZB-T0, VRZB-TT-TW

TABLE 11.2. Validation region strategy for Signal regions A and B

Since this dissertation focuses on the author's contribution to the analysis, namely understanding the $t\bar{t}$ background, only the post-fit yields for the relevant regions are listed below. Table 11.3 shows the expected yields for the $t\bar{t}$ control region for SRA and SRB, whereas Table 11.4 lists the expected yields for the complementary validation region.

CRttbarAB	**Number of Events**
Observed events	246
Fitted bkg events	245.98 ± 15.68
Fitted Z events	1.18 ± 0.19
Fitted st events	25.72 ± 14.98
Fitted ttbar events	183.12 ± 23.89
Fitted ttZ events	3.84 ± 0.77
Fitted W events	24.78 ± 8.69
Fitted QCD events	0.00 ± 0.00
Fitted group_ZW_WW_ZZ events	2.62 ± 1.70
Fitted group_tZ_tWZ_ttX events	4.71 ± 0.44
MC exp. SM events	251.92
MC exp. Z events	1.14
MC exp. st events	33.64
MC exp. ttbar events	171.18
MC exp. ttZ events	4.55
MC exp. W events	33.96
data-driven exp. QCD events	0.00
MC exp. group_ZW_WW_ZZ events	2.75
MC exp. group_tZ_tWZ_ttX events	4.71

TABLE 11.3. Background-only fit results for the control regions CRttbarAB, corresponding to an 139 fb^{-1}. The errors shown are the statistical plus systematic uncertainties, except for the error on the background estimate in the control region, which is the systematic uncertainty only. Uncertainties are symmetrized where appropriate, and the negative error truncated when reaching zero event yield.

VRttbarAB	Number of Events
Observed events	589
Fitted bkg events	578.68 ± 62.14
Fitted Z events	69.92 ± 7.62
Fitted st events	17.84 ± 15.23
Fitted ttbar events	447.55 ± 68.57
Fitted ttZ events	16.92 ± 3.15
Fitted W events	15.61 ± 5.76
Fitted QCD events	0.00 ± 0.00
Fitted group_ZW_WW_ZZ events	0.00 ± 0.00
Fitted group_tZ_tWZ_ttX events	0.00 ± 0.00
MC exp. SM events	563.18
MC exp. Z events	67.76
MC exp. st events	23.15
MC exp. ttbar events	419.66
MC exp. ttZ events	20.17
MC exp. W events	21.48
data-driven exp. QCD events	0.00
MC exp. group_ZW_WW_ZZ events	0.00
MC exp. group_tZ_tWZ_ttX events	0.00

TABLE 11.4. Background-only fit results for the control regions VRttbarAB, corresponding to an 139 fb^{-1}. The errors shown are the statistical plus systematic uncertainties, except for the error on the background estimate in the control region, which is the systematic uncertainty only. Uncertainties are symmetrised where appropriate, and the negative error truncated when reaching zero event yield.

11.2.1. Expected Yields Summary

Table 11.5 lists the final normalization factors estimated by the fit and applied to obtain the final expected yields. Figures 11.3 and 11.4 compare the expected yields to the observed data for the AB analysis with the scale factors applied. Table 11.6 summarizes the selections between SRB, and its $t\bar{t}$ background estimation regions.

Floating Parameter	Initial Value	Final Value
μ_{ST}	1.0000	$7.7 \times 10^{-1} \pm 3.2 \times 10^{-1}$
μ_{Wjets}	1.0000	$7.3 \times 10^{-1} \pm 2.5 \times 10^{-1}$
μ_{Zjets}	1.0000	$1.031 \pm 7.8 \times 10^{-2}$
$\mu_{t\bar{t}+Z}$	1.0000	$8.4 \times 10^{-1} \pm 1.5 \times 10^{-1}$
$\mu_{textrmt\bar{t}}$	1.0000	$1.07 \pm 1.8 \times 10^{-1}$

TABLE 11.5. Table of fit parameters for the background only fit for SRAB .

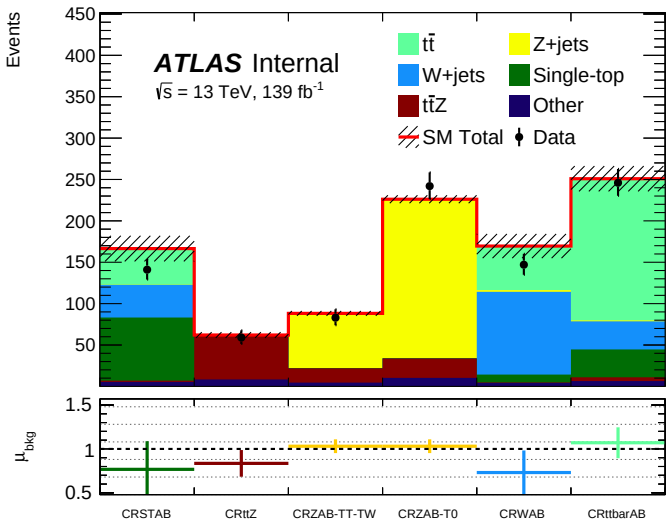

FIGURE 11.3. Single-bin normalization plots for each control region used in the background only fit. The top pad represents the pre-fit background composition, and the lower pad denotes the pre-fit μ for each respective background being normalized.

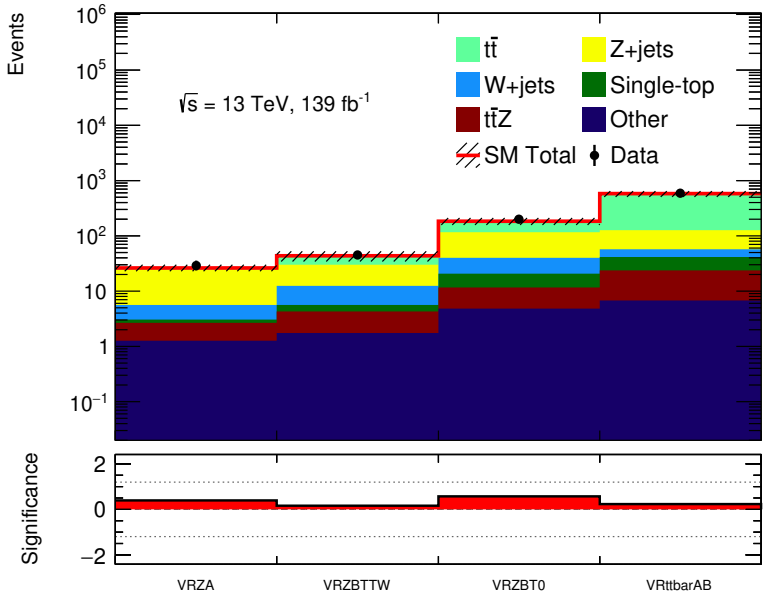

FIGURE 11.4. Single-bin normalization plots for each validation region used in the background only fit. The top pad represents the post-fit yields compared to data, and the bottom pad denotes the significance, calculated using BinomialObsZ.

Variable	SRB-TT	SRB-TW	SRB-T0	CRTAB	VRTAB
Trigger	$E_{\mathrm{T}}^{\mathrm{miss}}$			same	same
$E_{\mathrm{T}}^{\mathrm{miss}}$	> 250 GeV			same	same
signal ℓ	0			exactly 1	same
p_{T}^{ℓ}	–			$4.5\,(4.0) < p_{\mathrm{T}}^{e\,(\mu)} < 20$ GeV	same
additional baseline ℓ	0			0	same
$m_{\mathrm{T}}\left(\ell, E_{\mathrm{T}}^{\mathrm{miss}}\right)$	–			< 120 GeV	same
$\mathrm{N_{jets}}$	≥ 4			same	same
p_{T}^{j2}	> 80 GeV			same	same
p_{T}^{j4}	> 40 GeV			same	same
$\min\left\lvert\Delta\phi\left(\mathrm{jet}^{1-4}, E_{\mathrm{T}}^{\mathrm{miss}}\right)\right\rvert$	> 0.4			same	same
$\mathrm{N_{b-jet}}$	≥ 2			same	same
$\mathrm{m}(J_1; \mathrm{R} = 1.2)$	> 120 GeV			same	same
$\mathrm{m}(J_2; \mathrm{R} = 1.2)$	> 120 GeV	$[60, 120]$ GeV	< 60 GeV	–	–
$m_{\mathrm{T}}^{b,\mathrm{min}}$	> 200 GeV			> 150 GeV	$[150, 200]$ GeV
$m_{\mathrm{T}}^{b,\mathrm{max}}$	> 200 GeV			–	–
m_{T2,χ^2}	< 450 GeV			–	–
Object based $E_{\mathrm{T}}^{\mathrm{miss}}$ sig.	$> 14\sqrt{\ \mathrm{GeV}}$			same	same
$\Delta R\,(b_1, b_2)$	> 1.4			same	same
τ veto	✓			–	same

TABLE 11.6. Comparison between selection criteria for the $t\bar{t}$ control regions and validation regions and the Signal Region B selection criteria. The term "same" indicates that the selection criteria is the same as the respective signal region; "–" indicates that no selection is applied.

11.2.2. SRAB Results

Once the normalization factors have been calculated, we apply the corrections to the SR and compare to what we observe in data. Figure 11.5 and Tables 11.7 and 11.8 show the expected yields after corrections.

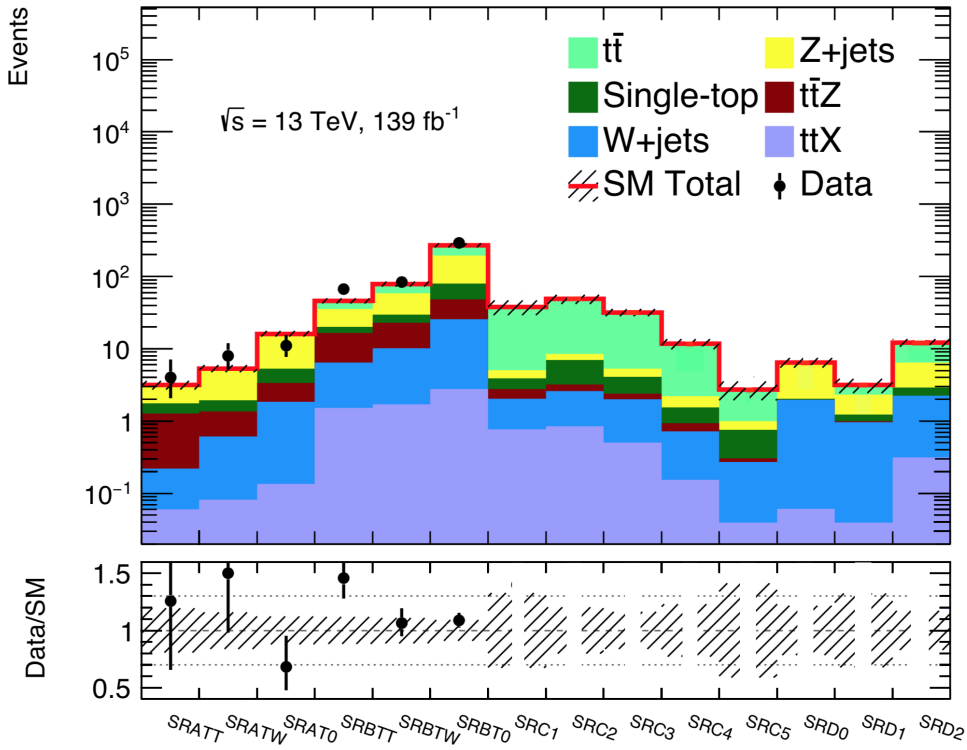

FIGURE 11.5. Summary of expected yield and observed data for all Signal Regions.

Region	SRATT	SRATW	SRAT0
Observed events	4	8	11
Fitted bkg events	3.22 ± 0.50	5.58 ± 0.66	17.32 ± 1.72
Fitted Z events	1.35 ± 0.28	3.22 ± 0.42	10.48 ± 1.31
Fitted st events	0.50 ± 0.31	0.59 ± 0.29	1.95 ± 0.75
Fitted ttbar events	0.08 ± 0.07	0.16 ± 0.10	0.36 ± 0.36
Fitted ttZ events	1.05 ± 0.29	0.74 ± 0.17	1.50 ± 0.34
Fitted W events	0.16 ± 0.07	0.53 ± 0.20	1.71 ± 0.62
Fitted QCD events	0.00 ± 0.00	0.00 ± 0.00	0.00 ± 0.00
Fitted group_ZW_WW_ZZ events	0.02 ± 0.00	0.27 ± 0.23	1.20 ± 0.21
Fitted group_tZ_tWZ_ttX events	0.06 ± 0.02	0.08 ± 0.01	0.12 ± 0.02
MC exp. SM events	3.59	6.01	18.46
MC exp. Z events	1.30	3.15	10.13
MC exp. st events	0.64	0.75	2.55
MC exp. ttbar events	0.07	0.16	0.34
MC exp. ttZ events	1.26	0.88	1.79
MC exp. W events	0.22	0.72	2.32
data-driven exp. QCD events	0.00	0.00	0.00
MC exp. group_ZW_WW_ZZ events	0.02	0.27	1.20
MC exp. group_tZ_tWZ_ttX events	0.06	0.08	0.12

TABLE 11.7. Background-only fit results for the signal region SRA, corresponding to a luminosity of 139 fb^{-1}. Nominal (pre-fit) SM background estimations are given for comparison. The errors shown are the statistical plus systematic uncertainties, except for the error on the background estimate in the control region, which is the systematic uncertainty only. Uncertainties are symmetrised where appropriate, and the negative error truncated when reaching zero event yield.

Region	SRBTT	SRBTW	SRBT0
Observed events	67	84	292
Fitted bkg events	46.69 ± 6.89	81.68 ± 7.46	275.96 ± 24.11
Fitted Z events	15.57 ± 3.29	28.74 ± 3.35	117.21 ± 13.56
Fitted st events	3.50 ± 1.16	7.01 ± 3.05	31.02 ± 14.67
Fitted ttbar events	10.52 ± 5.28	20.48 ± 6.37	72.29 ± 19.41
Fitted ttZ events	9.94 ± 2.51	12.51 ± 2.48	22.68 ± 4.30
Fitted W events	4.93 ± 1.95	8.53 ± 3.61	22.83 ± 8.71
Fitted QCD events	0.00 ± 0.00	0.00 ± 0.00	0.00 ± 0.00
Fitted group_ZW_WW_ZZ events	0.72 ± 0.17	2.72 ± 2.37	7.27 ± 1.24
Fitted group_tZ_tWZ_ttX events	1.51 ± 0.23	1.69 ± 0.18	2.65 ± 0.18
MC exp. SM events	50.51	87.42	289.36
MC exp. Z events	15.02	28.00	113.38
MC exp. st events	4.61	9.17	40.72
MC exp. ttbar events	10.05	19.35	67.14
MC exp. ttZ events	11.86	14.84	27.05
MC exp. W events	6.74	11.81	31.04
data-driven exp. QCD events	0.00	0.00	0.00
MC exp. group_ZW_WW_ZZ events	0.72	2.55	7.36
MC exp. group_tZ_tWZ_ttX events	1.49	1.71	2.66

TABLE 11.8. Background-only fit results for the signal region SRB, corresponding to a luminosity of 139 fb^{-1}. Nominal (pre-fit) SM background estimations are given for comparison. The errors shown are the statistical plus systematic uncertainties, except for the error on the background estimate in the control region, which is the systematic uncertainty only. Uncertainties are symmetrised where appropriate, and the negative error truncated when reaching zero event yield.

CHAPTER XII

INTERPRETATIONS AND OUTLOOK

12.1. Confidence Levels and p-Values

Once the MC background predictions have been properly normalized and compared to data, we can begin to interpret any excess or lack thereof. While optimizing the SRs, a crude significance is calculated based on the number of signal and background events (statistics) passing the selections:

$$\sigma_{basic}^{stat} \sim \frac{N_{sig}}{\sqrt{N_{BG}}}. \tag{12.1}$$

We can consider the signal statistics in the denominator and introduce an uncertainty on our background estimation to create a slightly better definition:

$$\sigma_{better}^{stat} \sim \frac{N_{sig}}{\sqrt{N_{BG} + N_{sig} + 0.3\ N_{BG}^2}}. \tag{12.2}$$

When interpreting the results after all uncertainties have been accounted for, the 30% uncertainty can be replaced by their true values.

In data, we do not know what events are background and which are signal. Therefore, we consider a significance definition based on the difference between the observed data yields and the expected MC values, assuming no signal is present (null hypothesis H_0). Explicitly, the p-value is the probability that the observed data is consistent with the null hypothesis:

$$p \equiv \int_{N_{obs}}^{\infty} f(N_{obs}|H_0)dN \tag{12.3}$$

This value can be translated into the *observed Z significance*, by interpreting its position on the tail of a Gaussian distribution Φ

$$Z_{obs} \equiv \Phi^{-1}(1-p) \tag{12.4}$$

There exists a value α for which the null hypothesis of any given model is not rejected:

$$p_{model} \equiv \int_{N_{obs}}^{\infty} f(N_{obs}|H_0)dN \leq \alpha. \tag{12.5}$$

Once α is obtained, we can assign a *confidence level* (CL) value to the hypotheses tested by:

$$\text{Confidence Level (CL)} \equiv 1-\alpha. \tag{12.6}$$

When presenting exclusion results, we quote our CLs in rejecting any given model.

12.2. SRAB Sensitivity to Stop Models

Results are interpreted for both a discovery and an exclusion scenario. For the exclusion scenario, all signal regions are used where the SRA, SRB, and SRC sub-regions are statistically combined. For the discovery scenario, p-values are evaluated for discovery regions which are a subset of the signal regions: SRA-TT, SRB-TT, SRC3-5+Object based $E_{\mathrm{T}}^{\mathrm{miss}}$ sig. $> 12\sqrt{\text{ GeV}}$, and each one of the SRD regions.

SRA and SRB are orthogonalized through m_{T2,χ^2} and the two top candidate masses, yielding six orthogonal signal regions targeting non-compressed two-body stop decays. The signal regions can be statistically combined in order to maximize sensitivity across top decay topologies. Figures 12.1 and 12.2 show the expected sensitivity of SRA and SRB individually to stop models. Figure 12.3

shows the effect of the combining the two SRs, assuming no signal is observed. Figures 12.4 and 12.5 show the effects of systematics on the stop interpretation of the AB analysis. Figure 12.6 illustrates the stop models excluded assuming no signal. Finally, Figure 12.7 shows the observed limits on stop models.

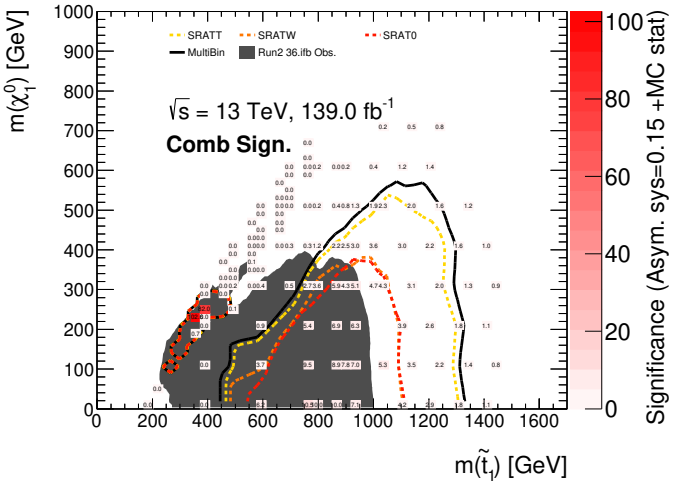

FIGURE 12.1. Expected exclusion plots for SRA as defined in Table 8.1. A statistical combination of the three categories is performed to maximize sensitivity.

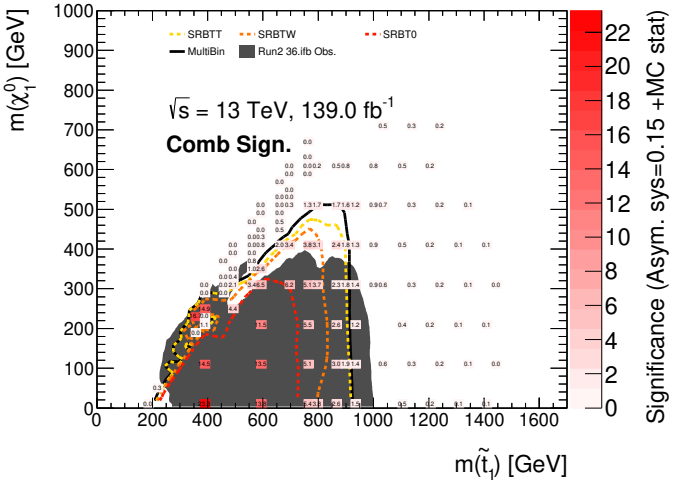

FIGURE 12.2. Expected exclusion plot for SRB as defined in Table 8.2. A statistical combination of the three categories is performed to maximize sensitivity.

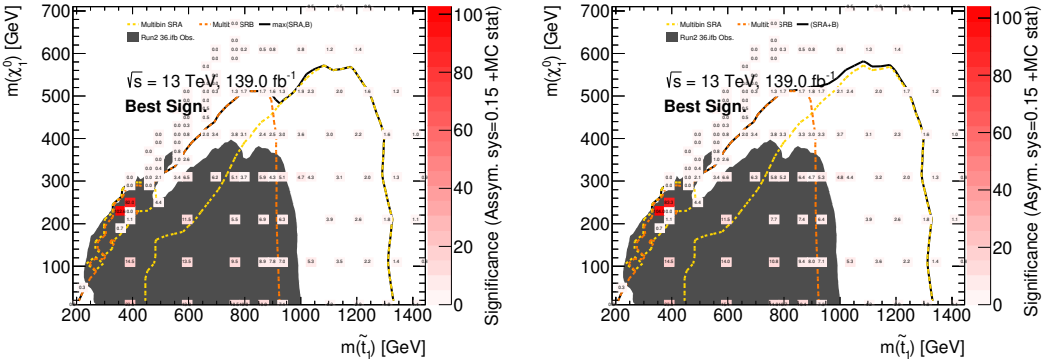

(a) Best of SRA or SRB (b) Statistical combination of SRA and SRB

FIGURE 12.3. Expected exclusion plot for SRA and SRB signal regions. Multibin combination is performed on three categories of SRA and three categories of SRB. (a) shows the expected exclusion reach based on the highest significance, whereas (b) shows the expected exclusion range when SRA and SRB significances are added in quadrature.

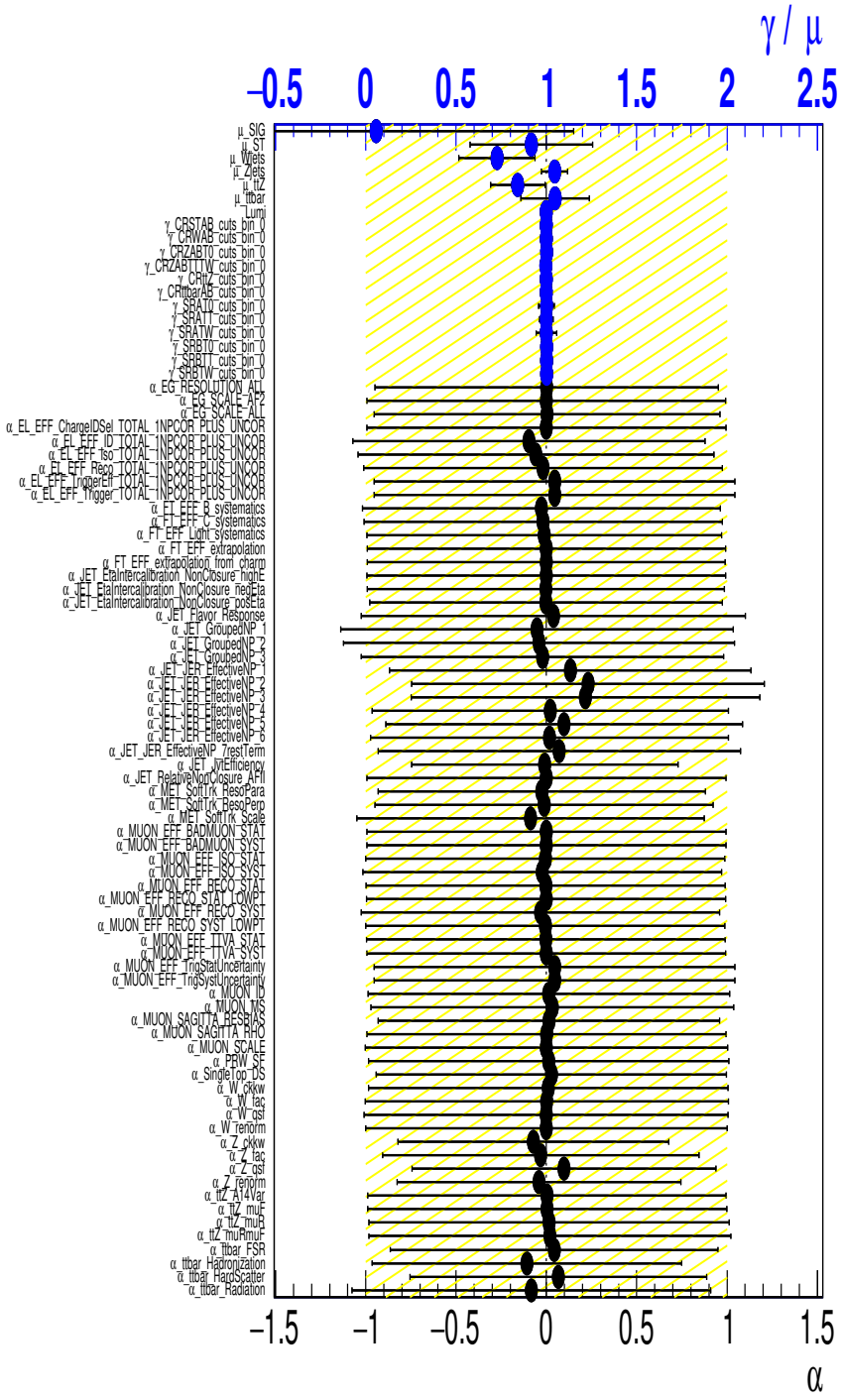

FIGURE 12.4. Nuisance parameter plot for the exclusion fit ((1300, 1) mass point) performed on region A and region B

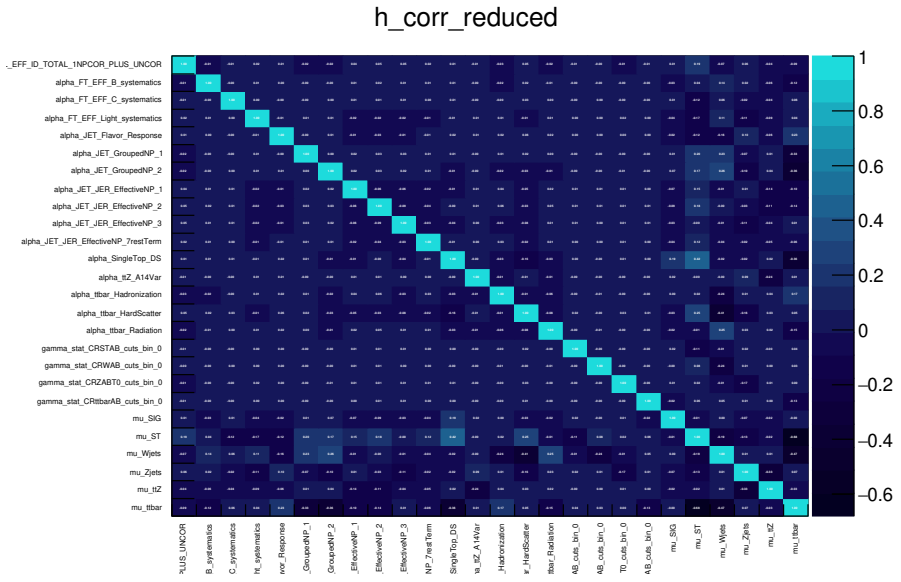

FIGURE 12.5. Correlation matrix for the exclusion fit ((1300, 1) mass point) performed on region A and region B

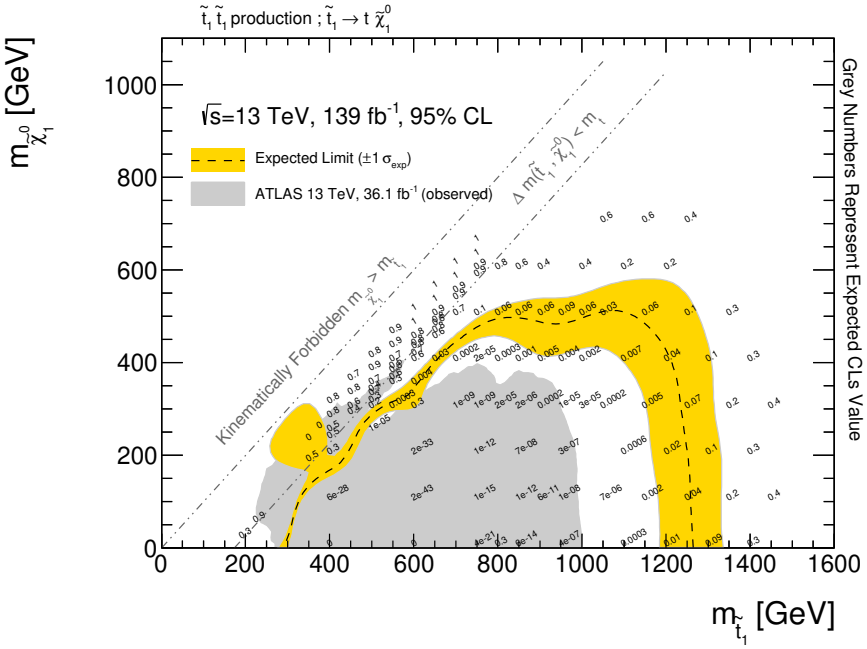

FIGURE 12.6. Expected limits for the combined fit performed on regions A and B.

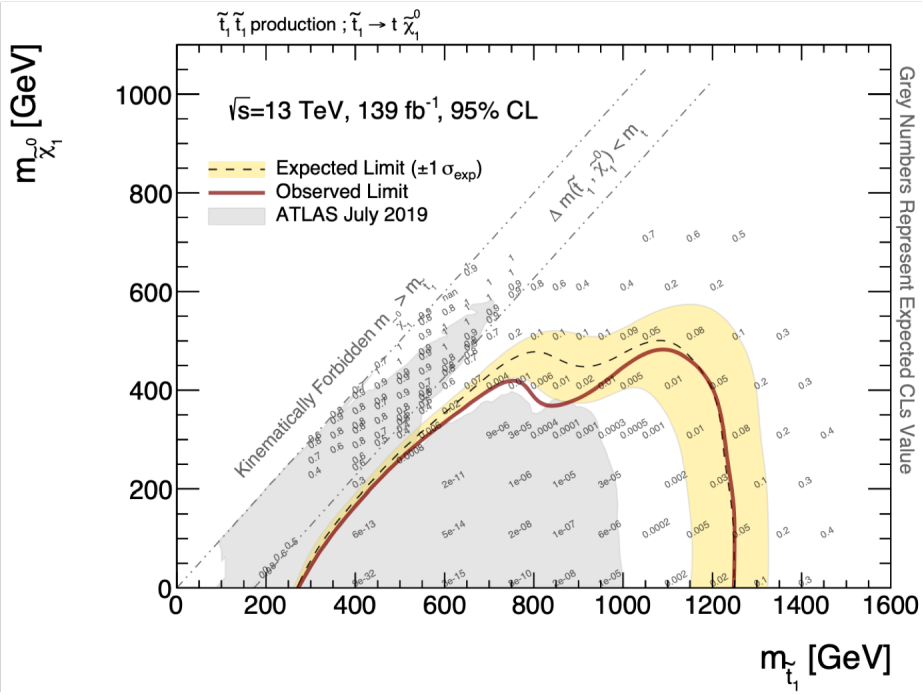

FIGURE 12.7. Observed limits for the combined fit performed on regions A and B.

12.3. Outlook

The yields shown in Section XI are independent of the model chosen for optimization; the reinterpretation of the observed yield can be done on any process sensitive to the SR selections. The analysis presented in this dissertation optimizes the Signal Region definitions with simplified supersymmetric models of new pair-produced scalar particles, each decaying to a top and an invisible supersymmetric neutralino. The selections chosen are also sensitive to certain Dark Matter and vector-like quark models, although these results are not included in this dissertation.

In regions A and B, the new Object-Based MetSig variable is used, in contrast to standard $E_{\mathrm{T}}^{\mathrm{miss}}$ in the previous iteration of the analysis. The choice of low Object-Based MetSig in the compressed regions (SRC), as well as the implementation of soft-flavor tagging in the four-body optimized regions (SRD), provided more coverage along the diagonal. No significant excesses over the simulated Standard Model background were observed. The stop reinterpretation of the observed yields leads to an exclusion of models with $m_{\tilde{t}} <$ 1.25 TeV. Compared to previous publications, the relative coverage in the $m_{\tilde{t}} - m_{\tilde{\chi}_1^0}$ exclusion plane has been extended by 25% (the 36 fb^{-1} result excluded models up to 1 TeV).

The data gain of future LHC runs could continue increasing sensitivity to models with high stop and neutralino masses, but the rate of data increase is approaching a plateau. The analysis is statistics-limited for higher stop mass models since the cross-section falls harshly with increasing stop mass. The pair-production cross-section for a 1.25 TeV stop is $\sim$ 1 fb and drops an order of magnitude just above 1.6 TeV stops, meaning that this analysis would need a dataset comparable to what is planned for the High-Luminosity LHC to achieve

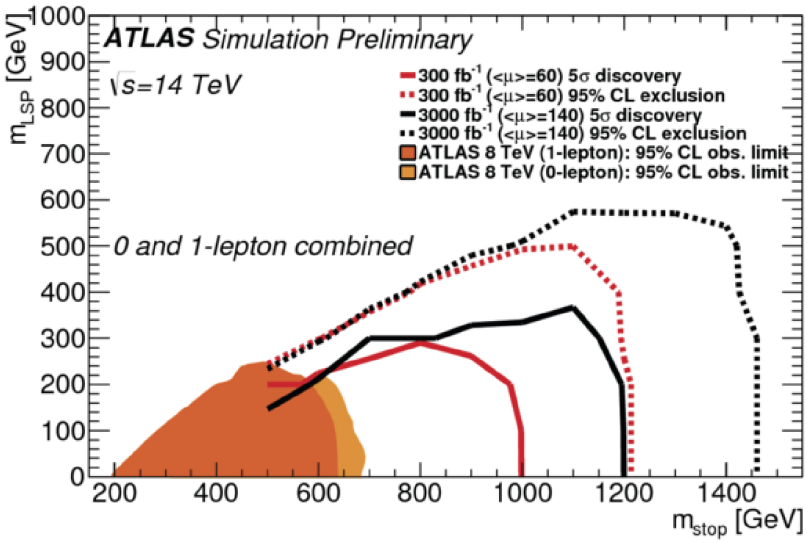

FIGURE 12.8. Sensitivity projections of the 8 TeV analysis with 300 (red) and 3000 (black) fb^{-1} of 14 TeV data. [35]

a sensitivity jump on the order of this search. Figure 12.8 shows the sensitivity projections before the start of Run 2; this analysis on Run 2 data has outperformed the expected sensitivity of the Run 1 stop search expected with Run 2 and 3 of the LHC.

One of the main limitations of the full Run 2 analysis was top reconstruction efficiency, and its improvement may provide more powerful discriminators against background. In future analyses, it is important to dedicate effort in recovering lost sub-leading top candidates (SRA-T0, SRB-T0). In scenarios with close-by tops, the sub-leading constituents can be 'eaten' by the leading reclustered jets. In addition, significant benefits to sub-20 GeV jet calibrations could lead to recovering soft partons.

We did not discover Supersymmetry (this time), but the methods studied and developed are crucial in the road to New Physics. The LHC is preparing to circulate protons in 2021, and we should use the time before new data is available

to make an educated choice of our next analysis effort. I am excited to contemplate our best chances for discovery and perform new analyses as I head into my career as an experimental particle physicist.

APPENDIX A

MINIMAL SUPERSYMMETRIC STANDARD MODEL

Nature does not need to respect a minimal theory, a clear example being the extension of a minimal SU(2)xU(1) with a Yukawa coupling term. SUSY in itself does not limit the number or classes of fields, and we have only a loose idea of what new particles could lie above the weak scale. We need to make a choice and hope that it is what nature also chose; we choose a *minimal supersymmetric* (MSSM) theory characterized by containing only the minimum number of super-multiplets necessary to completely describe the SM particles.

A.1. Superfields of the MSSM

There is a choice in the number of super-symmetries of the universe: we will consider just the single SUSY symmetry in our SM extension. The simplest choice of super-multiplet structure, called *chiral/matter* multiplets, has $n_B = n_f = 2$ and can be achieved by partnering a Weyl-fermion with two real scalars (equivalent to one complex scalar). The next simplest structure, the *gauge/vector* multiplet, has the same number of degrees of freedom and swaps the complex scalar for a vector boson, which must be massless (prior to SSB) in order to conserve gauge invariance. One may be curious if it is possible to pair a SM gauge-boson with a spin-$^3/_2$ fermion, but this leads to inconsistencies.

We can begin assigning SM particles to their appropriate super-multiplets and identifying their super-partners. We recognize that all SM fermions must reside in chiral super-multiplets, since they are the only structures with the transformation properties matching the observed SM particles (i.e. left- and right-handed fermions

Super-Multiplet		spin-0	spin-$\frac{1}{2}$	$SU(3)_C$, $SU(2)_L$, $U(1)_Y$
(s)quarks	Q	$\left(\tilde{u}_L, \tilde{d}_L\right)$	(u_L, d_L)	$\left(3, 2, \frac{1}{6}\right)$
	$\bar{u}$	$\tilde{u}_R^*$	$u_R^\dagger$	$\left(\bar{3}, 2, -\frac{2}{3}\right)$
	$\bar{d}$	$\tilde{d}_R^*$	$d_R^\dagger$	$\left(\bar{3}, 2, \frac{1}{3}\right)$
(s)leptons	L	$(\tilde{\nu}, \tilde{e}_L)$	(ν, e_L)	$\left(1, 2, -\frac{1}{2}\right)$
	$\bar{e}$	$\tilde{e}_R^*$	$e_R^\dagger$	$(1, 1, 1)$
Higgs(inos)	H_u	(H_u^+, H_u^0)	$\left(\tilde{H}_u^+, \tilde{H}_u^0\right)$	$\left(1, 2, \frac{1}{2}\right)$
	H_d	$\left(H_d^0, H_d^-\right)$	$\left(\tilde{H}_d^0, \tilde{H}_d^-\right)$	$\left(1, 2, -\frac{1}{2}\right)$

TABLE A.1. Particle contents of the MSSM

transform differently). The super-partners of SM gauge-bosons are called *gauginos* inherit the chiral transformation properties (e.g. handedness) and belong in *gauge* multiplets. One can construct higher order complex super-multiplets, but these have been shown to be reducible to the above two structures. Hence, SM fermions have scalar super-partners (explaining the 's' naming prefix) and SM gauge bosons have super-partners with spin$-1/2$ ('ino' suffix convention mirrors gaugino).

A.2. The MSSM Super-Potential

In addition to the particle (field) content described in Table A.1, the MSSM is characterized by their interactions in our choice of *super-potential* W_{MSSM}.

$$W_{MSSM} = \tilde{u} y_u Q H_u - \tilde{d} y_d Q H_d - \tilde{e} y_e L H_d + \mu H_u H_d \tag{A.1}$$

The μ term is the SUSY equivalent of the SM Higgs mass term. The y_u and y_d Yukawa couplings are set to the value of the parameter in SM, the biggest contributions come from the the third generation (s)quarks and (s)leptons. We can use this observation to motivate a simplification of the two 3x3 Yukawa matrices to

be non-zero on *only* the 3rd generation diagonal entires

$$y_{u/d/e} \approx \begin{pmatrix} 0 & 0 & 0 \\ 0 & 0 & 0 \\ 0 & 0 & y_{t/b/\tau} \end{pmatrix} \tag{A.2}$$

With this simplification, we can write the super-potential to expose the Yukawa couplings between the SM particles and their super-partners. An important feature of SUSY is that it provides the SM-like Higgs-quark-quark and Higgs-lepton-lepton interactions, in addition to new Higgs-quark-squark and Higgs-lepton-slepton interactions. Furthermore, the Higgs-fermion-fermion, Higgs-sfermion-sfermion, and Higgs-fermion-sfermion Yukawa terms all share a single Yukawa parameter y_i for each super-multiplet flavor.

$$\begin{aligned} W_{MSSM} =& y_t \left(\tilde{t}tH_u^0 - \tilde{t}bH_u^+\right) - y_d \left(\tilde{b}tH_d^- - \tilde{b}bH_d^0\right) - y_\tau \left(\tilde{\tau}\nu_\tau H_d^- - \tilde{\tau}\tau H_d^0\right) \\ &+ \mu \left(H_u^+ H_d^- - H_u^0 H_d^0\right) \end{aligned} \tag{A.3}$$

As is true in the SM, the dimensionless Yukawa interactions are a small contribution to sparticle production and/or decay – the dominant interactions are those involving SUSY-gauge couplings.

A.2.1. R-Parity

The super-potential in Equation A.1 is minimal and one can append holomorphic, gauge-invariant terms at will, although they would necessarily violate Baryon and/or Lepton number conservation. An example B-violating term, for an

extended MSSM with quark super-multiplets carrying $Q_{i,B} = \frac{1}{3}, \tilde{u}_{i,B} = \tilde{d}_{i,B} = -\frac{1}{3}$

$$B - Violating : W_{\Delta B=1} = \frac{1}{2}\lambda_B^{ijk}\tilde{u}_i\tilde{d}_j\tilde{d}_k \tag{A.4}$$

Similarly, we can introduce L-violation by introducing the following term for an extended MSSM with lepton super-multiplets carrying $L_{i,B} = 1$

$$L - Violating : W_{\Delta L=1} = \frac{1}{2}\lambda^{ijk}L_iL_j\tilde{e}_k + \lambda_L^{ijk}L_iQ_j\tilde{d}_k + \mu_L^iL_iH_u \tag{A.5}$$

The most direct consequence these L/B-violating terms with unsuppressed $\lambda_L^{ijk}, \lambda_B^{ijk}$ couplings is that the SM up quark is no longer stable. SUSY-mediators thus provide a decay pathway for the proton, which is measured to have a lifetime much longer than the current age of the universe. To avoid these terms, we can impose an additional symmetry to the MSSM: R-parity also known as matter parity. The symmetry assigns to each field a conveniently-defined quantum number and restricts each Lagrangian term to have positive R-parity

$$P_M = (-1)^{3(B-L)} \tag{A.6}$$

All quark and lepton super-multiplets then carry $P_M = -1$, while the Higgs super-multiplets bear $P_M = +1$; the gauge super-multiplets do not carry either B or L-number and consequently carry $P_M = +1$. One could imagine instead enforcing a B and L symmetry on the theory, but these are known to necessarily be violated in non-perturbative corrections at the weak-scale. On the other hand, R-parity includes a B/L-conservation mechanism in the perturbative regime while

providing a new exact symmetry of the universe without evidence against its non-conservation.

We can continue enforcing R-symmetry in our Lagrangian, but redefine the quantum number

$$P_R = (-1)^{3(B-L)+2s} \tag{A.7}$$

This definition is equivalent to Equation A.6, since the product $(-1)^{2s}$ of particles involved in any angular-momentum-conserving vertex is necessarily positive. The subtly occurs within the super-multiplets: with P_R the component particles of a super-multiplet no longer have the same quantum number. Therefore, the R-parity conserving MSSM has SM-like particles (including the Higgs) with $P_R = +1$, where as the new sparticles have opposite parity $P_R = -1$.

For the purpose of the search presented in this dissertation, the primary phenomenological consequences are as follows

- Sparticle pair-production: If we begin with only SM particles (protons at the LHC), the R-parity is $P_R = +1$. If there is to be any sparticle production, the process must be R-parity positive. Therefore, a sparticle cannot be produced singly; it must be produced in association to another sparticle, e.g. $pp \rightarrow \tilde{g}\tilde{g}, \tilde{g}\tilde{q}, or \tilde{q}\tilde{q}$.

- Stable LSP: When a sparticle is produced, it carries opposite R-parity to all SM particles. Thus, the final state must include a particle whose R-parity opposes any SM particle. In other words, there necessarily exists a *least-massive stable particle* (LSP) at the end of every SUSY decay chain.

- Dark Matter Candidate: If the LSP is neutral, by definition it does not interact with luminous matter. This makes it an attractive candidate

explaining the gravitationally-interacting particulate matter we call Dark Matter.

A.3. SUSY Breaking

We clearly do not live in a universe with unbroken SUSY, since we have looked and see no evidence of partner particles at the masses of already-discovered particles. If there is any chance of SUSY being a true symmetry of the universe, it must be in a broken manner. To provide a more realistic SUSY theory, we need to add SUSY-invariant terms to the Lagrangian that spontaneously break at high energies. There is no consensus on the exact mechanism of the symmetry breaking, but they always involve new, *very* high energy interactions and particles.

For the purpose of the search presented in this dissertation, the mechanism is irrelevant if one considers an effective MSSM and introduce (*soft*) SUSY-breaking terms. The allowable forms of these terms are restricted to SUSY-gauge mass terms M_a, scalar couplings a^{ijk} and b^{ij}, and scalar mass squared terms m^2

$$\mathcal{L}_{soft} = -\left(\frac{1}{2}M_a\lambda^a\lambda^a + \frac{1}{6}a^{ijk}\phi_i\phi_j\phi_k + \frac{1}{2}b^{ij}\phi_i\phi_j\right) + (c.c.) - \left(m^2\right)^i_j \phi^{j*}\phi_i \qquad \text{(A.8)}$$

The M_a terms are always allowed by gauge symmetry. The $(m^2)^i_j$ terms are allowed for any scalar ($i = j$) of a broken-SUSY theory. The remaining terms are further restricted by additional gauge symmetries imposed on the theory.

The most general set of gauge-invariant, SUSY-breaking terms conserving matter-parity under the MSSM is

$$\begin{aligned}\mathcal{L}_{soft}^{MSSM} =& \frac{1}{2}\left(M_3\tilde{g}\tilde{g} + M_2\tilde{W}\tilde{W} + M_1\tilde{B}\tilde{B} + (c.c)\right) \\ & - \left(\tilde{\bar{u}}a_u\tilde{Q}H_u - \tilde{\bar{d}}a_d\tilde{Q}H_d - \tilde{\bar{e}}a_e\tilde{L}H_d + (c.c)\right) \\ & - \tilde{Q}^\dagger m_Q^2\tilde{Q} - \tilde{L}^\dagger m_L^2\tilde{L} - \tilde{\bar{u}}m_{\bar{u}}^2\tilde{\bar{u}}^\dagger - \tilde{\bar{d}}m_{\bar{d}}^2\tilde{\bar{d}}^\dagger - \tilde{\bar{e}}m_{\bar{e}}^2\tilde{\bar{e}}^\dagger \\ & - m_{H_u}^2 H_u^* H_u - m_{H_u}^2 - m_{H_u}^2 H_d^* H_d - m_{H_d}^2 - (bH_uH_d + (c.c.))\end{aligned} \tag{A.9}$$

The first line are the mass terms of the gluino, wino, and bino gauginos, with respective couplings M_3, M_2, M_1. The second line comes from the second term of Equation A.8 and is a cubic coupling between scalars whose magnitude matrices $a_{u/d/e}$, which are commonly to be related to the Yukawa matrices of the super-potential. Similarly, the squark and slepton mass terms, $(m^2)_i^j$, expand into the third line for the MSSM. The last line of the soft SUSY-breaking terms above are the contributions to the Higgs potential. Furthermore, since we expect nature to break SUSY softly we can notice that the mass parameters above must be on the order of the SUSY-breaking scale

$$m_{soft} \sim M_1, M_2, M_3, a_u, a_d, a_e \tag{A.10}$$

$$m_{soft}^2 \sim m_Q^2, m_L^2, m_{\bar{u}}^2, m_{\bar{d}}^2, m_{\bar{e}}^2, m_{H_u}^2, m_{H_d}^2, b \tag{A.11}$$

To restrict the fine tuning of a broken-SUSY to an acceptable level, the SUSY-breaking mass scale is not expected to be much larger than 10^3 GeV. Despite these arguments, the MSSM has 105 more free parameters than the SM.

A.3.1. Phenomenological MSSM

One way to explain the (empirically driven) choice of removing CP-violation and flavor-mixing from the MSSM is by assuming nature is *flavor-blind*. More specifically, we can assume that nature treats the generations *universally* and set the mixing matrices above to be strictly diagonal

$$\mathbf{m}^2_{L/Q/u/d/e} = m^2_{L/Q/u/d/e}\mathbb{1} \tag{A.12}$$

We can restrict the form of the cubic scalar coupling matrices by associating their flavor connections to the corresponding Yukawa coupling matrices.

$$\mathbf{a}_{u/d/e} = A_{(u/d/e)0}\mathbf{y}_{u/d/e} \tag{A.13}$$

Furthermore, we can assume that the only CP-violating object in the theory to be the CKM and PMNS matrices. The simplest mechanism to perform this restriction is to remove any complex phases and assuming the mass terms of the gauginos to be strictly real numbers

$$Im(M_1) = Im(M_2) = Im(M_3) = Im(A_{(u/d/e)0}) = 0 \tag{A.14}$$

The *phenomenological* MSSM (pMSSM) is a subset of the MSSM with all the above modification reducing the 105 new parameters to a more manageable 19.

APPENDIX B

IN-SITU JER OF C/A R=0.2 JETS AT $\sqrt{S} = 13$ TEV

The aim of the studies presented here is to perform the relative JER measurement for 13 TeV MC and data using a similar strategy as the 7 TeV studies. The reconstructed jets of interest, C/A R=0.2, are clustered using the FastJet tool [124] and seeded directly from locally calibrated calorimeter topoclusters (CaloCalTopoClusters). The resulting C/A jets then have a MC-based JES calibration applied based on the jets' η and p_T.

This following subsections focus on calculating the relative JER for reconstructed calorimeter jets clustered from calorimeter objects using the Cambridge-Aachen algorithm with a cone-radius parameter of 0.2 (C/A R=0.2). Due to the small cone-size, and other physics effects such as pile-up, soft-radiation, and even ISR, the number of reconstructed C/A R=0.2 jets in a 'dijet' event tends to be greater than two. As a result, the sample size available in either MC or data with a requirement of exactly two back-to-back jets would be too strict to perform this study. One way to calculate the relative JER from events with more than two jets is to study the behavior of the relative JER when imposing varying upper p_T requirements on the third-leading C/A R=0.2 jet $\left(p^3_{T,max}\right)$. The relative JER is studied for values of $p^3_{T,max} \in [10, 24]$ GeV and then extrapolated to $p^3_{T,max} = 0$, i.e. when there is no third-leading C/A R=0.2 jet.

B.1. Sample Details

The sample derivations available are defined in the Jet/EtMiss documentation [125]. Two of the derivations listed were considered: JETM6 and

JETM8. Both derivation schemes have several sample sets (production tags) with varying event-levels skims. The most impactful skim is on the leading anti-k_{T} R=1.0 jet. The JETM8 derivations also have more variable information (branches and predefined objects) than JETM6, but its trade-off is having fewer total events than the JETM6 derivation.

JETM6 has all the information necessary to perform the study and higher statistics, thus this derivation scheme is used. The production tag for MC used is p2794, whereas p2813 for data; the production tags are different, but the changes are minimal and do not affect this study. For both of these sample sets, the event-level jet skim requires at least one anti-k_{T} R=1.0 jet with a p_T above 100 GeV.

In MC, dijet samples are generated with the PYTHIA8 generator in slices binned in R=0.6 anti-k_{T} leading truth jet p_T, as listed in the last column of Table B.1. The JZ0W and JZ1W slices were studied, but omitted due to low statistics and high weights, stemming from the event-level skim in the derivations. The weight per MC event is

$$\text{weight} = \frac{\text{eventGeneratorWeight} * \text{eventPileupWeight} * \text{sliceCrossSection}}{\text{sliceSumWeights}} \tag{B.1}$$

The JETM6 selection is applied to recorded data to reduce the dataset size and perform a first-pass selection of events. The p2813 tag is available only for data16 periods A, B, C, D, E, F, G, I, and K. Though there are other data recorded, this version of production was only done for the aforementioned periods. Table B.2 details the number of events per period in the samples used.

DiJet Slice	NFiles	Total Number of Events	Cross-Section [fb]	anti-k_{T} R=0.6 p_T Slice [GeV]
JZ0W	8	110,838	7.842e13	[0,20]
JZ1W	13	332,767	7.842e13	[20,60]
JZ2W	51	1,721,610	2.4332e12	[60,160]
JZ3W	385	7,884,491	2.6454e10	[160,400]
JZ4W	403	7,979,794	2.5463e8	[400,800]
JZ5W	408	7,977,593	4.5535e6	[800,1300]
JZ6W	97	1,893,399	2.5753e5	[1300,1800]
JZ7W	90	1,770,198	1.6215e4	[1800,2500]
JZ8W	89	1,743,198	6.2502e2	[2500,3200]
JZ9W	91	1,813,199	1.9639e1	[3200,3900]
JZ10W	104	1,995,999	1.196	[3900,4600]
JZ11W	103	1,993,199	4.2258e-2	[4600,5300]
JZ12W	101	1,974,598	1.037e-3	[5300,∞)

TABLE B.1. JZXW JETM6 dataset information extracted from AMI.

data16 Period	NFiles	Total Number of Events
A	741	30,484,876
B	1,136	47,580,794
C	1,800	73,194,353
D	3,039	127,524,559
E	944	44,275,524
F	2,043	80,912,777
G	2,546	97,051,426
I	3,435	135,662,779
K	1627	56,275,031

TABLE B.2. Data JETM6 dataset information extracted from AMI. Only periods available under the p2813 tag are listed.

B.2. Trigger Selection

For this study, we divide the range of R=0.2 C/A $\bar{p}_T$ into non-intersecting bins and choose one single-jet trigger per bin (HLT_jXX). Upon normalizing the asymmetry distributions, the effects of prescales are eliminated, to first-order. Prescales change between runs and luminosity blocks, since they are connected to the instantaneous luminosity, but these effects do not affect the physics captured by each separate trigger, again to first-order. Table B.3 lists the triggers used for each $\bar{p}_T$ bin in this study.

To chose the appropriate trigger for each bin, trigger efficiencies were plotted as a function of average leading-subleading R=0.2 C/A jet p_T, as on Figure B.1. The trigger used is the highest threshold trigger that is fully efficient on the entire bin range. The efficiency of prescaled triggers is defined as

$$\epsilon = \frac{\text{Trigger Of Interest}}{\text{Trigger Of Interest} \text{ —— } \text{Preceding Trigger}} \tag{B.2}$$

The efficiencies do not plateau at unity because of the non-zero probability that an event above the trigger of interest threshold is not recorded due to the prescaling on both that trigger and the preceding trigger. The plateau value of the trigger of interest is the expectation value of the trigger efficiency (eqn. B.2), where the expectation values of the trigger of interest and the preceding trigger is their respective average prescale values, PS_I and PS_P. Explicitly, $\langle\epsilon\rangle = \frac{PS_P}{PS_I+PS_P}$

The lowest unprescaled trigger is HLT_j380. Since all events above its turn-on are recorded by this trigger, this is the only trigger used for the high p_T bins; its efficiency definition is

$$\epsilon = \frac{\text{HLT\_j380 \&\& HLT\_j260}}{\text{HLT\_j260}} \tag{B.3}$$

$\bar{p}_T$	HLT Trigger Used	Typical HLT Prescale	L1 Trigger Seed	Typical L1 Prescale	Aggregated Prescale
50-60	HLT_j55	50-51	L1_J15	2-5 x 10^3	1-3 x 10^5
60-70	HLT_j60	23-24	L1_J20	7-22 x 10^2	2-5 x 10^4
70-80	HLTj60	23-24	L1_J20	7-22 x 10^2	2-5 x 10^4
80-100	HLT_j85	16-17	L1_20	7-22 x 10^2	1-4 x 10^4
100-150	HLT_j110	1-5	L1_J30	2-7 x 10^2	1-5 x 10^3
150-200	HLT_j150	12-13	L1_J40	9-27 x 10^1	1-4 x 10^3
200-300	HLT_j175	4-5	L1_J50	2-12 x 10^1	2-6 x 10^2
300-400	HLT_260	1-2	L1_J75	3-8 x 10^1	2-10 x 10^1
400-600	HLT_j380	1	L1_J100	1	1
600-800	HLT_j380	1	L1_J100	1	1
800-1000	HLT_j380	1	L1_J100	1	1

TABLE B.3. Triggers used and their associated prescales. All HLT triggers used in study are performed with anti-k_{T} R=0.4 jets seeded from topoclusters, calibrated at the EM scale, with both pileup subtraction and JES factors applied.

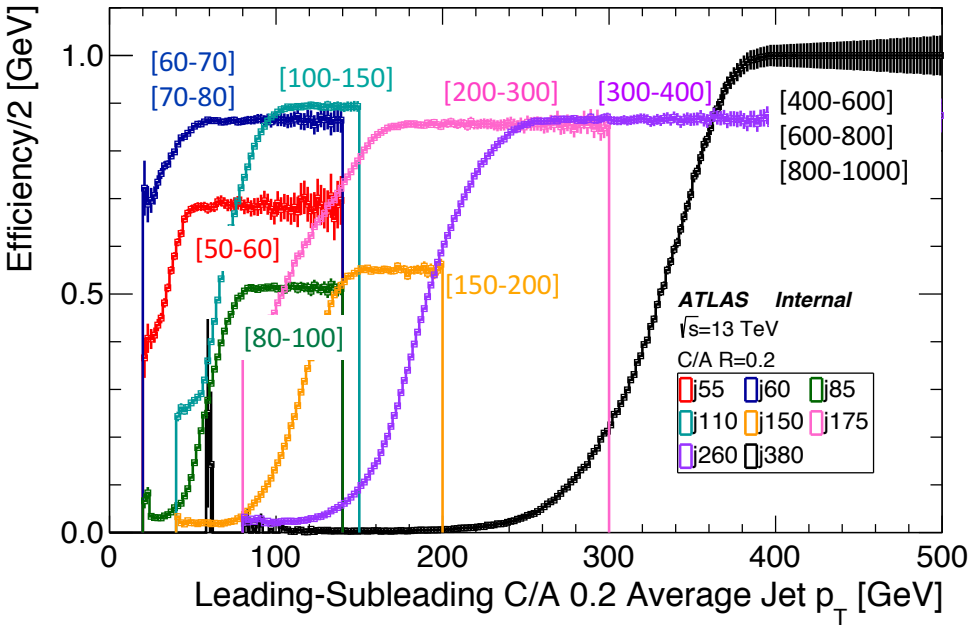

FIGURE B.1. Trigger efficiency curves for triggers used in JER measurement.

B.3. Event and Object Selection

The event selection of this study parallels that of the Run I with a few differences. The first is that the vertex requirement is simply to have at least one primary vertex in the xAOD VertexContainer. The second difference is with the requirements on the anti-k_{T} R=0.4 jets. We apply a requirement of $|\eta| < 2.5$ on both of the two leading jets to ensure proper jet calibration. Two well-calibrated anti-k_{T} jets must be present in an event to pass. These jets are well studied, hence why they are used to perform event-level vetos. Particularly, events are vetoed if they fail any of the following Data Quality attributes:

- Any **isBad** anti-k_{T} R=0.4 jets
- Any LAr errors
- A badTile flag

– A badSCT flag

– An incomplete event flag

– Less than 2 well-calibrated anti-k_{T} EMTopo R=0.4 jets, each passing the Jet Vertex Tagger tool

The back-to-back requirement of $\Delta\phi_{1,2} \geq 2.8$ is applied to the matched C/A jets (see Section B.4 on matching), which is listed in the final selection criteria in Section B.4.1

Table B.4 summarizes the jet definition criteria for the jet sets used in this study. Truth jets are used to subtract the physics effects from the measured relative JER from reconstructed events in both MC and Data (See Section B.6).

Reconstructed C/A R=0.2	
Cut	Value
p_T	$p_{\mathrm{T}} > 7$ GeV
η	$\lvert\eta\rvert < 2.5$

Reconstructed anti-k_{T} R=0.4	
Cut	Value
$p_T^{1,2}$	$p_{\mathrm{T}} > 25$ GeV
η	$\lvert\eta\rvert < 2.5$
JVT Tool	True

Truth C/A R=0.2	
Cut	Value
p_T	$p_{\mathrm{T}} > 5$ GeV
η	$\lvert\eta\rvert < 2.5$
Matched to	Closest (ΔR) C/A R=0.2 Reco Jet

TABLE B.4. Object selection criteria applied in Run 2 study. Note the selection restricts the study to $|\eta| < 2.5$, since no MCJES calibrations exist above this region.

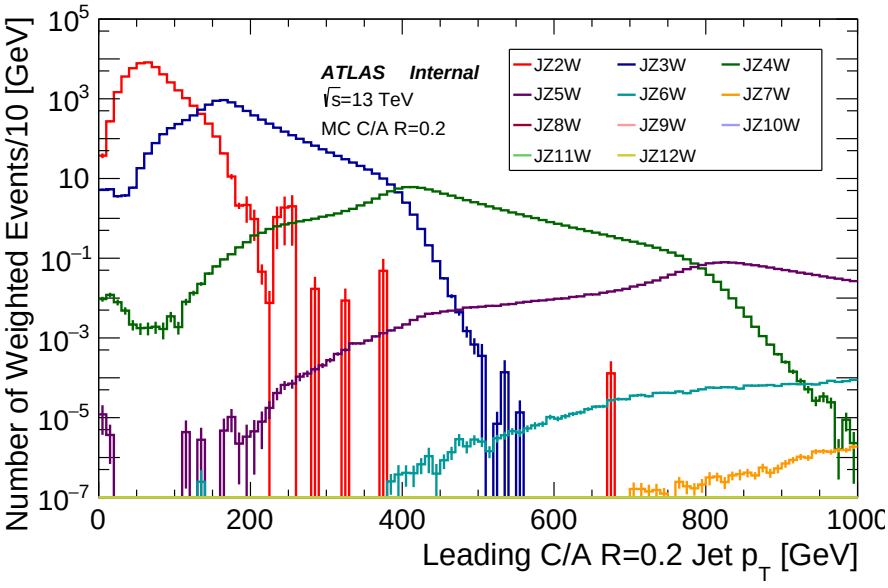

(a) Leading C/A R=0.2 p_T Distribution in MC after Event Selection

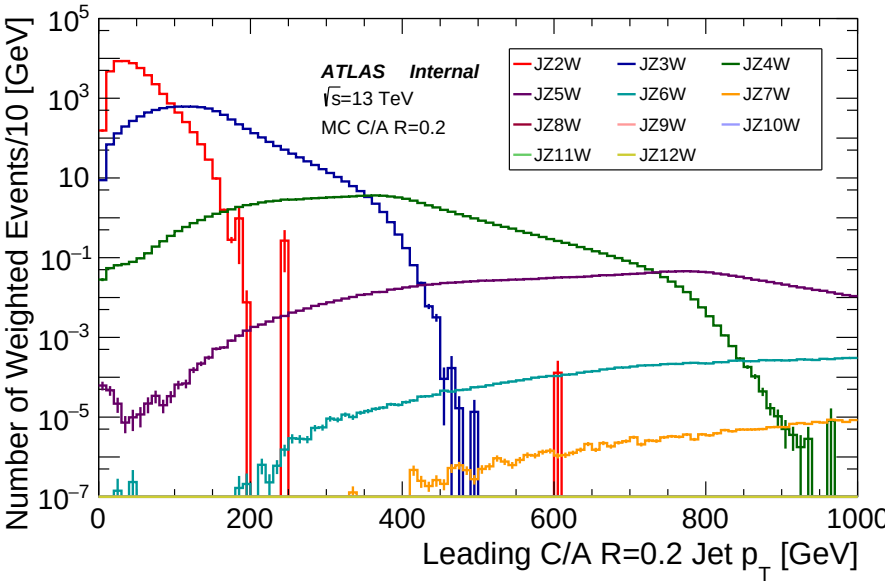

(b) Subleading C/A R=0.2 p_T Distribution in MC after Event Selection

FIGURE B.2. p_T profiles of leading and subleading, matched, C/A R=0.2 reconstructed jets. The event selection applied in the distributions includes requiring at least 2 well-calibrated R=0.4 anti-k_{T} jets. In addition, we require successfully matching C/A R=0.2 to both anti-k_{T} jets, and that the two leading, matched, C/A jets are back-to-back.

B.4. Matching Reconstructed R=0.2 C/A Jets to anti-k_{T} R=0.4 Jets

anti-k_{T} R=0.4 jets are well understood and serve as the base-line reconstructed jets used throughout ATLAS. The dijet MC samples are sliced in p_T ranges of anti-k_{T} R=0.6 truth jets (see Table B.1), and the HLT triggers considered in this study use anti-k_{T} R=0.4 jets. Hence, we use anti-k_{T} jets as reference objects.

The cone-size of C/A jets under investigation, R=0.2, tends to be too small to encompass full particle showers, especially at lower p_T. As a result, a single-parton shower may appear as multiple C/A R=0.2 jets. In the cases of this *jet splitting*, the ordering of the C/A jets becomes complex. Hence, we reorder the small-R jets to ensure the 'leading' and 'subleading' jets are indeed the most appropriate jets to include in the asymmetry distributions.

Consider the case of a dijet event with balanced leading and subleading anti-k_{T} R=0.4 jets, and a soft, third-leading jet. When we use C/A R=0.2 jets, this same event can have the leading and/or subleading jet split into two or more small-R jets. When this happens, the two highest p_T R=0.2 C/A jets may not necessarily be back-to-back; it may be that the two highest p_T R=0.2 jets are part of the same R=0.4 jet. The third-highest p_T jet may also no longer be associated to the soft jet from the anti-k_{T} collection. Thus, we use the leading and subleading R=0.4 anti-k_{T} jets as references objects to match the leading and subleading R=0.2 C/A jets.

The leading C/A R=0.2 jet is defined as the highest p_T jet within $\Delta R = 0.4$ of the leading anti-k_{T} R=0.4 jet. The subleading C/A R=0.2 is defined as the highest p_T jet within $\Delta R = 0.4$ of the subleading anti-k_{T} R=0.4 jet. Finally, the third-leading C/A R=0.2 jet is defined as the highest p_T jet in the event not already matched in the previous two steps. Following the matching, we can see that

most events have the third-leading jet collinear with one of the leading C/A R=0.2 jets, illustrated in Figure B.3.

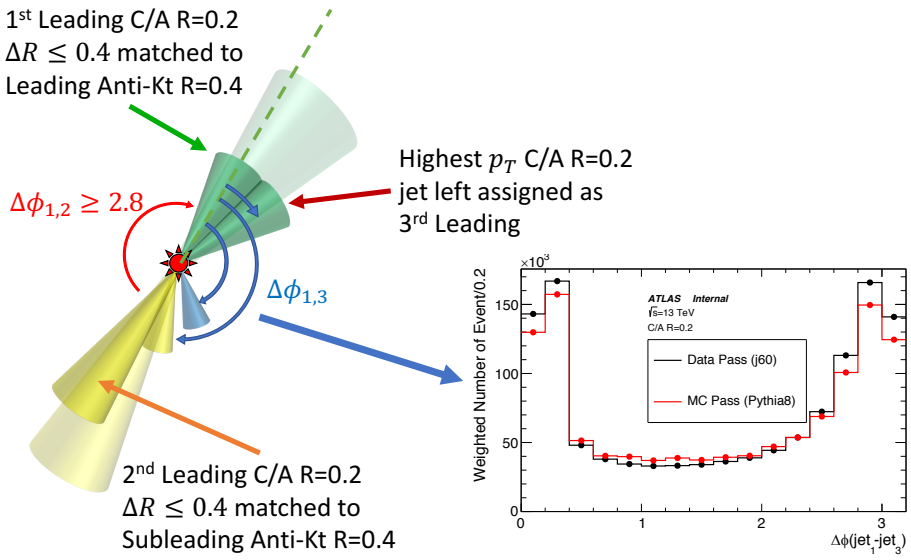

FIGURE B.3. Possible jet splittings from anti-k_T R=0.4 to C/A R=0.2 jets and a $\Delta\phi$ distribution between the matched first and third leading C/A R=0.2 jets. Passing criteria is having two back-to-back ($\Delta\phi \geq 2.8$) C/A R=0.2 matched jets, with $|\eta| < 0.8$. The data events populating the histogram are triggered with HLT_j60.

B.4.1. Fitting the Asymmetry Distributions

The relative JER and the width of the p_T asymmetry distribution are related by

$$\text{relative JER} = \frac{\sigma(\bar{p}_T)}{\bar{p}_T} = \sqrt{2}\sigma_A, \tag{B.4}$$

where $\bar{p}_T$ is the average p_T of the leading and subleading C/A R=0.2 jets selected using the procedure described in Section B.4. For each $\bar{p}_T$ bin, there is a separate asymmetry distribution per value of $p^3_{T,max} \in [10, 24]$. The distributions are inclusive in $p^3_{T,max}$, that is each distribution is a subset of the distributions with higher $p^3_{T,max}$ cuts. The full set of requirements is summarized in Table B.5.

Cut	Value
Data Quality	Pass
NJets	$N_{Akt}^{R=0.4} \geq 2$
Rapidity Constraint	$\lvert\eta_{C/A}^{1,2}\rvert \in [0, 0.8]$ or $\in [0.8, 2.5]$
Back-to-Back	$\Delta\phi(jet_{C/A}^{1}, jet_{C/A}^{2}) \geq 2.8$
$\bar{p}_T$-window	50-60 GeV
	60-70 GeV
	70-80 GeV
	80-100 GeV
	150-200 GeV
	200-300 GeV
	300-400 GeV
	400-600 GeV
	600-800 GeV
	800-1000 GeV
$p_{T,max}^{3}$	$p_{T,C/A}^{3} \leq p_{T,max}^{3} \in [10, 24]$ GeV

TABLE B.5. Summary of event-selection criteria for Run 2.

When calculating the asymmetry of the two-leading, matched, C/A R=0.2 jets, the randomized sign appearing in the asymmetry definition (Eqn: 5.7) is generated using the uniform distribution tool of the TRandom3 class. The $p_{T,3}^{max}$ range is [10,24] with a step size of 1 GeV. The range is kept above 10 GeV in order to have enough statistics to perform a fit. Once populated, the asymmetry distributions are fitted to Gauss functions using Root's histogram fitting machinery through TF1 objects. For any particular $\bar{p}_T$ bin, balanced jets with both leading and subleading jet p_T close to the $\bar{p}_T$ make up the central core of the distribution. Since there is no requirement placed on the p_T of the individual leading C/A R=0.2 jets, the distribution is also populated by events with higher (lower) p_T (sub)leading jets that are not well balanced; these higher p_T, imbalanced jets tend to populate the tails of the distributions. To mitigate this effect, we truncate the Gaussian fit to the central core of varying ranges between [-0.5,0.5] to [-

0.075,0.075], chosen based on goodness of fit to the central core of the distribution. The asymmetry bin-size is of 0.05 GeVfor most $\bar{p}_T$-bins, though this is increased to 0.1 for the bins suffering from low statistics.

B.5. Relative JER Extrapolation

To perform the extrapolation to $p^3_{T,max} = 0$ GeV, we measure the relative JER of a particular $\bar{p}_T$ bin at all values of $p^3_{T,max}$ and plot them as a function of the $p^3_{T,max}$ range. This allows us to examine the behavior of the relative JER and fit a function to the trend to $p^3_{T,max} = 0$ GeV. The fit used in the extrapolation is a simple line, where the y-intercept of the fit is the extrapolated JER and the uncertainty in the parameter fit becomes the uncertainty used in the $\bar{p}_T$ fits (Section B.6.1). Throughout the various $\bar{p}_T$ bins, the relative JER decreses with lower $p^3_{T,max}$ values. The lower values of $p^3_{T,max}$ have the largest uncertainty, due to low statistics. The width of the asymmetry distributions increase with decreasing $\bar{p}_T$, in part due to low statistics and the derivation skim requiring an R=1.0 anti-k_{T} jet with p_T of at least 100 GeV.

B.6. Removing Physics Effects from Measured Relative JER

An important detail is that the MC and data events used to measure the relative JERs have both detector and physics effects included. More specifically, MC events are simulated with a particular generator, in this case PYTHIA8, which produces the physics of the event, i.e. hadronization and showering. These simulations are then processed through a detector simulator that applies resolution and other effects inherent to the ATLAS detector, to more closely simulate data. Thus, the asymmetry distributions obtained have physics and detector effects

included. What is most useful to the collaboration is the detector-related relative JER behavior of the jets, hence we must subtract the physics effects from both MC and data. Since the truth MC objects are used as input for the detector simulation, they only capture the physics effects. Therefore, we can subtract the resolutions in quadrature as:

$$\left(\frac{\sigma(p_T)}{p_T}\right)^2_{measured} = \left(\frac{\sigma(p_T)}{p_T}\right)^2_{physics} + \left(\frac{\sigma(p_T)}{p_T}\right)^2_{detector} \tag{B.5}$$

$$\downarrow$$

$$\left(\frac{\sigma(p_T)}{p_T}\right)_{detector} = \sqrt{\left(\frac{\sigma(p_T)}{p_T}\right)^2_{data/MC} - \left(\frac{\sigma(p_T)}{p_T}\right)^2_{truth}} \tag{B.6}$$

The truth jets are ghost-matched to the (matched) C/A R=0.2 reconstructed jets and used to measure the physics effects. We associate the closest truth jet (in ΔR) to the reconstructed R=0.2 C/A jet in question. The corrections are performed after the relative JERs (asymmetry distribution widths) have been measured and the distributions are not altered. The subtraction occurs immediately before fitting the points to a line in extrapolations to $p^3_{T,max} = 0$ GeV, as shown in Figure B.4.

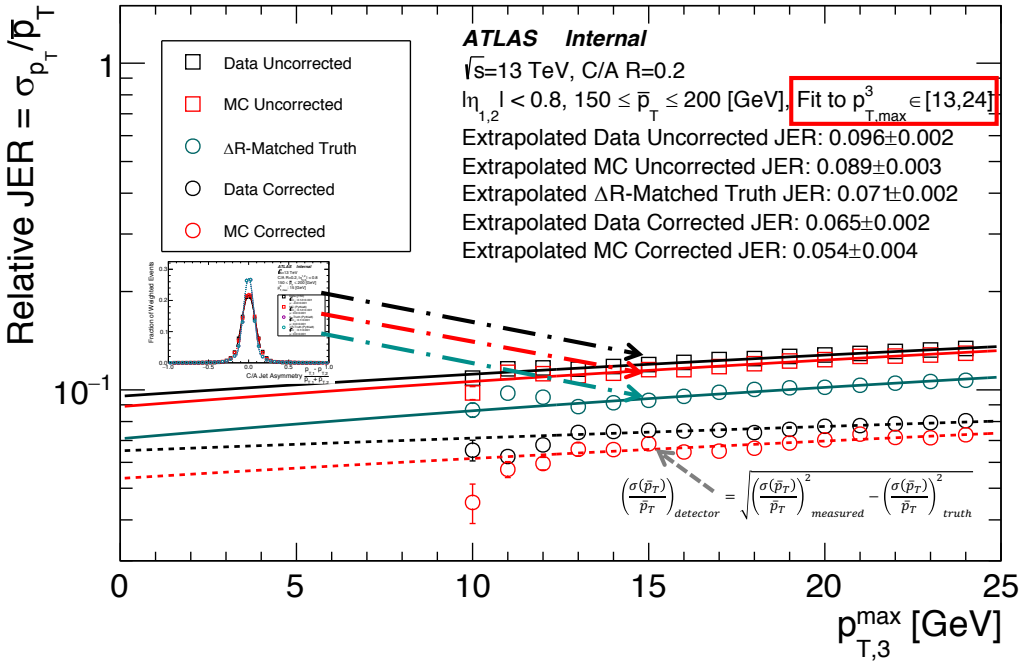

FIGURE B.4. Extrapolation of the relative JER against the range of $p^3_{T,max}$. Each asymmetry distribution's calculated relative JER becomes a single point on the graph, whose uncertainty is the Gaus width parameter fit uncertainty. The measured relative JER (square points) is subtracted in quadrature from its corresponding truth relative JER (teal circles) to yield the corrected (detector-effects) relative JER (red/black circles)

B.6.1. Relative JER as a Function of $\bar{p}_T$

Once the extrapolated JERs have been calculated for all $\bar{p}_T$ bins, with physics effects removed, we can examine the extrapolated JER as a function of $\bar{p}_T$, by fitting the points to the function:

$$\sqrt{\frac{a^2}{x^2} + \frac{b^2}{x} + c^2} \tag{B.7}$$

The parameter c can be interpreted as an asymptotic lower bound on the relative JER.

Figure B.5 shows the extrapolated JER for the entire $\bar{p}_T \in [50, 1000]$ GeV range for two eta ranges, $|\eta| \in [0, 0.8]$ and $[0.8, 2.5]$, and the fits to the distributions in data and MC. Each plot also shows the ratio of data/MC of the fitted functions.

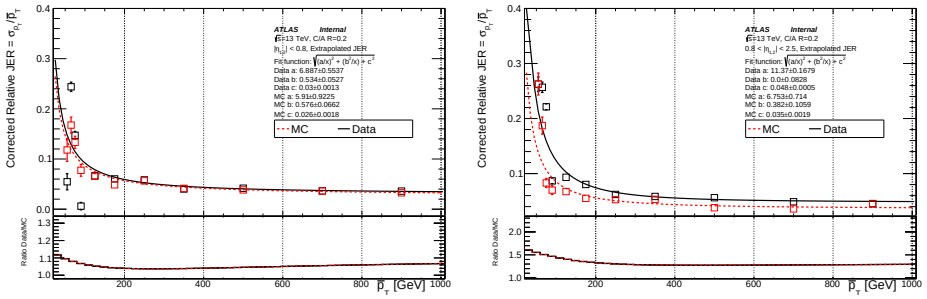

(a) Extrapolated relative JER vs. $\bar{p}_T$. Left is for $0 < |\eta| < 0.8$, right is for $0.8 < |\eta| < 2.5$

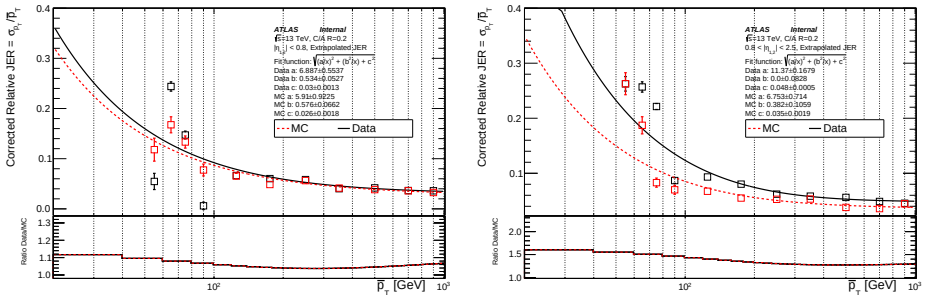

(b) Extrapolated relative JER vs. $\bar{p}_T$ with logarithmic $\bar{p}_T^{C/A}$. Left is for $0 < |\eta| < 0.8$, right is for $0.8 < |\eta| < 2.5$

FIGURE B.5. For each $\bar{p}_T$ bin, the relative JER is extrapolated as the y-axis of the fitted line. These extrapolations are then plotted against the range of $\bar{p}_T$ and fit to eqn. B.7.

B.7. Systematics Studies

It is important to quantify the systematic uncertainties of the selections used in the study. Table B.5, lists the cuts used in this analysis. The first required at least two R=0.4 anti-k_T jets. This cut's effects are not studied since decreasing the

cut will lead to matching failure of the C/A R=0.2 reco jets and increasing the cut to NJets≥3 cuts away too many events.

Regarding the pseudo rapidity requirement, the cut of $|\eta| \leq 2.5$ cannot be increased, since there are no calibrations for C/A R=0.2 jets above this value. The behavior within that range is studied by splitting it into two bins: $|\eta| < 0.8$ and $0.8 < |\eta| < 2.5$. It could be useful to further split the higher region further, but only these two regions are investigated in this study. The $\bar{p}_T$ range is split into several ranges, whereas the $p^3_{T,max}$ cut behavior is apparent through the extrapolation plots. Although no other cut was placed on the third-leading jet, a study to understand the behavior two types of events was done. The cross-check investigated the difference in behavior of events with 'co-linear' and 'uncorrelated' third jets. In Figure B.3, one can see that the bulk of the events are 'colinear', i.e. the third C/A jet is close to either the leading or subleading C/A jets. It can be argued that the third jet in colinear events may be a result of jet-splitting due to the restricted jet cone size.

The only requirement that can be properly studied through variations on the cut is that on the $\Delta\phi$ between leading jets. The cut is varied by ± 0.1 and the fit range of the gaussian function is chosen based on the Goodness of Fit of the truth distribution; the same fit range is used for MC, Data, and truth for a particular choice of $\bar{p}_T$ and $p^3_{T,max}$. Asymmetry distributions and extrapolations are summarized with Figure B.6. In conclusion, the variations only significantly affect the lowest $\bar{p}_T$ bins, where the events are already biased by the derivation skim. For any particular $\bar{p}_T$ bin, the distributions for lower $p^3_{T.max}$ cuts have greater variance

in the measured relative JER. In all, the effects are

$$\Delta \left(\frac{\sigma(p_T)}{p_T} \right)_{measured} \leq 0.02 \tag{B.8}$$

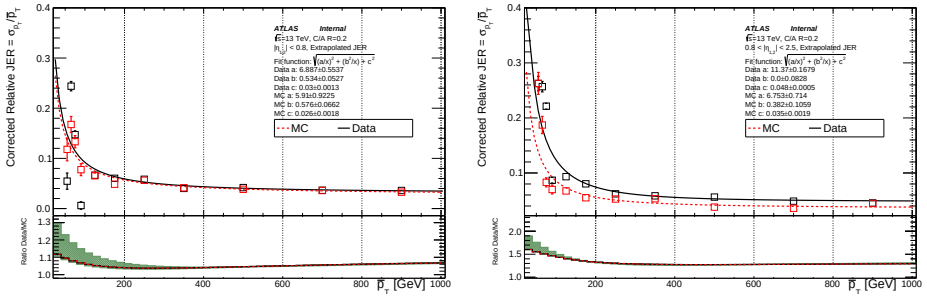

(a) Extrapolated relative JER vs. $\bar{p}_T$. Left is for $0 < |\eta| < 0.8$, right is for $0.8 < |\eta| < 2.5$

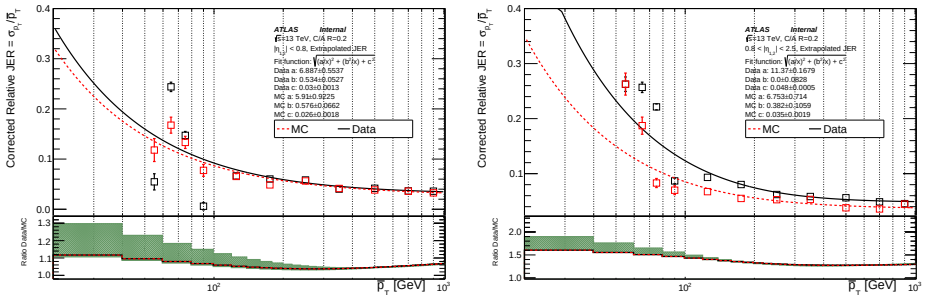

(b) Extrapolated relative JER vs. $\bar{p}_T$ with logarithmic $\bar{p}_T^{C/A}$. Left is for $0 < |\eta| < 0.8$, right is for $0.8 < |\eta| < 2.5$

FIGURE B.6. For each $\bar{p}_T$ bin, the corrected (detector-related) relative JER is extrapolated as the y-axis of the fitted line. These extrapolations are then plotted against the range of $\bar{p}_T$ and fit to eqn. B.7. Effects of variations on the $\Delta\phi$ cut of ± 0.1 corrected relative JER are shown by the shaded region.

B.8. Outlook of JER Studies

The most significant limitation of this study comes from skimming selection on the samples available. In the current JET/EtMiss derivations, only the JETM6 and JETM8 productions have the CaloCalTopoClusters needed to make the C/A jets. Of the derivations made, all productions have a skim on AntiKt10EMTopo

jets, the loosest being 100 GeV (used in this study). This skim removes low p_T events and its effects are evident in the bins at and below the $\bar{p}_T^{C/A} \in$ 80-100 GeV bin. The effect becomes intolerable below the 50-60 GeV bin, making it the lowest bin included in this study. Though the current resources do not allow for a JER measurement below this bin, it is important to produce samples with looser skims; ideally, we would have measurements down to a 20-30 GeV bin.

One motivation of measuring the JER to 20 GeV stems from the needs of the stop 0-lepton analysis which currently uses anti-k_{T} R=0.4 jet inputs to recluster top candidates with thresholds between 20-80 GeV. Given the small radius of the jets, the analysis would need a well-measured JER at least to 20 GeV, if not lower. The HEPTopTagger is another potential client of the results of this study–their worst uncertainties are in the low p_T range, hence measuring lower bins is what is most needed form this study for the tagger.

A consideration that can be further studied is the effect of the choice of shower generator on the JER measurements in MC. This study uses samples generated with PYTHIA8, as it may be of use to analysis teams using these results to know if similar results are obtained with other shower generators, e.g. Herwigg and Sherpa. An additional cross-check that could be useful is an investigation on closure with truth C/A R=0.2 jets, i.e. verify that the asymmetry of truth and reconstructed jets, on an event-by-event basis, are consistent.

Following these systematics studies, we would like to revisit JES calibrations. The current scheme calibrates C/A R=0.2-0.6 jets in increments of 0.05 by comparing truth to reconstructed jets in MC, i.e. MCJES calibrations. There are other possible calibration schemes that are data-driven, which are interesting to

consider. Finally, once the R=0.2 C/A jet studies have been fully understood, we can repeat the studies for C/A R=0.3 jets.

REFERENCES CITED

[1] Julia Woithe, Gerfried J Wiener, and Frederik F Van der Veken. Let's have a coffee with the Standard Model of particle physics! *Phys. Educ.*, 52(3): 034001. 9 p, 2017. doi: 10.1088/1361-6552/aa5b25. URL `http://cds.cern.ch/record/2270087`.

[2] Standard Model Summary Plots Summer 2019. Geneva, Jul 2019. URL `http://cds.cern.ch/record/2682186`.

[3] E. V. Karukes, P. Salucci, and G. Gentile. The dark matter distribution in the spiral NGC 3198 out to 0.22 R_{vir}. *Astron. Astrophys.*, 578:A13, 2015. doi: 10.1051/0004-6361/201425339.

[4] Douglas Clowe, Marusa Bradac, Anthony H. Gonzalez, Maxim Markevitch, Scott W. Randall, Christine Jones, and Dennis Zaritsky. A direct empirical proof of the existence of dark matter. *Astrophys. J.*, 648:L109–L113, 2006. doi: 10.1086/508162.

[5] Jong Soo Kim, Krzysztof Rolbiecki, Roberto Ruiz, Jamie Tattersall, and Torsten Weber. Prospects for natural SUSY. *Phys. Rev.*, D94(9):095013, 2016. doi: 10.1103/PhysRevD.94.095013.

[6] Christoph Borschensky, Michael Kraemer, Anna Kulesza, Michelangelo Mangano, Sanjay Padhi, Tilman Plehn, and Xavier Portell. Squark and gluino production cross sections in pp collisions at $\sqrt{s}$ = 13, 14, 33 and 100 TeV. *Eur. Phys. J.*, C74(12):3174, 2014. doi: 10.1140/epjc/s10052-014-3174-y.

[7] ATLAS Collaboration. Search for a scalar partner of the top quark in the jets plus missing transverse momentum final state at $\sqrt{s}$=13 TeV with the ATLAS detector. *JHEP*, 12:085, 2017. doi: 10.1007/JHEP12(2017)085.

[8] SUSY October 2019 Summary Plot Update. Geneva, Oct 2019. URL `https://cds.cern.ch/record/2697155`.

[9] Esma Mobs. The CERN accelerator complex. Complexe des accélérateurs du CERN. *CERN Document Server*, Jul 2016. URL `https://cds.cern.ch/record/2197559`. General Photo.

[10] Jean-Luc Caron. The LHC injection complex.. L'ensemble d'injection du LHC. AC Collection. Legacy of AC. Pictures from 1992 to 2002., May 1993. URL `https://cds.cern.ch/record/841568`.

[11] A. D. Martin, W. J. Stirling, R. S. Thorne, and G. Watt. Parton distributions for the LHC. *Eur. Phys. J.*, C63:189–285, 2009. doi: 10.1140/epjc/s10052-009-1072-5.

[12] CERN. Lhc machine outreach, 2019. URL `http://lhc-machine-outreach.web.cern.ch/lhc-machine-outreach/collisions.htm`.

[13] ATLAS Collaboration. Online luminosity public results, 2019. URL `https://twiki.cern.ch/twiki/bin/view/AtlasPublic/LuminosityPublicResultsRun2`.

[14] Michi Hostettler. LHC Luminosity Performance. *CERN Document Server*, May 2018. URL `https://cds.cern.ch/record/2319396`. Presented 21 Jun 2018.

[15] Morad Aaboud et al. Luminosity determination in pp collisions at $\sqrt{s} = 8$ TeV using the ATLAS detector at the LHC. *Eur. Phys. J.*, C76(12):653, 2016. doi: 10.1140/epjc/s10052-016-4466-1.

[16] CERN. Diagram of an LHC dipole magnet. Schéma d'un aimant dipôle du LHC. Public Image on CERN Document Server, Jun 1999. URL `https://cds.cern.ch/record/40524`.

[17] CERN. Slice through an LHC focusing magnet. Tranche quadripolaire LHC à travers la masse froide. Public Image on CERN Document Server, 2017. URL `https://cds.cern.ch/record/2284291`.

[18] G et al. Aad. The ATLAS Experiment at the CERN Large Hadron Collider. *JINST*, 3:S08003. 437 p, 2008. doi: 10.1088/1748-0221/3/08/S08003. URL `https://cds.cern.ch/record/1129811`. Also published by CERN Geneva in 2010.

[19] Matthias Schott and Monica Dunford. Review of single vector boson production in pp collisions at $\sqrt{s} = 7$ TeV. *Eur. Phys. J.*, C74:2916, 2014. doi: 10.1140/epjc/s10052-014-2916-1.

[20] Christian Lippmann. Particle identification. *Nucl. Instrum. Meth.*, A666: 148–172, 2012. doi: 10.1016/j.nima.2011.03.009.

[21] Dan (Ed.) Green. *At The Leading Edge*. World Scientific, 2010.

[22] M (CERN) Aleksa, W (Pittsburgh) Cleland, Y (Tokyo) Enari, M (Victoria) Fincke-Keeler, L (CERN) Hervas, F (BNL) Lanni, S (Oregon) Majewski, C (Victoria) Marino, and I (LAPP) Wingerter-Seez. ATLAS Liquid Argon Calorimeter Phase-I Upgrade Technical Design Report. Technical Report CERN-LHCC-2013-017. ATLAS-TDR-022, ATLAS, Sep 2013. URL `https://cds.cern.ch/record/1602230`. Final version presented to December 2013 LHCC.

[23] ATLAS Collaboration. *ATLAS liquid-argon calorimeter: Technical Design Report*. Technical Design Report ATLAS. CERN, Geneva, 1996. URL `https://cds.cern.ch/record/331061`.

[24] Ana Maria Henriques Correia. The ATLAS Tile Calorimeter. Technical Report ATL-TILECAL-PROC-2015-002, CERN, Geneva, Mar 2015. URL `https://cds.cern.ch/record/2004868`.

[25] Particle Data Group. Review of particle physics. *Phys. Rev. D*, 98:030001, Aug 2018. doi: 10.1103/PhysRevD.98.030001. URL `https://link.aps.org/doi/10.1103/PhysRevD.98.030001`.

[26] ATLAS Collaboration. *ATLAS muon spectrometer: Technical Design Report*. Technical Design Report ATLAS. CERN, Geneva, 1997. URL `https://cds.cern.ch/record/331068`.

[27] Morad et al. Aaboud. Performance of the ATLAS Trigger System in 2015. Performance of the ATLAS Trigger System in 2015. *Eur. Phys. J. C*, 77 (CERN-EP-2016-241. 5):317. 76 p, Nov 2016. doi: 10.1140/epjc/s10052-017-4852-3. URL `https://cds.cern.ch/record/2235584`. 77 pages in total, author list starting page 61, 50 figures, 1 table. Published in Eur. Phys. J. C. All figures including auxiliary figures are available at http://atlas.web.cern.ch/Atlas/GROUPS/PHYSICS/PAPERS/TRIG-2016-01/.

[28] Stefan Hoche. Introduction to parton-shower event generators. *arXiv*, pages 235–295, 2015. doi: 10.1142/9789814678766_0005.

[29] C Kourkoumelis and S Vourakis. HYPATIA—an online tool for ATLAS event visualization. *Physics Education*, 49(1):21–32, dec 2013. doi: 10.1088/0031-9120/49/1/21. URL `https://doi.org/10.1088`.

[30] Matteo Cacciari, Gavin P. Salam, and Gregory Soyez. The Anti-k_t jet clustering algorithm. *JHEP*, 04:063, 2008. doi: 10.1088/1126-6708/2008/04/063.

[31] M. Aaboud et al. Jet energy scale measurements and their systematic uncertainties in proton-proton collisions at $\sqrt{s} = 13$ TeV with the ATLAS detector. *Phys. Rev.*, D96(7):072002, 2017. doi: 10.1103/PhysRevD.96.072002.

[32] Baptiste Abeloos, Steven Patrick Alkire, Jonathan David Bossio Sola, Eric Edward Corrigan, Jeffrey Dandoy, Meghan Frate, Christopher Grud, Arthur James Horton, Aliaksei Hrynevich, Rebecca Anne Linck, Bogdan Malaescu, Yasuyuki Okumura, Jacob Henry Rawling, Maximilian Swiatlowski, Nikola Makovec, and Katherine Pachal. Jet energy scale public plots for Moriond 2017. Geneva, Feb 2017. URL `https://cds.cern.ch/record/2253211`.

[33] ATLAS Collaboration. Search for the Supersymmetric Partner of the Top Quark in the Jets+Emiss Final State at sqrt(s) = 13 TeV. Technical Report ATLAS-COM-CONF-2016-064, CERN, Geneva, Jul 2016. URL `https://cds.cern.ch/record/2200175`.

[34] ATLAS Collaboration. Search for a scalar partner of the top quark in the jets plus missing transverse momentum final state at $\sqrt{s} = 13$ TeV with the ATLAS detector, 2017.

[35] Frederik Rühr. Prospects for BSM searches at the high-luminosity LHC with the ATLAS detector. *Nucl. Part. Phys. Proc.*, 273-275:625–630, 2016. doi: 10.1016/j.nuclphysbps.2015.09.094.

[36] Matthew D. Schwartz. *Quantum Field Theory and the Standard Model*. Cambridge University Press, 2014. ISBN 1107034736, 9781107034730.

[37] J. Alwall et al. The automated computation of tree-level and next-to-leading order differential cross sections, and their matching to parton shower simulations. *JHEP*, 07:079, 2014. doi: 10.1007/JHEP07(2014)079.

[38] Stefano Catani, Leandro Cieri, Giancarlo Ferrera, Daniel de Florian, and Massimiliano Grazzini. Vector boson production at hadron colliders: a fully exclusive QCD calculation at NNLO. *Phys. Rev. Lett.*, 103:082001, 2009. doi: 10.1103/PhysRevLett.103.082001.

[39] Michał Czakon, Paul Fiedler, and Alexander Mitov. Total Top-Quark Pair-Production Cross Section at Hadron Colliders Through $\mathcal{O}(\alpha_S^4)$. *Phys. Rev. Lett.*, 110:252004, 2013. doi: 10.1103/PhysRevLett.110.252004.

[40] Michal Czakon and Alexander Mitov. NNLO corrections to top pair production at hadron colliders: the quark-gluon reaction. *JHEP*, 01:080, 2013. doi: 10.1007/JHEP01(2013)080.

[41] Michal Czakon and Alexander Mitov. NNLO corrections to top-pair production at hadron colliders: the all-fermionic scattering channels. *JHEP*, 12:054, 2012. doi: 10.1007/JHEP12(2012)054.

[42] Peter Bärnreuther, Michal Czakon, and Alexander Mitov. Percent Level Precision Physics at the Tevatron: First Genuine NNLO QCD Corrections to $q\bar{q} \to t\bar{t} + X$. *Phys. Rev. Lett.*, 109:132001, 2012. doi: 10.1103/PhysRevLett.109.132001.

[43] Matteo Cacciari, Michal Czakon, Michelangelo Mangano, Alexander Mitov, and Paolo Nason. Top-pair production at hadron colliders with next-to-next-to-leading logarithmic soft-gluon resummation. *Phys. Lett.*, B710:612–622, 2012. doi: 10.1016/j.physletb.2012.03.013.

[44] Michal Czakon and Alexander Mitov. Top++: A Program for the Calculation of the Top-Pair Cross-Section at Hadron Colliders. *Comput. Phys. Commun.*, 185:2930, 2014. doi: 10.1016/j.cpc.2014.06.021.

[45] J. J. Thomson. On the structure of the atom: an investigation of the stability and periods of oscillation of a number of corpuscles arranged at equal intervals around the circumference of a circle; with application of the results to the theory of atomic structure. *Phil. Mag. Ser.6*, 7(39):237–265, 1904. doi: 10.1080/14786440409463107.

[46] E. Rutherford. Collision of alpha particles with light atoms. IV. An anomalous effect in nitrogen. *Phil. Mag. Ser.6*, 37:581–587, 1919. doi: 10.1080/14786431003659230. [Phil. Mag.90,no.sup1,31(2010)].

[47] Albert Einstein. The Collected Papers of Albert Einstein, Volume 2 (English): The Swiss Years: Writings, 1900-1909. (English translation supplement) . *Princeton University Press*, pages 140–174, 1990.

[48] Yvette Kosmann-Schwarzbach. *The Noether Theorems: Invariance and Conservation Laws in the Twentieth Century*. Springer, 2011.

[49] Emmy Noether. Invariant Variation Problems. *Gott. Nachr.*, 1918:235–257, 1918. doi: 10.1080/00411457108231446. [Transp. Theory Statist. Phys.1,186(1971)].

[50] Yvette Kosmann-Schwarzbach. *The Noether Theorems: Invariance and Conservation Laws in the Twentieth Century*. Springer, 2011.

[51] J. Goldstone. Field Theories with Superconductor Solutions. *Nuovo Cim.*, 19: 154–164, 1961. doi: 10.1007/BF02812722.

[52] The ATLAS Collaboration. Observation of a new particle in the search for the Standard Model Higgs boson with the ATLAS detector at the LHC. Observation of a new particle in the search for the Standard Model Higgs boson with the ATLAS detector at the LHC. *Phys. Lett. B*, 716 (arXiv:1207.7214. CERN-PH-EP-2012-218):1–29. 29 p, Aug 2012. doi: 10.1016/j.physletb.2012.08.020. URL `http://cds.cern.ch/record/1471031`. Comments: 24 pages plus author list (38 pages total), 12 figures, 7 tables, revised author list.

[53] The CMS Collaboration. Observation of a new boson at a mass of 125 GeV with the CMS experiment at the LHC. Observation of a new boson at a mass of 125 GeV with the CMS experiment at the LHC. *Phys. Lett. B*, 716 (CMS-HIG-12-028. CMS-HIG-12-028. CERN-PH-EP-2012-220):30–61. 32 p, Jul 2012. doi: 10.1016/j.physletb.2012.08.021. URL `http://cds.cern.ch/record/1471016`.

[54] Luigi Di Lella and Carlo Rubbia. The Discovery of the W and Z Particles. *Adv. Ser. Dir. High Energy Phys.*, 23:137–163, 2015. doi: 10.1142/9789814644150_0006. URL `https://cds.cern.ch/record/2103277`.

[55] Dirk Graudenz. The physics of the Standard Model Higgs boson at the LHC. *CERN Document Server*, pages 65–70. 6 p, Apr 1995. URL `https://cds.cern.ch/record/279995`.

[56] Takaaki Kajita. Atmospheric neutrino results from Super-Kamiokande and Kamiokande: Evidence for neutrino(mu) oscillations. *Nucl. Phys. Proc. Suppl.*, 77:123–132, 1999. doi: 10.1016/S0920-5632(99)00407-7. [,123(1998)].

[57] P. A. R. Ade et al. Planck 2013 results. I. Overview of products and scientific results. *Astron. Astrophys.*, 571:A1, 2014. doi: 10.1051/0004-6361/201321529.

[58] Vera C. Rubin and W. Kent Ford, Jr. Rotation of the Andromeda Nebula from a Spectroscopic Survey of Emission Regions. *Astrophys. J.*, 159:379–403, 1970. doi: 10.1086/150317.

[59] Douglas Clowe, Marusa Bradac, Anthony H. Gonzalez, Maxim Markevitch, Scott W. Randall, Christine Jones, and Dennis Zaritsky. A direct empirical proof of the existence of dark matter. *Astrophys. J.*, 648:L109–L113, 2006. doi: 10.1086/508162.

[60] Morad Aaboud et al. Search for squarks and gluinos in final states with jets and missing transverse momentum using 36 fb^{-1} of $\sqrt{s} = 13$ TeV pp collision data with the ATLAS detector. *Phys. Rev.*, D97(11):112001, 2018. doi: 10.1103/PhysRevD.97.112001.

[61] ATLAS Collaboration. A search for top squarks with R-parity-violating decays to all-hadronic final states with the ATLAS detector in $\sqrt{s} = 8$ TeV proton–proton collisions. *JHEP*, 06:067, 2016. doi: 10.1007/JHEP06(2016)067.

[62] CMS Collaboration. Search for direct production of supersymmetric partners of the top quark in the all-jets final state in proton-proton collisions at 13 TeV. *JHEP*, 10:005, 2017. doi: 10.1007/JHEP10(2017)005.

[63] O.S. Bruning et al. (eds.). Lhc design report, vol. 1: The lhc main rings, 2004.

[64] E. Cockcroft J., Walton. Disintegration of lithium by swift protons. *Nature*, 129:649, 1932. doi: 10.1038/129649a0.

[65] Per F. Dahl. Rolf Wideroe: Progenitor of Particle Accelerators. *FermiLab Library Server*, 1992.

[66] Ernest O. Lawrence and M. Stanley Livingston. The production of high speed light ions without the use of high voltages. *Phys. Rev.*, 40:19–35, 1932. doi: 10.1103/PhysRev.40.19.

[67] Edwin M. McMillan. The Synchrotron-A Proposed High Energy Particle Accelerator. *Phys. Rev.*, 68:143–144, 1945. doi: 10.1103/PhysRev.68.143.

[68] CERN, editor. *Convention for the establishment of a European organization for nuclear research: Paris, 1st July, 1953 : as amended. Convention pour l'établissement d'une Organisation européenne pour la Recherche nucléaire. Paris, le 1er juillet 1953 : telle qu'elle a été modifiée*. CERN Document Server, Geneva, 1971. URL `https://cds.cern.ch/record/330625`.

[69] Luigi Di Lella and Carlo Rubbia. The Discovery of the W and Z Particles. *Adv. Ser. Dir. High Energy Phys.*, 23:137–163, 2015. doi: 10.1142/9789814644150_0006. URL `https://cds.cern.ch/record/2103277`.

[70] Thomas Taylor and Daniel Treille. The Large Electron Positron Collider (LEP): Probing the Standard Model. *Adv. Ser. Direct. High Energy Phys.*, 27: 217–261, 2017. doi: 10.1142/9789814749145_0007.

[71] Jorg Wenninger. Operation and Configuration of the LHC in Run 2. *CERN Document Server*, Mar 2019. URL `https://cds.cern.ch/record/2668326`.

[72] Daniel Boussard and Trevor Paul R Linnecar. The LHC Superconducting RF System. Technical Report LHC-Project-Report-316. CERN-LHC-Project-Report-316, CERN, Geneva, Dec 1999. URL `https://cds.cern.ch/record/410377`.

[73] S et al. Chatrchyan. The CMS experiment at the CERN LHC. The Compact Muon Solenoid experiment. *JINST*, 3:S08004. 361 p, 2008. doi: 10.1088/1748-0221/3/08/S08004. URL `https://cds.cern.ch/record/1129810`. Also published by CERN Geneva in 2010.

[74] K et al. Aamodt. The ALICE experiment at the CERN LHC. A Large Ion Collider Experiment. *JINST*, 3:S08002. 259 p, 2008. doi: 10.1088/1748-0221/3/08/S08002. URL `https://cds.cern.ch/record/1129812`. Also published by CERN Geneva in 2010.

[75] A Augusto et al. Alves. The LHCb Detector at the LHC. *JINST*, 3 (LHCb-DP-2008-001. CERN-LHCb-DP-2008-001):S08005, 2008. doi: 10.1088/1748-0221/3/08/S08005. URL `https://cds.cern.ch/record/1129809`. Also published by CERN Geneva in 2010.

[76] Sergei Nagaitsev. Fermilab Antiproton Source, Recycler Ring, and Main Injector. *FermiLab Library Server*, 2013.

[77] Lyndon R Evans and Philip (eds.) Bryant. LHC Machine. *JINST*, 3:S08001. 164 p, 2008. doi: 10.1088/1748-0221/3/08/S08001. URL `http://cds.cern.ch/record/1129806`. This report is an abridged version of the LHC Design Report (CERN-2004-003).

[78] ATLAS Collaboration. Luminosity Determination in pp Collisions at sqrt(s) = 7 TeV using the ATLAS Detector in 2011. *CERN Document Server*, 2011.

[79] ATLAS Collaboration. Luminosity determination in *pp* collisions at $\sqrt{s} = 13$ TeV using the ATLAS detector at the LHC. Technical Report ATLAS-CONF-2019-021, CERN, Geneva, Jun 2019. URL `http://cds.cern.ch/record/2677054`.

[80] B. Muratori and T. Pieloni. Luminosity levelling techniques for the LHC. *CERN Yellow Report*, pages 177–181. 5 p, Oct 2014. doi: 10.5170/CERN-2014-004.177. URL `https://cds.cern.ch/record/1957033`. Comments: 5 pages, contribution to the ICFA Mini-Workshop on Beam-Beam Effects in Hadron Colliders, CERN, Geneva, Switzerland, 18-22 Mar 2013.

[81] L Rossi. State-of-the-art superconducting accelerator magnets. *IEEE Trans. Appl. Supercond.*, 12(LHC-Project-Report-541. CERN-LHC-Project-Report-541. 1):219–227. 9 p, Mar 2002. doi: 10.1109/TASC.2002.1018387. URL `https://cds.cern.ch/record/592967`.

[82] ATLAS Collaboration. ATLAS: letter of intent for a general-purpose pp experiment at the large hadron collider at CERN. *CERN Document Server*, 1992. URL https://cds.cern.ch/record/291061.

[83] Manuella G. Vincter and Juergen Thomas. Commissioning of the ATLAS Experiment. *PoS*, 2008LHC:028, 2008. doi: 10.22323/1.055.0028.

[84] J Moss. Commissioning and Operation of the ATLAS Pixel Detector. Technical Report ATL-INDET-PROC-2010-038, CERN, Geneva, Nov 2010. URL https://cds.cern.ch/record/1305879.

[85] Alessandro La Rosa and Alessandro La Rosa. The ATLAS Insertable B-Layer: from construction to operation. Technical Report ATL-INDET-PROC-2016-004. 12, CERN, Geneva, Oct 2016. URL https://cds.cern.ch/record/2221972.

[86] Alessandro La Rosa. The ATLAS Insertable B-Layer: from construction to operation. *JINST*, 11(12):C12036, 2016. doi: 10.1088/1748-0221/11/12/C12036.

[87] J Tojo. ATLAS SemiConductor Tracker Operation and Performance. *CERN Document Server*, Jul 2011. URL https://cds.cern.ch/record/1363645.

[88] JM Stahlman. Commissioning and Performance of the ATLAS Transition Radiation Tracker with First High Energy pp and Pb-Pb collisions at LHC. Technical Report ATL-INDET-PROC-2011-005, CERN, Geneva, Sep 2011. URL https://cds.cern.ch/record/1381599.

[89] A Vogel. ATLAS Transition Radiation Tracker (TRT): Straw Tube Gaseous Detectors at High Rates. Geneva, Apr 2013. URL https://cds.cern.ch/record/1537991.

[90] H H J ten Kate. ATLAS superconducting toroids and solenoid. *IEEE Trans. Appl. Supercond.*, 15(2 pt.2):1267–1270. 4 p, 2005. doi: 10.1109/TASC.2005.849560. URL https://cds.cern.ch/record/912244.

[91] Morad Aaboud et al. Performance of the ATLAS Trigger System in 2015. *Eur. Phys. J.*, C77(5):317, 2017. doi: 10.1140/epjc/s10052-017-4852-3.

[92] ATLAS Collaboration. Performance of the ATLAS Trigger System in 2015. *Eur. Phys. J. C*, 77:317, 2017. doi: 10.1140/epjc/s10052-017-4852-3.

[93] Catrin Bernius. HL-LHC prospects from ATLAS and CMS. Technical Report ATL-PHYS-PROC-2019-023, CERN, Geneva, Mar 2019. URL https://cds.cern.ch/record/2666331.

[94] ATLAS Collaboration. Topological cell clustering in the ATLAS calorimeters and its performance in LHC Run 1. *Eur. Phys. J.*, C77:490, 2017. doi: 10.1140/epjc/s10052-017-5004-5.

[95] Benjamin Nachman, Pascal Nef, Ariel Schwartzman, Maximilian Swiatlowski, and Chaowaroj Wanotayaroj. Jets from Jets: Re-clustering as a tool for large radius jet reconstruction and grooming at the LHC. *JHEP*, 02:075, 2015. doi: 10.1007/JHEP02(2015)075.

[96] Stephen P. Martin. A Supersymmetry primer. *arXiv*, pages 1–98, 1997. doi: 10.1142/9789812839657_0001, 10.1142/9789814307505_0001. [Adv. Ser. Direct. High Energy Phys.18,1(1998)].

[97] ATLAS Collaboration. The ATLAS Simulation Infrastructure. *Eur. Phys. J. C*, 70:823, 2010. doi: 10.1140/epjc/s10052-010-1429-9.

[98] S. Agostinelli et al. Geant4 - a simulation toolkit. *Nuclear Instruments and Methods in Physics Research Section A: Accelerators, Spectrometers, Detectors and Associated Equipment*, 506(3):250–303, 2003. doi: https://doi.org/10.1016/S0168-9002(03)01368-8.

[99] Torbjörn Sjöstrand, Stephen Mrenna, and Peter Z. Skands. PYTHIA 6.4 Physics and Manual. *JHEP*, 05:026, 2006. doi: 10.1088/1126-6708/2006/05/026.

[100] Torbjörn Sjöstrand, Stephen Mrenna, and Peter Z. Skands. A Brief Introduction to PYTHIA 8.1. *Comput. Phys. Commun.*, 178:852–867, 2008. doi: 10.1016/j.cpc.2008.01.036.

[101] Anders Ryd, David Lange, Natalia Kuznetsova, Sophie Versille, Marcello Rotondo, David P. Kirkby, Frank K. Wuerthwein, and Akimasa Ishikawa. EvtGen: A Monte Carlo Generator for B-Physics, 2005.

[102] Richard D. Ball et al. Parton distributions with LHC data. *Nucl. Phys.*, B867: 244–289, 2013. doi: 10.1016/j.nuclphysb.2012.10.003.

[103] ATLAS Collaboration. ATLAS Pythia 8 tunes to 7 TeV data. ATL-PHYS-PUB-2014-021, 2014. URL `https://cds.cern.ch/record/1966419`.

[104] Leif Lönnblad and Stefan Prestel. Merging multi-leg NLO matrix elements with parton showers. *JHEP*, 03:166, 2013. doi: 10.1007/JHEP03(2013)166.

[105] Wim Beenakker, Christoph Borschensky, Michael Krämer, Anna Kulesza, and Eric Laenen. NNLL-fast: predictions for coloured supersymmetric particle production at the LHC with threshold and Coulomb resummation. *JHEP*, 12: 133, 2016. doi: 10.1007/JHEP12(2016)133.

[106] W. Beenakker, M. Krämer, T. Plehn, M. Spira, and P. M. Zerwas. Stop production at hadron colliders. *Nucl. Phys. B*, 515:3, 1998.

[107] Wim Beenakker, Silja Brensing, Michael Krämer, Anna Kulesza, Eric Laenen, and Irene Niessen. Supersymmetric top and bottom squark production at hadron colliders. *JHEP*, 08:098, 2010. doi: 10.1007/JHEP08(2010)098.

[108] Wim Beenakker, Christoph Borschensky, Raphael Heger, Michael Krämer, Anna Kulesza, and Eric Laenen. NNLL resummation for stop pair-production at the LHC. *JHEP*, 05:153, 2016. doi: 10.1007/JHEP05(2016)153.

[109] Jon Butterworth et al. PDF4LHC recommendations for LHC Run II. *J. Phys.*, G43:023001, 2016. doi: 10.1088/0954-3899/43/2/023001.

[110] T. Gleisberg, Stefan. Hoeche, F. Krauss, M. Schonherr, S. Schumann, F. Siegert, and J. Winter. Event generation with SHERPA 1.1. *JHEP*, 02: 007, 2009. doi: 10.1088/1126-6708/2009/02/007.

[111] Simone Alioli, Paolo Nason, Carlo Oleari, and Emanuele Re. A general framework for implementing NLO calculations in shower Monte Carlo programs: the POWHEG BOX. *JHEP*, 06:043, 2010. doi: 10.1007/JHEP06(2010)043.

[112] Johannes Bellm et al. Herwig 7.0/Herwig++ 3.0 release note. *Eur. Phys. J.*, C76(4):196, 2016. doi: 10.1140/epjc/s10052-016-4018-8.

[113] ATLAS Collaboration. Studies on top-quark Monte Carlo modelling for Top2016. ATL-PHYS-PUB-2016-020, 2016. URL `https://cds.cern.ch/record/2216168`.

[114] John Kenneth Anders and Monica D'Onofrio. V+Jets theoretical uncertainties estimation via a parameterisation method. Technical Report ATL-COM-PHYS-2016-044, CERN, Geneva, Jan 2016. URL `https://cds.cern.ch/record/2125718`.

[115] ATLAS Collaboration. Selection of jets produced in 13 TeV proton–proton collisions with the ATLAS detector. ATLAS-CONF-2015-029, 2015. URL `https://cds.cern.ch/record/2037702`.

[116] ATLAS Collaboration. Tagging and suppression of pileup jets with the ATLAS detector. ATLAS-CONF-2014-018, 2014. URL `https://cds.cern.ch/record/1700870`.

[117] ATLAS Collaboration. Jet Smearing Twiki, 2019. URL `https://twiki.cern.ch/twiki/bin/view/AtlasProtected/JetSmearing`.

[118] Vasiliki Kouskoura, Walter Hopkins, Michael Samuel Albergo, Michael Begel, Johan Sebastian Bonilla, David Dodsworth, Melissa Franklin, Nicolas Maximilian Kohler, Dave Lewis, Christian Luedtke, Stephanie Majewski, Mario Martinez-Perez, Fabrizio Miano, Philipp Mogg, Frank Paige, George Redlinger, Andrea Rodriguez Perez, Christopher Sean Rogan, Frederik Ruehr, Pasquale Fabrizio Salvatore, Ian Michael Snyder, Siyuan Sun, Kerim Suruliz, Martin Tripiana, Chaowaroj Wanotayaroj, Iacopo Vivarelli, Davide Costanzo, Calum Michael Macdonald, Silvia Fracchia, Matthias Saimpert, Matthew Anthony, Baptiste Ravina, Samuel David Jones, and Siqi Yuan. Search for the Supersymmetric Partner of the Top Quark in the Jets+ETmiss Final State at $\sqrt{s} = 13$ TeV . Technical Report ATL-COM-PHYS-2016-1625, CERN, Geneva, Nov 2016. URL `https://cds.cern.ch/record/2231921`.

[119] ATLAS Collaboration. Measurements of top-quark pair spin correlations in the $e\mu$ channel at $\sqrt{s} = 13\,\text{TeV}$ using pp collisions in the ATLAS detector. *Eur. Phys. J.*, 2019.

[120] James Ferrando, Matthias Saimpert, Markus Cristinziani, and Geoffrey Gilles. ATLAS b-jet identification performance and efficiency measurement with $t\bar{t}$ events in pp collisions at $\sqrt{s} = 13$ TeV - Paper draft of ANA-FTAG-2018-01: Paper draft of ANA-FTAG-2018-01. Technical Report ATL-COM-PHYS-2019-056, CERN, Geneva, Feb 2019. URL `https://cds.cern.ch/record/2655511`.

[121] ATLAS Collaboration. $E_{\text{T}}^{\text{miss}}$ performance in the ATLAS detector using 2015–2016 LHC pp collisions. ATLAS-CONF-2018-023, 2018. URL `https://cds.cern.ch/record/2625233`.

[122] ATLAS Collaboration. ATLAS simulation of boson plus jets processes in Run 2. Technical Report ATL-PHYS-PUB-2017-006, CERN, Geneva, May 2017. URL `http://cds.cern.ch/record/2261937`.

[123] M. Baak, G. J. Besjes, D. Côté, A. Koutsman, J. Lorenz, and D. Short. Histfitter software framework for statistical data analysis. *The European Physical Journal C*, 75(4):153, Apr 2015. ISSN 1434-6052. doi: 10.1140/epjc/s10052-015-3327-7. URL `https://doi.org/10.1140/epjc/s10052-015-3327-7`.

[124] Matteo Cacciari, Gavin P. Salam, and Gregory Soyez. FastJet User Manual. *Eur. Phys. J.*, C72:1896, 2012. doi: 10.1140/epjc/s10052-012-1896-2.

[125] ATLAS Collaboration. JSV Production Twiki, 2019. https://twiki.cern.ch/twiki/bin/view/AtlasProtected/JsvProduction.